Øyvind Østrem

Cathode wear in Hall-Héroult cells

Thesis for the degree of Philosophiae Doctor

Trondheim, February 2013

Norwegian University of Science and Technology
Faculty of Natural Sciences and Technology
Department of Materials Science and Engineering

NTNU – Trondheim
Norwegian University of
Science and Technology

NTNU
Norwegian University of Science and Technology

Thesis for the degree of Philosophiae Doctor

Faculty of Natural Sciences and Technology
Department of Materials Science and Engineering

ISBN 978-82-471-4159-5 (printed ver.)
ISBN 978-82-471-4160-1 (electronic ver.)
ISSN 1503-8181

Doctoral theses at NTNU, 2013:34
IMT-Report 2013:171

Printed by NTNU-trykk

“Medio tutissimus ibis.”

(You will be safest in the middle.)

Ovid (43 BC – 17 AD), Metamorphoses

Preface

This thesis is submitted to the Norwegian University of Science and Technology (NTNU) in partial fulfilment of the requirements for the degree of Philosophiae doctor. The doctoral work has been performed at the Department of Materials Science and Technology at NTNU under supervision of adjunct Professor Christian Rosenkilde and Egil Skybakmoen (Head of Research, SINTEF Materials and Chemistry). The work was financed by Norsk Hydro ASA and the Research Council of Norway, through the user-driven innovation project “Process Innovations for Higher Current Densities” (PI-HCD).

Initially, the doctoral work was focused on microscopy investigations of industrial cathode samples, and the main task during the first year was development of sampling techniques and sample preparation. To increase the scientific yield, it was later decided to include work on laser scanning of industrial cathodes and some fundamental laboratory scale experiments.

The thesis is divided into eight chapters. An introduction to the topic, a literature survey and some thermodynamics are covered in the first three chapters. Chapter 4 treats laser scanning of industrial cathodes, a work managed by E. Skybakmoen. The doctoral candidate assisted in the planning and execution of measurement campaigns, the treatment of obtained results, and in the writing of the two papers enclosed in Appendix A. The microscopy investigation of samples from industrial cathodes is found in Chapter 5, and Chapter 6 covers the laboratory experiments. In Chapter 7, a more comprehensive discussion, based on results from the three previous chapters as well as the literature, is given in an attempt to intertwine the different findings and derive a wider hypothesis for the cathode wear phenomenon. The conclusions from this work are finally recapitulated in Chapter 8.

Acknowledgments

Though this work is my own and I carry all responsibility for its quality (for better or worse), I have received a great deal of help from many people and would not have managed alone. I would like to take this opportunity to thank everyone who have, in one way or another, supported and helped me through the last few years. In fear of making a tediously long list, I name only a few. To those I have failed to include here, I do apologize.

First and foremost I would like to thank my supervisor, adjunct Professor Christian Rosenkilde, for good counsel and guidance when I could not see the path ahead. I also appreciate his patience with me in the slow periods where work dragged on and results were scarce. My co-supervisor, Egil Skybakmoen, whose workspace is located in the immediate vicinity of my "playground", also deserves my sincere gratitude. As I encountered barriers, he was often first in line to help me past the manageable problems, or to point me in the right direction. Especially, I would like to thank him for the successful laser scanning campaigns, which came to be a substantial part of my doctoral work.

As mentioned in the preface, the doctoral work was a part of the innovation project "Process Innovations for Higher Current Densities" (PI-HCD). This project was led by Dr. Nancy Jorunn Holt, and I am grateful for the project meetings where the PhD candidates were given a great arena to present our work and receive comments and advice, as well as being nice social events. In particular I would like to thank the members in sub-project 4 (cathode wear), Dr. Stanislaw Jarek, Dr. Eirik Hagen, Dr. Jørn Rutlin and Dr. Ingo Eick, for fruitful discussions, good advice and for help with arranging sampling campaigns at industrial plants.

Financial support from Norsk Hydro ASA and the Research Council of Norway is gratefully acknowledged.

I am grateful for all the help I have received from colleagues at NTNU and SINTEF, and Hydro employees at the plants I have visited. I would like to thank Stein Rørvik for showing me how to operate the optical microscope, as well as other tricks of the trade. I am thankful for the discussions I have had with adjunct Professor Asbjørn Solheim, often giving me a new angle of perspective on the problems at hand. I would also like to thank the "refractory twins", Dr. Kati Tschöpe and Zhaohui Wang, who were also a part of the PI-HCD project, for the cooperation and good company.

Professor Emeritus Jomar Thonstad also deserves my gratitude. When looking for information about previous studies, but no traces of publications could be found on the internet or no one could quite remember, Thonstad's extensive knowledge and superb memory were of great help.

During the doctoral work one also encounter numerous technical and administrative obstacles, and the technical and administrative staff at NTNU has been an invaluable resource. Especially, I would like to give thanks to Kjell Røkke and Martha Bjerknes. How many times I have come to them for help is beyond my count.

When in the middle of things it is easy to get tunnel vision and forget the greater perspective. All in all a Ph.D. degree is not that important. What really matters are the people we surround us with. Though I have always known this, I do not think I have really realized the truth of it until lately. There have been periods, especially during the finishing stages of my work, where I have not been very sociable and pleasant. Nevertheless, my family have given me their unconditional support and been very understanding. I truly am grateful, and I hope they can forgive me for my shortcomings. To conclude, I would like to address my family. I may not have said it before, but you are the most important thing in my life and I love you. For better or for worse, I will do my best never to forget it.

Summary

Cathode wear is regarded as the main limiting factor for the operational lifetime of modern Hall-Héroult aluminium reduction cells. The wear is non-uniform and the heaviest wear zones are located at the cathode periphery. It is in particular the wear rate in these zones that limits the cell lifetime, and a more uniform cathode wear with a reduction of the highest wear rates would yield a profitable increase of the cell life. The main focus for improvements of the Hall-Héroult cell is usually to promote the productivity, and the measures taken do seldom coincide with a long pot life. On the contrary, the conditions in the cells are getting more extreme and the cathode wear is accelerated.

The wear mechanisms are divided into two groups: physical abrasion and chemical corrosion. The exact mechanisms and their relative impact are not known, but there is a general agreement that the wear is enhanced by increased current density and flow in the aluminium metal pad.

The present work comprise investigations of shut down cells in macroscale, by on-site observations and laser scanning of the cathode surface; in microscale, by microscopy investigations of cathode samples; and of laboratory experiments. The objective was, in general, to reveal new information and contribute to the discussion about cathode wear mechanisms.

Two successful laser scanning campaigns were executed, and it has been shown that laser scanning technology can be implemented in cathode wear investigations and give very detailed 3D models of the cathode surface that can be used to assess the cell performance.

The microscopy study showed no significant differences between cathode samples taken from different areas of the cell, indicating that the wear mechanisms are similar over the entire cathode, though at varying rates. The wear also seems to be non-preferential, i.e. there is not found any obvious difference in wear resistance between the graphite aggregate particles and the filler material in the cathode blocks.

An aluminium carbide surface layer, up to more than 200 µm thick, is formed at the carbon cathode during operation. Due to low conductance, this layer cannot be thick, dense and cover the entire cathode. The thick layers (>20 µm) were found to be stratified, with bath filled cracks. The bath filled cracks allows mass transport from the carbon cathode to the metal pad or the bath film in between.

The laboratory experiments showed that cathode wear occurs at potentials somewhat anodic of aluminium deposition. As no aluminium was present at the cathode surface, it is likely that the wear was caused by an electrochemical reaction. At potentials cathodic of aluminium deposition the wear rate is somewhat higher. Then there may also be chemical wear as aluminium reacts with the cathode carbon.

The findings in the present work, together with previous studies, give reason to believe that physical abrasion is a minor wear mechanism and that the main mechanisms are chemical and electrochemical corrosion. The main influencing parameters on wear rate are current density and mass transport. Disregarding the electrical properties, the carbon material in itself does not seem to influence the wear rate in any significant way.

It is believed that the main reason for high local wear rates is the poor current distribution in the cathode, resulting in high local current densities and metal flow velocities. Three initiatives have been recommended for reducing cathode wear and prolonging the cell lifetime. Further improvements in magnetic field compensation may reduce the metal flow and thereby reduce mass transport. Variable resistivity graphite (VRG) cathodes may give a good current distribution, and thus lower metal flow velocities and a more even wear. The most effective measure is believed to be improvements of the current collector bars. With a better design and higher electrical conductivity of the current collector bars, a better current distribution may be achieved, as with VRG cathodes. In addition, a lower electrical resistance will yield a lower voltage drop through the cathode and increased energy efficiency.

Contents

Chapter 1

Introduction

1.1 Background

Today, cathode wear is regarded as the main limiting factor for the lifetime of aluminium reduction cells. The carbon cathode serves both as an electronic conductor and a vessel containing the molten aluminium and electrolyte, and when worn out, the entire cell has to be taken out of operation. Considerable costs are related to cell shutdowns in terms of metal production delay, deconstruction of the pot and relining of a new one. In addition, the spent pot lining (SPL) is classified as hazardous waste [1] and the disposal costs can easily run to more than $1000 per tonne SPL [2].

A typical aluminium plant operates hundreds of reduction cells, each of a size in the range of 25–80 m^2. Qatalum aluminium plant (a joint venture between Qatar Petroleum and Hydro), for example, operates 704 cells with a total annual metal production of up to 585,000 tonnes [3]. The average lifetime of modern reduction cells is about 6 years [2], which means Qatalum may expect more than a hundred cell shutdowns every year. Improving the operational lifetime will reduce the annual amount of shutdowns, which would obviously yield considerable economic advantages.

The wear of the cathode is not uniform, some areas are highly worn, and other areas are hardly worn at all. If the wear, at some point, is allowed to progress all the way down to the steel current collector bars beneath the carbon cathode, without proper measures being taken, an uncontrolled tap-out of aluminium and electrolyte will occur. This is, of course, an unwanted scenario, and care is taken to monitor the cells and detect signs of an imminent tap-out before there is any real danger. As it is the highest local wear rate that limits the cells lifetime, large amounts of cathode carbon still remains intact in the cell. If able to even out the wear distribution and reduce the highest wear rates, one would not only obtain longer life expectancy for the cells, but also a reduced amount of SPL waste.

Figure 1.1: Image from pot room SU4 at Hydro Sunndal, Norway, showing a side-by-side line of aluminium reduction cells coupled in series. The current pass through the anodes at the top of the cell to the cathode at the bottom, and then up to the anodes of the next cell in the line. One pot line may consist of more than hundred cells (or pots). Photo: A. Johansen. © Norsk Hydro

Figure 1.2: Image of a close to 1.2 km long pot room building at the Qatalum plant. Photo: H. Moland. © Norsk Hydro

1.2 Aim of the present work

Aluminium smelters have continuously been trying to increase the productivity of their cells by increasing the amperage [4]. In order to reduce the increasing voltage drop over the cathode due to increasing current densities, carbon materials with high electrical conductivity has been preferred and there has been a transition to more graphitic and graphitized carbon grades in the cathode, replacing anthracitic qualities. This transition has been followed by reports of increased wear relative to the former anthracitic carbon blocks [4]. This raises an interesting question: Are the graphitic and graphitized cathode blocks inferior to the anthracitic blocks with regard to wear resistance, or is the increased wear simply a result of the increased amperage?

The cathode wear phenomenon has been studied for decades, by small scale laboratory experiments and observations from industrial pots. The possible wear mechanisms can be divided into two groups, physical and chemical wear. There is a general agreement that both physical and chemical wear occur, but no consensus have been reached regarding the exact mechanisms and the relative importance of the different mechanisms.

The objective of the present work is to acquire an overview of the current knowledge about cathode wear in aluminium reduction cells, and try to contribute to the wear mechanism discussion with new information from own observations and experiments. The work comprise investigations of shut down cells in macroscale, by on-site observations and laser scanning of the cathode surface; in microscale, by microscopy study of cathode samples; and of lab-scale electrochemical experiments.

1.3 Brief about the Hall-Hèroult process and cell design

Aluminium is produced by electrolytic reduction of alumina (Al_2O_3), dissolved in molten salt, between carbon electrodes according to reaction (1.1). Oxidation and CO_2 evolution occurs at the anodes, which are consumed and have to be replaced at regular intervals. At the cathode, aluminium is reduced and deposited.

$$2Al_2O_3(diss) + 3C(s) \rightarrow 4Al(l) + 3CO_2(g) \quad (1.1)$$

The Hall-Hèroult process is today and for the foreseeable future the only method by which aluminium is produced industrially [5]. The process is named after its inventors, Charles M. Hall (1863 – 1914) and Paul L. T. Hèroult (1863 – 1914), who simultaneously but independently developed and patented the production of aluminium by electrolytic reduction of alumina dissolved in molten cryolite (Na_3AlF_6). Though the cell design and operating procedures have undergone substantial improvements over the time, the cell

design of modern Hall-Hèroult cells (Figure 1.3) is still quite similar to the earliest cell designs (Figure 1.4).

The main parts of the Hall-Hèroult cell is a steel shell with various lining materials, cathode current collector bars of steel connected with the carbon cathode, a molten aluminium pad, molten electrolyte bath, and consumable carbon anodes. The cell concept is still the same as in the early days, not for the lack of trying to alter it, but for the same reason that made the process possible in the first place: the extremely aggressive cryolite.

Not many materials can withstand molten cryolite, which is why it is used, as it can dissolve the very stable alumina. Much effort has been put into producing an inert material to replace the carbon electrodes. So far, all materials have failed due to one or more of the following reasons: the material not being inert in cryolite melt, not being inert in molten aluminium, loosing ability to lead current, contaminating the aluminium product, and, of course, due to high cost. Though not inert, carbon is quite resistant against the aggressive cryolite. If exposed to air, however, the carbon parts are vulnerable to oxidation. To avoid air burn the side lining and anodes are covered with electrolyte crust and alumina.

At the side walls, exposed to metal waves and alternating coverage of molten aluminium and cryolite, the side lining would corrode readily if it was not for the freeze lining. By operating the cell close to the bath liquidus temperature (typically between 950°C and 965°C [5]), and keeping a good control on the thermal balance and heat flow out of the cell walls, a ledge of frozen bath is obtained at the side walls. With the side lining protected, the carbon cathode is the weakest link, limiting the cell life time.

The industrial bath composition is a compromise between properties such as electrical conductivity, alumina and metal solubility, liquidus temperature, and density. Typically, the bath consists of cryolite (Na_3AlF_6) and additions of AlF_3 and CaF_2 in amounts of 10 wt% and 5 wt%, respectively. Other additives like LiF and MgF_2 are also common in the electrolyte of some smelters [6]. Alumina is added to the bath in small doses at regular intervals through automated point feeders. The feeding cycles and amounts are adapted to the dissolution rate so that as little alumina as possible sinks to the bottom of the cell, creating a viscous sludge on the carbon cathode surface. The formation of gas bubbles (CO_2) at the anodes and temperature gradients creates convection in the bath, which is important for the alumina distribution.

A less beneficial movement of liquid is the metal flow, induced by a strong magnetic field created by the large currents in the pot room. Without going into details, the magnetic field works in a vertical direction in the metal pad, which means a macroscopic force (often called Lorentz force) will be exerted on electrical conductors carrying current in a horizontal direction. Ideally, this would not affect the metal pad, as long as the current

goes straight down from the anode to the cathode, i.e. parallel to the magnetic field. This is, however, not the case. The current flows where it encounters the least resistance. Molten aluminium has a very low electrical resistance, and the current will take long detours in the aluminium pad towards areas on the carbon cathode yielding the lowest total resistance on the way to the current collector bars and out of the cell. The result is horizontal currents and magneto-hydrodynamic flow in the molten aluminium. The movements, especially vertical movements, in the metal pad limit the possibilities of reducing the interpolar distance, the distance between the anode and the metal pad, due to the risk of short circuits. A lower interpolar distance would give a lower voltage drop in the cell and thus a higher energy efficiency of the aluminium production. Another unwanted effect of the metal movements is the increased wear of the carbon cathode, an effect that will be treated in more detail later in this thesis.

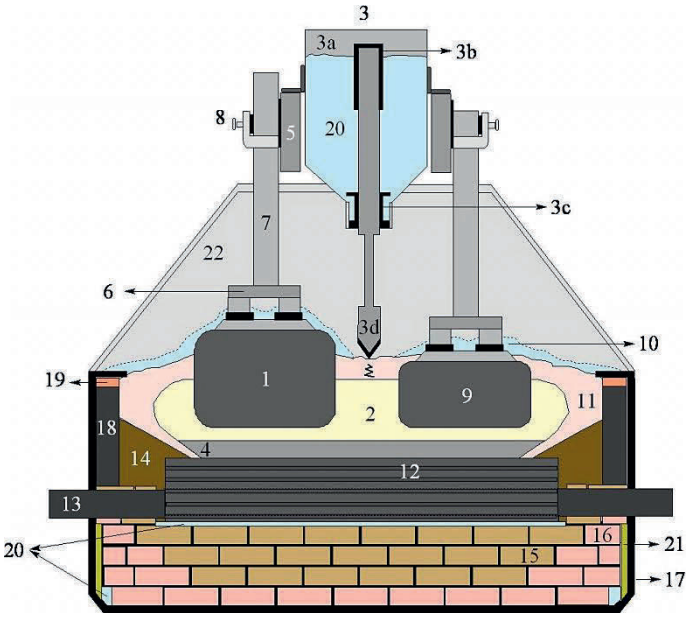

Figure 1.3: Schematic drawing of the main features of an Hall-Hèroult aluminium reduction cell: (1) anode (prebaked); (2) electrolyte (bath); (3) alumina point feeder, (3a) alumina hopper, (3b) air cylinder, (3c) metering chamber, (3d) crust braker; (4) molten aluminium pad 8 (typically ; (5) anode beam (current supply); (6) anode yoke and stubs; (7) anode rod; (8) anode clamp; (9) spent anode (butt); (10) alumina crust/cover; (11) side ledge and crust; (12) cathode carbon block; (13) current collector bar (steel); (14) ramming paste; (15) refractory; (16) insulation; (17) steel shell; (18) sidewall block; (19) castable; (20) alumina; (21) rockwool; and (22) gas collection hood (removable). The details in the lining may vary. From Tschöpe [7].

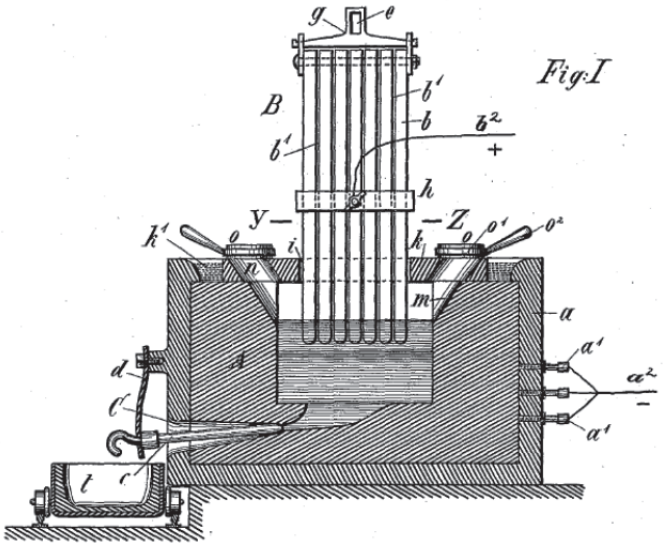

Figure 1.4: Cell design for production of aluminium patented in 1892 by Hèroult [8]. Carbon anodes are lowered into molten cryolite contained in a thick cathodically polarised carbon crucible with steel casing. The metal tap hole in the bottom is not present in modern Hall-Hèroult cells, as the metal is siphoned off from the top by a tapping vehicle or crane.

From an electrochemical point of view, the aluminium pad is the acting cathode, as this is where the aluminium deposition occurs. In the aluminium industry the entire lower part of the cell, i.e. the steel shell and all its contents, is referred to as the cathode. In this work, however, if not specified otherwise, the cathode is referred to as the carbon part of the cathode structure, i.e. the carbon blocks and the ramming joints in between.

1.4 Carbon cathodes

In the early cells, a monolithic rammed carbon cathode made up the entire lining. In the 1920's, prebaked carbon bottom blocks made its appearance, followed by several improvements in the electrical contact between the carbon and current collector bars, and in the thermal and electric insulation of the cell [9]. Today, probably all industrial cathodes are made of prebaked carbon blocks [2]. The cathode construction principles and various designs are shown in Figures 1.5 and 1.6. Of the block varieties in Figure 1.6, only full-length blocks are used in modern high-amperage pots [2].

Along with the development of more efficient and productive cells, the carbon cathode has undergone changes in both design and material. Though made up by the same elementary carbon, there exist a wide variety of carbon materials with varying properties

due to structural differences. Before elaborating further on the carbon cathode, a brief introduction to the carbon materials encountered may be in order.

Terms such as graphite, graphitic, graphitized and amorphous carbons are used in the description of cathodes in Hall-Hèroult cells. In the following, some brief definitions of the encountered terms are given.

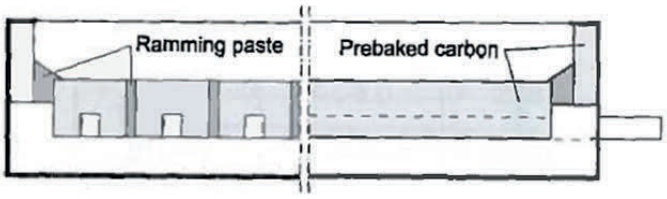

Figure 1.5: Construction principle of pot lining with prebaked carbon blocks with carbon paste in seams and joints [2]. On the left: side view showing cross section of cathode blocks. On the right: carbon block seen from the short side of the cell, as in Figure 1.3.

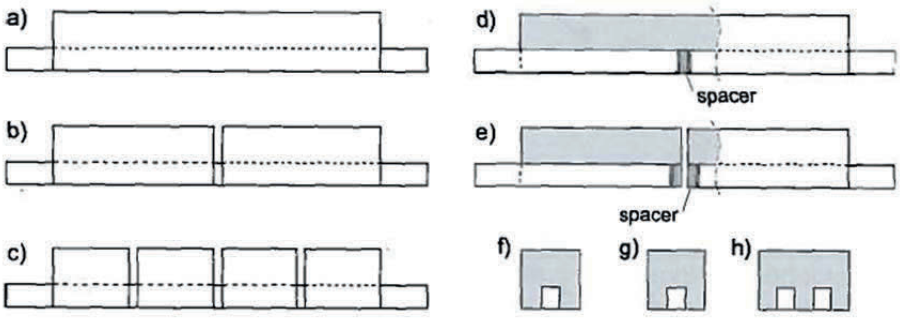

Figure 1.6: Bottom blocks can be both full length (a) or split (b and c). The collector bars may be split (d and e). The slot is rectangular (f) or "swallow-tail" (g). Dual slots are also used (h). From Sørlie and Øye [2].

Graphite

Graphite is an allotropic form of the element carbon consisting of layers of hexagonally arranged carbon atoms in a planar condensed ring system. The layers are stacked parallel to each other. There are two allotropic forms with different stacking arrangements, hexagonal and rhombohedral, the latter being thermodynamically unstable. The chemical bonds within the layer are covalent with sp^2 hybridization. The bonds between the layers are of Van der Waals type [10]. A key feature of graphite is that the structure is perfect. A sketch of the graphite unit cell is shown in Figure 1.7.

Graphitic carbon

Graphitic carbons include all varieties of substances consisting of the element carbon in the allotropic form of graphite irrespective of the presence of structural defects [10].

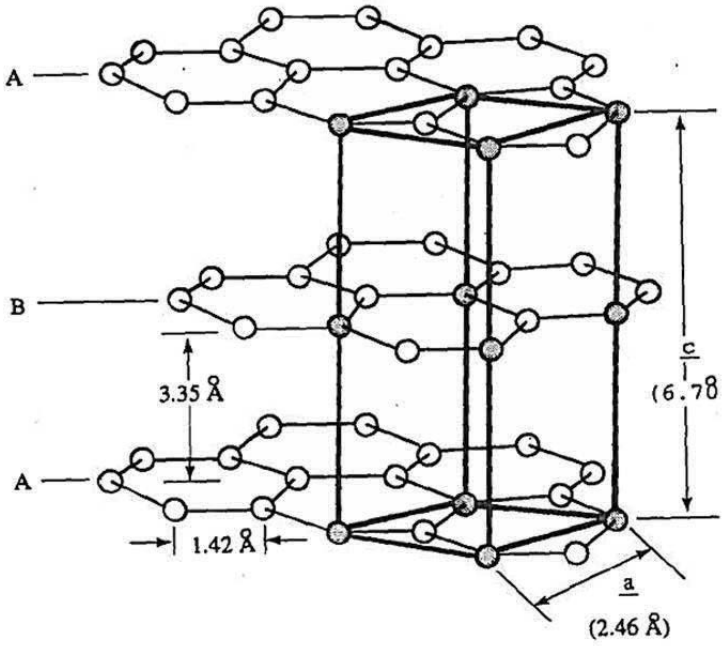

Figure 1.7: The unit cell of graphite [11].

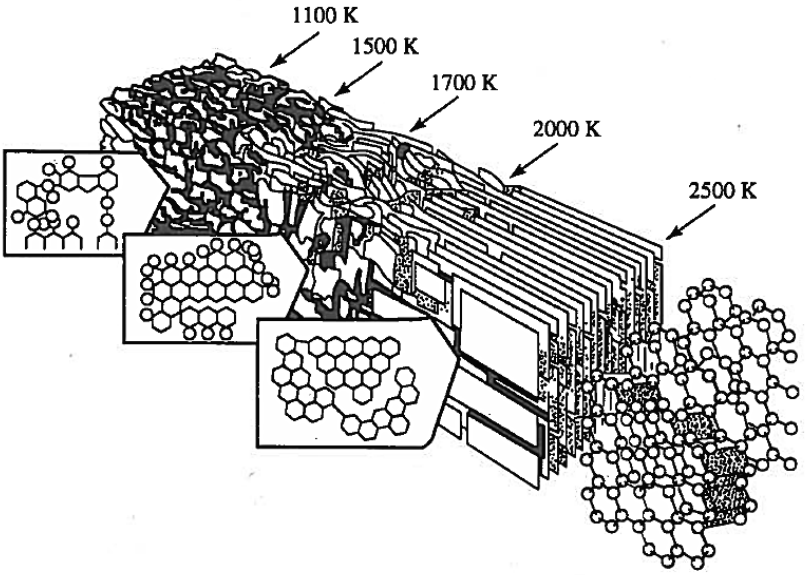

Figure 1.8: Schematic representation of the structural changes that take place in graphitizable carbons with increased heat treatment temperature [12].

Non-graphitic carbon

Non-graphitic carbons are all varieties of substances consisting mainly of the element carbon with two-dimensional long range order of the carbon atoms in planar hexagonal networks, but without any measurable crystallographic order in the third direction (c-direction) apart from more or less parallel stacking [10].

Graphitized carbon

Graphitic carbon with more or less perfect three-dimensional crystalline order obtained from non-graphitic carbon by graphitization heat treatment [10]. Graphitization heat treatment is industrially performed at temperatures in the range between 2500 and 3300 K, to achieve transformation into graphitic carbon (Figure 1.8).

Graphitizable carbon

Graphitizable carbon is a non-graphitic carbon wich upon graphitization heat treatment converts into graphitic carbon [10].

Non-graphitizable carbon

Non-graphitizable carbon is a non-graphitic carbon which cannot be transformed into graphitic carbon solely by high temperature treatment up to 3300 K under atmospheric or lower pressure [10].

Amorphous carbon

Amorphous carbon is a carbon material without long range crystalline order. The deviation of C-C interatomic distances from the interatomic distances in graphite, including those in the basal plane, is greater than 5% [10].

Anthracite

Anthracite is a naturally occuring carbonaceous material of fossil origin, and is geologically one of the most ancient coal material known. It differs from other coal deposits by its strength and hardness and low content of volatiles [2].

Coke

Coke is a highly carbonaceous product of pyrolysis of organic material at least parts of which have passed through a liquid or liquid-crystalline state during the carbonization process and which consists of non-graphitic carbon [10]. Carbonization is a process of formation of material with increasing carbon content from organic material, usually by pyrolysis, ending with an almost pure carbon residue at temperatures up to about 1600 K [10].

Based on the above definitions, Sørlie and Øye [13] proposed the following classification of cathode carbon materials for aluminium electrolysis (which are in use today).

- **Graphitized:** The whole block (aggregate and binder) consisting of graphitizable materials has been heat treated, usually to 3000°C, giving a graphitic material.
- **Semi-graphitized:** The whole block (filler and binder) consisting of graphitizable materials has been heat treated to about 2300°C.
- **Semi-graphitic:** The aggregate is graphitized but the block (binder coke) has only been heated to normal baking temperatures (≈1200°C).
- **Amorphous:** None or only part of the filler material is graphitized. The block is baked to ≈1200°C. The amorphous carbon qualities can be further sub-classified:
  - Gas or kiln calcined amorphous carbon: Aggregate is usually anthracite which has been evenly calcined and no graphitization has occurred (GCA).
  - Electrocalcined amorphous carbon: Filler material usually anthracite and due to the process some of the material is graphitized (ECA).
  - Amorphous carbon with graphitic additions (Partly graphitic carbon): Graphitic filler material is added to the material. The addition is usually in the range of 20–70 wt% of the dry aggregate.

More recently (2010), Sørlie and Øye [2] proposed a revised classification of cathode carbon materials, possibly due to frequent misuse of the semi-graphitic classification.

- **Graphitized:** The whole block (filler and binder) consisting of graphitizable materials has been heat treated in a graphitizing furnace up to a temperature of ≈3000°C.
- **Graphitic:** The aggregate is graphitized petroleum coke and/or scrap electrode graphite but the block has only been baked up to ≈1200°C. The binder coke has therefore not been graphitized.
- **Anthracitic or Amorphous:** Graphite filler can be substituted for some of the anthracite. Typical additions are 30–50 %. Baking up to ≈1200°C. The anthracitic carbon qualities can be further sub-divided:
  - Gas or kiln calcined anthracite: The anthracite has been evenly calcined and no graphitization has occurred (GCA). GCA is generally a hard and brittle material.
  - Electrocalcined anthracite: Due to the high temperature in parts of the furnace some of the anthracite is partially graphitized (ECA). The ECA tends to be “softer” than GCA.

The production of the different cathode block types is illustrated in the flow sheet in Figure 1.9. The main difference lies in the raw materials and heat treatment. The forming

is performed by extruding or vibrating the raw materials (coke and/or graphite) and the pitch binder into rectangular blocks, which are baked at temperatures between 1000°C and 3000°C. Graphitized blocks are sometimes impregnated with pitch and re-baked, one or several times, in order to reduce open porosity.

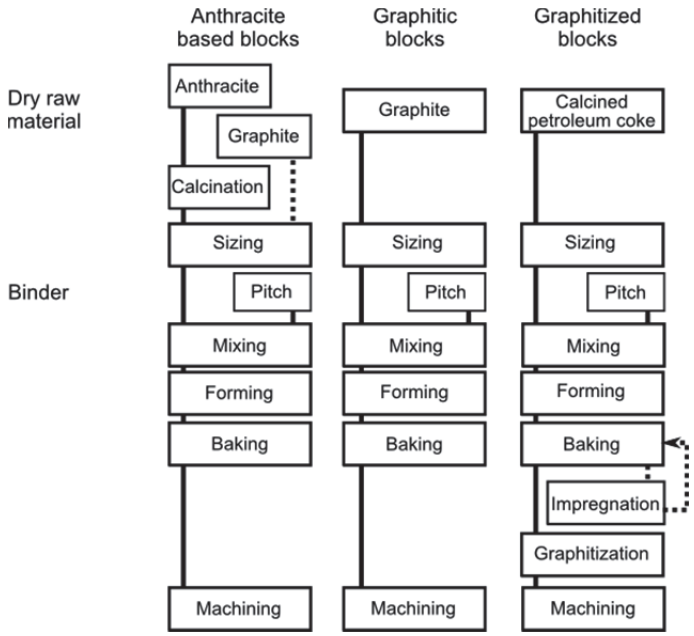

Figure 1.9: Typical flow sheets for production of cathode blocks of different types. Redrawn from [2].

A comparison of the relative properties of the three main cathode block types is given in Table 1.1. In addition to the raw material and heat treatment temperature, the properties of the finished carbon blocks are also affected by the forming method. The particles tend to orient parallel to the extrusion direction and perpendicular to the vibration direction, giving directionally dependent properties. The electrical resistivity in graphite, for example, is much lower within the basal plane than between the planes (in the c-direction).

Anthracite based blocks are still widely used, but with the continuous surge for improvements in efficiency and productivity of the cells, they are no longer dominating the market [2]. The superior electrical conductivity, as well as the resistance to thermal shock and sodium swelling, makes graphitic and graphitized cathode blocks a preferred choice for modern high amperage cells.

Ramming paste is used to seal the gaps in between the carbon blocks and at the cathode periphery, with the purpose of protecting the inner parts of the cathode against bath and

metal penetration. It consists of a filler component, anthracite (and graphite additions), and a binder based on coal tar or coal tar pitch with softener additions. The softeners vaporise during baking and do not contribute much to the formation of binder coke, and as a result, the rammed parts have a rather porous binder matrix and low density [2]. The properties of the rammed parts obviously differ from the cathode blocks, especially from graphitized blocks. The electrical resistivity of the rammed joints, for example, may be up to double of that of anthracite based blocks, and ten times that of graphitized ones [2, 14].

Table 1.1: A qualitative comparison between various properties of the three main "families" of cathode carbon blocks. From Fourcault and Samanos [15], as reported by [2].

Comparative properties	Amorphous based	Graphitic	Graphitized
Relative price	1	1.5 – 1.8	2 – 3
Abrasion resistance	excellent	good	poor
Thermal shock resistance	acceptable	very good	excellent
Thermal conductivity	moderate	high	very high
Electrical resistance			
- room temperature	high	low	very low
- pot temperature	medium	very low	very low
Crushing strength	high	adequate	low
Swelling/sodium	adequate	low	very low

As can be seen from Table 1.1 the amorphous based (or anthracitic) cathode blocks are superior in regard to mechanical properties. The good mechanical properties give the blocks an excellent resistance against mechanical wear and abrasion, the weak link being risk of cracking due to thermal shock and sodium swelling. For graphitic and graphitized grades this risk is significantly lowered, with the expense of lowered abrasion resistance. While the relative abrasion resistance of the different cathode qualities can be found readily by abrasion wear tests, the resistance against chemical wear is a more complicated matter. To be able to assess the actual wear resistance of the different cathode block types, including both physical and chemical wear, more knowledge about the different wear mechanisms and their influence on the wear of industrial cathodes is needed.

Chapter 2

Literature review

2.1 Introduction

The problems with cathode wear have been scrutinized for decades, and though the modern cathodes look fairly similar to the cathodes used 50 years ago, many improvements have been made over the years to increase the productivity and prolong the cathode lifetime. However, increasing the productivity is often in conflict with obtaining longer lifetimes for the cells. Thus, the efficiency and productivity has undergone substantial improvements the last decades, but the cell lifetime has not been noticeably prolonged. On the contrary, the industry often reports of reduced lifetimes after enterprises for increasing productivity.

This chapter reviews some of the many published works on cathode wear and related topics. The chapter is divided into three main sections, treating laboratory scale studies of cathode wear and some fundamental studies on aluminium carbide, experiments and observations from the industry, and finally theoretical investigations of possible wear mechanisms.

2.1.1 Early works

Paulsen [16] conducted a literature review, based on papers published from the early 1950's to 1967, on the problems regarding the preparation and the durability of the cathodic parts of the aluminium reduction cell. According to this work, cathode failure became to be regarded as a critical issue at the time when cells were being run at more than 50–70 kA. Rapid heating during start-up of a cell, resulting in high thermal gradients and cracking, was the main limiting factor for the cell lifetime. At the time electrolysis had started, cracking due to sodium penetration (and accompanying expansion of the cathode material) was regarded as the main problem.

It is also mentioned in Paulsen's work [16] that reaction products formed by contact between electrolyte, aluminium metal and the carbon cathode, e.g. aluminium carbide, could limit the cells' lifetime. Even if the cathodes did not fail at an early stage, they still would have to be taken out of operation due to increased voltage drop as a non-conductive layer formed at the bottom of the cells.

In modern cells, using graphitic or graphitized cathode blocks, the problem with cracking due to sodium expansion is reduced. Better control during the start-up gives less early failures, and the steady wear of the carbon cathode during operation is now regarded as the main limiting factor.

2.2 Laboratory scale studies

2.2.1 Abrasion

The relevant carbon materials for aluminium electrolysis are inhomogeneous, and measuring its mechanical properties by traditional micro hardness tests is of little use. Instead, it is thought to be better to employ methods that imitate the mechanical stresses on the cathode carbon during actual industrial aluminium electrolysis to decide the abrasion resistance.

Liao and Øye [17] developed a method for determination of abrasion resistance, where carbon samples were rotated in slurry composed of sodium polytungstate (SPT) aqueous solution and alumina at room temperature (Figure 2.1). Their test showed that the viscosity and density of the slurry, both dependent on the alumina content, have strong influences on the abrasion. Increasing the velocity also gave an increase of the wear rate, as expected. Two different abrasion mechanisms were proposed: friction wear, which will dominate at low velocities and high content of abrasive particles; and impact wear, which will be the dominating mechanism at high velocities and low content of abrasive particles.

Tests of different carbon materials by this method resulted in the following ranking of carbon materials with respect to abrasion resistance:

$$\text{Graphite} \approx \text{Semi-graphitized} < \text{Semi-graphitic} < \text{Anthracitic}$$

Liao and Øye [18] also did similar tests in cryolitic melts with alumina at temperatures above 960°C. These tests gave smaller wear rates than with the aqueous SPT-alumina slurry [17], but other than that the results matched well. The lower wear rate was explained by that the alumina particles become less abrasive as their edges preferentially dissolve in cryolitic melts, the moving alumina particles are less compact as the surface

tension of cryolitic melts is higher than that of SPT and that the cryolitic-alumina slurry does not wet the carbon materials.

In order to obtain results in a reasonable amount of time, the velocities used in the test were higher than what can be expected from the metal flow in industrial cells. Liao and Øye [18] therefore extrapolated their results to velocities in the range 0.1–0.5 m/s to give an estimate of the wear rates that can be expected on industrial cathodes. Furthermore, it was mentioned that the pressure acting on the sample surface due to gravity in the study was much smaller than the pressure acting on the cathode in industrial cells, which with a metal and electrolyte height of 45 cm would be about 17 times greater. As the wear rate had been found to be proportional to pressure in the room temperature study [17], the wear rate in industrial cells was assumed to be approximately 17 times that in the laboratory test. Extrapolated wear rates for the test and expected wear rates for industrial cells are shown in Table 2.1.

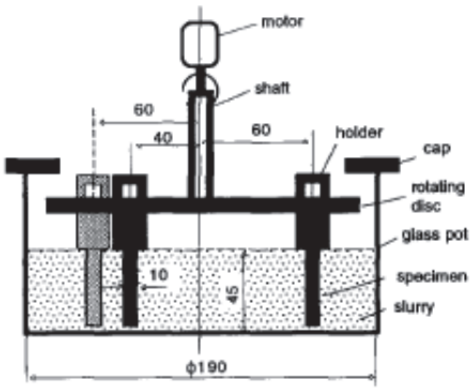

Figure 2.1: The set-up of Liao and Øye's [17] room temperature abrasion test, dimensions in mm.

Table 2.1: Estimated wear rates in cm/year of CS graphite under industrial smelting conditions by extrapolation of the experimental results. From Liao and Øye [18].

Velocity [m/s]	0.10	0.15	0.20	0.25	0.30	0.40	0.50
Laboratory wear rate	0.04	0.08	0.13	0.19	0.26	0.44	0.65
Industrial wear rate	0.6	1.3	2.2	3.2	4.5	7.5	11.1

Toda and Wakasa [19] investigated the abrasion resistance of various cathode block materials in a slurry of water and alumina. The abrasion rate of graphitized carbon was found to be three times larger than that of anthracitic carbon. It was also concluded that

the abrasion resistance of graphitized blocks is dependent on the graphite crystalline texture, and that reducing the crystallite size improves the resistance considerably.

2.2.2 Chemical and electrochemical wear

2.2.2.1 Aluminium carbide formation

It is well known that aluminium can react with carbon to form aluminium carbide according to reaction (2.1). Due to the aluminium oxide layer that typically covers the liquid aluminium, however, this reaction does not occur readily at normal aluminium melting temperatures. Dorward [20] demonstrated that the presence of cryolite has a catalytic effect on the carbide formation reaction, explained by dissolution of the aluminium oxide layer.

$$4Al(l) + 3C(s) \rightarrow Al_4C_3(s) \tag{2.1}$$

Grjotheim et al. [21] investigated the formation of aluminium carbide in a carbon crucible with aluminium and cryolite melts of varying composition, in inert argon atmosphere at 1050°C and with a carbon stirrer. The crucible, the stirrer and the melt (the aluminium was removed) were crushed after the experiments and mixed with acid. The amount of carbide formed (both solid and dissolved in the melt) was then determined by barometric analysis and gas chromatography, based on the reaction:

$$Al_4C_3(s) + 12H^+(aq) \rightarrow 3CH_4(g) + 4Al^{3+}(aq) \tag{2.2}$$

The results showed that the amount of carbide formed does not change with the content of alumina above 4 wt%, but a dramatic decrease of the carbide formation is seen when the alumina concentration is increased from 0 to 4 wt% (Figure 2.2). Increasing the cryolite ratio from 2.4 to 3.8 gave a reduction of the carbide formation, as seen in Figure 2.3(a). Experiments with different carbon materials (with different pore volumes) showed that the materials with the largest pore volume yields the most Al_4C_3 (Figure 2.3(b)).

A recent study by Novak et al. [22] showed that aluminium and carbon (in inert atmosphere) reacts to form carbide at 1100 – 1200 °C. Two visibly different layers were observed between the carbon and the aluminium metal, as can be seen in Figure 2.4. EDS measurements revealed presence of oxygen in the layer closest to the aluminium, and it was assumed that this layer was either a mixture of aluminium carbide and aluminium oxide, or possibly aluminium oxycarbide. A possible reaction mechanism was proposed (illustrated in Figure 2.5), involving formation and diffusion of a gaseous sub-oxide, $Al_2O(g)$, from the metal-oxide interface to the oxide-carbon interface.

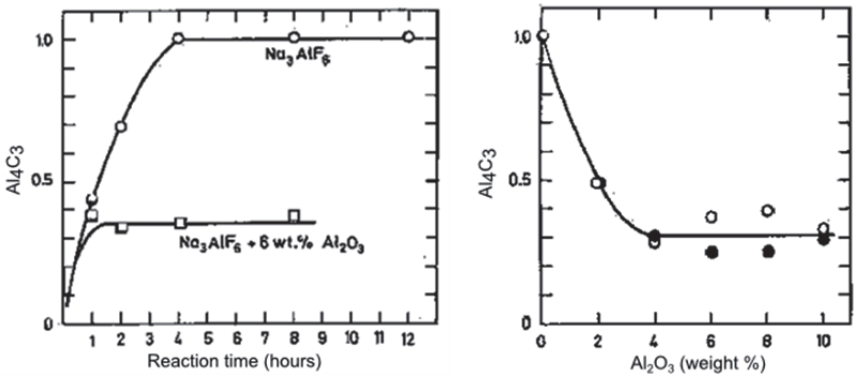

(a) (b)

Figure 2.2: Results from Grjotheim et al. [21]. (a) Relative amounts of Al_4C_3 produced as a function of time in a pure Na_3AlF_6 melt (open circles) and Na_3AlF_6 with 6 wt% Al_2O_3 (open squares). (b) Relative amounts of Al_4C_3 formed in a Na_3AlF_6 melt with additions of Al_2O_3 after 4 hours reaction time. Open and closed circles represents two independent sets of experiments.

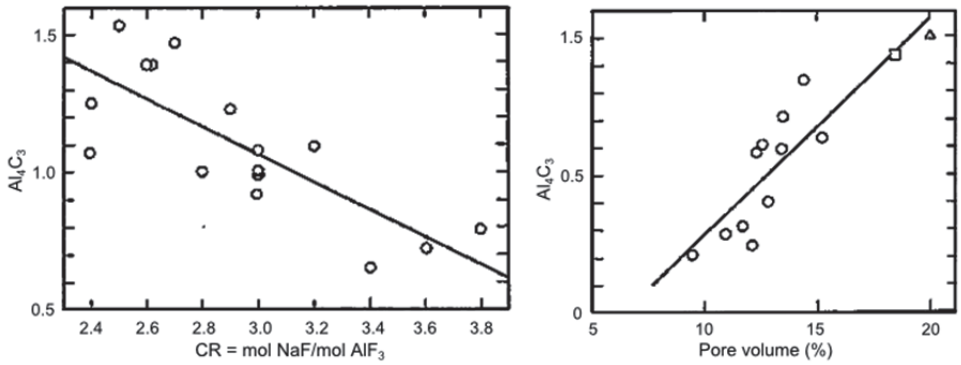

(a) (b)

Figure 2.3: Results from Grjotheim et al. [21]. (a) Relative amounts of Al_4C_3 produced as a function of the cryolite ratio. (b) Relative amounts of Al_4C_3 formed vs. pore volume for 11 commercial carbon lining materials (open circles), AGR-graphite (open triangle) and reactor graphite (open square) in a Na_3AlF_6 melt with 6 wt% Al_2O_3. Solid lines represent a least square fit.

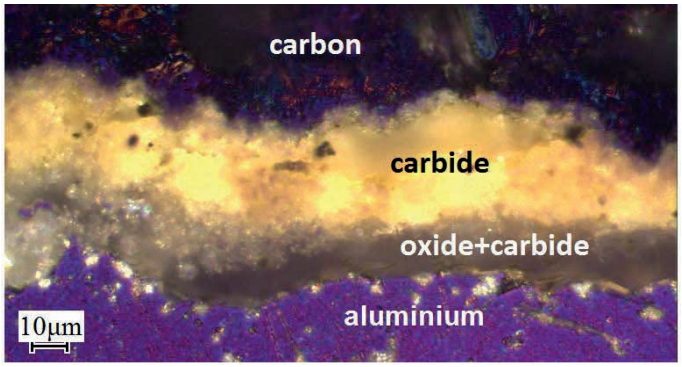

Figure 2.4: Optical micrograph of the Al/C interface after 96 h at 1200°C. From Novak et al. [22].

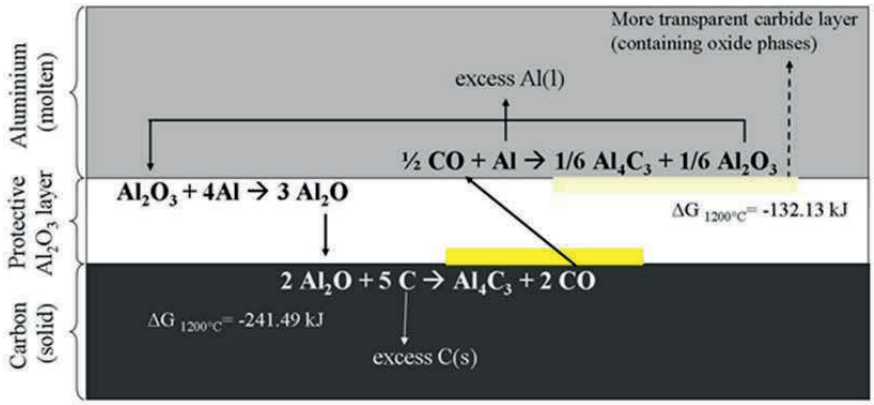

Figure 2.5: Proposed gas transport mechanism for aluminium carbide formation through an oxide layer. From Novak et al. [22].

2.2.2.2 Electrical resistivity of aluminium carbide

To gain a better understanding of the voltage drop that can be expected at the cathode due to formation of an aluminium carbide layer at the aluminium-carbon interface, King and Dorward [23] measured the electrical resistivity of Al_4C_3 at temperatures of interest for the aluminium industry (990–1240 K). The results are shown in Figure 2.6.

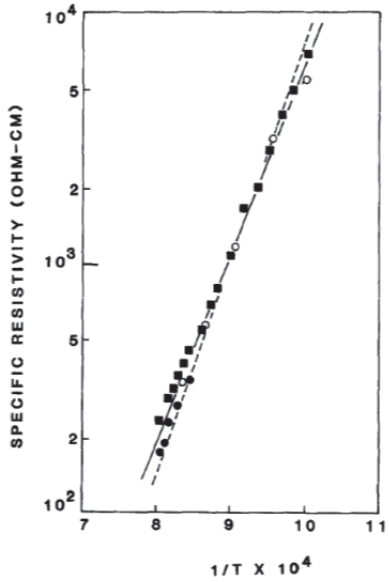

Figure 2.6: Specific resistivity of Al_4C_3 as a function of temperature [K]. From King and Dorward [23].

2.2.2.3 Solubility of aluminium carbide

Ødegård et al. [24, 25] studied the aluminium carbide solubility in cryolitic melts. Aluminium and NaF–AlF_3 melt was kept in graphite crucibles with tight lids at 1020–1335°C. After five hours, sufficient time for the reaction between aluminium and graphite to saturate the melt with aluminium carbide, samples were taken from the melt and quenched. The samples were then ground and treated with a 10% HCl solution which together with aluminium carbide forms methane and hydrogen. The evolved gas was analysed by a gas chromatograph, and the amount of carbide was calculated on basis of reaction (2.2).

They found that the solubility increase with increasing temperature and decreasing alumina concentration and that addition of CaF_2 decreases the carbide solubility. The parameter that had the largest influence on the solubility, however, was the cryolite ratio (Figure 2.7). At 1020 $\pm$ 2°C a maximum solubility was found at CR = 1.8; the basis for the proposed dissolution reaction:

$$Al_4C_3(s) + 5AlF_3(diss) + 9NaF(l) \leftrightarrow 3Na_3Al_3CF_8(diss) \qquad (2.3)$$

Ødegård et al. [24] also derived some estimates for thermodynamic data concerning the aluminium carbide dissolution reaction, e.g. the Gibbs free energy of formation $\Delta G^0_{Na_3Al_3CF_8}$.

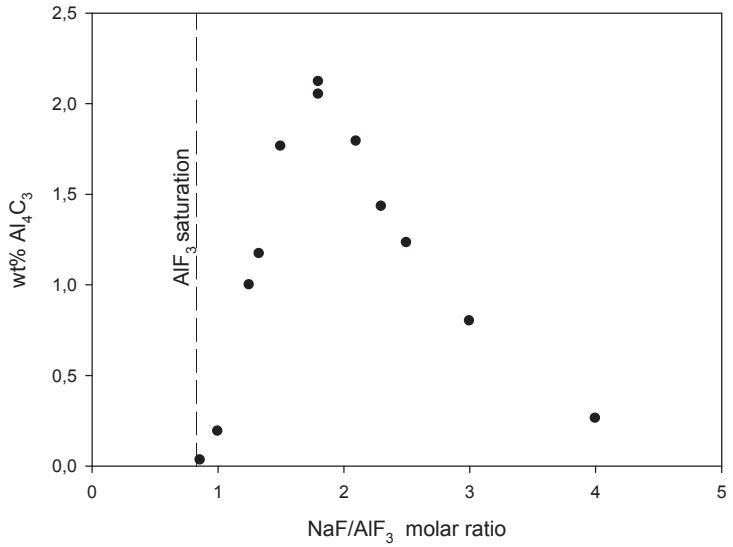

Figure 2.7: Solubility of Al4C3 as a function of CR in NaF–AlF3 melts at 1020 ± 2°C. Replotted from Ødegård [25].

Chrenková et al. [26] studied the solubility of carbon and Al_4C_3 in cryolite and their effect on the liquidus temperature by cryoscopy. They found that up to 0.7 wt% carbon may be dissolved in cryolite, lowering the melting point by 10°C. The solubility of aluminium carbide was found to be up to 2.2 wt%, having almost the same effect on the melting temperature of cryolite, reducing it by 11°C. The experimental results corresponded well with a theoretical liquidus curve of cryolite under assumption that three moles of a new compound were formed for each mole Al_4C_3 added.

Subsequently Chrenková et al. [26] analysed the reaction products of dissolution of carbon and Al_4C_3 in cryolite by X-ray diffraction and IR spectroscopy. It was concluded that the product of dissolution probably is $Na_3Al_3CF_8$ for both carbon and Al_4C_3, as suggested by Ødegård [25].

2.2.2.4 Chemical wear

Hollingshead and Brown [27] measured the rate of solution of rotating carbon cylinders in aluminium and cryolite melt exposed to air (Figure 2.8). The carbon cylinders, 38 mm diameter by 190 mm long consisting of extruded graphite of 1.68 g/cm^3 bulk density, were suspended approximately 110 mm into molten aluminium contained in graphite crucibles of 150 mm diameter. The depth of cryolite on top of the aluminium was about 65 mm. The wear was estimated from measuring with a micrometer the diameter at 120° intervals (three measurements) at each of 25, 50 and 75 mm from the lower end of the carbon

specimen. Alumina, formed by oxidation of dissolved metal and aluminium carbide, crystallised at the upper part of the carbon cylinders and were removed daily to prevent interference with the rotation. At 975°C, the rate of solution increased from 0.05 kg/m^2 per day without rotation to 0.30 kg/m^2 per day with a peripheral velocity of 30 cm/s (150 rpm). The correlation between the rate of solution and the rotation speed was found to be linear. Additionally, at peripheral velocities of 20 cm/s and temperatures between 900 and 1025°C, the wear increased by a factor of 1.095 for each 10°C increase in temperature. For the tests at 975°C and above, synthetic cryolite plus 10% calcium fluoride was used. A mixture of synthetic cryolite, 10% lithium fluoride and 10% smelter-grade aluminium fluoride was used at lower temperatures.

Variations of carbon materials gave decrease in the linear rate of solution with increasing bulk density, but the gravimetric rate did not vary significantly with the kind of material (anthracite-based baked carbon versus graphite) nor with bulk density.

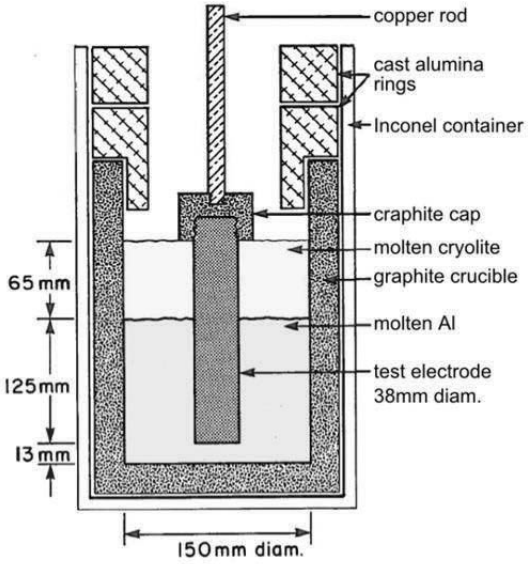

Figure 2.8: Hollingshead and Brown's set-up for determining the rate of solution of carbon in molten aluminium [27].

Xue and Øye [28] did similar rotation tests, but with a few alterations. The carbon specimens were partly covered by alumina tubes so that they avoided direct exposure of the specimen to the bulk melt and obtained a more exact surface area of the aluminium-carbon interface. Alumina lining was also used in the crucible, thus making the carbon specimen the only source of carbon in the system. The set-up used is depicted in Figure 2.9.

The rotation tests were carried out at 950°C and under argon atmosphere and the cylinders were rotated at a speed of 150 rpm (a peripheral velocity of 11.9 cm/s). After the rotation tests the specimens were cleaned by 15% $AlCl_3$ solution and/or 3M H_2SO_4 solution. Wear was determined by volume change before and after the experiments, which was found by measurements of the Archimedes' force applied to the specimen immersed in pure isopropanol using a balance with accuracy of 0.01 mg. Volume change was plotted against holding time for two melt compositions, Al_2O_3-saturated melt and Al_2O_3-oversaturated melt. The results yielded a lower wear rate for the Al_2O_3-oversaturated melt, but both had a maximum volume change corresponding to an Al_4C_3 content of 1.37 wt% in the melt. The trend of wear was higher in the early period and diminished as the carbide concentration in the melt approached saturation. Large amounts of yellow crystals on the melt-lining interface were observed after breaking the crucibles, indicating that the melts had indeed been saturated by aluminium carbide. The abrasive effect of the alumina particles, the original purpose to investigate the wear for alumina-oversaturated melt, was found to be more than compensated by a protective effect (an alumina-rich fluoride protective coating). It was however stressed that this might not be the case with the horizontal carbon blocks in real cells where the abrasive forces may be stronger.

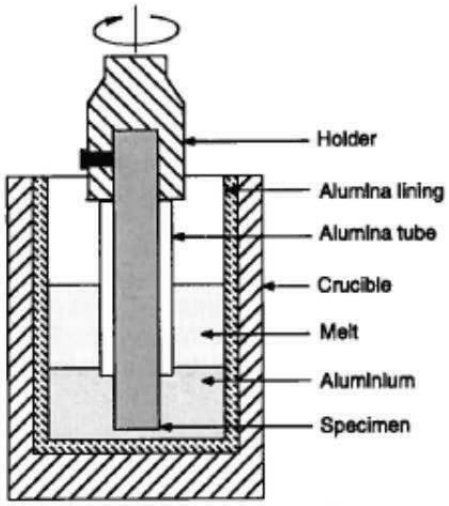

Figure 2.9: The set-up of Xue and Øye's rotation test [28].

Liao and Øye [18] studied the effect of holding time, velocity and excess (undissolved) alumina on the wear rate of graphite and anthracitic carbon. The samples, core drilled graphite with diameter of about 9.98 mm and length of about 60 mm, were mounted in holders with the centre located 50 mm from the rotating axis of a rotating disc. The melt was cryolite-based with CR = 2.2, 5 wt% CaF_2 and 5–6 wt% aluminium, it held a temperature of 990°C and was contained in a graphite crucible with an inner diameter of

144 mm. Except for the test of the effect of velocity, the velocity of the specimen was kept constant at 0.55–0.60 m/s. After the experiments the samples were cleaned in H_2SO_4 solution and their volume measured in distilled water. Not surprisingly, the volume change was found to increase with time in the cryolitic melt, but the increase slowed down significantly after 4 hours. This was explained by the formation of a carbide film, functioning as a diffusion barrier. The wear rate increased with rotating velocity and decreased rapidly with excess alumina content, corresponding well to the findings of Xue and Øye [28]. The wear rates were found to be similar for both materials used, indicating that the resistance to chemical corrosion is approximately the same for graphite and anthracitic carbon.

2.2.2.5 Electrochemical wear

The influence of current density on the wear rate of graphite in cryolite and aluminium melt during electrolysis was studied by Liao and Øye [29]. While rotating samples without electrolysis, they found that the wear rate increased when lowering the samples closer to the metal pad. This was related to increased mass transfer and possibility of short-circuits creating galvanic cells. The wear was found to be very small without short-circuit, and was hence attributed galvanic corrosion.

Figure 2.10 shows the results from the electrolysis experiment. The current density was estimated on the basis of the immersion depth of the carbon sample. Liao and Øye operated with an immersed surface area of 10.2 cm^2. Given that this area was fairly equal for all the trials, the plot in Figure 2.10 give the trend of wear rate as a function of current density. The correlation between wear rate and current density suggests that the cathode wear has an electrochemical reaction mechanism.

Adding aluminium carbide to the melt gave an increase of the wear rate at low currents. The wear increase decelerated more rapidly as the current increased, however, and above 0.4 A/cm^2 the wear rate was higher in melt without carbide additions. Liao and Øye [29] suggested destabilization of alumina colloids that might adhere to the carbon cathode, improved wetting between the melt and the carbon cathode and lower cell voltage for aluminium deposition from aluminium carbide than from alumina, as possible explanations for the higher wear rate in Al_4C_3-containing melt.

Wilkening and Reny [30] performed similar studies, but with axial vibration of the cathode sample instead of rotation. They observed the same trend of increased wear with increased current density as Liao and Øye. They also found that increasing the AlF_3 content, i.e. lowering the CR, gave higher wear. At zero current density no erosion was observed, indicating that chemical attack and motion of bath alone do not create any eroding effect. Their results are shown in Figure 2.11.

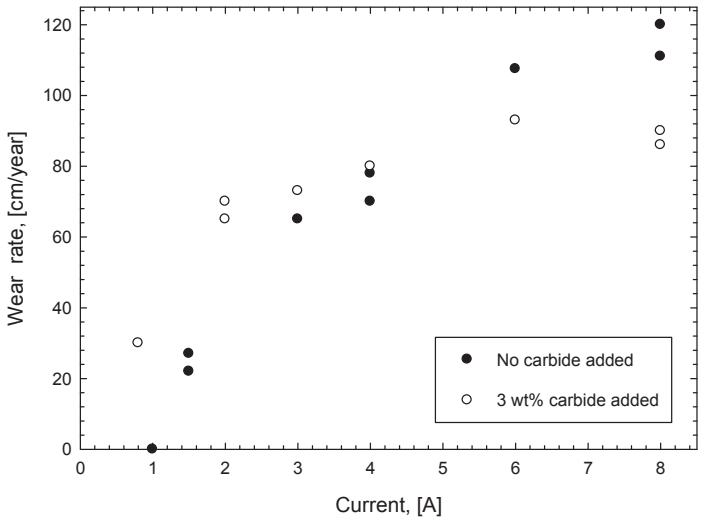

Figure 2.10: Wear rate of CS graphite as a function of current. Sample velocity: 0.55–0.6 m/s, temperature: 980°C, 3 hours test time and no aluminium added. Cathodic current density: 0.073–0.873 A/cm^2. Replotted from Liao and Øye [29].

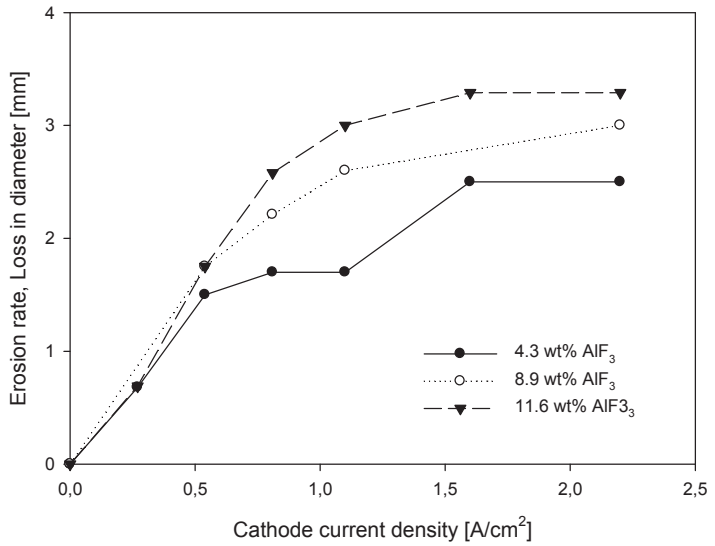

Figure 2.11: Wear rate as a function of current density. Replotted from Wilkening and Reny [30].

Rafiei et al. [31] performed electrolysis in excess of 96 hours in alumina saturated cryolite with 10 wt% AlF_3 and 5 wt% CaF_2. Cylindrical cores, 30 x 110 mm, of different carbon materials (graphitic and anthracitic) were used as cathode and a carbon crucible worked as anode. The average cathodic current density applied was 0.75 A/cm^2, the temperature

was kept at 975°C and a flow of nitrogen was maintained to achieve an inert atmosphere. They found that the graphitic cathodes had a slower and more uniform wear than the anthracitic. The anthracitic cathode showed irregular wear and degradation.

Vasshaug [32] investigated the influence of bath composition, cathodic current density, electrolysis time, convection and the presence of aluminium on cathode wear. Experiments with a vertical rotating cathode in cryolitic melts without aluminium and experiments with a horizontal cathode covered by aluminium metal were conducted (Figure 2.12).

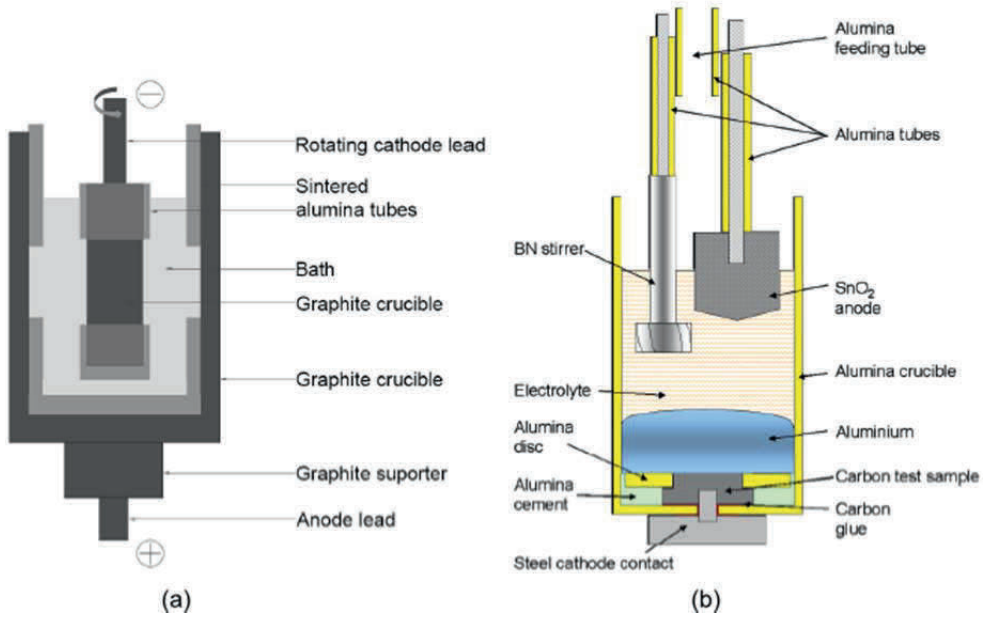

Figure 2.12: Schematic drawings of Vasshaug's set-ups for (a) experiments with rotating cathode, and (b) experiments with horizontal cathode and liquid aluminium present at start [32].

The experiments with the vertical rotating cathode showed a moderate increase of wear rate with increasing rotation speed. As a function of cryolite ratio, the carbon consumption indicated a similar trend of wear as the solubility of aluminium carbide in cryolite found by Ødegård [25], that is, highest wear at CR = 1.8 when the solubility is at a maximum.

While most studies on the carbon consumption as a function of current density have been based on experiments where the electrolysis time has been kept constant, Vasshaug [32] chose to treat the total amount of electrical charge passed through the cathode as a

constant, thus varying the electrolysis time. In the low current density region, the carbon consumption was found to decrease with increasing current density, as can be seen from Figure 2.13(a). It was suggested that increasing the current density will lead to increased activity of NaF at the cathode surface, thus increasing the cryolite ratio and decreasing the carbide solubility, resulting in lower carbon consumption. At higher current densities there seemed to be little correlation between carbon consumption and current density. An explanation for this might be that the wear is an electrochemical process and is dependent of the actual charge passed. As the charge was kept constant in all the experiments, the carbon consumption would also be expected to remain the same.

When converting the amount of carbon consumed into wear rate in cm per year, the trend is different. Figure 2.13(b) shows an increase in wear rate with increased current density, though only slightly at CR = 2.25.

The data from Vasshaug's experiments with the horizontal cathode beneath a molten aluminium pad were insufficient to draw any conclusions, but some trends are worth mentioning. The effect of current density on carbon consumption and wear rate seemed to agree with the findings from the experiments with the vertical cathode. The effect of the cryolite ratio, however, seemed to be different, as the wear rate was higher at CR = 2.25 than at CR = 1.80. The wear rates for the horizontal cathode were found to be in the range 4–8 cm/y, which was considerably lower than for the vertical cathode and more comparable to the wear rates in industrial cells.

Gudbrandsen, Sterten and Ødegård [33] demonstrated that carbon can dissolve cathodically in cryolitic melts, according to reaction (2.4). Their experiments were conducted with a similar set-up as Vasshaug's vertical cathode set-up, Figure 2.12(a), but with a stationary cathode and a steel stirrer on the side. Galvanostatic electrolysis was performed in the range of 0 – 0.2 A/cm^2.

$$C(s) + 3AlF_3(l) + 4Na^+ + 4e^- \rightarrow Na_3Al_3CF_8(l) + NaF(l) \qquad (2.4)$$

The results given in Figure 2.14(a) show that the rate of carbon dissolution increased with increasing current density, until a steady state was reached. The carbon consumption was less than theoretical because some of the current drives other electrochemical reactions, such as formation of dissolved metal species and reduction of impurities. Figure 2.14(b) show the partial current density for carbon dissolution according to reaction (2.4) plotted as a function of the total cathodic current density. Gudbrandsen et al. [33] denoted the break in the curve as a limiting current. An additional increase of current beyond this limit led to a reduced current efficiency for the carbon dissolution reaction.

As the aluminium deposition potential is about 125 mV more negative than the theoretical potential for the carbide dissolution reaction, it was assumed that aluminium deposition could hardly be expected before the limiting current density was exceeded.

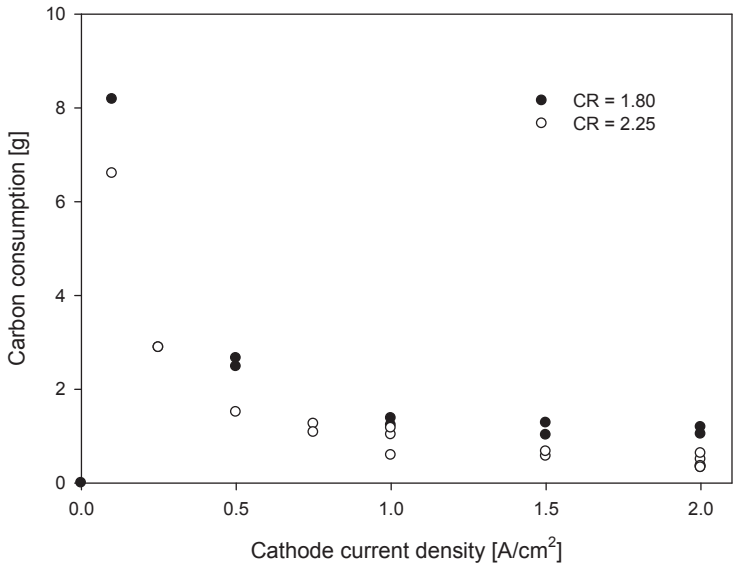

(a)

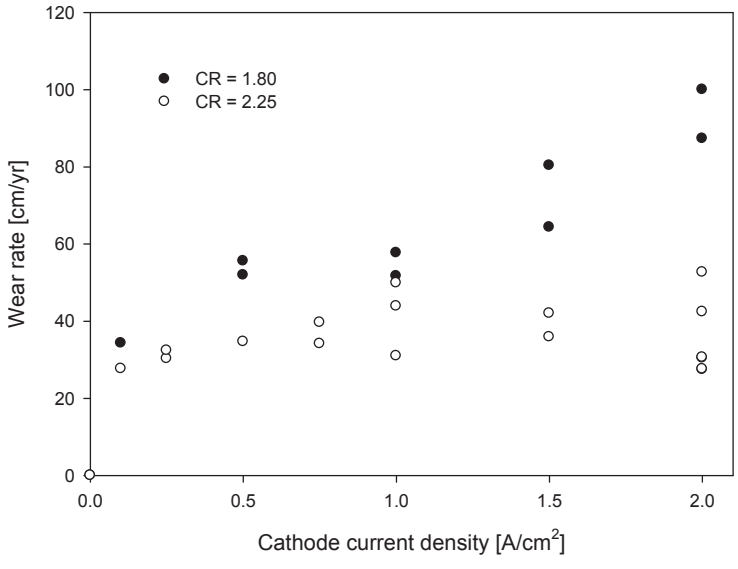

(b)

Figure 2.13: (a) carbon consumption and (b) wear rate as a function of the cathode current density at various cryolite ratios, cathode rotation speed of 40 rpm and fixed charge. Replotted from Vasshaug [32].

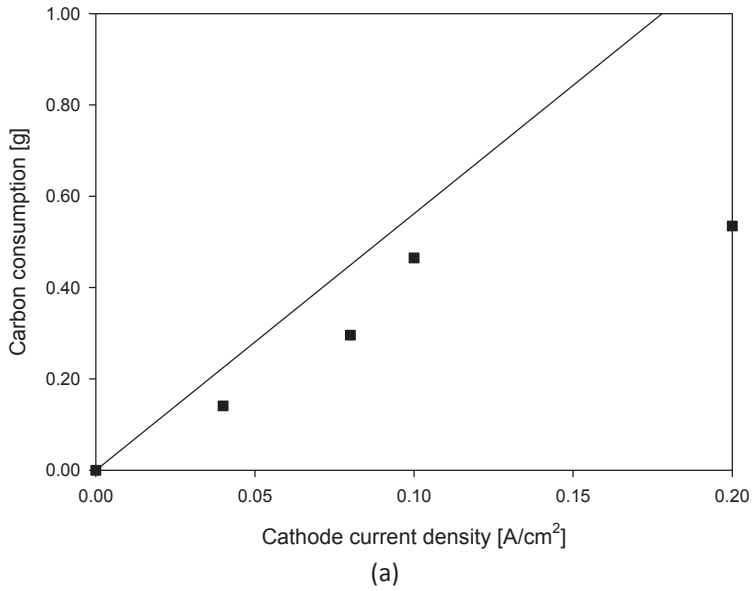

(a)

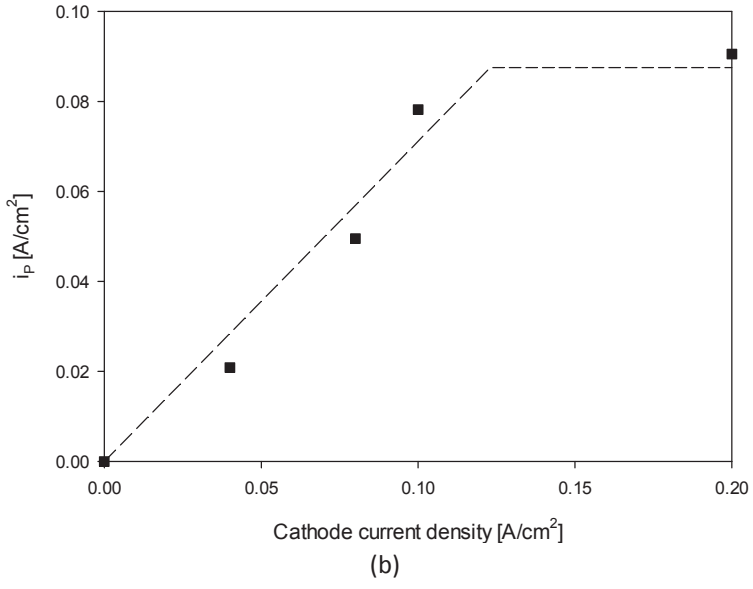

(b)

Figure 2.14: Results from electrolysis at 940°C, CR = 1.8, alumina saturated melt. Replotted from Gudbrandsen, Sterten and Ødegård [33]. (a) Carbon consumption as a function of cathodic current density. Straight line — theoretical weight loss. (b) Partial current density (I_P) according to reaction (2.4) for dissolution of carbon versus total current density. Horizontal line — limiting current.

During the electrolysis tests, Gudbrandsen et al. [33] observed a significant drop in the cell voltage, shown in Figure 2.15. They could divide the electrolysis run into three periods with distinctly different potential/time behaviour. In the first period in the beginning of the experiments, when no dissolved metal or any dissolved aluminium carbide would be present in the bulk electrolyte phase, the main cathode reactions were assumed to be cathodic dissolution of carbon according to reaction (2.4), as well as reduction of impurities in the melt and production of dissolved metal species. At the anode, the main reaction was assumed to be formation of $CO_2(g)$. In the third period, with dissolved aluminium carbide in the electrolyte, the main reaction at the anode was assumed to be deposition of carbon, which occurs at a lower anodic potential. With the main cathodic reaction being dissolution of carbon, the main overall reaction during this period would be a transfer of carbon from the cathode to the anode.

A second series of experiments were conducted after pre-electrolysis of the electrolyte, which removed impurities and introduced high concentrations of carbide and dissolved metal in the melt. The main anode reaction was thus anodic deposition of carbon, resulting in lower cell potential. As impurities had been removed, higher current efficiency for the carbon dissolution was obtained in the second series. The current efficiency was found to be about 86% at the limiting current density of about 0.11 A/cm^2, while the first series gave about 80% at a limiting current density of about 0.9 A/cm^2.

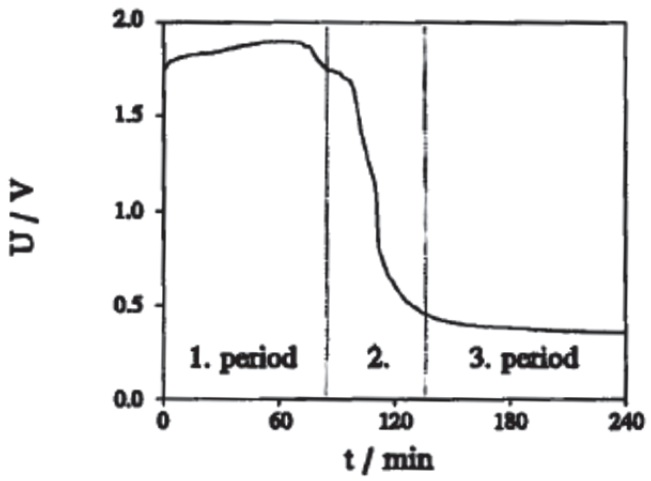

Figure 2.15: Cell voltage as a function of time from a carbon dissolution experiment. Current density, i = 0.08 A/cm^2, CR = 1.8, T = 490°C, alumina saturated melt. From Gudbrandsen, Sterten and Ødegård [33].

Tschöpe et al. [34] investigated the wear on rotating slotted cylindrical cathodes, Figure 2.16(a), and compared with FEM-simulations of current density distribution and electrolyte flow. After 24 hours of electrolysis in cryolitic melt (74.8 wt% Na_3AlF_6, 12.0 wt% AlF_3, 8.2 wt% Al_2O_3, 5.0 wt% CaF_2) at 960°C, cathode rotating speed of 50 rpm, and apparent cathodic current density of about 1 A/cm^2, considerable wear was observed, especially at the slot corners facing the rotation direction (corners labelled 1 in Figure 2.16(b)). FEM-simulations showed that a higher current density could be expected at the slot corners, and that that higher electrolyte velocity and thereby higher material transport would occur at the slot corners where the highest wear was observed, relative to the corners facing away from the rotation direction (labelled 2 in Figure 2.16(b)). The lowest values of current density and velocity of electrolyte relative to the cathode were found inside the deepest slots (5 mm), where also the least wear was observed. It was thus concluded that the wear is significantly influenced by both hydrodynamics and current density.

Tschöpe et al. [35] also investigated the wear rate on three different types of carbon cathode materials with a similar set-up, but without slots in the electrode. They found no significant difference in the electrochemical wear rate of high-density graphitized, graphitized and anthracitic cathodes. Their observations did point to a marginal advantage for the graphitized material, though, with the anthracitic cathode as the least favourable in regard to electrochemical wear resistance.

Patel, Hyland and Hiltmann [36] found that porosity in the cathode material is of great concern regarding wear. From their laboratory electrolysis experiments they demonstrated that formation of aluminium carbide occurs within cathode pores. Highly porous cathode samples showed uneven wear, which they attributed particulate detachment due to formation, dissolution and growth of aluminium carbide in the pores. It was proposed that increasing open porosity will increase bath penetration and subsequent aluminium carbide formation. Porosity, bath composition and current density, especially in combination, were found to have the most pronounced effect on cathode wear.

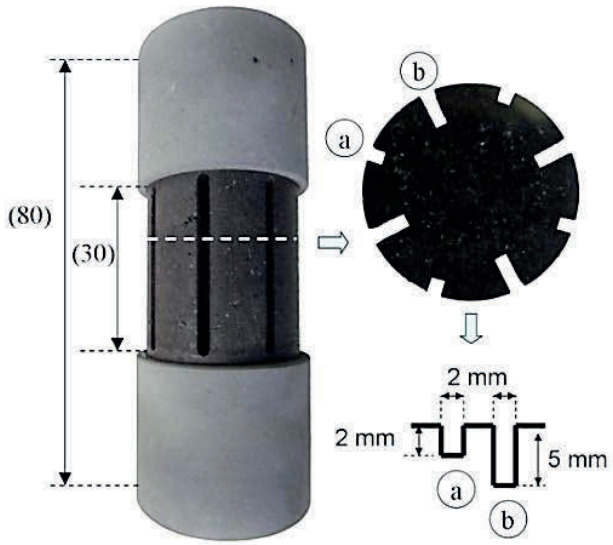

(a)

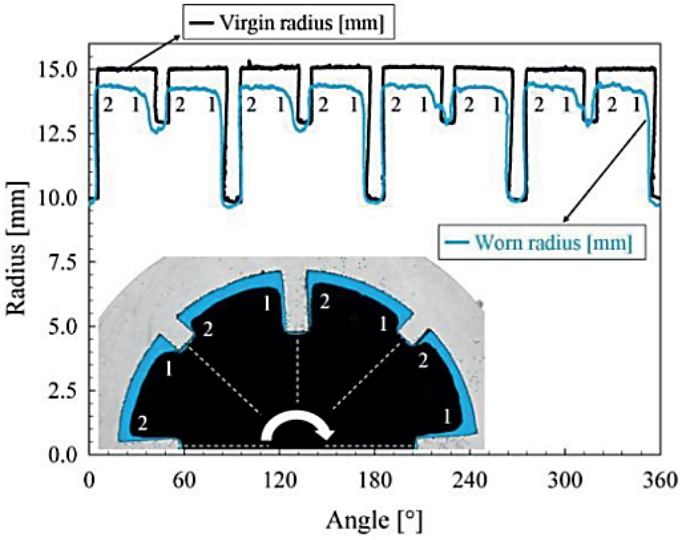

(b)

Figure 2.16: From Tschöpe et al. [34]. (a) Image of cathode with slots and with Si_3N_4 covered ends. Eight vertical slots with two different depths were cut evenly distributed around the periphery. (b) Graphical representation of the cathode surface before (virgin) and after (worn) 24 hours electrolysis.

2.2.2.6 Cyclic voltammetry studies related to Al_4C_3

Raj and Skyllas-Kazacos [37] conducted cyclic voltammetry in cryolite based melts to evaluate the current efficiency of aluminium deposition on TiB_2/C composite electrodes. They used graphite and TiB_2/C composite as working electrodes, the carbon crucible containing the melt as counter electrode, and tungsten as reference electrode. On the graphite electrode (Figure 2.17) they observed aluminium deposition and reoxidation of the deposited aluminium in region A and B, respectively. The increasing current in region x was attributed sodium intercalation and y correspondingly sodium deintercalation. The broadness of the anodic peak (B) was explained by aluminium being stripped as a partially soluble product or as Na-Al alloy of varying activity. Simultaneous oxidation of aluminium carbide and aluminium was also proposed as a plausible cause for the broad nature of peak B.

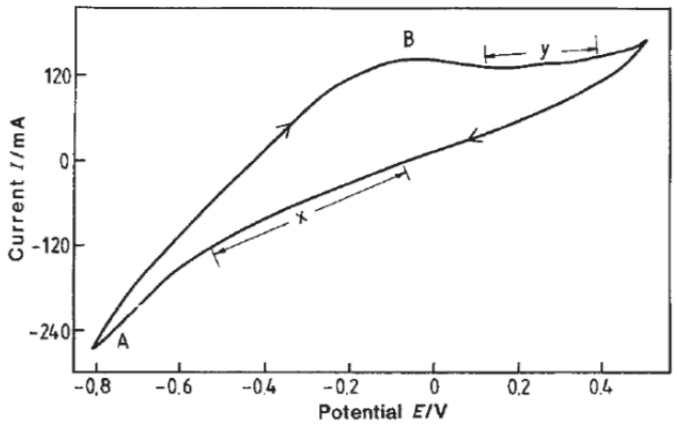

Figure 2.17: Cyclic voltammogram for graphite electrode against a tungsten reference electrode in Al_2O_3-saturated cryolite melt with 5 wt% excess AlF_3, sweep rate 0.1 V/s at 990°C [37].

The voltammogram for the TiB_2/C composite electrode in unsaturated cryolite melt, Figure 2.18, shows a more pronounced aluminium deposition and reoxidation. This was explained by enhanced wetting properties of the composite electrode, as well as higher mass transport compared to oxide saturated melts. The two smaller cathodic peaks, E and D, and the corresponding anodic peaks, F and G, were related to titanium and boron species introduced through the composite electrode.

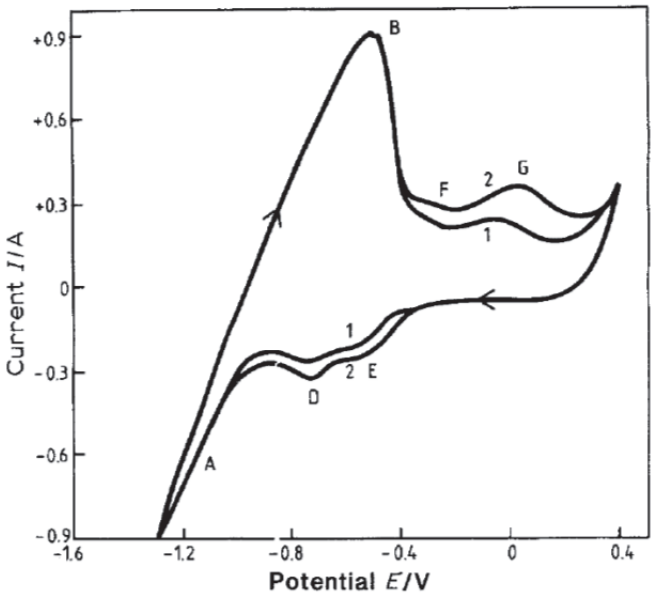

Figure 2.18: Cyclic voltammogram for composite electrode against a tungsten reference electrode in unsaturated cryolite melt with 3 wt% Al_2O_3, 8 wt% excess AlF_3, 5 wt% CaF_2, sweep rate 0.2 V/s at 980°C [37].

Brynjulfsen [38] studied the electrochemical behaviour of aluminium carbide in cryolitic melt with 1.8 CR at 940°C by cyclic voltammetry with graphite and tungsten as working electrode. She expected anodic peak currents related to oxidation of carbide close to the reversible aluminium deposition potential. On graphite electrodes, susceptible for sodium intercalation, oxidation of intercalated sodium will occur in the same potential area, however. Due to difficulties differing between currents related to aluminium carbide and sodium oxidation, tungsten was chosen as a more suitable working electrode (being inert to sodium at the relevant potentials).

After adding a small amount of Al_4C_3 to the melt, Brynjulfsen found higher anodic currents after the aluminium oxidation peak (Figure 2.19). By starting the sweep in anodic direction and with a starting point anodic of aluminium reduction, a peak current was observed at about 250 mV anodic of Al (Figure 2.20). The peak current was found to be proportional to the square root of the sweep rate ($v^{1/2}$), indicating a diffusion controlled reaction. The peak was not observed for Al_4C_3 concentrations above 0.64 wt%. A transition from diffusion control to kinetic control was proposed as a possible cause.

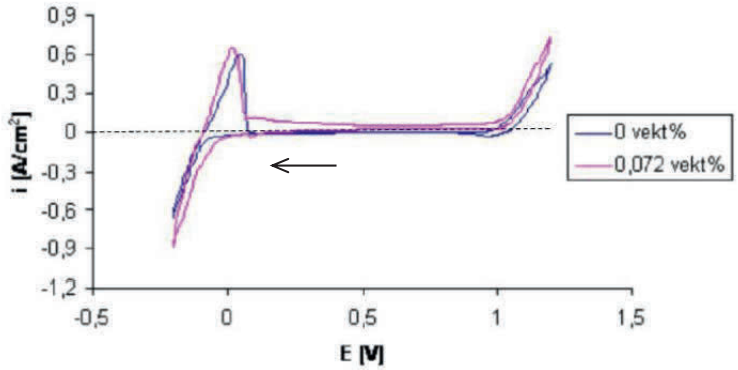

Figure 2.19: Cyclic voltammograms recorded on tungsten working electrode in cryolitic melt (CR = 1.8) at 940°C before and after addition of 0.072 wt% Al_4C_3 [38].

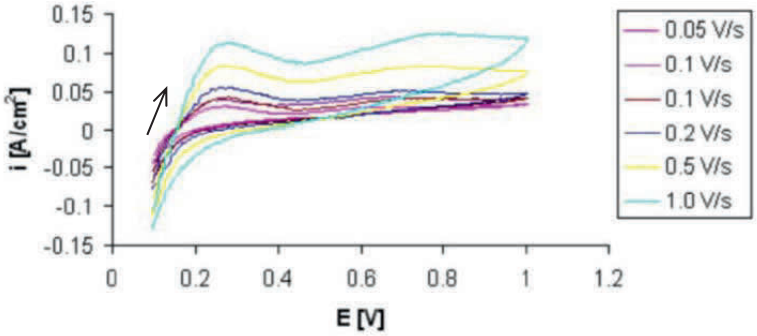

Figure 2.20: Cyclic voltammograms with varying potential sweep rates recorded on tungsten electrode in cryolitic melt (CR = 1.8) with 0.23 wt% Al_4C_3 at 940°C.

Liu et al. [39] investigated the cathodic behaviour of graphite in KF-AlF_3 melts. Figure 2.21 shows a voltammogram recorded on graphite at a potential scan rate of 100 mV/s in melt with cryolite ratio 1.3 (n_{KF} / n_{AlF3}) at 850°C. They claimed that the cathodic peak current A was associated with deposition of aluminium, while peak B was related to potassium intercalation. Correspondingly, the anodic peaks B_1 and B_2 were attributed to deintercalation of potassium and stripping of Al-K alloy. Peaks A_1 and A_2 were ascribed oxidation of carbon from dissolved and absorbed aluminium carbide. A_3 was claimed to result from stripping of liquid aluminium, while A_4 corresponded to extraction of aluminium bonded with carbon.

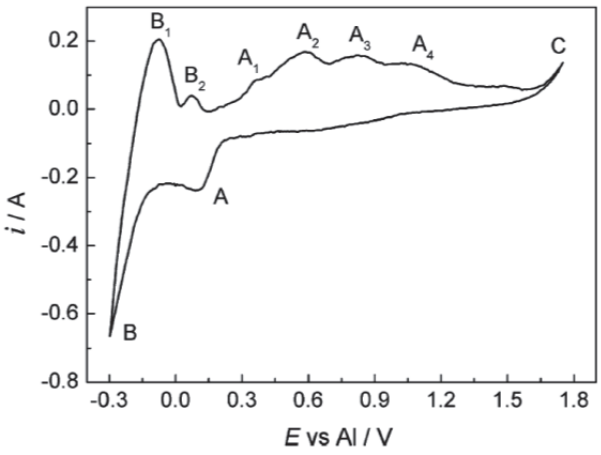

Figure 2.21: Cyclic voltammogram of 100 mV/s scan rate recorded on graphite electrode in KF-AlF_3 melt (CR = 1.3) at 850°C [39].

2.2.3 Sodium and bath penetration

Kvande et al. [40] investigated wetting and bath penetration in carbon electrodes. In a micro-electrolysis cell, they found that negatively polarized carbon had superior wetting compared to positive carbon. During electrolysis the bath spread evenly on the cathode, but tended to separate from the anode. Measurements of amount of bath penetration in carbon at different polarity coincided with the wetting experiment. The NaF content in cathodic graphite was much higher than in anodic graphite. It was also found that the wetting angle of the cathode decreases with increasing current density. For a given cathodic current density, the wetting angle also decreased with time. This was explained by the formation of aluminium at the cathode. Measured NaF content in the carbon electrode as a fuction of cathodic current density is shown in Figure 2.22.

Peyneau et al. [41] used the so-called Rapoport test, a laboratory test for in situ measuring of sodium expansion during electrolysis, to measure sodium expansion with varying bath composition, temperature, graphite content in the cathode and applied pressure. They concluded that expansion due to sodium penetration increase with decreasing temperature and with decreasing excess AlF_3 content (increasing cryolite ratio). The sodium expansion decreases as the graphite content increases, and the smallest expansion was found in graphitized material. Figure 2.23 shows the results from the experiments with varying graphite content and pressure, and as expected, it can be seen that applying pressure will decrease the expansion. For the graphitized material the expansion was measured to 0.039% without, and 0.018% with 30 kg/cm^2 pressure applied.

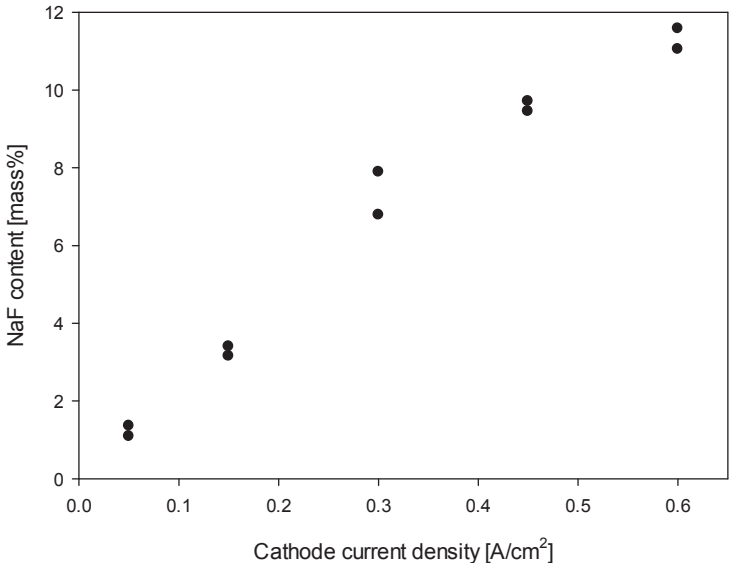

Figure 2.22: NaF content in carbon as a function of cathodic current density after one hour electrolysis at 1000°C. Replotted from Kvande et al. [40].

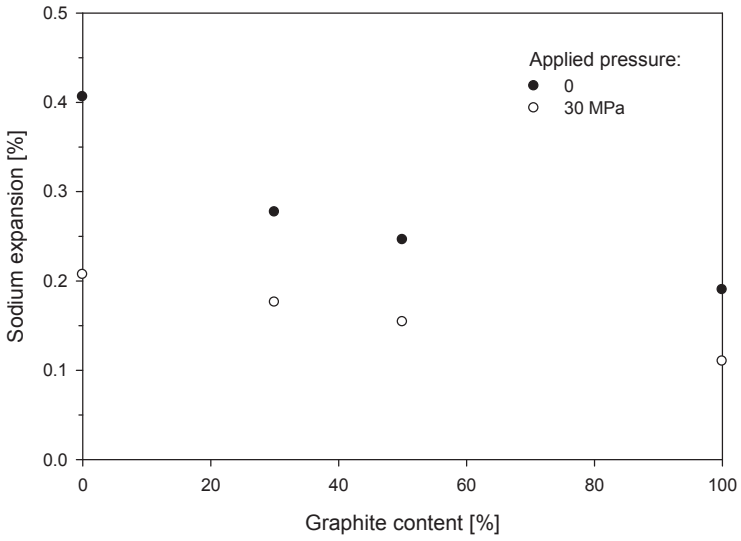

Figure 2.23: Sodium expansion as a function of graphite content in cathode materials with and without external pressure. Replotted from Peyneau et al. [41].

Brilloit et al. [42] found that the penetration velocity and saturation concentration of sodium increased with increased cryolite ratio of the melt and decreased graphitisation of the carbon material. Their experiments also showed that melt penetration was enhanced by polarisation and by formation of nitrogen compounds. The cryolitic bath penetrated the carbon cathodes during electrolysis, following, but not overtaking, the sodium front. When turning off the current to allow equilibration, the melt progression proceeded at a lower velocity in the experiments in nitrogen atmosphere. The same tendency was difficult to observe for the experiments in argon atmosphere, as the velocity of which the melt proceeded to progress was drastically lowered. X-ray diffraction analysis of cut cathode slices revealed the presence of the following phases: Na_3AlF_6, NaF or $Na_5Al_3F_{14}$, CaF_2, $Na_2O{\cdot}11Al_2O_3$, $NaAlO_2$, α-Al_2O_3, NaCN and AlN. In experiments without subsequent equilibration the oxide precipitated only as $Na_2O{\cdot}11Al_2O_3$ in argon atmosphere and as $Na_2O{\cdot}11Al_2O_3$ and $NaAlO_2$ in nitrogen atmosphere. For experiments with equilibration after electrolysis $Na_2O{\cdot}11Al_2O_3$ and α-Al_2O_3 were found, but no $NaAlO_2$.

Schreiner [43] used a modified experimental set-up to conduct the Rapoport test while applying pressure to the carbon samples. The results of his tests are in agreement with Peyneau et al.[41]; amorphous carbons have the largest expansion, increase of graphitic content decreases the expansion and graphitized carbon has the least expansion. As external pressure is applied, however, this difference in expansion between the carbon types is reduced. Figure 2.24 shows the expansion as a function of pressure relative to the expansion achieved without pressure. Regardless of the material, the reduction in the expansion is more conspicuous in the low pressure range, i.e. 0–1 MPa. The amorphous and semi-graphitic carbons were tested in two directions, parallel and perpendicular to the extrusion direction, and for the amorphous materials the expansion seemed to be larger perpendicular to the extrusion direction. No noticeable difference was observed for the semi-graphitic samples. Compressibility was also larger in the perpendicular direction, for the amorphous as well as the semi-graphitic carbons. Upon release of pressure the samples expanded in the direction they had been compressed. The most amorphous samples seemed to keep the elasticity during electrolysis, and expanded in the same magnitude as they were compressed. Reduction of elasticity was observed for the other samples. When no pressure was applied, Schreiner observed that the carbon sample continued to expand after the electrolysis.

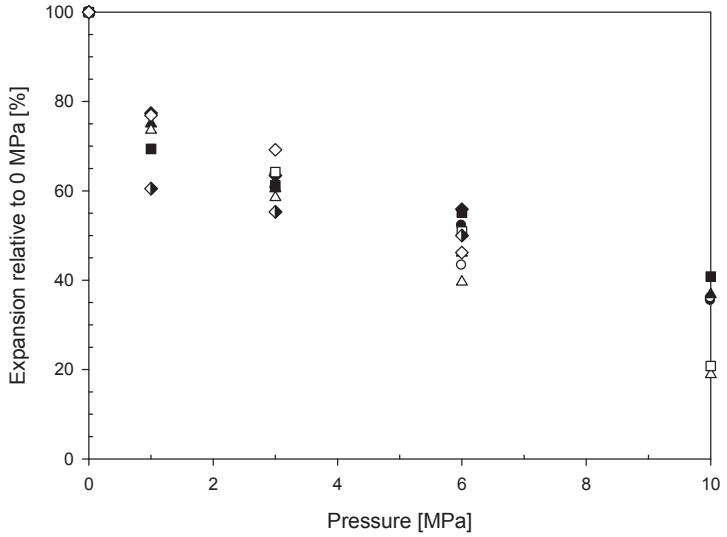

Figure 2.24: Expansion as a function of applied pressure relative to the expansion without pressure. Filled circle, filled triangle, filled diamond: amorphous carbons with 20–50 % electrographite added, parallel. Open circle, open triangle: amorphous carbons with 20–50 % electrographite added, perpendicular. Filled square: semi-graphitic, parallel. Open square: semi-graphitic, perpendicular. Semi-filled diamond: semi-graphitized, parallel. Open diamond: graphitized. Replotted from Schreiner [43].

The semi-graphitic samples that had undergone electrolysis with and without external pressure were investigated by back scatter imaging on a scanning electron microscope. It was clear that the sample electrolysed with a pressure of 10 MPa contained larger area of unreacted carbon compared to the unpressurised sample, although the sodium content found by titration did not reveal any significant difference within one cathode carbon due to pressure. The amount of reactive sodium was found by submerging pieces of the samples (not crushed) in HCl solution and back titration with NaOH. Schreiner reported that more than 1000 hours of reacting time was needed to obtain a steady value of the sodium content.

Schreiner [43] found a significant lowering of the electrical resistivity of the electrolysed samples compared to the virgin ones, but pressure did not seem to make any difference. The measurements were done after the samples had cooled down after the Rapoport test.

Mikhalev and Øye [44] studied the absorption of sodium vapour in commercial cathode materials within the range of 745–950°C and 0.4–80 kPa by thermogravimetry. The tested materials were: Gas-calcined anthracite (GCA) filler with about 30% graphite baked to about 1200°C, graphite filler baked to about 1200°C (semi-graphitic), Petroleum coke filler calcined to about 2300°C (semi-graphitized), and graphite. A sketch of the experimental set-up is shown in Figure 2.25.

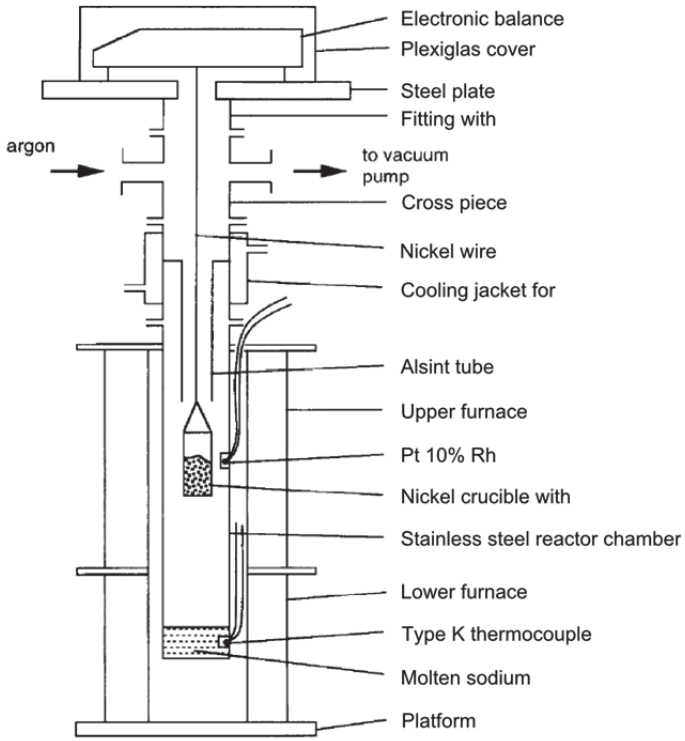

Figure 2.25: Schematic drawing of the equipment for thermogravimetry used by Mikhalev and Øye [44].

Isothermal experiments gave an increased degree of absorption with increasing sodium pressures, and isobaric experiments gave increased absorption with decreasing temperatures. Sodium absorption in graphite was found to be very low, and a minimum sodium pressure was required before weight increase occurred. The anthracitic carbon expectedly had the largest degree of sodium absorption, noticeable larger than for the semi-graphitic and the semi-graphitized material. From the results they calculated the BET isotherm ($\Delta W_m/W^0$, where ΔW_m is the weight of sodium in a monolayer and W^0 is the original weight of carbon) and the specific surface area. The values are given in Table 2.2.

Table 2.2: Calculated and measured parameters for carbon materials. From Mikhalev and Øye [44].

Parameters	GCA	Semi-graphitic	Semi-graphitized
BET isotherm, $\Delta W_m/W^0$ [g Na/g C]	0.034	0.0113	0.0025
Calculated specific surface area [m^2/g]	124	42	9
Specific surface area measured by helium adsorption [m^2/g]	0.85	0.95	0.95

Naas [45] investigated the interactions of alkali metal and cryolitic melts with cathode carbons, especially regarding the consequences of adding LiF or KF to the electrolyte. Alkali expansion measurements were conducted in Schreiner's [43] Rapoport test apparatus, with slight modifications. There were also developed experimental set-ups for measuring the compressive strength of the samples *in situ* immediately after electrolysis, and for measuring alkali metal absorption. Minor modifications of the latter, which was based on the apparatus used by Mikhalev and Øye [44], allowed for quenching and preparing samples for XRD and SEM analysis within an inert argon atmosphere. The various electrolyte compositions that were used are listed in Table 2.3, and Figure 2.26 shows the compressive strength of a semi-graphitic carbon material, perpendicular to the extrusion direction, as a function of electrolysis time for the respective electrolyte compositions.

Table 2.3: Electrolyte compositions in the experiments of Naas [45].

Electrolyte	LiF [mol%]	KF [mol%]	NaF [mol%]	CaF_2 [mol%]	MgF_2 [mol%]	Al_2O_3 [mol%]	MR**
A Reference	–	–	62.5	5.0	2.0	3.0	2.2
B High K	–	21.0	41.5	5.0	2.0	3.0	2.2
C $n_{LiF} = n_{KF}$	10.0	10.0	42.5	5.0	2.0	2.3*	2.2
D $n_{LiF} > n_{KF}$	13.8	6.2	42.2	5.0	2.0	2.0*	2.2
E High Li	19.0	–	43.5	5.0	2.0	1.2*	2.2

* Estimated alumina solubility

** $MR = (n_{NaF} + n_{KF} + n_{LiF})/n_{AlF_3}$

It can be seen from Figure 2.26 that KF in large amounts are very detrimental to the carbon cathode. Electrolysis at 830°C with an electrolyte containing 21 mol% KF caused complete loss of compressive strength after about one hour of electrolysis, and Naas [45] attributed this to formation of large cracks as the large potassium atoms react with the carbon. The small lithium atoms, obviously, do not have the same effect. The compressive strength of the carbon subjected to electrolysis in the electrolyte high on lithium was slightly less reduced compared to that of the carbon subjected to the reference electrolyte. This was explained by a reduced sodium activity as an effect of substitution of NaF with LiF.

The alkali expansion tests of Naas [45] revealed that the expansion decreases with increasing content of LiF in the electrolyte, while KF has an opposite and larger effect. It was also found that the expansion is higher at low temperatures. The results are shown in Figure 2.27.

The results from the sodium absorption experiments were similar to those of Mikhalev and Øye [44]. The BET isotherm was calculated to be 0.0154 g Na/g C and the specific surface area 84 m^2/g, assuming that each sodium atom touch one carbon surface. However, Naas [45] found it more likely that each sodium atom touched two graphene sheets, which would give a surface area of 168 m^2/g covered by sodium. The calculated mole fraction of Na corresponds with NaC_{124}. He mentioned a modification of the experimental set-up that placed the thermocouple closer to the crucible as a possible explanation for slight discrepancies with the results of Mikhalev and Øye [44].

Quenching experiments of semi-graphitic carbon gave C/Na ratio 83.8 and C/K ratio 38.9 at Na pressure of 18 kPa and K pressure of 6 kPa, respectively. SEM analysis and element mapping showed that the sodium penetration had caused formation of small cracks in the sample and that the sodium distribution was inhomogeneous; the concentration of sodium was higher in the binder phase than in the graphite grains. Interaction between potassium and the carbon material had led to formation of larger cracks, some extending across the sample. Potassium had reacted with both graphite and binder coke without any apparent preference for the binder.

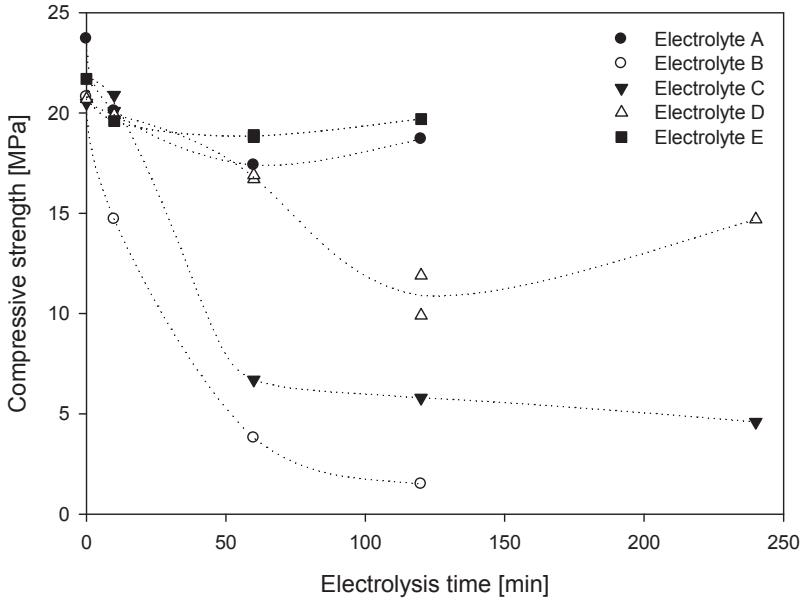

Figure 2.26: Compressive strength of semi-graphitic samples as a function of electrolysis time. Strength was measured perpendicular to the extrusion direction Current density: 0.6 A/cm^2. Temperature: 980° for electrolyte A, 830°C for electrolyte B, C, D, and E. Replotted from Naas [45].

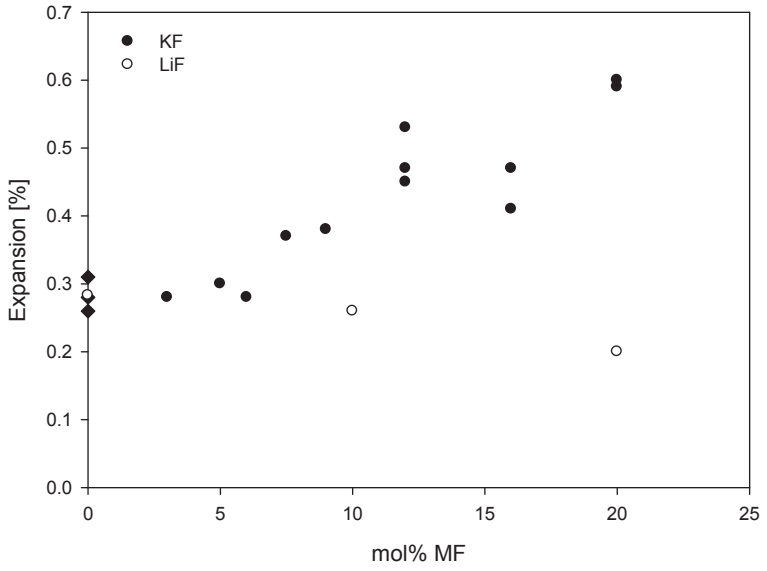

(a)

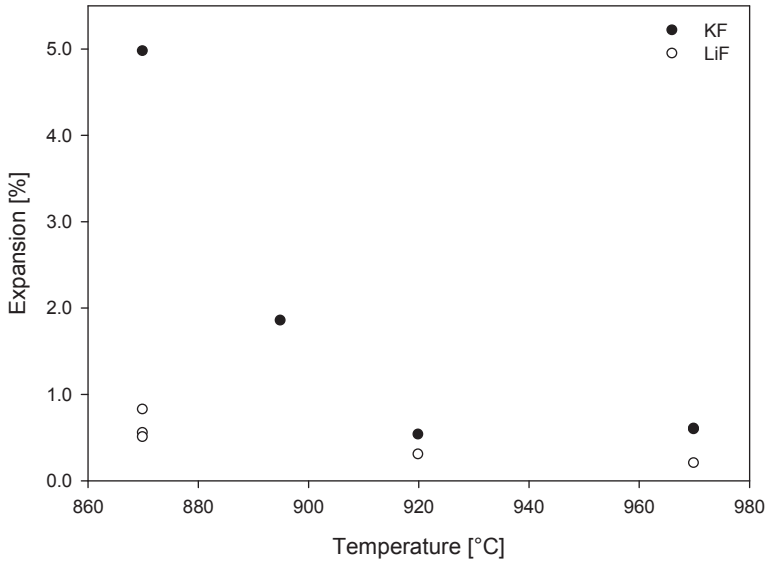

(b)

Figure 2.27: Alkali expansion in semi-graphitic material as a function of (*a*) KF or LiF content in electrolyte at 970°C (MF = KF, LiF), and (b) temperature with 20 mol% KF or LiF. MR = 2.2, current density 0.7 A/cm^2. Replotted from Naas [45].

Akuzawa et al. [46] investigated sodium intercalation in carbon materials with different graphitization degrees. Samples, mainly prepared from needle-like petroleum cokes, were heat-treated at different temperatures: 1500°C, 1750°C, 2200°C and 2400°C; and then subjected to metallic sodium under vacuum for periods ranging from one to five days. Changes in the carbon structure were examined by X-ray diffraction, electrical resistivity and electron spin resonance. The investigation showed that there was a large difference between the samples treated at 1500°C and 1750°C and the samples treated at 2200°C and 2400°C regarding the expansion of the carbon-carbon interlayer due to sodium intercalation. It was concluded that less graphitized carbons is highly reactive against sodium and well graphitized materials, such as the samples treated at 2200°C and 2400°C, has a poor reactivity. This also implies that less graphitized carbon blocks will be subjected to a higher stress in the matrix, which may cause degradation. The electrical resistivity increased only for the sample treated at 1500°C while it decreased for all the other samples. Thus it was suggested that increasing the graphitization temperature from 1500°C to 1750°C brought about an improvement in stress resistance.

2.3 Investigations and observations from industrial cells

2.3.1 Alumina sludge

Thonstad et al. [47] analysed samples of alumina sludge from commercial pots. They found an average of 40 wt% Al_2O_3, the remaining being mostly fluorides and some aluminium. To determine the exchange between sludge and bath, two parallel tests were performed on a number of 140 kA prebake pots serviced by a “rotating wheel” crust breaker on a two hours schedule. In some pots a tracer ($BaCO_3$) were added directly to the bath, and in the others the tracer was introduced via a synthetic sludge, composed of 44% Na_3AlF_6, 26% BaO and 30% Al_2O_3. Two to four days after adding the synthetic sludge to the pots, half the amount of tracer had appeared in the bath. When tracer was added to the bath, they saw a steady decrease of its concentration in the bulk bath and an increasing concentration in the sludge samples. They concluded that there is a fairly rapid exchange between the sludge and the bath in this type of pots, and that the most likely transport route is through a liquid film of bath between the metal and the side ledge. Circulation in bath and metal and crust breaking was also mentioned to promote the exchange process.

2.3.2 Metal oscillation

Johnson [48] developed a technique to measure the metal velocities in aluminium reduction cells by inserting iron rods vertically into the metal pad. The method is based on the assumption that the rate of which the iron rod dissolves is directly related to the metal velocity through an empirical mass transfer relationship. The dissolution patterns on the

iron rods showed that the flow direction of the metal pad differs from top to bottom, making it difficult to follow streamlines throughout the cell cavity. Johnson performed a test with a prebaked cell, where he increased the metal height from six to nine inches to see if it brought about any changes in the metal velocity. His hypothesis was that if the horizontal currents in the metal pad are a significant factor for the metal movement, adding metal and thus decreasing horizontal current density would result in a decrease in overall metal velocity. No change in the average velocity was detected, and it was concluded that other factors, such as muck and ledge formation override metal depth in influencing metal flow.

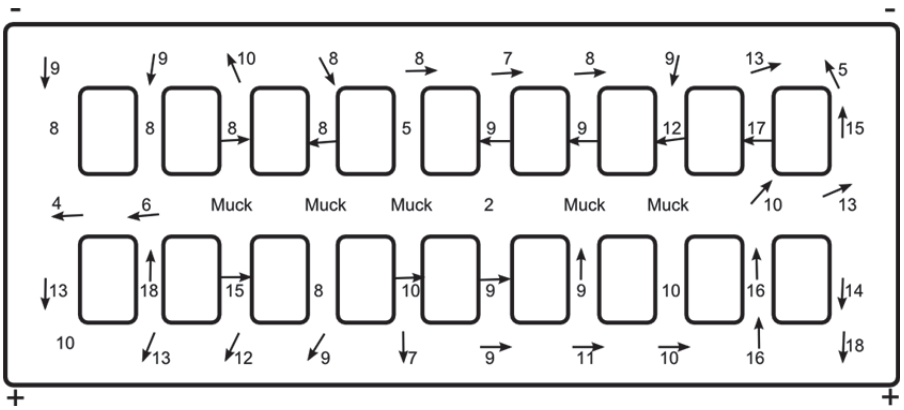

Figure 2.28: Metal pad velocities (cm/sec) at various locations in a reduction cell with 18 prebaked anodes. The numbers indicate average velocity and represent an average of eight measurements over twelve months. The arrows give the flow direction observed in more than 50 % of the tests. Where no arrows are shown, no specific direction could be determined for at least 50 % of the measurements. Redrawn from Johnson [48].

Tabereaux and Hester [49] used the technique developed by Johnson [48] to measure the metal pad movements in prebake and Søderberg cells. As they found that Johnson's empirically derived relationship used to calculate the metal velocities was based on calibrations made in a temperature range below those found in reduction cells, they redefined the relationship by conducting calibration with metal temperatures in the range of 950 to 965°C. Calibration tests with various iron alloys showed that only commercially pure iron could provide the reproducible results necessary for velocity measurements.

From the metal velocity measurements in commercial cells, Tabereaux and Hester could establish certain trends:

- The overall metal flow circulation pools and/or patterns for each cell are fairly constant, although there are some variations in the direction of metal flow at some points.
- Each cell design has a different and distinctive metal circulation pattern.

- Variable cell conditions caused by excessive muck, ledges, anode changes, etc. can disturb the metal flow and give variations in the flow direction and/or velocity.
- The highest metal velocities are generally found near the sidewalls at the end of the cells, and the lowest velocities are found in the middle of the cells where the metal pools generally converge.
- Low average metal velocity and low standard deviation of metal velocities indicate good metal pad stability.

Figures 2.29–2.31 show some results from the metal velocity measurements of Tabereaux and Hester, together with metal circulation patterns derived thereof.

Bradley et al. [50] also performed metal velocity measurements using the technique developed by Johnson [48], and like Tabereaux and Hester [49], they also calibrated the method to higher temperatures. Their measurements were conducted on several 130 kA Invergordon cells at eight or ten standard positions, typically between anodes. It was found that young cells all had similar flow patterns, while old cells showed wide variations. In cells younger than 150 days vortices at each end was found. The metal velocities were higher at the upstream side, and highest at the corners. Cells younger than 400 days showed the same pattern, but less distinct. The velocity measurements in older cells varied more and no general patterns could be deduced with any degree of certainty. The vectorial average metal flow can give the impression that cells with large variations in metal flow direction and velocity have lower metal velocities than the more stable cells. However, Bradley et al. found that the average velocity is almost independent of cell age.

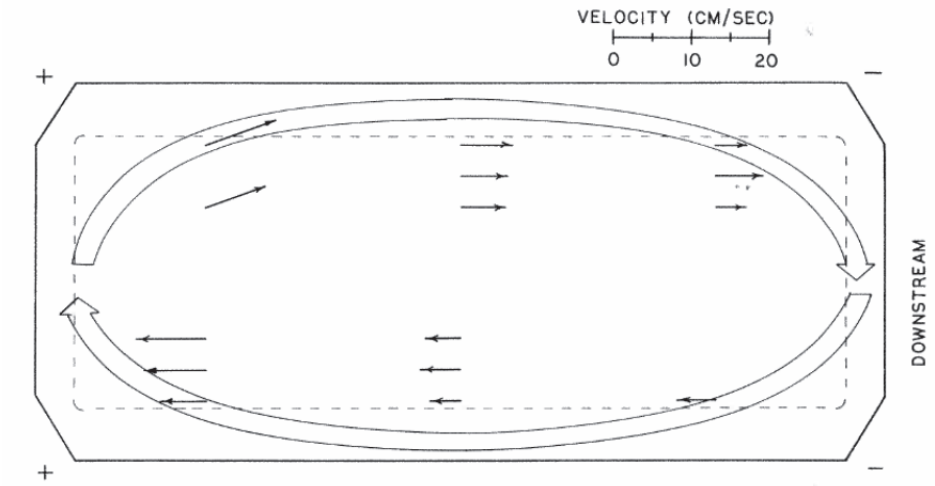

Figure 2.29: Metal flow velocities in a 110 kA Søderberg cell. From Tabereaux and Hester [49].

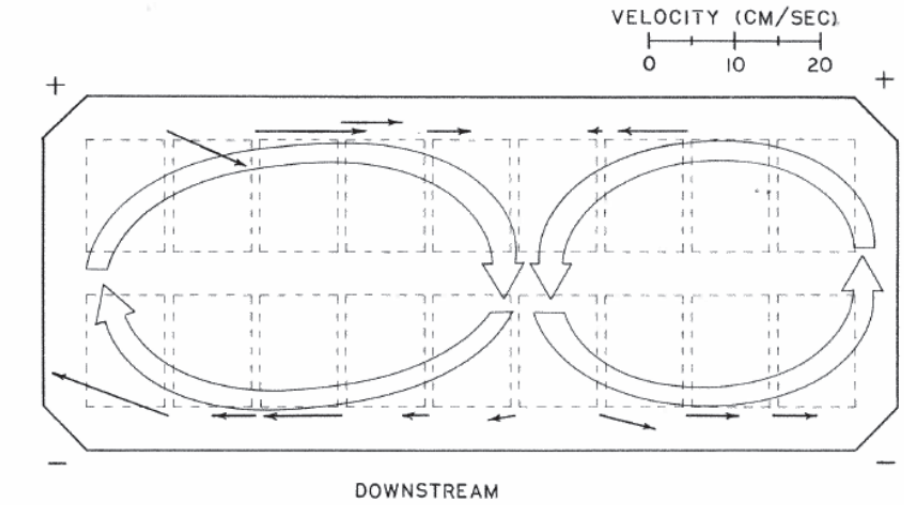

Figure 2.30: Metal flow velocities in a 150 kA end riser prebake cell. From Tabereaux and Hester [49].

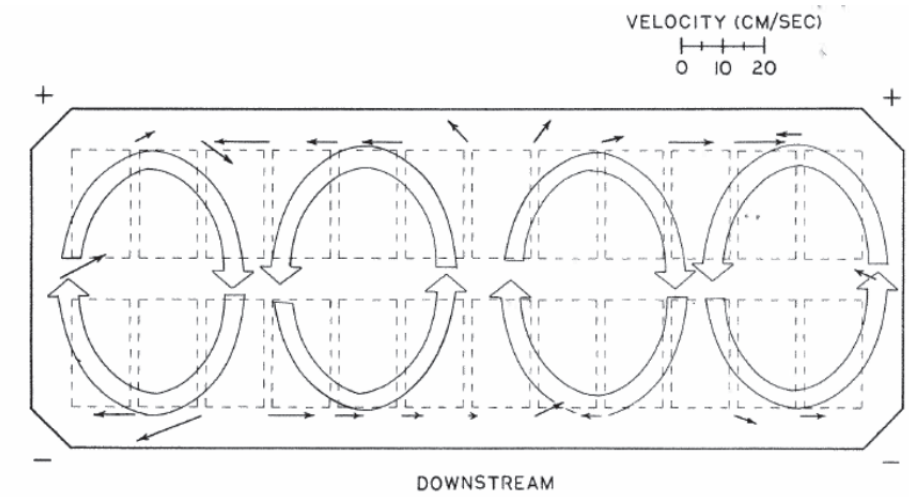

Figure 2.31: Metal flow velocities in a 150 kA quarter riser prebake cell. From Tabereaux and Hester [49].

Matsui and Era [51] developed a device for direct measurement of the vertical oscillation of the metal pad in industrial cells. The principle behind the device was to estimate the distance between a polarised probe and the metal interface by measuring the potential, and their measurements were performed on 130 kA side by side prebake cells. In stable cells they measured small oscillation values and assumed the real oscillation had amplitude as small as 5 mm. They also found larger oscillations, e.g. a nearly symmetrical

wave with 5 cm amplitude and with a period of about 40 seconds. This wave coincided with a fluctuation in the anode stem current by 7–8 kA. It was concluded that the fluctuation of the anode stem current, in most cases, is in good linear relation to the magnitude of the oscillation of the metal pad. The fluctuation of the cell voltage was also found to be roughly proportional to the oscillation. Based on their results, Matsui and Era stated that measuring the anode stem current can be an alternative way to estimate the metal turbulence.

Cherchi and Degan [52] used measurements of the anode stem current to estimate the oscillation of the metal pad in 150 kA side by side prebake cells with and without magnetic compensation. The uncompensated cells were exposed to a mean vertical magnetic field of about -20 Gauss, while the compensated ones were exposed to a mean vertical field of 3–5 Gauss. Three main types of oscillation were found in the uncompensated cells: small amplitude oscillations with fluctuations of about 1–2 kA in each of the 16 anode stems, which did not influence the cell voltage and dampened spontaneously; medium amplitude oscillations, which did influence the cell voltage and could easily be handled by the process computer; and strong oscillations with current fluctuations greater than 5 kA, where intervention to remove the disturbance took longer and was more complex. Interpretation of the anode current measurements gave a wave-like phenomenon with two peaks that moves clockwise with a period of about 40–50 seconds. The velocity was found to be greatest at the upstream side, while the average amplitude was higher on the downstream side. Magnetic compensation reduced the oscillation drastically. While about half of all the uncompensated cells exhibited regular oscillations, only about one out of ten compensated cells showed regular oscillation. Also the amplitude was reduced with magnetic compensation. The average amplitude of the cells with compensation showing regular oscillations was about 0.5 cm, while the average for the uncompensated was 1–3 cm.

2.3.3 Sodium uptake

Mittag et al. [53] used registered values for consumption of sodium fluoride and aluminium fluoride in 100 kA cells to plot the sodium uptake electrolysis time. The sodium uptake was initially very high, declined fast and stabilised after some months. A clear difference could be seen between pots with semi-graphitic carbon cathodes and pots with anthracite and 50% graphite. The anthracite based cathode both started and stabilised at higher levels of sodium uptake than the semi-graphitic cathode. In both cases the sodium consumption was much too high to be attributed solely to uptake in the carbon blocks, indicating sodium penetration all the way through the cathode and into the isolation materials. Measurements of the forces acting on the pot shell revealed a thermal expansion during the preheating, followed by a relaxation of the forces due to a rise of the

temperature in the pot shell. As electrolysis proceeds and sodium penetrates the cathode, the carbon blocks expand and the forces acting on the pot shell increase.

2.3.4 Cathode wear rate

Taberaux et al. [54] measured changes in the top level of cathode blocks due to erosion in 180 kA prebake cells for three consecutive years in order to determine the wear rate for different types of cathode blocks. Two anodes on the upstream side and two anodes on the downstream side were removed, and the measurements were made using a sidewall ledge profile rod attached to a levelling arm and a measuring board. The results indicated high, linear wear rates (2 to 3 cm/year for the first four years) for graphitized blocks, with the rate slowing after 1600 days. The average wear rates for the first four years were 1.2–1.8 cm/year for graphitic blocks and about 0.9–2.2 cm/year for semi-graphitic blocks with 15–30% graphite aggregate. All the mentioned rates were measured beneath anodes, where the maximum wear areas occur. Some of the areas were more worn than others and the wear pattern was found to be rougher and more pitted in these areas. The ram carbon seams between the cathode blocks were generally less eroded. Indications of initially higher wear rate at the tap hole was found, but it tended to stabilise after several years and thereafter progress similar to the wear of the block under the anode. The measured wear rate at the tap hole varied significantly for different cells and plants.

Reny and Wilkening [55] studied the cathode wear in AP30 pots at Aluminerie Alouette Inc. A surveyor's laser was used to accurately measure the depth of which a rod could be lowered into the pot at certain positions, allowing measuring of the wear on operating pots during normally scheduled anode change. One of the surveyed pots was stopped during the study and was thus used to validate the accuracy of the measurements of the live pot. The wear measurements performed during the delining of the pot showed that the wear measurements during operation were within 1.5 cm of the real value.

A typical W wear patter was documented on the long axis of the carbon blocks, and an unsymmetrical U pattern was found on the short axis. The ramming joints between the blocks were the least eroded areas and the most eroded areas seemed to be over one of the two upstream cathodic steel bars. From this Reny and Wilkening [55] could tell that mechanical abrasion caused by the dust grab and other machinery cannot be the main wear mechanism, as the ramming joints would then have been shaved off. The higher wear over one of the cathodic bars indicates that the cathodic current distribution plays an important role, and that higher local current accelerate cathode wear. The presence of small rounded holes in the cathode in the stopped pot was explained by mechanical erosion from small eddies, implying that both chemical and mechanical wear mechanisms erode the carbon.

In the deepest worn blocks, Reny and Wilkening [55] reported to have found that ledge or muck had formed in the bottom of the holes. They could tell simply by that a rough surface would be graphite and a smooth surface would be something else. This finding could explain the levelling of the wear rate observed by Taberaux et al. [54] after about 1600 days. There is a high heat flow through the collector bars, and the carbon close to the bars will therefore be colder. As a hole is eroding closer to the collector bar, the carbon may eventually be cold enough to freeze some bath or alumina sludge which would protect against further downwards erosion. Such an insulating layer would force current further in toward the centre, spreading the wear onto a larger area of the cathode surface.

2.3.5 Structural changes in the cathode material

Bacchiega and Letizia [56] investigated the changes in the physical properties of a (anthracitic) carbon block after 44 months of electrolysis in a 70 kA cell with current density of approximately 0.8 A/cm^2. They found significant changes in the electrical and thermal properties, as well as the mechanical properties. The apparent density of the carbon block was increased by 40% due to sodium impregnation. The compressive strength and the flexural strength were found to be much greater in the impregnated carbon than the original before electrolysis, in both transversal and longitudinal direction. The electrical resistivity was decreased with more than 50% and the electrical anisotropy of the original carbon seemed to have disappeared during electrolysis and sodium impregnation. After eliminating impregnation compounds by chemical purification the electrical resistivity increased, but it was, however, still lower than in the original carbon. This indicates that the carbon had been chemically graphitized to some extent during operation. The thermal expansion coefficients, measured between 20 and 200°C, increased up to three times after electrolysis, and the thermal conductivity measured at 40°C increased up to five times. Chemical purification, however, brought the thermal conductivity back to the normal value of the original carbon material.

The catalytic graphitization occurring in the carbon cathodes throughout the operative lifetime of the pot was studied by El-Raghy et al. [57]. Core drilled samples of different types of anthracite based cathodes in 155 kA Søderberg cells of different ages, were analysed by x-ray diffraction, differential thermal analysis (DTA), thermal gravimetric analysis (TGA), and inductively coupled plasma (ICP). Their results showed that the graphitic content in the cathodes increased significantly with electrolysis time and a linear decrease of electrical resistance versus cathode life time. The sodium content increased rapidly during the first year of operation and continued to increase more and more slowly afterwards. They concluded that amorphous cathodes are catalytically graphitized mainly due to sodium intercalation and that graphitization and melt penetration results in

decreased electrical resistivity. The DTA results indicated that the sodium also acts as a catalyst for the oxidation of carbon.

2.3.6 Variable resistivity graphite cathode

Dreyfus et al. [58] has investigated the possibility of increasing the pot life by introducing variable resistivity graphite (VRG) cathodes. The idea behind such cathodes is that a higher resistivity at the ends of the cathode blocks will give a more uniform current distribution throughout the cathode surface, thereby obtaining a more even wear profile. Success will mean longer lifetime for the pots and less SPL when they eventually are terminated. As VRG cathodes had been used in industrial cells for only a short time, no definitive conclusions could be drawn when Dreyfus et al. published their paper in 2004 [58]. They did, however, report perfect behaviour of the VRG cathodes to all stresses induced during casting, preheating and start-up, and also normal thermal balance in the cells. The change in cathode voltage drop was found to be negligible and in situ measurements of the erosion rate showed a tendency of decreased wear rates compared to standard graphite grades.

2.3.7 Ridged/grooved cathode blocks

In China, at Chongqing Tiantai Aluminium Co., Naixiang et al. [59] followed the performance of three tests cells with a novel cathode structure, started in 2008. The surface of the cathode blocks were ridged, as can be seen from the illustration in Figure 2.32. The cells were operated with a metal level of 5–6 cm and a bath level of 18–20 cm. It was assumed that the ridges would stabilize the aluminium metal pad, giving less vertical fluctuations and make it possible to lower the anode cathode distance. As a consequence, this would lead to lower cell voltage and reduced power consumption.

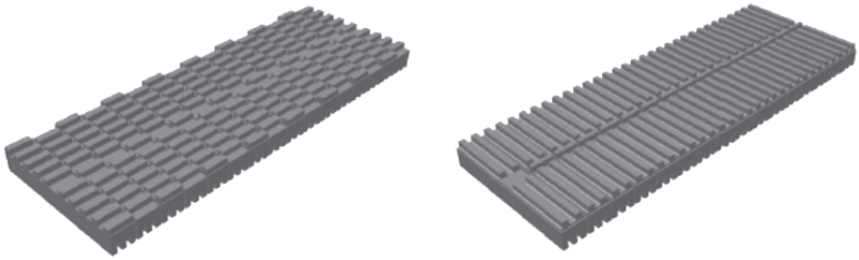

Figure 2.32: Schematic diagram of ridged cathodes from F. Naixiang et al. [59].

The results after one year of operation were positive. Compared to the average performance of 127 traditional 168 kA cells at the same plant, the average cell voltage of the test cells was reduced by 0.334 V and the power consumption was reduced by

1260 kWh/t-Al. Furthermore, the current efficiency was increased with 1.4 percentage points, from 91.8 % to 93.2 %.

2.3.8 Observations from Qatalum after power outage

Qatalum produced its first metal in December 2009 [60]. In August 2010 the aluminium plant experienced a serious power outage, leading to solidification of the bath in most of the electrolysis cells. The metal and bath had to be mechanically removed before restarting of the cells could commence. Disastrous as this event may have been, it also gave a unique opportunity to inspect the wear of modern industrial cathodes after only months or weeks of operation. The following information and picture was provided by Hydro employees that have been on site [61].

Figure 2.33: Solidified metal pad removed from a terminated cell at Qatalum. The picture was taken from beneath the metal pad, held up by a crane. The metal and bath remnants act as a cast of the cathode surface, showing the inverted pattern. The bumps in the lower right area on the photograph correspond to the holes or dimples in the cathode surface. Yellow flakes and dust, i.e. aluminium carbide, can also be seen. Photo: S. Jarek, Hydro.

Many of the cathodes that had been operated for just a few days were found to have a coarsened surface with many small holes or dimples. A kind of pitting erosion seemed to have taken place on the entire cathode. Crates after pre-heating and start-up were visible on the surface of cathodes after about one month of operation. In cells operated for more than a month the surface was rougher and the initial crates eroded away. In general, there was found few cathodes with evident erosion zones with considerable wear, but

coarsened and dimpled cathode surfaces was often seen. Cathodes run for six months and longer were more prone to have this coarse surface, and some were found to have begun to develop shallow erosion holes at corners and the tapping area.

The cathodes at Qatalum were, to a wide extent, found to be covered by a yellow layer, i.e. aluminium carbide. Yellow scaling was also observed on the side lining in some cells.

2.4 Theoretical work on cathode wear mechanisms

Solheim [62] has written a paper where he discusses three possible chemical and electrochemical wear mechanisms: stationary mass transport of carbon into the metal, non-stationary dissolution of carbon into a sludge layer that periodically forms and disappears, and electrochemical formation and dissolution of aluminium carbide within an aluminium carbide layer containing bath-filled pores.

In his model for stationary mass transport of carbon, Solheim [62] estimates the carbon flux through metal and bath; from carbon saturated metal at the bottom of the cell to zero carbon concentration at the interface between bath and the anode (or anode gas bubbles). For a typical aluminium reduction cell the cathode wear rate due to stationary mass transport of carbon was calculated to 2.0 cm/y. This value is reasonably representative for the average cathode wear, but due to the highly varying wear rates seen from industrial cathodes, Solheim [62] argued that there must be other important mechanisms. Though non-uniform wear in principle may be explained by assuming the mass transfer coefficient at the cell bottom is non-uniform due to variations in the metal flow, it is not reasonable that the flow variation is large enough to explain the typical “W” wear pattern.

For the model of non-stationary dissolution of carbon, Solheim [62] considered carbide diffusion into a stagnant sludge layer at the cell bottom which is periodically removed and renewed. The amount of carbide dissolved during one event, i.e. the covering by and removal of sludge, decreases with decreasing time per event. Decreasing duration of each event does, however, give a higher number of events per unit of time, and it was found that frequent removal and renewal of the sludge layer gives more rapid cathode wear than slowly occurring events. If the sludge is removed and renewed only at long intervals, sludge may act as a protection against cathode wear. An overview of the relation between the event duration (t_e) and the expected wear rate is given in Table 2.4.

In modern cells using cathodes with high electrical conductivity excessive wear has been observed at the periphery of the cathode blocks. Solheim and Tscöpe [62, 63] related this high wear to high local current densities, and proposed a conceptual wear model, a

"carbon pump", based on electrochemical formation and dissolution of carbide in bath filled pores in a solid aluminium carbide layer.

Table 2.4: Amount of carbon removed from the cathode by non-stationary dissolution of aluminium carbide into a stationary layer of alumina sludge. The density of the cathode was assumed to be 1650 kgm^{-3}. From Solheim [62].

Time t_e		N	m	mN	Wear rate
[s]	[-]	[Events/y]	[kgm^{-2}/event]	[kgm^{-2}/y]	[cm/y]
1	1 s	31536000	0.00010	3154	191
60	1 min	525600	0.00077	407	25
600	10 min	52560	0.0024	129	8
3600	1 h	8760	0.0060	53	3.2
36000	10 h	876	0.019	17	1.0
86400	1 day	365	0.029	11	0.7

It is assumed that the cathode is covered by a solid layer of aluminium carbide, at least spot-wise or during certain periods. As aluminium carbide is non-conductive, electrical current passes into the cathode either through metal-filled pores in the carbide layer or around the carbide spots. This leads to a potential gradient along bath-filled pores in the carbide layer, from the metal at the top to the carbon on the bottom. The potential gradient may enable electrochemical crystallisation of aluminium carbide at the bottom of the pore and dissolution of aluminium carbide at the top of the pore, as illustrated in Figure 2.34.

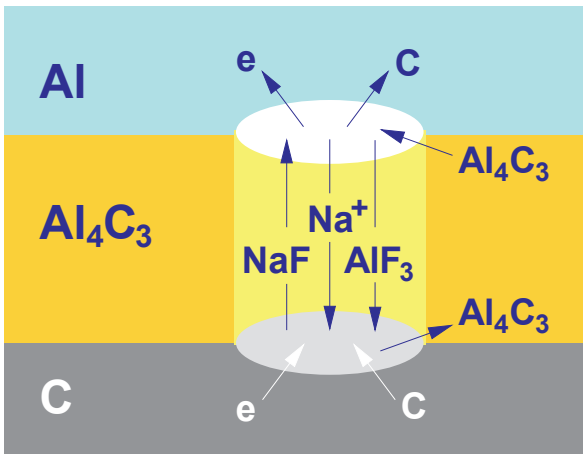

Figure 2.34: Schematic illustration of electrochemical formation and dissolution of aluminium carbide in a bath filled pore in the carbide layer [62].

According to Solheim and Tschöpe [62, 63], the reactions occurring at the carbon-carbide interface and the carbide-metal interface are, respectively, reactions (2.5) and (2.6). As the species on the reactant and product side of the total reaction are the same, the standard cell voltage is zero. The reversible voltage is thus dependent on the activity difference of NaF and AlF_3 between the top and bottom of the pore, as well as the activity of carbon dissolved at the metal interface. In addition to the reversible potential, the total voltage drop across the carbide layer is dependent of the ohmic voltage drop along the pore. Based on a cathode wear rate of 5 cm/y, Solheim and Tschöpe [63] estimated corresponding values of porosity of the carbide layer, i.e. fraction of carbide layer filled with bath, thickness of the carbide layer, and voltage drop across the layer (Figure 2.35).

$$4AlF_3(diss) + 3C(s) + 12Na^+ + 12e^- \rightarrow Al_4C_3(s) + 12NaF(l) \quad (2.5)$$

$$Al_4C_3(s) + 12NaF(l) \rightarrow 4AlF_3(diss) + 3C(in\ Al) + 12Na^+ + 12e^- \quad (2.6)$$

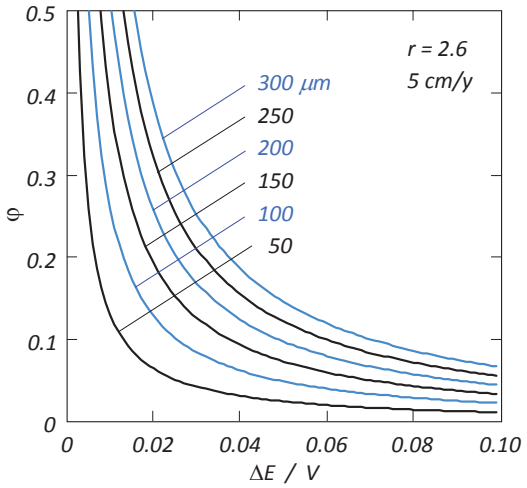

Figure 2.35: Corresponding values of porosity (φ) of the carbide layer, thickness of the layer, and voltage drop across the layer at a wear rate of 5 cm/y. The density of the carbon was taken to be 1650 kg/m^3 and the NaF/AlF_3 ratio (r) at the top of the pore was assumed to be 2.6. From Solheim and Tschöpe [63].

Solheim and Tschöpe [63] modelled the current density and potentials around a circular aluminium carbide "island", shown in Figure 2.36. High local current densities can be seen on the edges of the layer, and the current shielding effect results in a lower potential directly underneath the island than at the same horizontal level outside the island. The maximum potential difference between the top and the bottom of the carbide island was found to behave linearly with the horizontal dimensions. As an example, an aluminium carbide island of about 100 µm thickness and 30 mm^2 diameter on the cathode in an area

with current density in the order 10^5 A/m^2 (corresponding to the high wear areas in industrial cells), the maximum voltage drop was estimated to be in the order of 0.01 V.

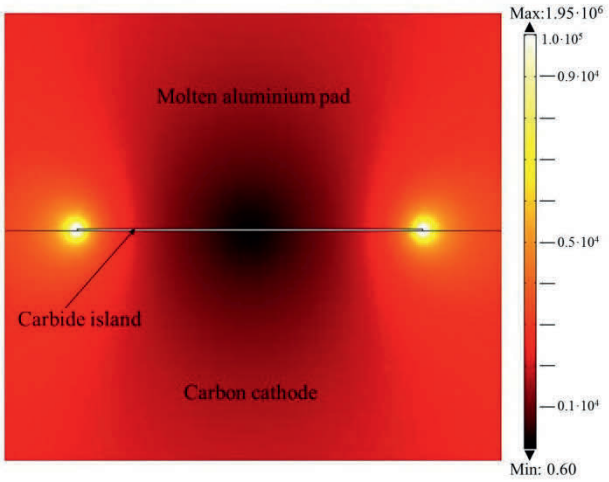

Figure 2.36: Current density around an aluminium carbide island (2 cm dia, 100 µm thick). The electrical conductivities were assumed to be 3.6×10^5 S/m for molten aluminium, 8.0×10^4 S/m for carbon, and 1.0 S/m for the carbide layer containing bath filled pores. From Solheim and Tschöpe [63].

Chapter 3

Thermodynamics of the Al–C and the Al–C–O system

Most studies of the Al–C and the Al–C–O systems have been performed at high temperatures, above 1600°C. For lower temperatures there are large discrepancies between the various thermochemical data presented [64]. At the temperatures relevant for aluminium smelting one should therefore be aware that the available data are rather uncertain.

3.1 The Al–C system

Except for gaseous compounds, the only known compound in the Al-C system is aluminium carbide, Al_4C_3 [65]. Al_4C_3 is an ionic carbide with discrete C^{4-} ions. Pure hexagonal Al_4C_3 crystals are colourless [66] but the carbide usually has a pale yellow or brown appearance. Al_4C_3 decomposes in water and acids yielding methane. Hydrolysis proceeds in water at room temperature and is rapidly accelerated at increased temperatures.

Thermochemical data for Al_4C_3 at temperatures between 298 and 1800 K according to Barin [67] are listed in Table B.2 in Appendix B. Lihrmann et al. [68] proposed the following equation for the standard Gibbs energy of formation of Al_4C_3 for 1000 K ≤ T ≤ 1500 K:

$$\Delta_f G^0 = -209944.693 - 282.185012T + 51.158268TlnT - 153.16705 \times 10^{-4}T^2 + 3.633 \times 10^{-10}T^3 - 9551482T^{-1} + 7.929 \times 10^8 T^{-2} - 3.6 \times 10^{10}T^{-3} \quad (3.1)$$

There are only minor differences between the two data sets in the relevant temperature region, as can be seen from the chart in Figure 3.1. In addition, data have been collected from the thermochemical software and database, FactSage™ [69] and VLab [70]. Here the Gibbs energy of formation deviates from the data given by Barin [67] and Lihrmann et al. [68] by about -10 kJ/mol. In the case of electrochemical formation of aluminium carbide at 1000°C according to reaction (3.12), the deviation amounts to approximately

10 mV. Further thermochemical calculations performed in this work are mainly based on data from Barin

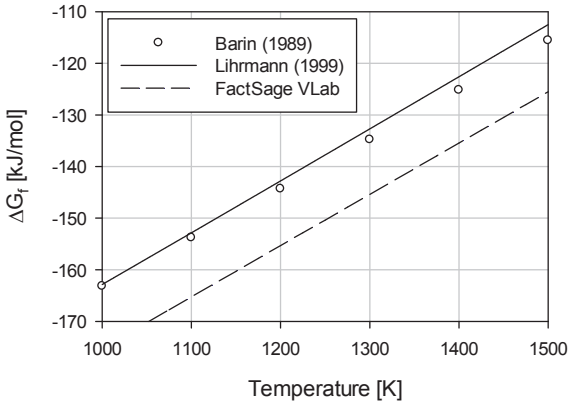

Figure 3.1: Comparison of the Gibbs free energy of formation for aluminium carbide, Al_4C_3 (s), given by Barin [67], Lihrmann et al. [68], and from FactSage VLab [69, 70].

The phase diagram for the system Al–C as reported by Motzfeldt et al. [65] is shown in Figure 3.2. The reported carbon solubility in aluminium at temperatures of about 960–980°C varies from 6 ppm [71] to 300 ppm [72].

It is clear that Al_4C_3 is stable at the temperatures found in aluminium electrolysis cells and at room temperature (in absence of oxygen). However, the oxide layer on the aluminium surface prevents wetting of aluminium on carbon [20], and this layer must be broken for the Al_4C_3 formation reaction to proceed.

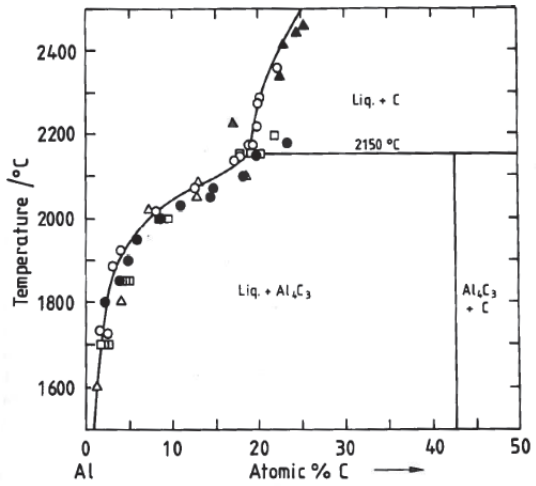

Figure 3.2: Phase diagram for the system Al-C. From Motzfeldt et al. [65]. Filled triangles: as reported by Baur and Brunner [73]. Open triangles: as reported by Stroup [74]. Filled circles: as reported by Ginsberg and Sparwald [75]. Open circles: as reported by Gjerstad [76]. Squares: as reported by Oden and McCune [77].

3.2 The Al–C–O system

Two solid aluminium oxycarbides are known, Al_4O_4C and Al_2OC, of which only the first is stable at temperatures below 1715°C [78]. A schematic diagram of the system Al–C–O is given in Figure 3.3, and phase diagrams for the system Al_2O_3–Al_4C_3 are shown in Figure 3.4 and Figure 3.5. The oxycarbide, Al_4O_4C, is stable at temperatures relevant for aluminium smelting and can be formed by reacting alumina with aluminium carbide (3.2).

$$Al_4C_3 + 4Al_2O_3 \leftrightarrow 3Al_4O_4C \tag{3.2}$$

According to Lihrmann et al. [68], the standard Gibbs energy of formation of Al_4O_4C follows equation (3.3) in the temperature interval 1000 K ≤ T ≤ 1500 K.

$$\begin{aligned}\Delta_f G^0 = {} & -2352531.936 + 3888.627099T + 13.959135TlnT - 123.56643 \times 10^{-4}T^2 \\ & +3443.7 \times 10^{-10}T^3 + 12253419.34T^{-1} + 2.643 \times 10^{8}T^{-2} - 1.2 \times 10^{10}T^{-3}\end{aligned} \tag{3.3}$$

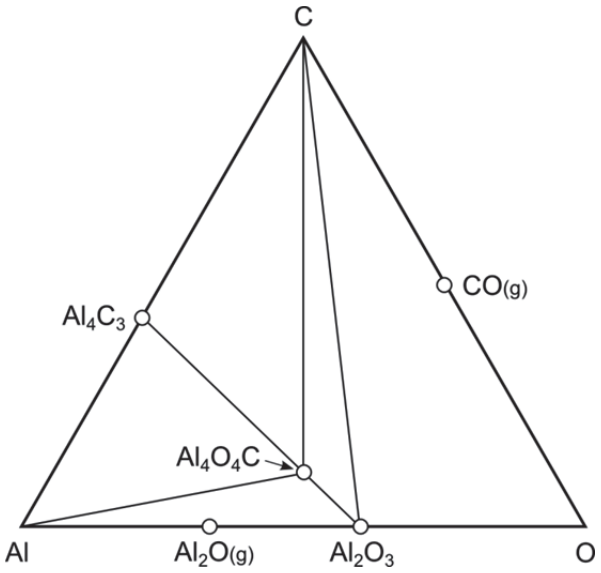

Figure 3.3: Schematic diagram of the Al–C–O system (at temperature < 1905°C). Redrawn from Motzfeldt et al. [65].

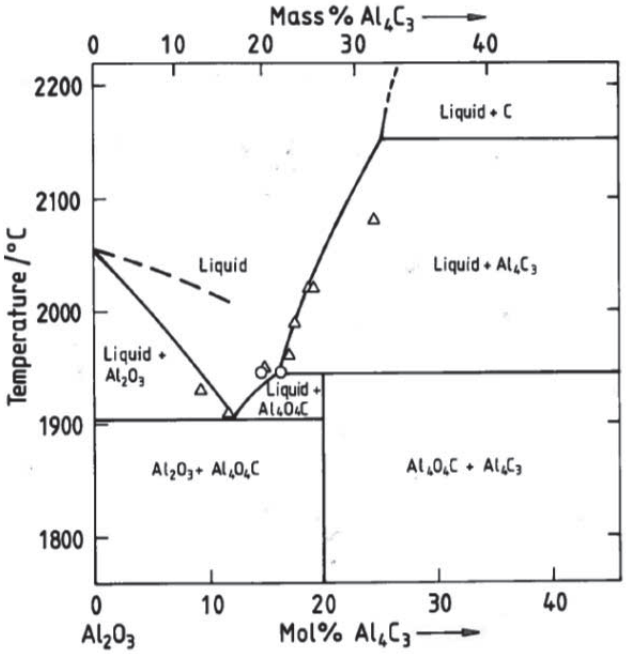

Figure 3.4: Phase diagram of the system Al_2O_3 – Al_4C_3 [65], as reported by Sandberg [64]. Circles: as reported by Gjerstad [76]. Triangles: as reported by Ginsberg and Sparwald [75].

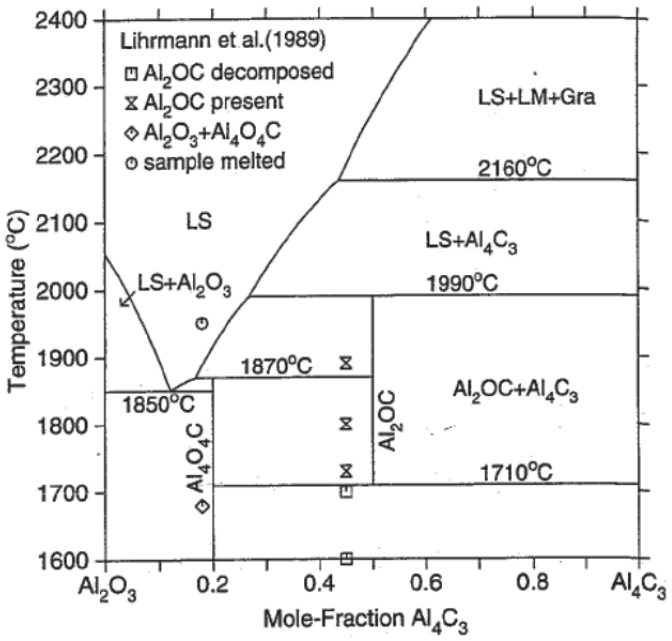

Figure 3.5: Calculated phase diagram of the Al_2O_3–Al_4C_3 system in comparison to experimental observations [78]. From Qui and Metselaar [79].

3.3 Aluminium carbide and oxycarbide in cryolitic melts

Aluminium carbide can occur as a solid or as dissolved specie in the cryolite melt. Based on reaction (2.3), Ødegård [25] estimated thermodynamic data for the dissolved specie, $Na_3Al_3CF_8$(diss). These data are given in Table 3.1. To the author's knowledge, no data for dissolution of oxycarbide are available.

$$Al_4C_3(s) + 5AlF_3(diss) + 9NaF(l) \leftrightarrow 3Na_3Al_3CF_8(diss) \tag{2.3}$$

Table 3.1: Δ_fG^0 and Δ_fH^0 for $Na_3Al_3CF_8$(diss) as reported by Ødegård [25].

T [K]	Δ_fH^0 [kJ/mol]	Δ_fG^0 [kJ/mol]
1100	-4273.370	-3614.092
1200	-4555.761	-3548.806
1300	-4544.207	-3465.363
1400	-4532.816	-3382.799

Several reactions have been proposed for the formation of aluminium carbide and oxycarbide in the aluminium electrolysis cell. Some of the possible reactions, and their respective Gibbs free energies, are listed in Table 3.2. Gibbs energies of formation for the species involved in the reactions are listed in Table B.1 in Appendix B.

The potential (E) and the Gibbs energy of a reaction is proportionally dependent according to the following equation:

$$\Delta G = -nFE \tag{3.4}$$

where n is the number of electrons transferred and F is the Faraday constant.

Thus the standard potential (E^0) for various electrode reactions can be calculated based on the Gibbs formation energies. Table 3.3 shows half-cell reactions based on the reactions listed in Table 3.2, and their respective standard potentials relative to the aluminium formation/dissolution potential.

Table 3.2: Possible aluminium carbide and oxycarbide formation reactions with the Gibbs free energy of reaction, ΔG^0, at 1000°C.

Eqn.	Reaction	ΔG^0 [kJ]
(2.1)	$4Al(l) + 3C(s) \rightarrow Al_4C_3(s)$	-135.42
(3.5)	$4AlF_3(diss) + 12Na(C) + 3C(s) \rightarrow Al_4C_3(s) + 12NaF(l)$	-643.31
(3.6)	$8Al_2O_3(s) + 12Na(C) + 3C(s) \rightarrow Al_4C_3(s) + 12NaAlO_2(s)$	-75.99
(3.7)	$3AlF_3(diss) + 4Na(C) + C(s) \rightarrow Na_3Al_3CF_8(diss) + NaF(l)$	-385.40
(3.8)	$1.33AlF_3(diss) + 1.33Al_2O_3(s) + 4Na(C) + C(s) \rightarrow Al_4O_4C(s) + 4NaF(l)$	-225.54
(3.2)	$Al_4C_3(s) + 4Al_2O_3(s) \rightarrow 3Al_4O_4C(s)$	-33.30

For reactions including sodium in carbon, Na(C), data for Na(l) was used. The real ΔG^0 for these reactions should therefore be somewhat more positive.

Table 3.3: Possible cathode reactions with standard potentials relative to Al/Al^{3+} at 1000°C.

Eqn.	Half-cell reaction	E^0 [V]
(3.9)	$NaF(l) + e^- \rightarrow Na(l) + F^-$	-0.439
(3.10)	$8Al_2O_3(s) + 3C(s) + 12e^- \rightarrow Al_4C_3(s) + 12AlO_2^-$	-0.373
(3.11)	$Al^{3+} + 3e^- \rightarrow Al(l)$	0
(3.12)	$4Al^{3+} + 3C(s) + 12e^- \rightarrow Al_4C_3(s)$	0.117
(3.13)	$1.33Al^{3+} + C(s) + 1.33Al_2O_3 + 4e^- \rightarrow Al_4O_4C(s)$	0.146
(3.14)	$3AlF_3(diss) + C(s) + 4e^- \rightarrow Al_3CF_8^{3-} + F^-$	0.560

3.4 Thermodynamic calculations with Factsage™

FactSage is an integrated database computing system for chemical thermo-dynamics and a convenient tool for prediction of occurrences of species at various conditions. With the addition of the database Virtual Lab (VLAB), created specifically for the aluminium industry [70], the software can be used to estimate carbide and oxycarbide stabilities in cryolite melts.

From the standard potentials in Table 3.3 we can expect formation of dissolved carbide ($Na_3Al_3CF_8$) first, and then solid carbide and oxycarbide before aluminium, whilst increasing the potential in cathodic direction. FactSage has been used to model the stability of the carbides at varying potentials and oxide concentrations in a typical industrial bath composition, and the results correlate well with the manually calculated values in Tables 0.05 and 0.06. As potential is not a valid parameter in the FactSage calculations, the activity of aluminium (a_{Al}) is used instead, as it is directly related to the potential.

Figure 3.6 shows an activity diagram in cryolitic melt with carbon, aluminium and alumina at 1000°C, with the logarithms of Al activity and Al_2O_3 activity along the axes. According to this diagram, Al_4C_3(s) is stable at aluminium activities larger than $10^{-1.5}$. At $a_{Al} = 10^{-1.5}$ the Gibbs free energy of the aluminium carbide formation reaction (2.1) is zero, $\Delta G_{(2.1)} = 0$. At unit aluminium activity, i.e. standard conditions, $\Delta G_{(2.1)} = \Delta G^0_{(2.1)}$. Thus, the reversible potential at which Al_4C_3(s) is formed, relative to Al^{3+}/Al, is the same as the standard potential for the reaction, $E^{rev}_{(2.1)} = E^0_{(2.1)} = E^0_{(\mathbf{3.12})} = 117$ mV (or 127 mV when calculated with data from FactSage and VLab). At lower aluminium activities carbide will only be stable as dissolved species. In the right topmost corner, with oxide activity above $10^{-0.25}$, Al_4O_4C(s) is the stable carbide specie. This activity corresponds to about 9 wt% Al_2O_3 in cryolite smelt with CR = 2.2 at 1300 K [80].

Figure 3.7 shows various carbon containing species' dependency on the aluminium activity in oxide free bath. The dissolved carbide species reaches a maximum at about $a_{Al} = 10^{-1.5}$, where solid aluminium carbide is formed and carbon in its pure form is no longer stable with presence of aluminium. Figure 3.8 shows a similar diagram for oxide saturated bath. Compared to the previous diagram the stability of carbon has been shifted somewhat in anodic direction, i.e. lower aluminium activity, and Al_4O_4C(s) is the stable carbide species at high activities. This can be seen more clearly in Figure 3.6. At very low aluminium activities, or high anodic potentials, carbon exists in the form of CO_2(g) and various carbonates.

A phase diagram of the $Al_2O_3 - Al_4C_3$ system modelled with FactSage is shown in Figure 3.9.

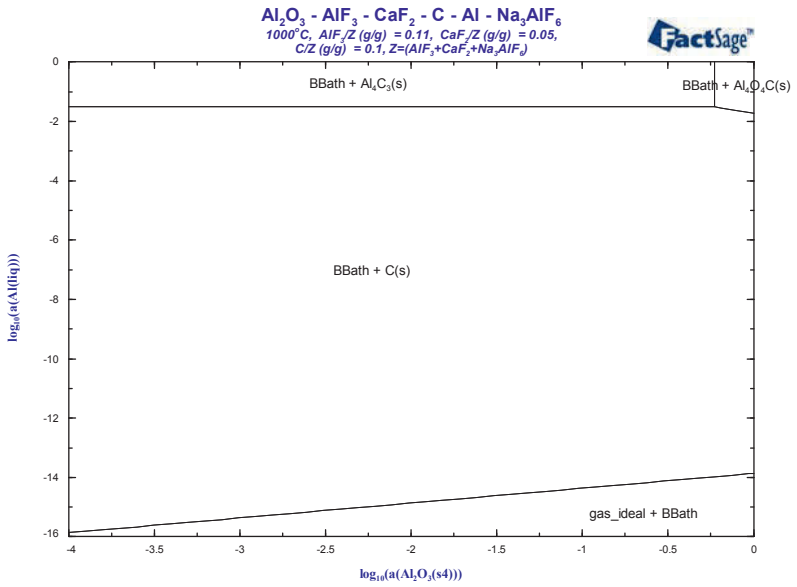

Figure 3.6: Activity diagram illustrating the stability regions of Al_4C_3 and Al_4O_4C in cryolitic melt at 1000°C. "BBath" is bulk bath, i.e. cryolitic melt, and "gas_ideal" is mainly CO_2(g).

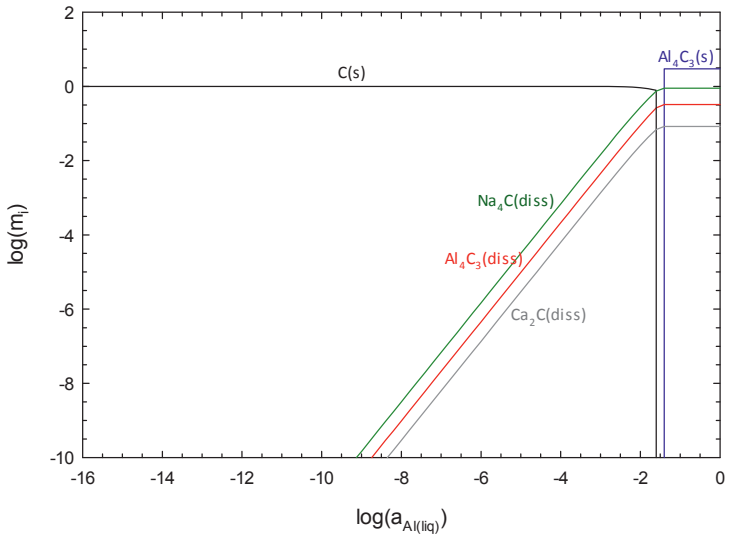

Figure 3.7: Diagram showing the mass of species i, m_i, as a function of aluminium activity, a_{Al}, in Na_3AlF_6 (85 wt%) – AlF_3 (10 wt%) – CaF_2 (5 wt%) melt at 1000°C. Initial mass of carbon and melt is 1 g and 100 g, respectively.

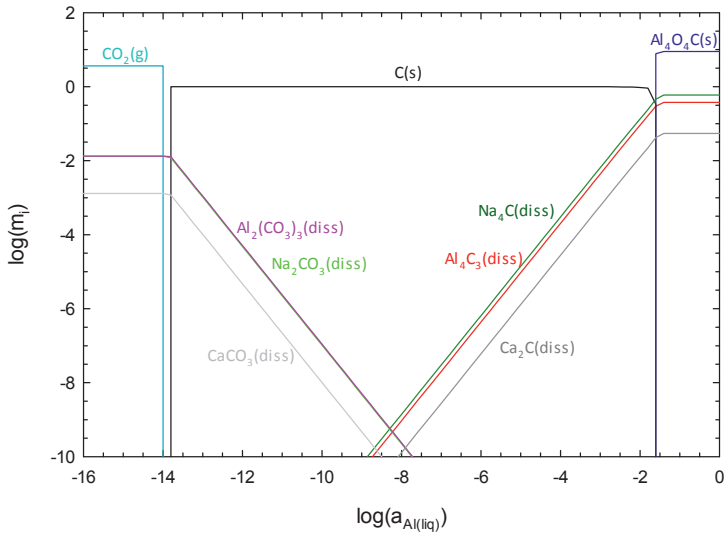

Figure 3.8: Diagram showing the mass of species i, m_i, as a function of aluminium activity, a_{Al}, in alumina saturated Na_3AlF_6 (85 wt%) – AlF_3 (10 wt%) – CaF_2 (5 wt%) melt at 1000°C. Initial mass of carbon and melt is 1 g and 100 g, respectively.

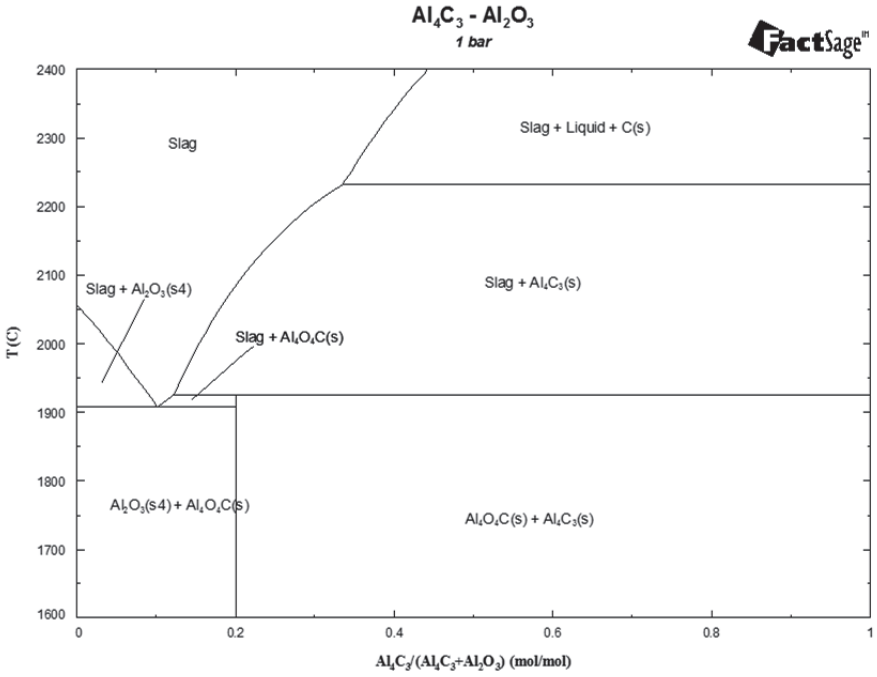

Figure 3.9: Phase diagram of the Al_2O_3 – Al_4C_3 system calculated with Factsage and VLab.

Chapter 4

Laser scanning of cathode surface

4.1 Introduction

After shutting down an electrolysis cell and cleaning the cathode of residual electrolyte and aluminium, the exposed cathode surface shows a wear pattern that can provide information about the wear mechanisms in the cell. Documentation of the wear is important for successive analysis and assessment of the cathode and lining materials performance. At present, the wear pattern is measured and documented manually, usually with levelling rod and telescope, measuring 3–7 points on each cathode block. For rough measurements, this is convenient, but the workload increases dramatically when there is need for a more detailed documentation of the wear pattern.

Laser scanning is a well-known technology used for creating 3D models of buildings, bridges and other structures. This technology can also be used for creating 3D models of the cathode, thus documenting the wear pattern in superior detail compared to manual measurements.

A method for laser scanning of cathode surfaces was developed, and two cells at Hydro Sunndalsøra (cells D105 and D107) were successfully scanned and modelled. A thorough description of the method and discussion about the results are published in two papers written by Skybakmoen et al. [81, 82]. These papers can be found in Appendix A.

4.2 The method development

The idea of implementing laser scanning technology for mapping of cathode wear was conceived while discussing the possible wear mechanisms from looking at topographic plots of a worn cathode measured by the current method. With a resolution of 7 data points per cathode block, it was evident that a lot of information was lost in these plots.

Prof. K.R. Holm (Department of civil and transport engineering, NTNU) was contacted for his extensive experience in laser scanning, to discuss the feasibility of creating 3D models of cathode surfaces in the primary aluminium industry. After a visit at Hydro's plant in Sunndalsøra, planning of the first laser scanning campaign could commence.

Figure 4.1: Picture of the laser scanner (Riegl LMS-Z420i) used in this work. Dimensions without camera: length 463 mm, diameter 210 mm, weight 16 kg.

As Hydro Sunndalsøra has a separate building for disassembly of worn cathodes, problems with equipment being affected by the magnetic fields in the electrolysis halls was avoided. This was one of the main arguments for doing the laser scanning there. Alf Engen a.s., a contractor located in Sunndalsøra, was engaged to construct a tall rack for the laser scanner, and also to assist in practical matters during the measurement campaign. The rack was placed on the steel shell of the cathode and the laser scanner mounted in the rack about 5 m above the cathode surface. To achieve reliable data for the entire cathode and avoid shadow effects, three overlapping scans were made from different positions above the cathode. Reflecting markers were placed on the steel shell and on the cathode surface as reference points for data processing. A camera was mounted on the laser scanner to supplement the XYZ coordinate data with RGB colour values. The collected data were treated with suitable software to generate plots such as those shown in Figures 4.4–4.7.

Performing the laser scans, including on-site preparations, took the better part of a work day, while the actual scanning lasted about 15 minutes for each scan. With a permanent movable rack for the laser scanner, e.g. mounted from the roof, it should be possible to perform a cathode scan within an hour.

Figure 4.2: Prof. K.R. Holm and the author inspecting the cathode while Hydro employee, dr. J. Hajasova, vacuum-cleans the cathode before laser scanning.

Figure 4.3: Mounting of the laser scanner on the rack, about 5 m above the cathode.

Figure 4.4: A 3D model of cell D105, where the coordinate data points have been ascribed RGB colour values from the photographs taken by the camera mounted on the laser scanner.

4.3 Some results and discussion

The topographic plots of the two cathode surfaces, shown in Figures 4.6 and 4.7, display a typical wear trend for high current density cells. For most of the cathode blocks the highest wear is found at the sides while very little wear can be observed at the middle. Between the highly worn sides and the much less worn middle, a local high point and a local low point can be seen. This wear pattern has been named as "WW wear profile", as topographic line plots in the longitudinal direction of the cathode blocks looks like two w's (Figure 4.5).

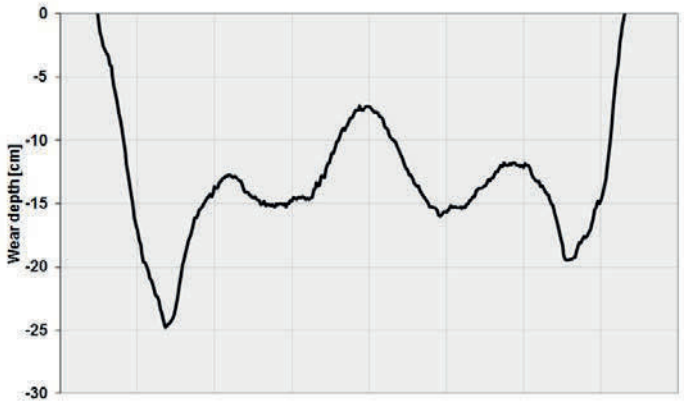

Figure 4.5: A topographic line plot of cathode block 8 in cell D105 in longitudinal direction, showing the characteristic WW wear profile. Data from the laser scanning.

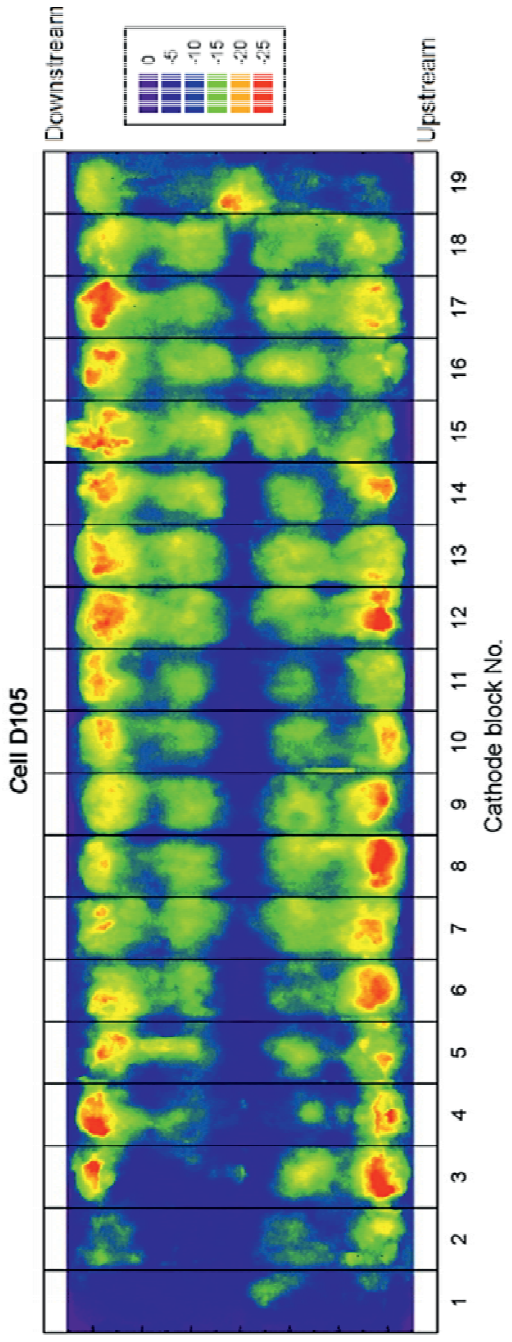

Figure 4.6: Topographic plot from laser scan of cell D105, shut down after 2088 days of operation. The legend on the right show the relative height difference compared to the initial level of the cathode surface. Cathode heave is not taken into account, and the actual wear of the cathode may therefore be higher.

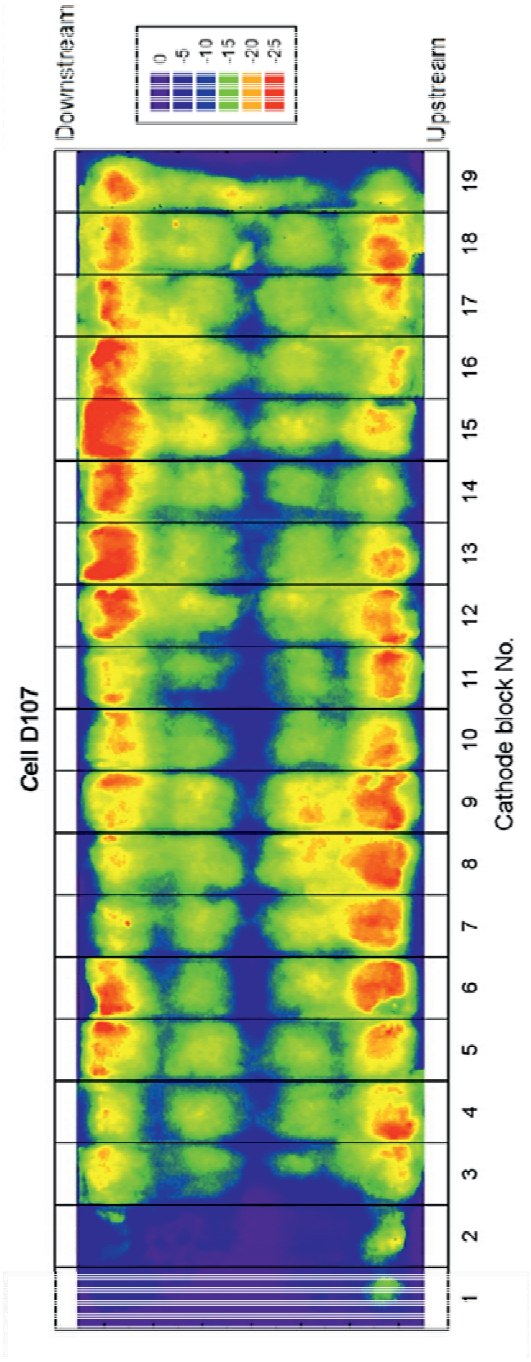

Figure 4.7: Topographic plot from laser scan of cell D107, shut down after 2184 days of operation. The legend on the right show the relative height difference compared to the initial level of the cathode surface. Cathode heave is not taken into account, and the actual wear of the cathode may therefore be higher.

If the carbon cathode is allowed to be worn down to the current collector bars, an uncontrolled tap out will occur, i.e. the metal flows out beneath the cell. To avoid this, the cathodes are regularly controlled for critically worn areas. Such areas are identified by a higher current pull at the respective current collector bars, a higher temperature of the steel shell at the respective area and by probing the cathode surface with a rod. Increased concentration of Fe in the produced metal is the final indication of cathodes worn down to their collector bars. When critically worn areas are detected, two measures can be taken to protect this area from further wear and prolong the cell lifetime; filling with corundum or cutting the steel current collector bars to the respective cathode block. Corundum filling is done by tossing bags with corundum (α-alumina) into the bath where pothole formations have been located at the cathode. A metal rod is then used to ram the corundum into the pothole where it sinters and creates a low-soluble protective layer. About 50 kg corundum is typically used per filling. Information about corundum fillings and cutting of current collector bars for the two investigated cells is provided in Figure 4.8.

The 3D model of a cathode surface gives a much better foundation for prospective investigations and statistical analyses of cathode wear than the current method. Supplemented by models and measurements of metal flow, current distribution, sludge distribution and extent of side/bottom ledge, the value of the 3D model would be greatly enhanced.

Operational data for the two investigated cells, such as temperature, bath composition and anode effect occurrences, was provided by Hydro. These data indicated normal cell lives and no significant differences were found between the two cells [83].

Although detailed data for metal flow, current distribution, sludge distribution and extent of side/bottom ledge for the cells studied here are not available, some assumptions can be made based on previous experience and generally accepted hypotheses. The bottom ledge of frozen bath is expected to cover the edges of the cathode blocks and protect against wear. The current density, and consequently the metal flow, is highest at the long sides of the cathode, which corresponds well to the highly worn areas. Almost no current passes through the considerably less worn middle section of the cathode [84]. The less conductive anthracite based ramming paste used in the joints between the cathode blocks carries little current as well. These ramming joints are notably less worn and protrude by several cm.

As it is known that the bottom ledge protects the edges of the cathode blocks from wear, the plots from the laser scanning (Figures 4.6 and 4.7) can be used to assess and quantify the ledge thickness. With detailed plots for a sufficient amount of cells of the same technology, trends may be observed regarding this ledge. If the non-worn area at the cathode block edges is found to be too large or too small, something may have to be done

with the cell design and the heat transmission. In such a case, the laser scans provide a good assessment tool for optimization.

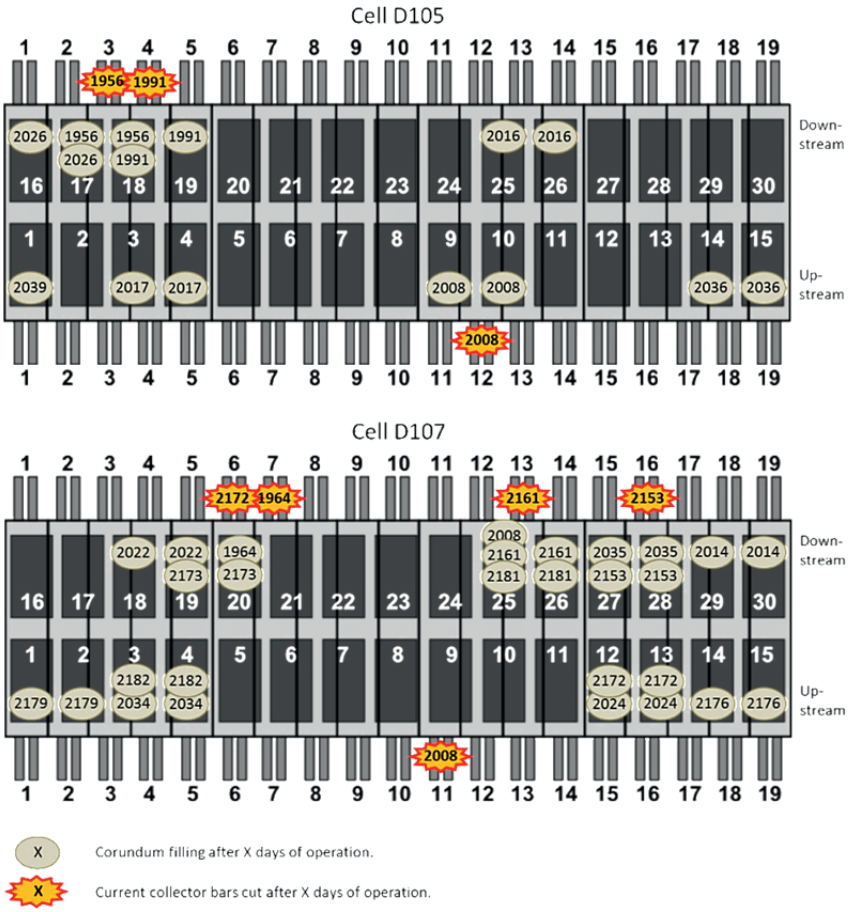

Figure 4.8: Overview of corundum fillings and cutting of current collector bars during operation for cells D105 and D107 at Hydro Sunndalsøra. Corundum filling is done during anode change. The dark rectangles with white numbering represent the anode positions in the cell.

The high wear at the sides and the low wear at the middle of the cathode are generally ascribed to differences in current density and metal flow, but the local high and low points in between demands a more complex explanation. Solheim [62] has proposed a model based on non-stationary dissolution of aluminium carbide into a layer of sludge that periodically forms and disappears according to the alumina feeding cycles. He suggests that stationary sludge protects the cathode while mobile sludge enhances wear by rapid dissolution of carbide. This hypothesis calls for further investigations and modelling of metal flow and sludge movement at the cathode surface.

A tap-hole can be found in the middle of cathode block 19. This is where metal is tapped out of the cell at regular intervals, giving rise to high local metal flow. At the opposite end, i.e. the suction end, cathode block 1 and 2 are clearly less worn than the rest of the cathode blocks. This may be explained by a slightly lower temperature, an increased bottom ledge, less metal flow and sludge build-up.

Assuming the extent of cathode heave is known, very precise estimates can be made for average wear rates and carbon consumption, locally or as a whole. For the cells in this work the total carbon consumption was estimated to 8024 kg and 8940 kg for D105 and D107, respectively. That is about 30% of the entire carbon cathode. In addition to the deterioration of the cathode and the economic consequences of having to replace cells, the carbon loss also affects the productivity of the cell. Assuming that all the carbon has been removed as Al_4C_3, one can easily calculate the amount of aluminium metal lost in the same process. For cell D105 and D107, respectively, the metal losses amount to 24 and 27 tonnes of aluminium. This corresponds to about 0.5% loss in current efficiency in a 300 kA cell.

A 300 kA cell running at 100% current efficiency will produce about 5.3 kilotonnes Al in 6 years. Assuming the solubility of carbide in aluminium is 35 ppm [85], corresponding to a carbon solubility of 8.76 ppm, the maximum amount of dissolved carbon that can have been removed with the metal in the same period is less than 50 kg. This is negligible compared to the total amount of carbon lost at the cathode and a good indication that carbide is transferred into the electrolyte where it is oxidised at the anodes.

Both cells in this work were taken out due to elevated Fe contents in the produced metal. As stated previously, this indicates that the carbon cathode has been worn down to the current collector bars. Thus, the collector bars can be assumed to be on level with the maximum wear observed. As the cathodes of cell D105 and D107 were not removed to examine the cathode heave, the point of zero wear was determined on the basis of this assumption. I.e. the maximum wear, added with the distance between the current collector bars and the surface in fresh cathode blocks, was set as zero wear.

The cathode can easily be divided into sectors to compare the wear between different areas of the cells. Table 4.2 shows the wear at each quadrant of the two cells, divided between upstream and downstream side, and between tap end and suction end. It is obvious that the suction end is less worn than the tap end, which can be interpreted as an indication of that a cold zone exists in the suction end of the cells, resulting in an extensive bottom ledge. Table 4.2 also shows that the quadrants on the downstream side have both the highest wear and the lowest wear. At the suction end, the upstream side is somewhat more worn, while it is the opposite at the tap end. This diagonal wear is illustrated in the plots in Figures 4.9 and 4.10.

Table 4.1: Wear and wear rates for the two cells, D105 and D107, calculated from laser scanning data.

Cell	Age [days]	Avg. wear [cm]	Avg. wear rate [cm/year]	Max. wear [cm]	Max wear rate [cm/year]
D105	2088	12.4	2.1	27	4.7
D107	2184	13.8	2.3	27	4.5

Table 4.2: Wear and wear rates in the different quadrants of cells D105 and D107, calculated from laser scanning data.

	Position	Downstream		Upstream	
Cell		Avg. wear [cm]	Wear rate [cm/year]	Avg. wear [cm]	Wear rate [cm/year]
D105	Suction end	11.2	2.0	11.9	2.1
	Tap end	13.8	2.4	12.5	2.2
D107	Suction end	12.2	2,0	12.8	2,1
	Tap end	16.1	2,7	14.1	2,4

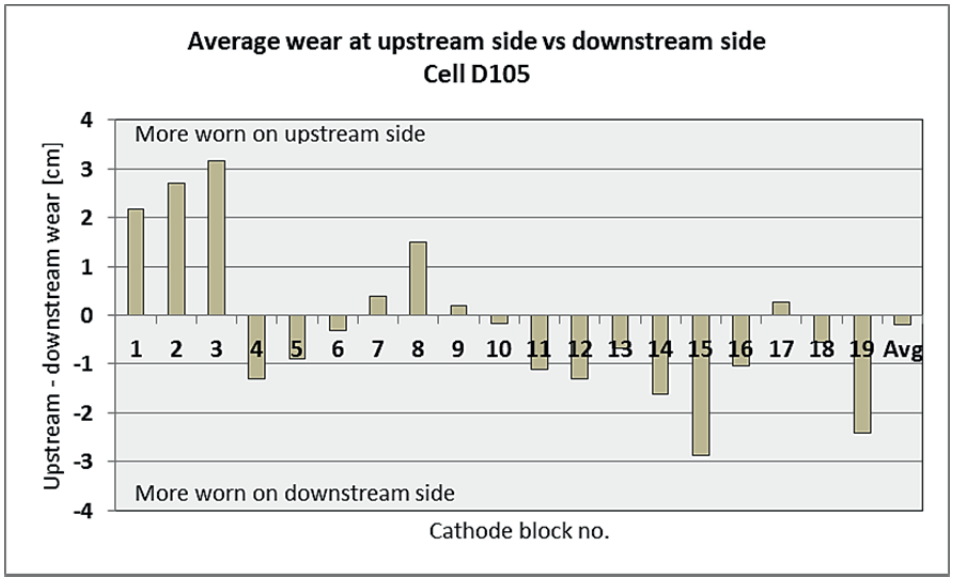

Figure 4.9: Plot of the difference in average wear between upstream and downstream side for each cathode block of cell D105. Positive values means the cathode block is more worn at the upstream side, negative values means more wear at the downstream side.

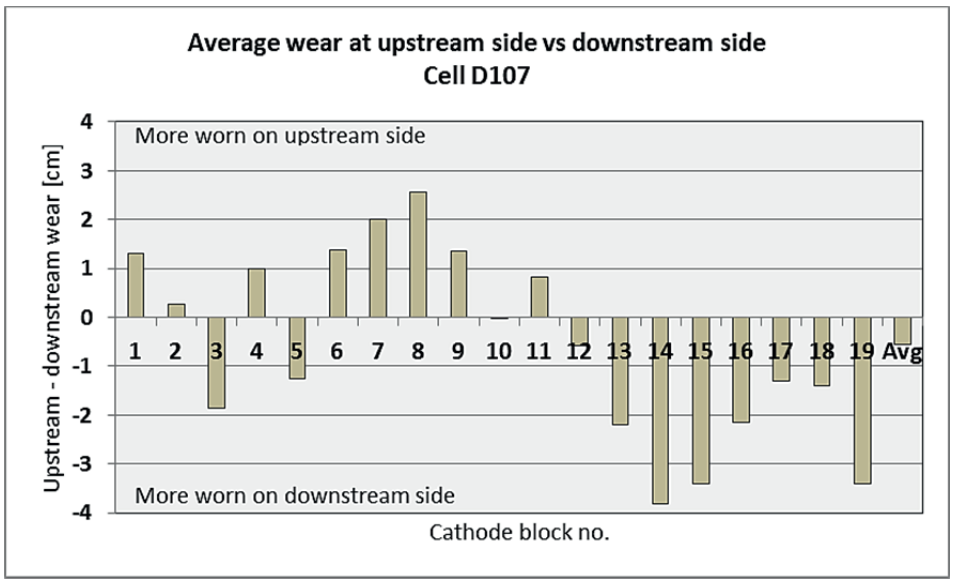

Figure 4.10: Plot of the difference in average wear between upstream and downstream side for each cathode block of cell D107. Positive values means the cathode block is more worn at the upstream side, negative values means more wear at the downstream side.

In modern prebake cells, the alumina is fed through multiple point feeders placed along the centreline of the cell. The placement of the feeders and the amount of alumina fed through each feeder per feeding cycle have been determined on the basis of alumina dissolution rates and bath circulation. In areas with high bath circulation, the alumina will be readily spread and dissolve faster. In low convection areas, there is a bigger risk that alumina sink to the bottom as sludge. Before feeding, an automated pneumatic hammer breaks a hole in the bath crust to allow the alumina to flow freely into the bath. The crust that is broken off and the feed alumina do not always dissolve completely, even in the areas with high bath circulation. Thus, sludge will form beneath the point feeders. Assuming the sludge beneath the feeders protects the cathode from wear, it should be possible to reveal the position of the point feeders by studying the topographic plots of the cathode surfaces. The actual positions of the point feeders, according to Hydro, are shown on top of the topographic plots in Figure 4.11. The areas close to the feeders do in fact seem to be less worn. This supports the earlier mentioned hypothesis of Solheim [62].

Just as the approximate positions of the point feeders could be revealed by the wear pattern on the cathodes, the topographic plots may also give some indications for the metal flow. It is generally accepted that high current densities and high metal velocities tend to coincide with high cathode wear. With this in mind, one can produce relative estimates of the metal velocities based on the amount of wear at different positions in the cell, as shown in Figure 4.12. This, together with occasional flow measurements, provides

valuable information that could be implemented in the magnetohydrodynamic flow models most modern aluminium smelters are developing for each new cell design.

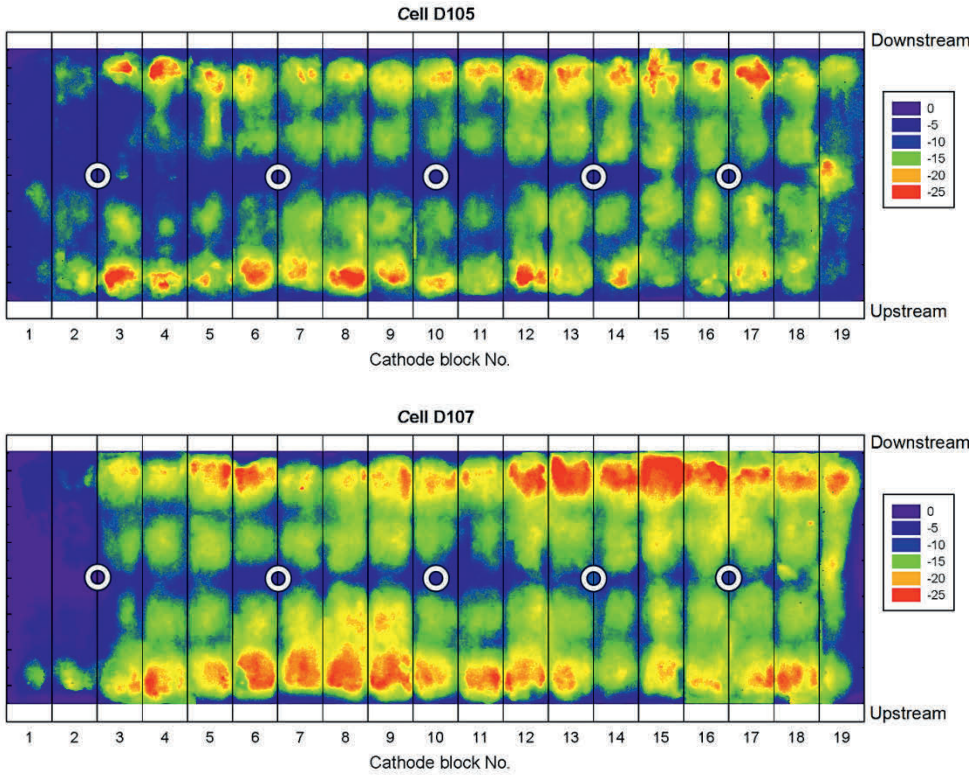

Figure 4.11: The positions of the point feeders marked as white circles on top of the topographic plots of the cathode surfaces of cell D105 and D107. The areas close to the feeders may be protected against wear due to sludge formation.

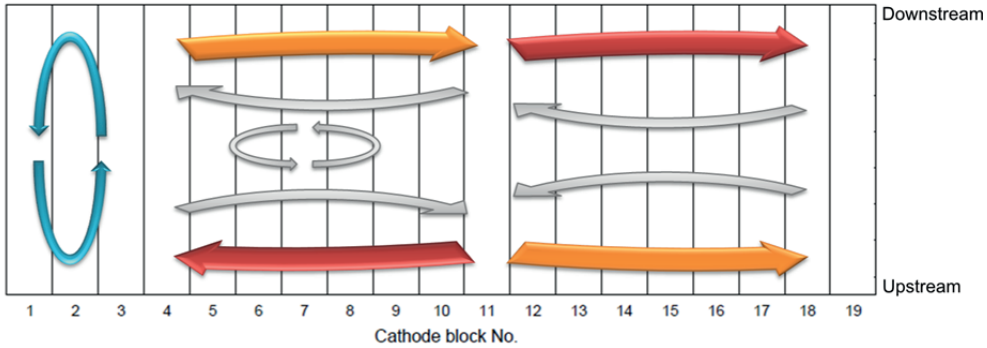

Figure 4.12: The author's suggestion of how the metal flow may have been in the investigated cells. The blue arrows represent low velocity flow at the suction end. The orange and red arrows represent higher velocities, of which red the highest velocity. The grey arrows illustrate one of many possible flow patterns in the central part of the cell and are very uncertain. The suggestion is based on earlier flow measurements, similar to those of Johnson [48] and Tabereaux and Hester [49], and the wear pattern revealed by the laser scanning method.

Chapter 5

Microscopy investigation of industrial cathodes

5.1 Introduction

A number of cathode samples from various aluminium electrolysis cells at three different Hydro Aluminium smelters have been investigated by optical and scanning electron microscope. The main objective of this investigation was to identify possible differences between cathode samples taken at different areas of the same cells and between different cells with different cathode materials. Any findings could potentially shed light on the cathode wear mechanism. Furthermore, the microscopic studies also give a detailed general picture of the surface wear.

Table 5.1: Overview of the investigated cathodes.

Plant	Cell	Cathode type	Sampling date	Operational lifetime	Technology
Karmøy	C070	SGZi	23.01.2008	1795 days	End-to-end
Sunndalsøra	A044	GZ	17.11.2008	2168 days	Side-by-side
Sunndalsøra	D095	GZ	21.03.2009	1725 days	Side-by-side
Sunndalsøra	L006	SGv	15.09.2009	2431 days	End-to-end
Sunndalsøra	D105	SGZi	08.04.2010	2088 days	Side-by-side
Sunndalsøra	D107	SGZi	11.08.2010	2184 days	Side-by-side
Årdal	I-31	SGZv	24.05.2011	2200 days	End-to-end
Sunndalsøra	C106	GZi	14.10.2011	2631 days	Side-by-side

Table 5.2: Explanation of cathode type abbreviations.

GZ	Graphitized
GZi	Graphitized and impregnated
SGZi	Semi-graphitized and impregnated
SGZv	Vibrated, semi-graphitized with anisotropic coke filler
SGv	Vibrated, semi-graphitic with graphitized petrol coke filler

5.2 Sample extraction and preparation

Aluminium carbide is a key factor in discussions about cathode wear phenomena. It was therefore important to prevent deterioration of any carbide present on the extracted cathode samples. As aluminium carbide is prone to react with water to form aluminium hydroxide and methane, efforts were made to avoid contact with water and limit exposure to moisture during sample extraction and preparation.

Samples were extracted from the cathode with an angle grinder as shown in Figure 5.1. Slots were cut and the samples were broken loose with a chisel. The samples were mounted in epoxy at low pressure (Figure 5.2) and stored in a glove box with argon atmosphere, pending microscopy investigation. Grinding and polishing of the samples were performed directly prior to microscopy to avoid problems with oxidation of the surface. Grinding and polishing were performed with ethanol (≥99.8%, Sigma-Aldrich) as coolant/lubrication.

Figure 5.1: The author extracting samples from the cathode with an angle grinder. The sides of the cuboid samples were typically 3–5 cm.

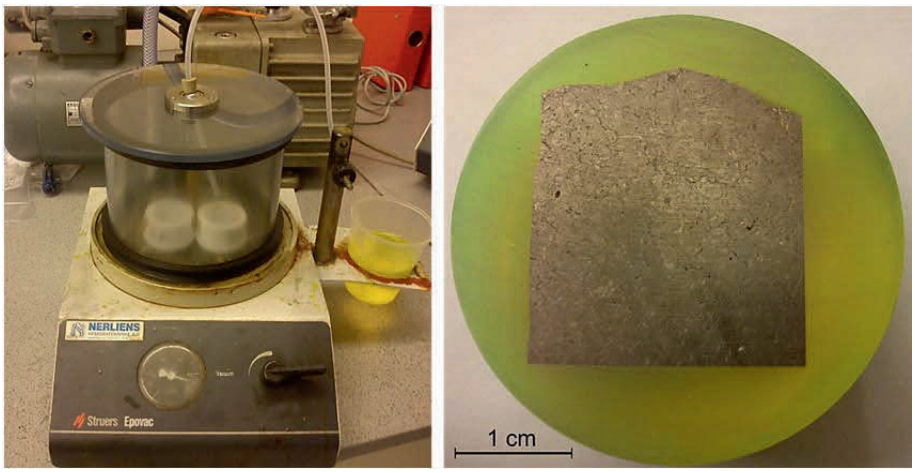

(a) (b)

Figure 5.2: (a) The samples were mounted in epoxy at low pressure in a Struers Epovac. (b) A cathode sample during preparation for microscopy, about halfway in the polishing procedure.

Samples that have been stored in glass jars outside of the glove box (after microscopy investigation) are depicted in Figure 5.3, clearly showing the challenges with oxidation of species in the samples. Storage of samples in glove box with argon atmosphere gave a satisfactory protection against oxidation for several months.

(a) (b)

Figure 5.3: Some samples were stored in glass jars in ambient atmosphere. (a) A cathode sample mounted in epoxy after about four months in ambient atmosphere. (b) A cathode sample, not mounted in epoxy, after about six months in ambient atmosphere. Oxidation of sodium and carbide has disintegrated the sample completely.

Sampling was typically conducted a week after shutdown of the respective cells. In the meantime the cell was allowed to cool and remnants of bath and metal were removed. In this period of time, some sodium and aluminium carbide at the surface will have undergone oxidation. In order to investigate intact layers of aluminium carbide, some samples were always taken from areas still covered by a thin layer of sludge or aluminium.

The sampling from cell I-31 at Hydro Aluminium Årdal deviated from the other sampling campaigns. Samples were extracted from this cell only one and a half day after shutdown, i.e. before it was cooled properly. The surface temperature was measured to be about 500°C, and it was not considered safe to extract samples as described above. Instead an excavator with a pneumatic hammer was used to break of some pieces of the cathode. Due to the risk of damaging the pneumatic hammer, the sampling was concluded after extracting only four samples.

5.3 Microscopy techniques

5.3.1 Optical microscopy

A Reichert-Jung MeF3A inverted metallographic microscope was used for optical microscopy of the cathode samples. Two optical microscopy techniques, bright field (Figure 5.4(a)) and polarised light (Figure 5.4(b)), were used to obtain informative micrographs of the cathode samples. The bright field technique makes use of reflection and absorption to create contrast. Surfaces perpendicular to the ingoing light will reflect the light back into the objective lens, while inclinations will reduce the amount of light reaching the objective. The amount of light reaching the objective also depends on the reflectivity of the materials; polished metal will reflect most of the light and appear bright, while particles that absorb light will appear dark.

Light can be described as a transverse wave where the electric and magnetic vector oscillates perpendicularly to the propagation direction. In natural light from the sun and most artificial light sources the oscillation direction change frequently and irregularly, and within any measurable amount of time all possible oscillation directions will occur. In polarised light, on the other hand, the oscillation directions are repeated regularly. With a polariser one can obtain light with only one oscillation direction, so-called planar polarised light. Planar polarised light can be used in microscopy to identify optically isotropic and anisotropic materials.

Amorphous materials and materials with cubic symmetry are optically isotropic [86]. These materials have identical optical properties in all directions. In optically anisotropic materials the optical properties are dependent on the oscillation direction of the incoming

light. When rotating an anisotropic sample in the microscope, using polarised light, the operator will experience that the intensity and colour of the reflected light varies.

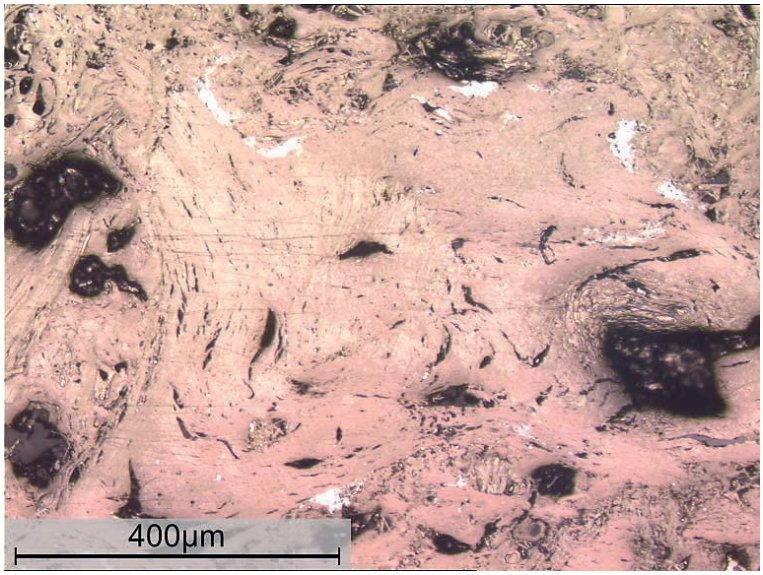

(a)

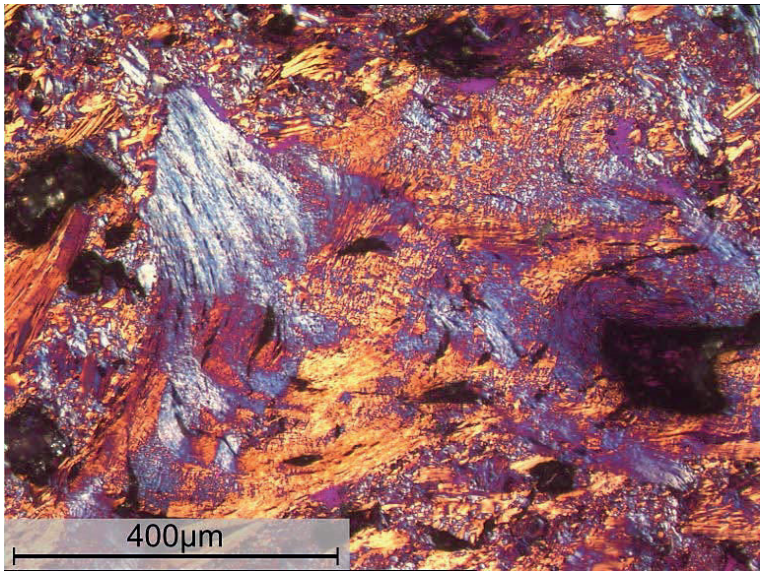

(b)

Figure 5.4: A (a) bright field and a (b) polarised micrograph of a carbon grain, clearly showing the anisotropy of carbon. At a closer look, bright spots can be seen at the grain boundary in the bright field micrograph. The corresponding spots in the polarised micrograph have a purple appearance. This indicates aluminium carbide. The dark pores contain bath.

In the polarised micrographs in the present work, graphite, which is anisotropic, will appear orange or blue, depending on the orientation of the graphene sheets. Amorphous materials and other isotropic compounds will appear purple. In the magnification range relevant for this work, metal, aluminium carbide, aluminium oxide and amorphous carbon falls into the latter category. As with the bright field technique, the metal reflects the light effectively and shines brightly in the micrographs. Furthermore, it has been found that aluminium carbide also appears relatively bright, while the more transparent bath often appears dark.

Optical microscopy has proved to be convenient and useful for the investigation of cathode samples. It is possible to differentiate between metal, aluminium carbide, aluminium oxide and bath. It also provides a good overview of the carbon material itself, showing coke grains, filler material and porosity.

5.3.2 Electron microscopy

A Hitachi S-3400N VP SEM (Variable Pressure Scanning Electron Microscope), with BSE (backscatter electron) and EDS (energy-dispersive X-ray spectroscopy) detectors, was used to differentiate and identify the different compounds within the cathode samples. Phases with high mean atomic number appear bright on BSE micrographs as heavy elements backscatter electrons more strongly than lighter elements. Qualitative and semi-quantitative element analysis was obtained by EDS, making it possible to identify the different phases. The SEM analyses were done at low vacuum (6–10 Pa) to reduce polarisation effects.

The list of arithmetic mean atomic numbers ($\overline{Z}$) shown in Table 5.3 gives little reason to believe there will be any atomic number contrast between the fluoride species, aluminium oxide, and aluminium carbide. The signal intensity from the backscattered electrons is, however, not perfectly proportional to the mean atomic number. A root mean square of the atomic number ($\overline{Z}_{RMS}$) might be a better fit [87]. The micrographs in Figure 5.5 show that there is in fact a distinguishable contrast between the mentioned species.

$$\overline{Z} = \sum_{i=1}^{n} x_i Z_i \tag{5.1}$$

$$\overline{Z}_{RMS} = \sqrt{\sum_{i=1}^{n} x_i Z_i^2} \tag{5.2}$$

x_i and Z_i are the atomic fraction and the atomic number of element i in a species with n elements.

Table 5.3: Mean atomic numbers for relevant species.

Species	Mean atomic number	
	$\overline{Z}$	$\overline{Z}_{RMS}$
C	6.00	6.00
O	8.00	8.00
F	9.00	9.00
NaF	10.00	10.05
Na_3AlF_6	10.00	10.09
AlF_3	10.00	10.15
Al_2O_3	10.00	10.30
Al_4C_3	10.00	10.58
Na	11.00	11.00
Al	13.00	13.00
CaF_2	12.67	13.69
Si	14.00	14.00
Ca	20.00	20.00
Fe	26.00	26.00

As mentioned the EDS analyses were only semi-quantitative, and especially for the light elements, such as carbon, oxygen and fluorine, the results are inaccurate. Nevertheless, the analysis method gives a good indication of the species present. A high reading of Al and C, and small amounts of other elements, would for instance indicate presence of aluminium carbide. Some examples of typical EDS results for different species found in cathode samples are given in Table C.1 in Appendix C.

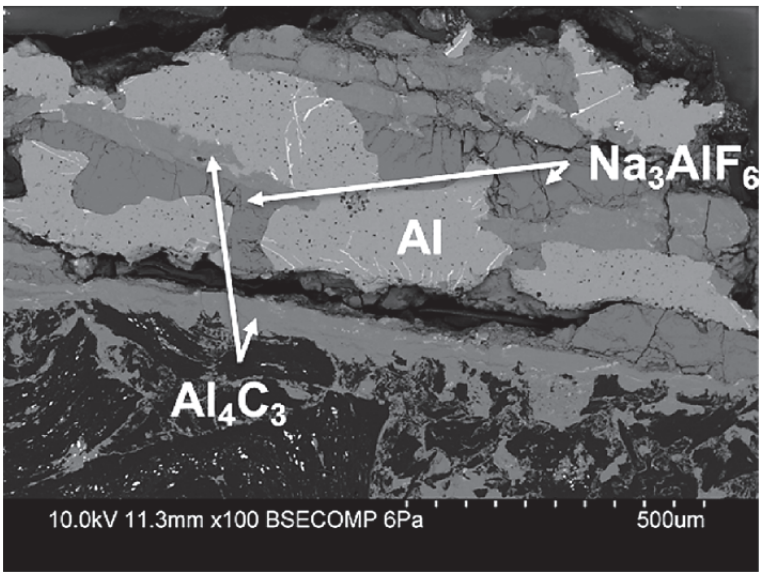

(a)

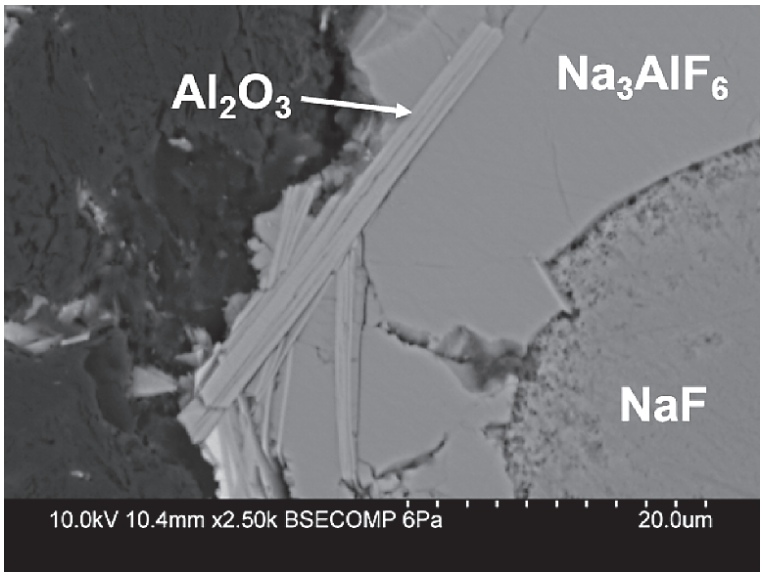

(b)

Figure 5.5: SEM BSE micrographs of different components at the surface (a) and in a pore (b) in a cathode sample. The difference in mean atomic number makes it possible to differentiate between the components.

5.4 Observations and discussion

5.4.1 Aluminium carbide layer

Aluminium carbide has been found at the surface and/or in superficial pores of all investigated cathodes. Some samples were deliberately taken from areas with large amounts of carbide, obvious from the yellow dust covering the cathode surface. These samples show a continuous aluminium carbide layer with a thickness of about 50 µm up to more than 200 µm. The thick layers seem to be stratified, with bath enclosed between the sub layers. Samples taken from areas where there has been less yellow dust have also been found to have a carbide layer at the surface, but not as continuous and much thinner.

The areas with large amounts of carbide were, seemingly, located randomly on the cathode. The extent of the visually observable carbide layers varied from small specks in the size of a fingernail to areas of close to 1 m^2.

Figure 5.6 shows a picture of a sample taken from a yellow, carbide rich area on a GZ cathode. A thick and continuous bright layer, i.e. aluminium carbide, was observed at the carbon interface. At higher magnification such layers appeared to be stratified, illustrated by the micrographs in Figure 5.7. Figure 5.8 shows micrographs of a thin carbide layer at the surface and in a superficial pore on a SGZi cathode. This sample was taken from an area with a hue of white and yellow, but not as obviously carbide rich as the areas where the samples in Figures 5.6 and 5.7 were extracted.

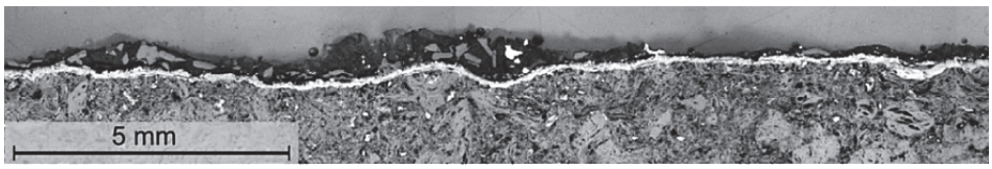

Figure 5.6: An overview picture of the surface of a sample from a GZ cathode block, put together by several optical micrographs. A thick continuous layer of aluminium carbide covers the surface. A layer of sludge (bath, alumina and some metal) covers the carbide layer.

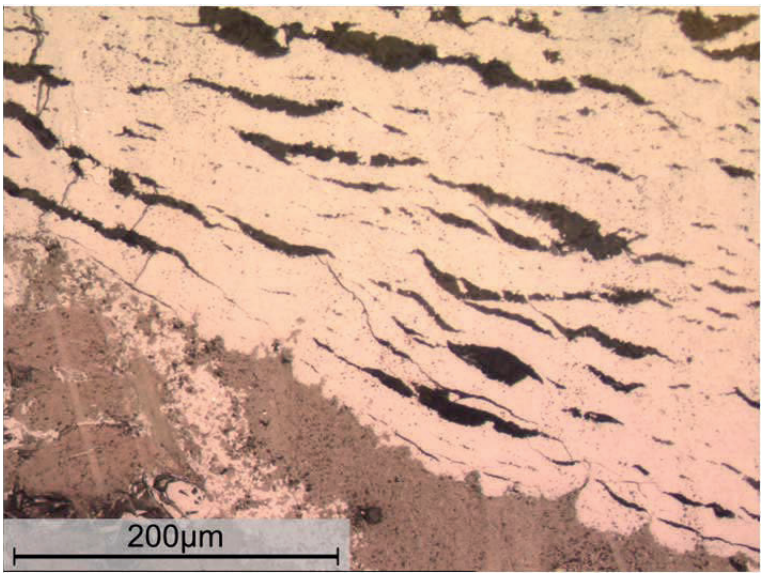

(a)

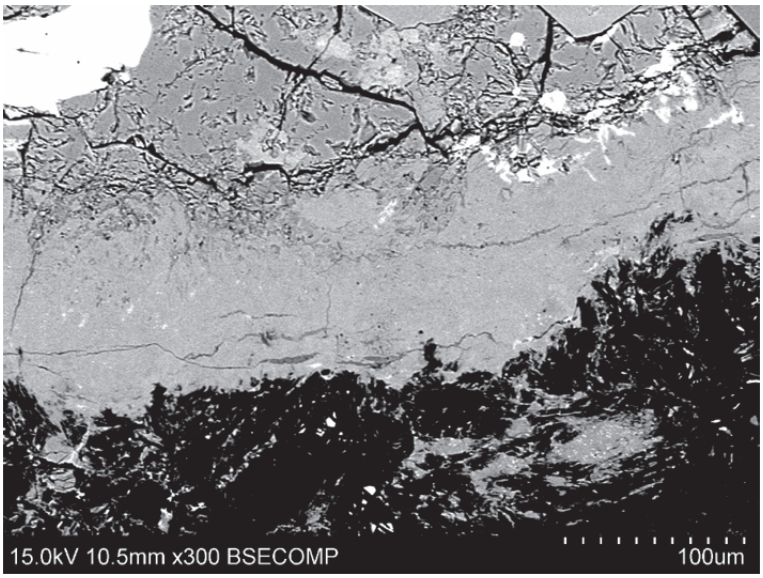

(b)

Figure 5.7: (a) Optical micrograph of a thick stratified aluminium carbide surface layer on a sample from a SGZi cathode block. The dark areas within the carbide layer were found to contain bath. (b) SEM micrograph of a thick stratified aluminium carbide surface layer on a sample from a GZ cathode block. The darker grey compound over the carbide layer is cryolite, and aluminium metal can be seen at the upper left corner.

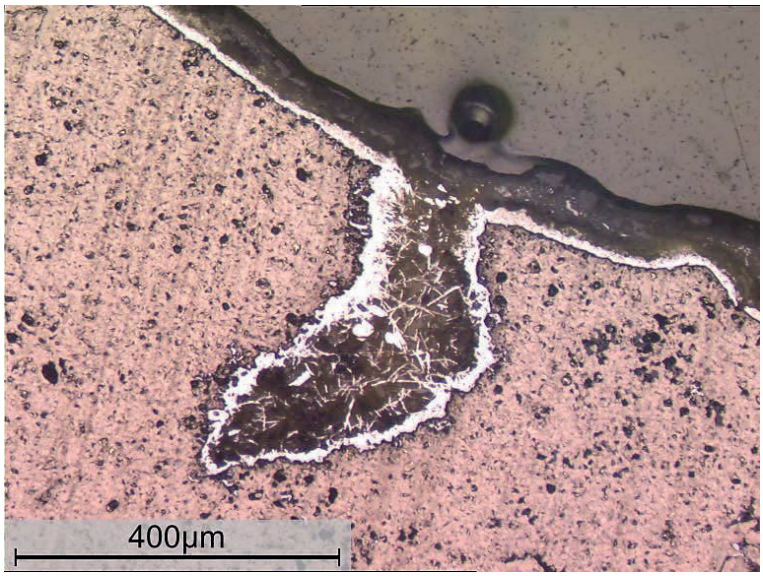

(a)

(b)

Figure 5.8: Optical micrographs of a thin aluminium carbide surface layer on a sample from a SGZi cathode block. (a) Bright field lens. (b) Polarising lens.

The thick stratified aluminium carbide layers that have been observed have always been found beneath a layer of bath, aluminium or corundum, which will have protected the carbide from oxidation. In areas where aluminium and bath remnants have been

completely removed and the cathode surface has been exposed for several days, layers of aluminium carbide have not been found. Fresher samples extracted shortly after cell shut down, from areas where bath and metal were completely removed, did show a thin non-continuous carbide layer. It is quite possible that these thin layers were in fact thick and stratified before cleaning, and that most of the carbide was removed along with metal and bath. This theory is supported by the picture of the solidified metal pad in Figure 2.33, showing flakes of aluminium carbide attached to the removed pad.

No noticeable differences have been observed between samples from different areas of the cathode regarding the presence of aluminium carbide. The thick surface layer is typically found on samples taken from areas that appear yellow upon cathode investigation, and the occurrence of this yellow dust does not seem to have any preference to any specific areas on the cathode. The amount of aluminium carbide does, however, vary between different cells. For example a side-by-side cell with graphitized cathode blocks was found to have a thick and dense layer of aluminium carbide at several areas of the cathode, while the investigation of an end-to-end cell at another aluminium plant, using vibrated semi-graphitic cathode blocks, revealed only a very thin layer of aluminium carbide. Variation in the carbide amount on the surface was also found between neighbouring cells with the same technology, same cathode material and roughly the same age. This indicates that the amount of aluminium carbide found on the surface of the cell after shut down is dependent on something else than the three mentioned parameters, i.e. technology, cathode material and age.

The aluminium carbide layer on the cathode surface is either formed during operation or by precipitation of carbide dissolved in metal and bath remaining in the cell during cooling. In situ investigation of aluminium carbide formation in the electrolysis cell is challenging, and to the authors knowledge the formation of carbide layers during operation has yet not been proven. However, estimations of the maximum amount of aluminium carbide that is available for precipitation during cooling may give an indication whether or not the carbide can be solely the product of precipitation.

The ratio between the thickness of the aluminium pad (t_{Al}) and the precipitated aluminium carbide layer ($t_{Al_4C_3(p)}$) from carbon dissolved in metal is estimated from equation (5.3). Assuming the precipitated carbide layer has similar density as pure aluminium carbide ($\rho_{Al_4C_3(p)} = \rho_{Al_4C_3} = 2.36$ g/cm^3), the molten aluminium has a density of 2.3 g/cm^3, and that the concentration of carbon in the aluminium ($c_{Al_4C_3\ in\ Al}$) is at saturation (35 ppm Al_4C_3 [85]), the ratio between aluminium and carbide is 2.93 cm Al per µm Al_4C_3. Similarly for carbide saturated bath, assuming a density of 2.1 g/cm^3 [5] and a carbide concentration of 2.0 wt% [25], the ratio would be 56.2 µm bath per µm Al_4C_3.

$$\frac{t_{Al}}{t_{Al_4C_3(p)}} = \frac{\rho_{Al_4C_3(p)}}{\rho_{Al} \cdot c_{Al_4C_3\ in\ Al}} \tag{5.3}$$

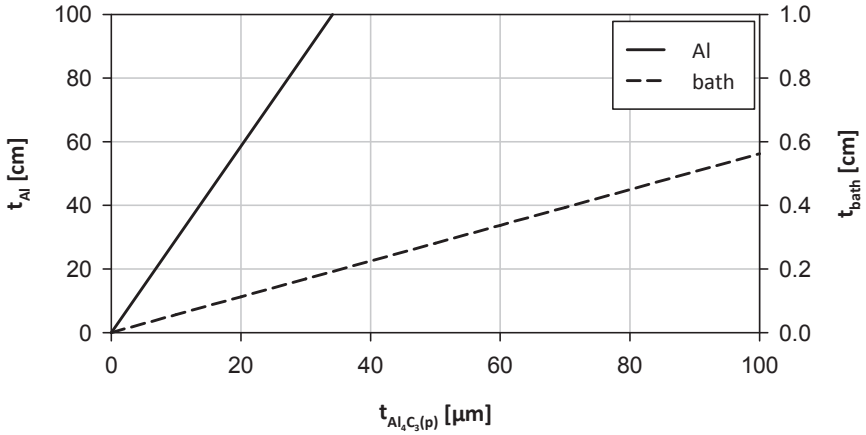

Figure 5.9: Graph showing the amount of aluminium and bath needed for precipitation of a dense aluminium carbide layer of thickness $t_{Al_4C_3(p)}$.

It is evident that the aluminium carbide observed cannot solely be a product of precipitation from aluminium remnants. A carbide layer of 50 µm would require almost 1.5 m of aluminium, which is more than five times the typical thickness of the metal pad during operation. The final tapping of metal and bath when the cell is shut down leaves much less liquid from which carbide can precipitate.

In the bath, the solubility of aluminium carbide is much higher. A carbide layer as shown in Figure 5.10 requires about 1 cm of carbide saturated bath. Based on this, it cannot be ruled out that much of the aluminium carbide observed on the cathode surface has precipitated from bath and sludge.

There are other factors making the precipitation route less likely, however. During operation the heat is evolved from the electrolysis and the thermal gradient is negative downwards the cathode and into the insulation materials. After shutdown the gradient is reversed, i.e. heat is best preserved in the insulation and the remaining bath and metal is cooled from the surface and down. Based on this, it may be expected that carbide would precipitate first in the upper area of the bath or metal layer.

Furthermore, the relatively rapid cooling would more likely result in needle-like precipitations rather than an even and dense layer at the interphase. In the middle of the superficial pore/crack in Figure 5.8 and the pore in Figure 5.23 such needle-like carbide can be seen. Thus, it is not likely that carbide layer observed at the carbon interphase has

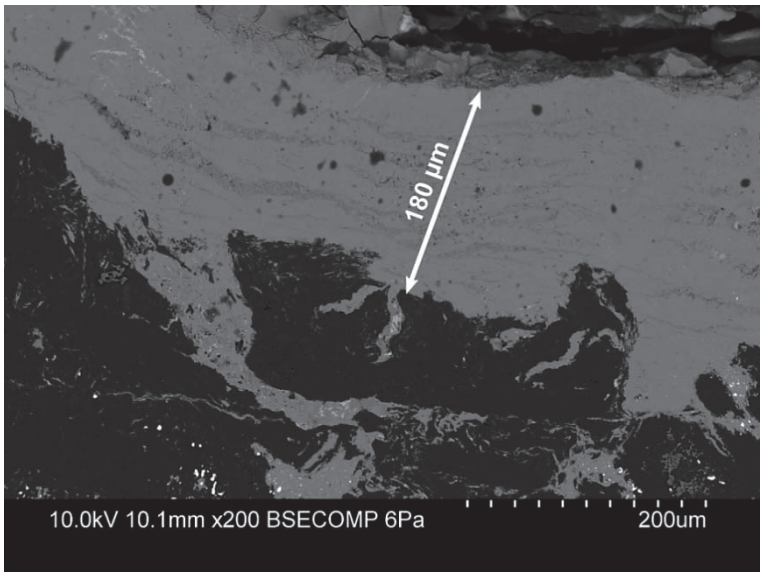

Figure 5.10: SEM micrograph of a thick aluminium carbide surface layer.

been formed by precipitation, which means that the layer is probably formed during operation.

It is known in the aluminium industry that the carbide layer can cause problems when restarting a cell that has been shut down. An insulating carbide layer hinders current flow through the cathode during pre-heating, i.e. before electrolyte is added to the cell, and aluminium carbide is therefore mechanically removed from the cathode surface before restarting can commence [88]. According to the data of King and Dorward [23], the specific resistivity of Al_4C_3 is about 250 Ωcm at temperatures around 950–960°C. This value is 6 orders of magnitude higher than the resistivity of the carbon blocks, but still far from an electrical insulator. Assuming a current density of 1 A/cm, the voltage drop through a dense carbide layer would amount to 25 mV for every µm of Al_4C_3. The thick carbide layers may thus be considered to be non-conductive, and it can be concluded that the cathode is not covered by a thick, dense and continuous carbide layer during operation. It is, however, possible that the cathode is covered by a continuous carbide layer of a few microns thickness, yielding a voltage drop of about 100 µV.

If there is in fact a thick carbide layer (e.g. 20 µm or thicker) covering the entire surface of the cathode during operation, the layer cannot be dense. The current must somehow flow through pores or cracks possibly filled with aluminium and bath. Pores and cracks in the carbide surface layer have been found to contain bath (Figure 5.11), but aluminium metal has seldom been observed within the carbide surface layer.

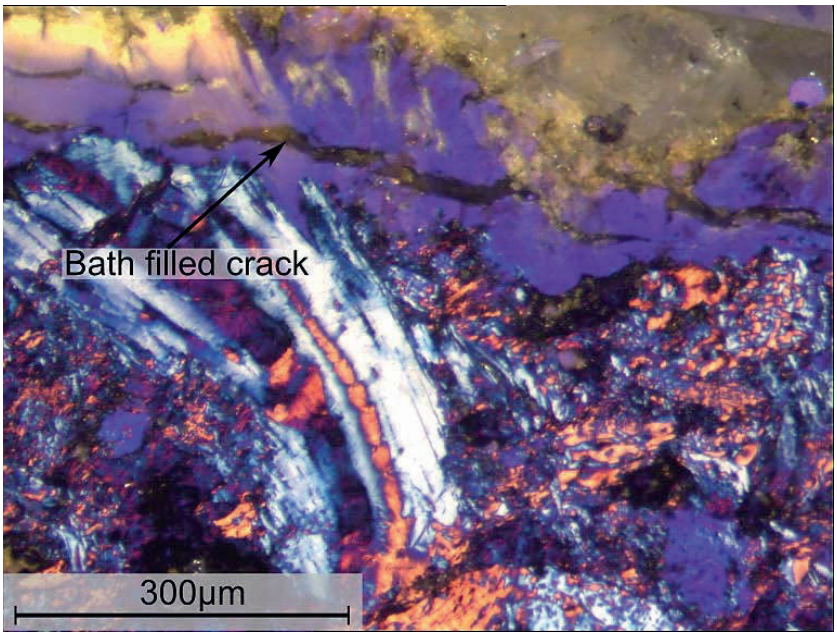

Figure 5.11: Optical micrograph (polarised) of a bath filled crack in the aluminium carbide surface layer on a sample from a GZ cathode block.

5.4.2 Aluminium carbide in cathode porosity

Aluminium carbide has also been found in pores, even in the cases where there has been found little or no carbide at the surface (Figures 5.12 and 5.13). Carbide is most abundant in the pores close to the surface, i.e. in open macro porosity, but has also been found in deeper pores.

Aluminium carbide in pores throughout the sample, as in Figure 5.14, was observed exclusively in samples from the mid-section of cell I-31 from Årdal. This cell was the only investigated cell with vibrated semi-graphitic cathode blocks, and also the one cell that was investigated very short after shutdown. Only four samples were extracted, two from the mid-section and two from the side of the cathode. The two samples from the side were similar to samples from other cells with regard to the depth of where carbide could be observed, i.e. aluminium carbide was restricted to the first centimetre beneath the surface. Both samples from the mid-section of the cathode were found to have carbide in pores throughout the sample.

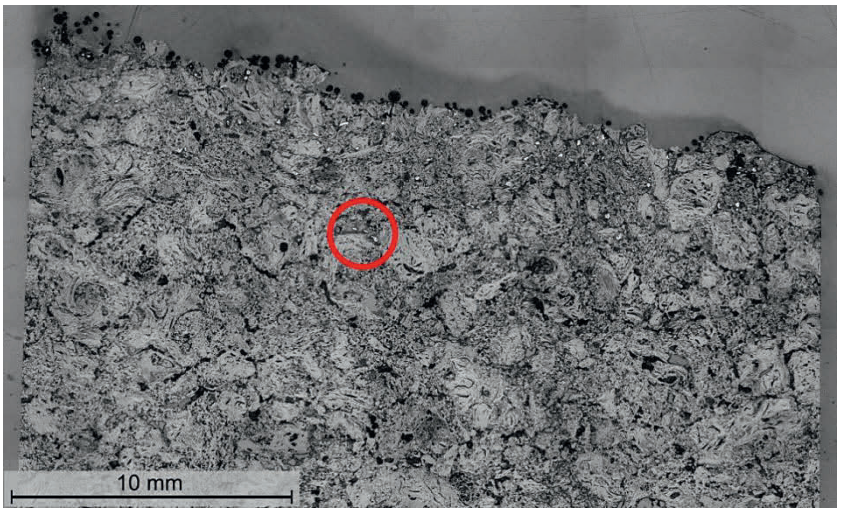

Figure 5.12: An overview picture of a sample from a GZ cathode block, put together by several optical micrographs. The deepest pores where aluminium carbide could be observed were about 5 mm below the surface, marked by the red circle. The barely visible bright spots are aluminium carbide. No carbide surface layer could be observed.

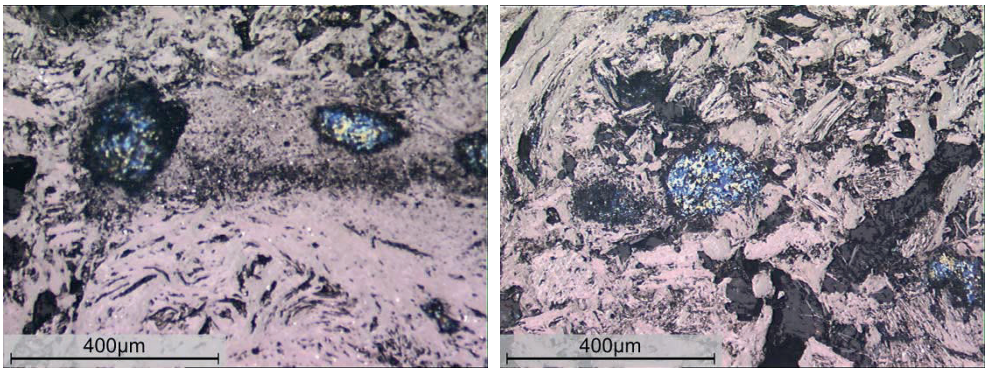

(a) (b)

Figure 5.13: Optical micrographs of the same sample as in Figure 5.12, showing aluminium carbide (with a blue appearance) in pores. (a) The deepest pores where aluminium carbide could be observed, marked by a red circle in Figure 5.12. (b) Pore about 2 mm below the surface.

The author has not been able to detect any differences between the middle and the sides of the cathode blocks regarding the microstructure of the carbon material. Differences in e.g. porosity could potentially explain variations of carbide “penetration” depth. There might also be a thermodynamic explanation to the finding, i.e. that aluminium carbide is more stable at the mid-section of the cell than at the sides.

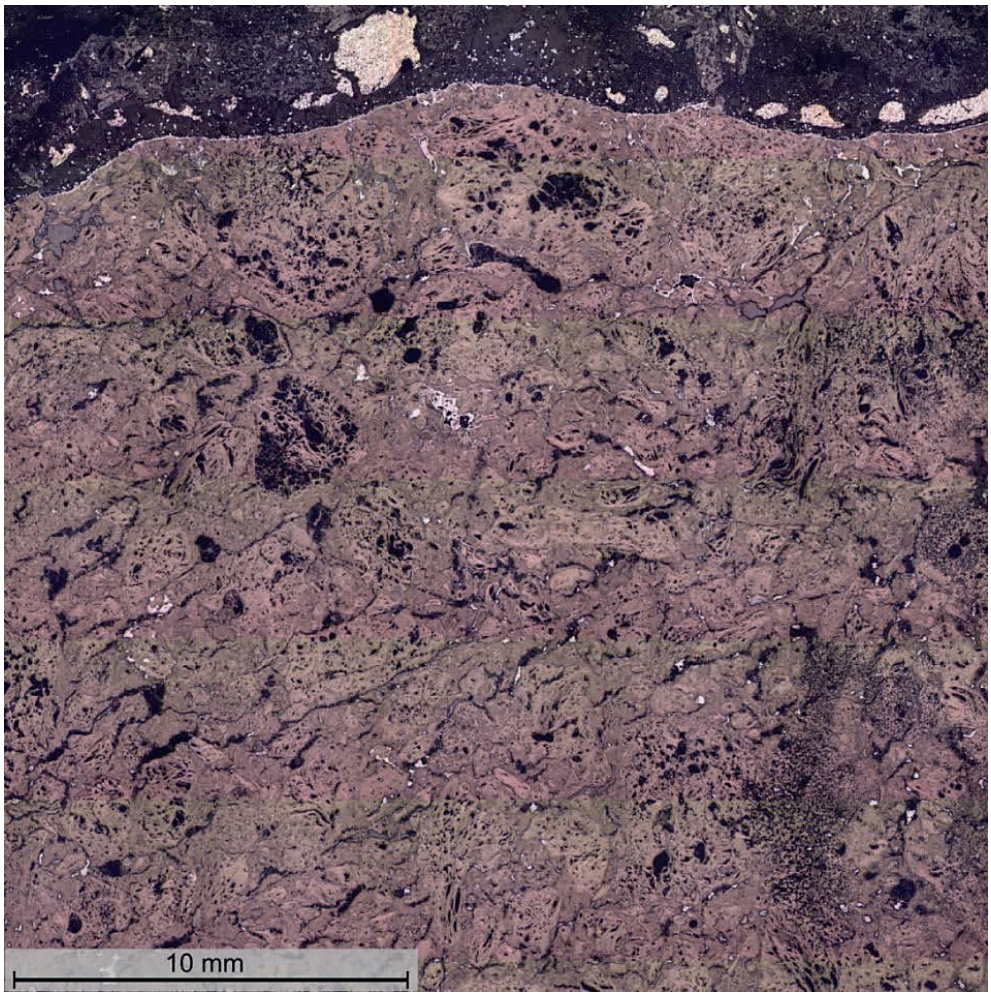

Figure 5.14: An overview picture of a sample from a SGv cathode block, put together by several optical micrographs. Bright spots, which are aluminium carbide, can be seen in pores throughout the sample. A rather continuous carbide layer could be seen on the cathode surface.

The electrochemical carbide formation reaction (3.5) is dependent on the activity of sodium fluoride and aluminium fluoride. Al_4C_3(s) is more stable at low cryolite rates (CR = mol NaF/mol AlF_3). It is known that the aluminium formation reaction gives rise to concentration gradients in the diffusion layer between bath and aluminium, resulting in a high CR at the interface [89], as illustrated in Figure 5.15. High current densities will give greater differences in the CR between bulk and the interface.

$$4AlF_3(diss) + 12Na(C) + 3C(s) \rightarrow Al_4C_3(s) + 12NaF(l) \qquad (3.5)$$

Assuming that there is a bath layer between the cathode and the metal pad and the correlation between CR and current density can be transferred to the interface between the carbon cathode and the bath layer beneath the aluminium pad, this would mean that aluminium carbide is more stable at the middle of the cathode blocks where the current density is lower.

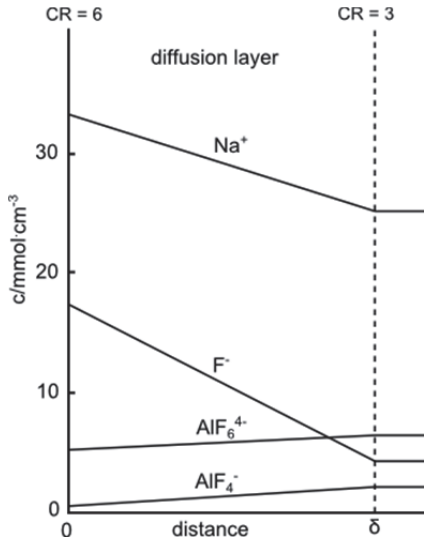

Figure 5.15: Concentration profile in the cathodic diffusion layer by electrolysis at 0.6 A/cm^2 and bulk melt CR = 3. Redrawn from Thonstad and Rolseth [89].

Due to the small amount of samples and the fact that the sampling procedure deviates from the standard, the observations from cell I-31 have questionable statistical value. Therefore it cannot be decisively concluded that there is a correlation between carbide occurrence in deep porosity and specific areas of the cell. Nor can it be concluded whether it is typical for SGv cathode blocks that aluminium carbide exists in the deeper cathode porosity.

Large amounts of carbide were found in cracks in between the rammed joints and the cathode blocks, as can be seen from Figures 5.16 and 5.17. Large cracks were often found in the rammed joints which have a lower resistance against thermal shock and sodium expansion. The bath transport within these cracks, and pores in general, is lower than at the cathode surface. The dissolution of the formed carbide should thus be slow, with thick carbide layers as a result.

Large amounts of carbide can be expected in carbon materials with a high amount of cracks and pores, i.e. a high surface area where carbide dissolution is slow. This finding is

in good agreement with the results of Grjotheim et al. [21] who found that the amount of Al_4C_3 formed increased with the pore volume (Figure 2.3(b)).

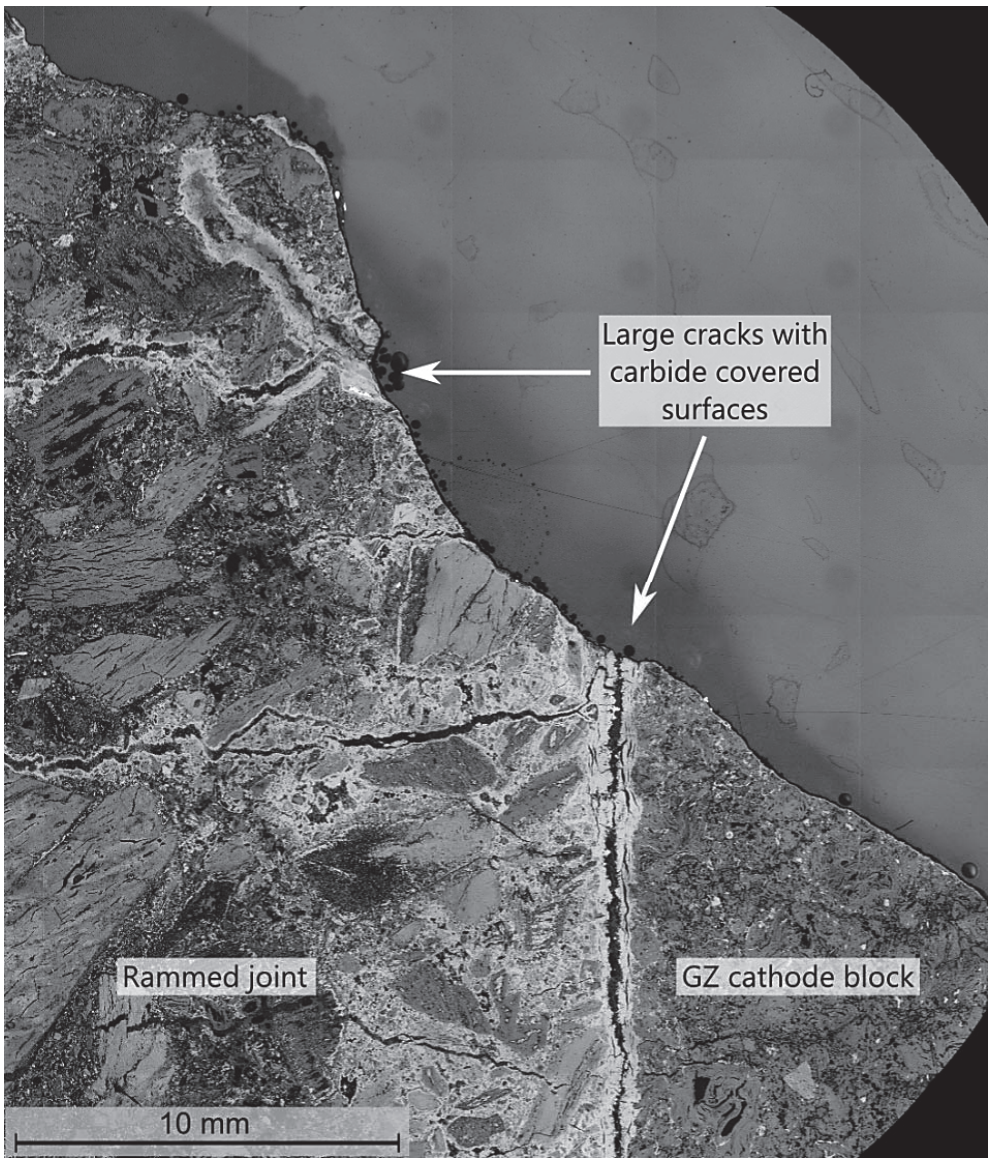

Figure 5.16: An overview picture of a sample from the joint between ramming paste and cathode block in a GZ cathode, put together by several optical micrographs. Large cracks in the rammed part and between the ramming and the cathode blocks are covered by carbide.

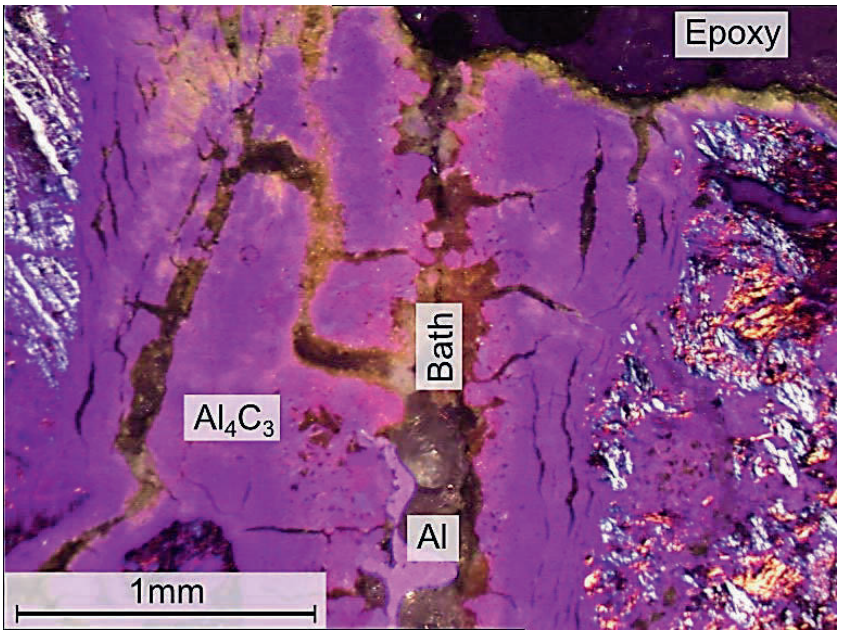

(a)

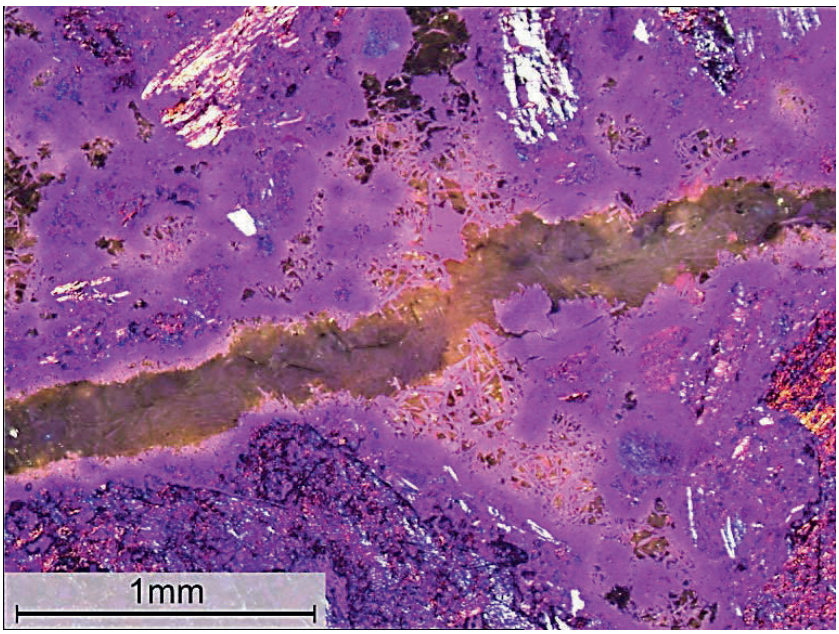

(b)

Figure 5.17: Polarised micrographs of (a) a vertical crack between the rammed joint and the cathode block and (b) a horizontal crack in the rammed part.

5.4.3 Aluminium oxycarbide

As mentioned in section 3.4, aluminium oxycarbide will be the stable phase in oxide rich systems, and Lebeuf et al. [90] found evidence of C-O-Al bonds by XPS analysis of a cathode sample from an experimental cell. One may therefore expect to find oxycarbide in industrial cathode samples, at least where alumina sludge is present. The microscopy techniques in this work are probably not suitable for identifying aluminium oxycarbide. It is not known whether oxycarbide is distinguishable from carbide or bath by optical microscopy or SEM, and the EDS measurements only indicate the elements present without information about chemical bindings. Thus, analysed areas containing Al, C, and O might be a mixture of Al_2O_3 and Al_4C_3 as well as aluminium oxycarbide.

Figure 5.18 shows a pore containing various bath compounds, including what might be aluminium oxycarbide. Assuming the EDS analysis (Table 5.4) is reliable and that all fluoride is in the form of Na_3AlF_6, the ratios of the remaining Al, C, and O are Al/C =2.4 and Al/O = 1.1. The Al/O ratio is close to that of aluminium oxycarbide, Al_4O_4C, but the Al/C ratio is 40% lower. This deviation may be attributed to the low accuracy of the EDS analysis, or that the compound is a mixture of Al_2O_3 and Al_4C_3 rather than aluminium oxycarbide.

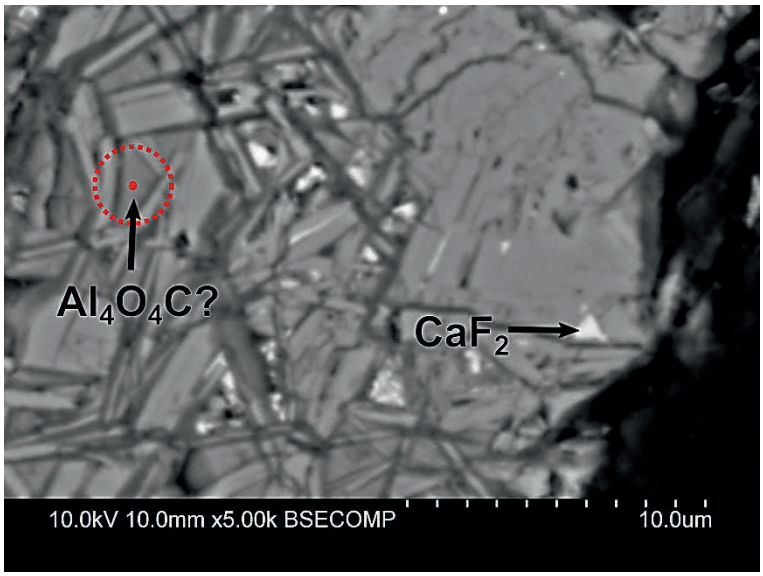

Figure 5.18: SEM micrograph showing the area for the EDS results shown in Table 5.4, marked by red dotted circle. Assuming all fluoride and sodium is in the form of Na_3AlF_6, the approximate ratio of the remaining elements Al, C, and O is Al/C = 2.4 and Al/O = 1.1, according to the EDS measurement. This might be Al_4O_4C or a mixture of alumina and carbide.

The micrographs in Figure 5.19 show a pore surrounding an aggregate grain. The content of the pore is clearly divided into three zones, with Al_2O_3 in one, Al_4C_3 in another, and bath in between. The clear segmentation of oxide and carbide may indicate that Al_4O_4C does not form readily in the cathode, even with abundance of oxide.

Table 5.4: Selected EDS results showing indications of oxycarbide or lack thereof.

From fig.	Probable compounds	EDS results [at%]				
		C	O	F	Na	Al
0.23	Na_3AlF_6 and Al_4O_4C / Al_2O_3 / Al_4C_3	7.3	16.0	35.5	17.9	23.3
0.24	Al_2O_3	5.5	58.4		3.1	33.0
0.24	NaF and AlF_3 (CR>3)	2.9		54.7	33.9	8.5
0.24	Al_4C_3	43.1	4.8	1.2		50.9

5.4.4 Metal in cathode porosity

Aluminium does not wet carbon and has not been observed directly at the carbon interface. At the surface Al was enclosed in bath or corundum, or there was a layer of aluminium carbide between the carbon and the metal. In pores Al was typically found enclosed in aluminium carbide (Figure 5.20). Most of the metal found in the porosity was found to be rich in iron with aluminium as a secondary component. Small amounts of silicon, probably from dissolved side lining, were also found in many of these metal droplets.

As can be expected, iron rich precipitations could be found in the remnants of the aluminium pad in cells which had been shut down due to elevated iron content in the tapped metal. The amount of iron found in the porosity was also highest for these cells, and within the same cells iron was most abundant in samples from the most worn areas close to the side walls. I.e. iron was most abundant where only a few centimetres of carbon separated the aluminium pad from the steel current collector bars. This could indicate that the iron is somehow introduced by the steel bars, possibly by dissolution of the bars, or during the cast in process before installation. The mechanism behind the occurrence of iron in cathode porosity has not been investigated further in this work.

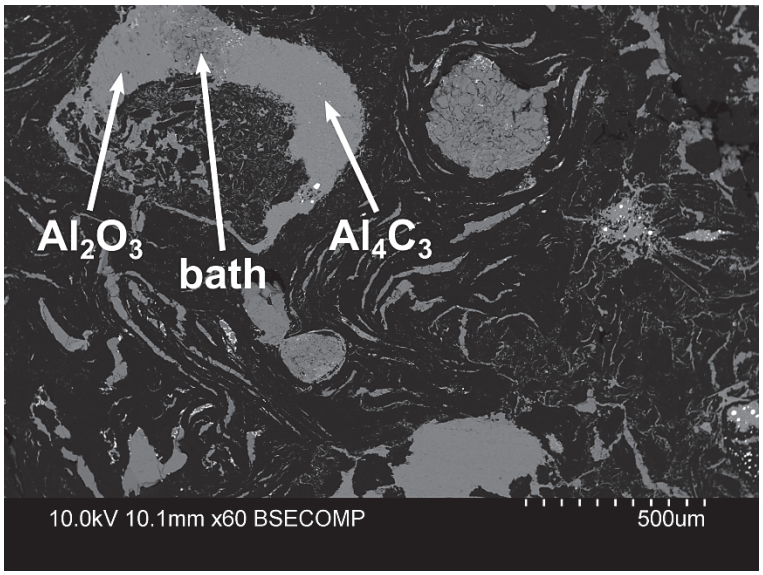

(a)

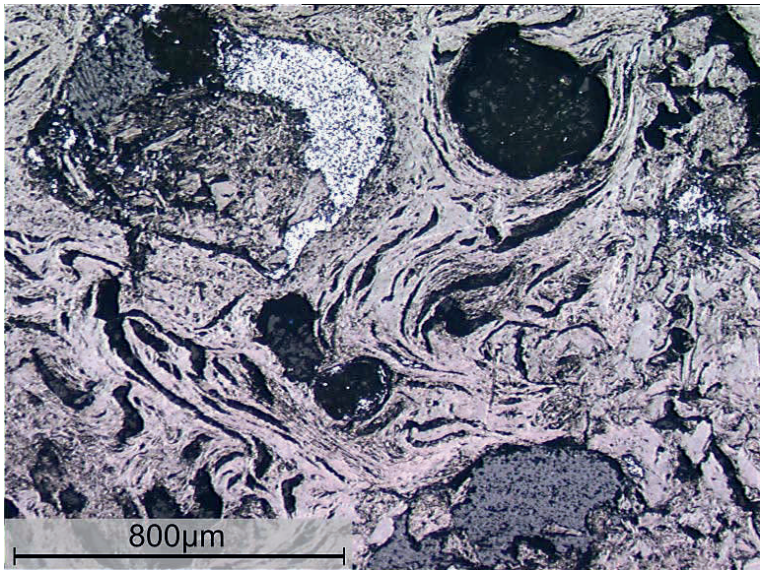

(b)

Figure 5.19: (a) SEM and (b) optical micrographs showing a pore with alumina, bath and aluminium carbide, according to EDS analysis (Table 5.4). Though alumina is present in abundance, no clear indication of aluminium oxycarbide was found.

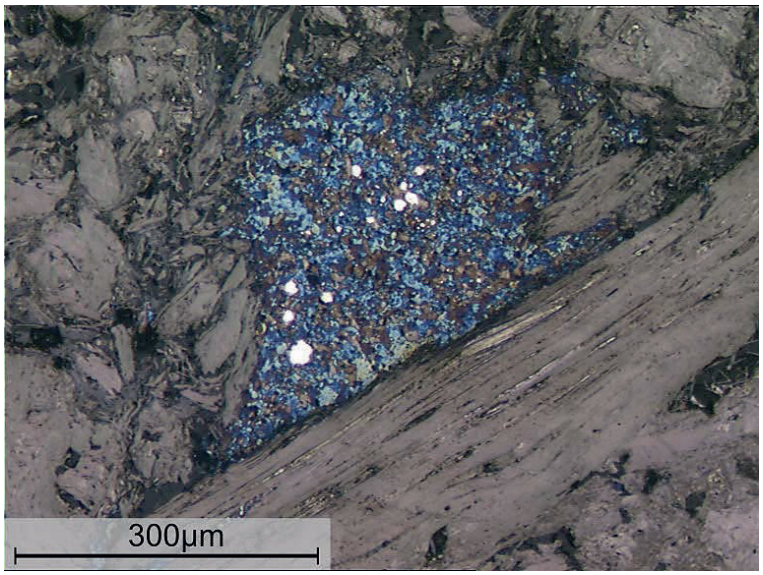

(a)

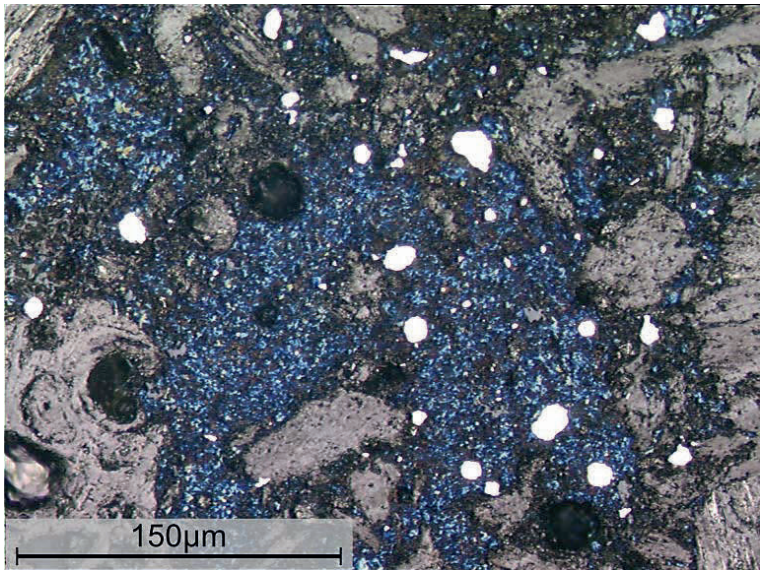

(b)

Figure 5.20: Optical micrographs of pore with aluminium carbide (blue) and bright metal droplets. According to EDS measurements the metal droplets consisted of iron, about 20 wt% aluminium and small amounts of silicon. The samples came from a (a) SGv and a (b) SGZv cathode.

5.4.5 Bath film and bath penetration

The solidified bath found on the cathode surface (Figure 5.21), often covering aluminium carbide layers, on a large amount of the cathode samples indicates that bath exists between the carbon cathode and the metal pad. The bath seemed to have solidified as continuous films at the cathode surface rather than being separate precipitated particles. The cracked appearance is probably due to thermally or mechanically induced stresses during cooling and cleaning of the cathode.

Bath penetrates the entire cathode and can be found in most of the cathode porosity. Upon solidification it seems to have precipitated into distinct phases: Na_3AlF_6, NaF, CaF_2, and Al_2O_3. The micrograph in Figure 5.22 shows bath penetration close to the cathode surface. The amount of bath in the porosity seemed to be similar throughout the samples. In the cases where both aluminium carbide and bath was found in a pore, the carbide tended to occur dense along the pore walls with crystallites growing into the bath phase in the middle, as can be seen in Figure 5.23.

The precipitation of NaF as a separate phase, and the lack of a separate AlF_3 phase, indicates that the cryolite ratio (CR) of the bath penetrating the cathode was greater than 3. This indicates that the CR in the bath film between the metal pad and the carbon cathode was also greater than 3, which is in accordance with the concentration profiles with raised concentrations of NaF and depletion of AlF_3 that are known to occur at the bath-metal interface Figure 5.15.

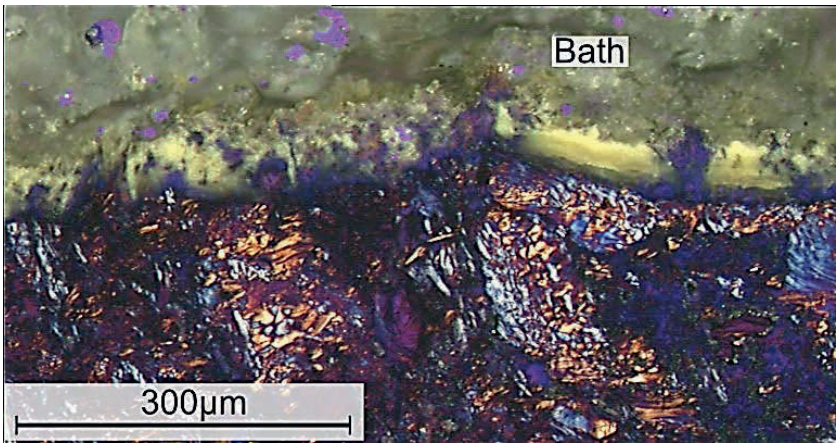

Figure 5.21: Polarised micrograph of the surface of a SGZv cathode block. The sample surface was covered by a layer of solidified bath.

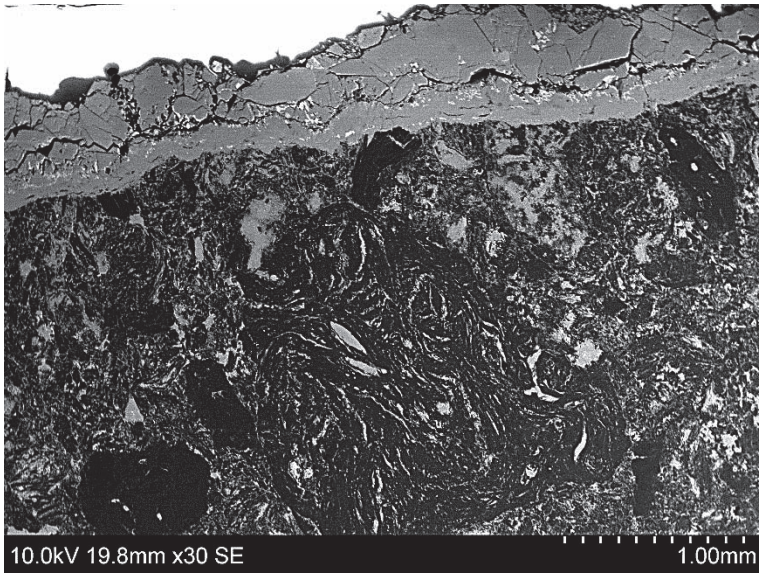

(a)

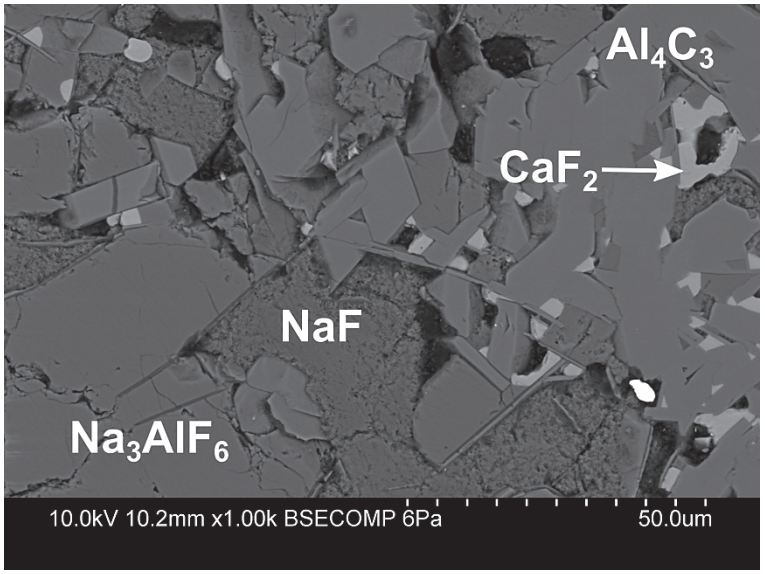

(b)

Figure 5.22: (a) SEM micrograph showing the extent of bath penetration in a sample from a GZ cathode block. (b) Higher magnification of one of the pores show bath precipitated into different phases.

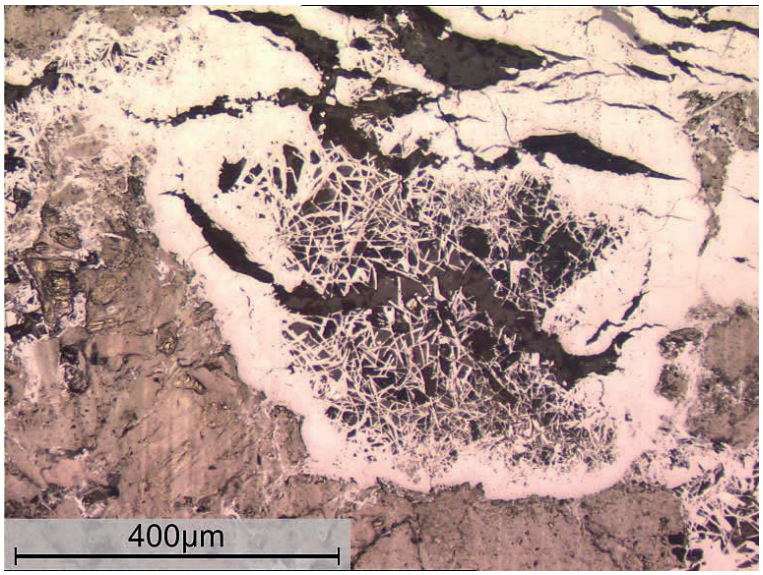

(a)

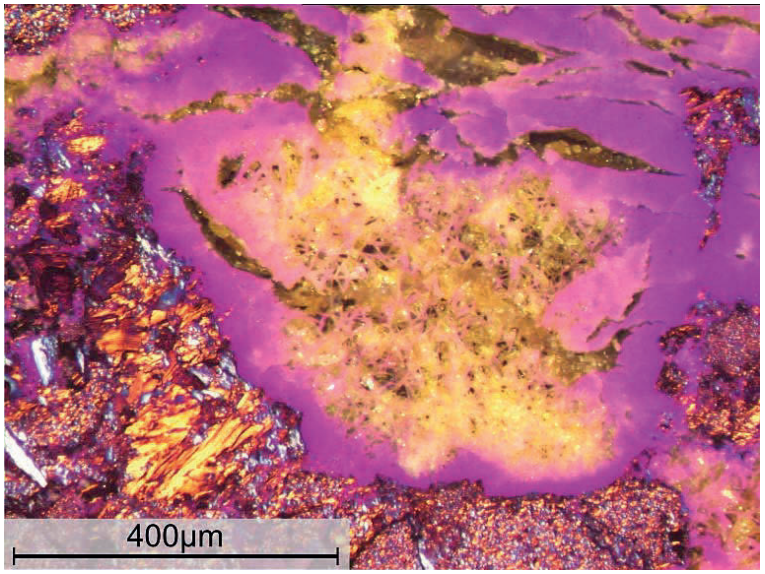

(b)

Figure 5.23: Optical micrographs of a pore with aluminium carbide and bath in a sample from a SGv cathode block. (a) Bright field lens. (b) Polarising lens.

5.4.6 Non-preferential wear of cathode blocks

In the case of preferential wear, the wear proceeds faster at one of the cathode material components, resulting in a rough surface. This is a common sight at the anodes, where preferential consumption of binder pitch coke leads to detachment of aggregate coke particles [5]. Similarly, a rough cathode surface would indicate detachments of aggregate particles. A smooth surface would indicate that the wear is non-preferential, i.e. that the wear rate is the same for filler material and aggregate.

For the cathodes investigated, samples have been found to have both crude and smooth surface areas, as can be seen in Figure 5.24. The smooth surfaces shown in Figures 5.25 and 5.26 clearly indicate non-preferential wear. The coarse areas must therefore have another explanation than preferential wear.

It is believed that the coarse areas are created by bath penetration and formation of aluminium carbide in the superficial porosity (Figure 5.26). Pores often exist around aggregate particles, and as these pores are worn (similarly as the rest of the cathode surface) the aggregate particles may detach from the cathode (Figure 5.27). Non-preferential wear and detachment of particles due to wear in the superficial porosity allows for coexistence of smooth and coarse surfaces at the cathode.

Figure 5.24: An overview picture of the surface of a sample from a GZ cathode block, put together by several optical micrographs. The rough surface is probably a result of particle detachment due to carbide formation and wear in the superficial porosity.

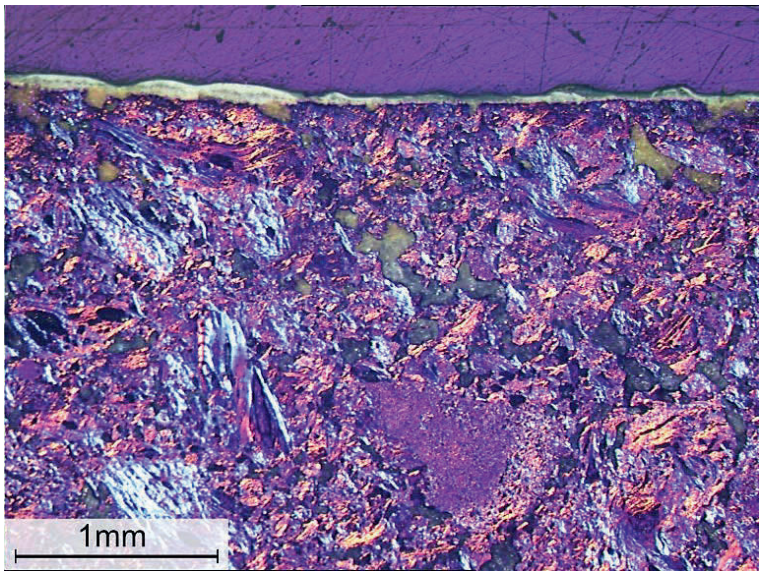

(a)

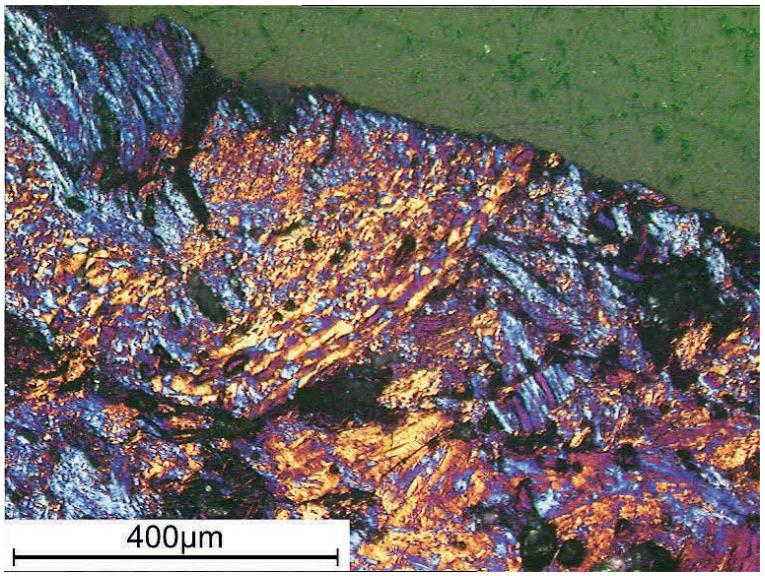

(b)

Figure 5.25: Optical micrographs (with polarising lens) of the cathode surface of a GZi cathode block. The smooth surface indicates non-preferential wear.

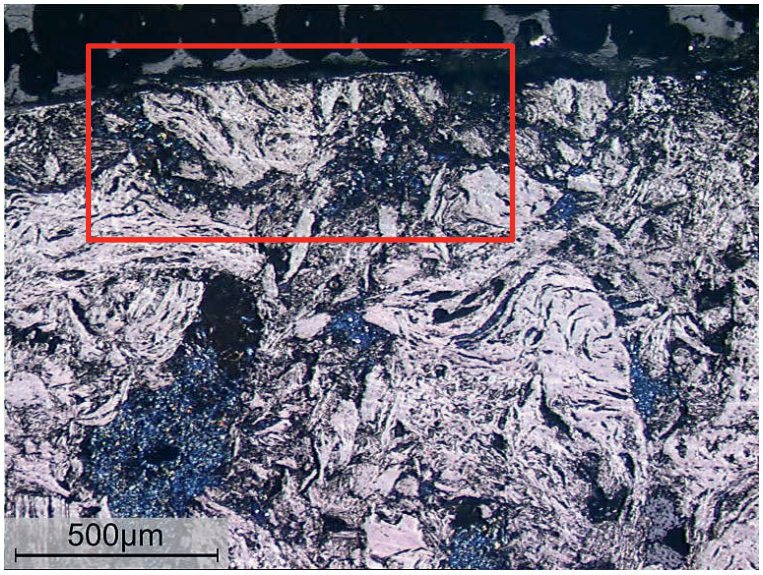

(a)

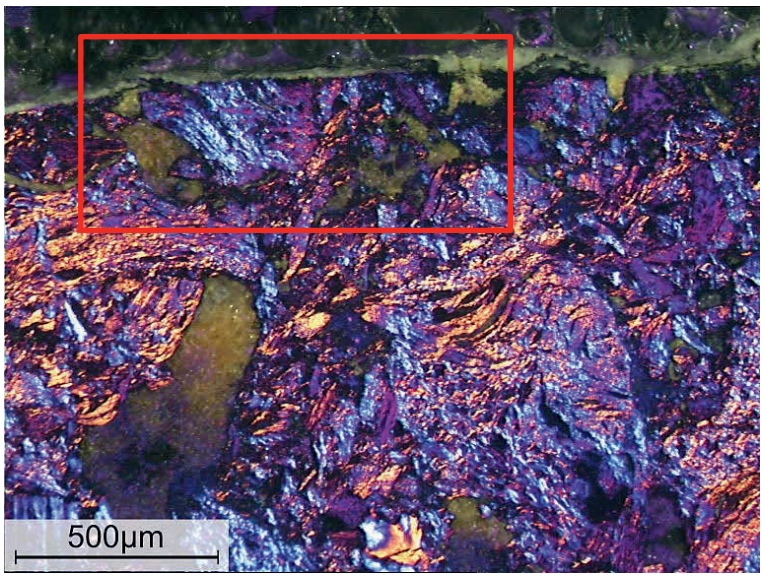

(b)

Figure 5.26: Optical micrographs of smooth cathode surface from a SGZv cathode block. Aluminium carbide has formed in superficial porosity around a carbon aggregate particle (marked by red box), which may eventually have detached from the cathode if the cell had not been taken out of operation. (a) Bright field lens. (b) Polarising lens.

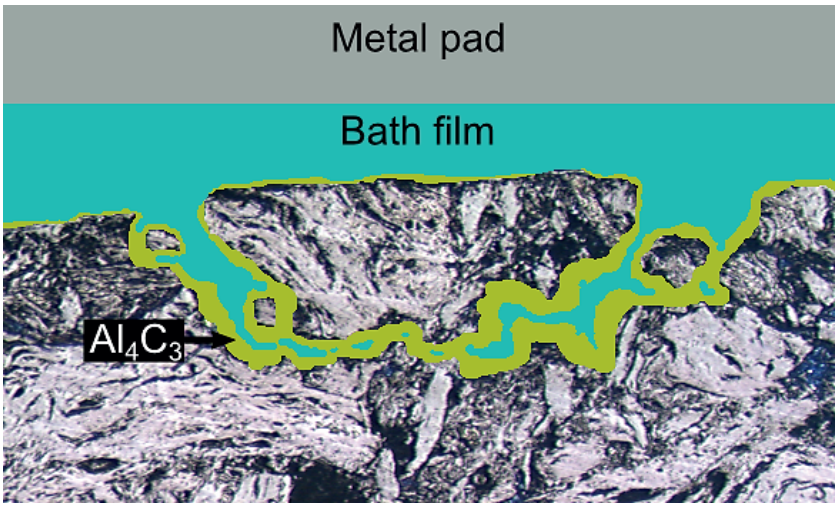

Figure 5.27: Illustration of bath penetration and aluminium carbide formation in superficial porosity, giving rise to wear around an aggregate particle and eventually detachment of the particle. The illustration is based on the micrograph in Figure 5.26(a).

5.4.7 Differences between high and low wear areas

One difference between the low wear area in the mid-section of the cell and the highly worn sides has been observed. In cells taken out of operation due to increased levels of iron in the metal, the iron content in the cathode porosity seems to be highest at the sides, close to the current collector bars.

Beyond this, the surface (the two or three upper centimetres of the cathode), has not been found to differ noticeably between different areas of the cell. It is likely that there would have been visible differences if e.g. abrasive wear was completely dominant in some areas, while chemical wear was dominant in other. A more likely case in the industry, however, is several competing mechanisms, complicating diagnostics dramatically. The lack of significant differences indicates that there are no fundamental differences in the cathode wear mechanism in different areas of the cell, though there are significant variations in the wear rate. Whether the high wear rates are caused by abrasion, chemical reactions or both, the current microscopy investigation does not provide any conclusive evidence. The presence of aluminium carbide does prove that chemical wear occur, though.

5.5 Summary

Thick layers of aluminium carbide, up to more than 200 µm thick, have been observed under protective layers of bath and metal. The amount of carbide is too large to have been formed by precipitation of carbon from the metal. Precipitation from the bath, which has much higher carbide solubility, cannot be ruled out, but the appearance of the carbide layer suggests it was formed during operation.

Aluminium carbide has been found in cracks and open porosity close to the surface. In the samples from the mid-section of cell I-31 with SGv cathode blocks, where the sampling deviated from the standard sampling method, aluminium carbide was observed in pores throughout the samples. In all the rest of the investigated cathode samples, the carbide seems to be restricted to the first centimetre beneath the surface.

The methods used are not suitable for identification of aluminium oxycarbide, though EDS results showing a mix of Al, O and C may possibly indicate the presence of Al_4O_4C.

Smooth surfaces on the cathode samples indicate that the wear is non-preferential and that aggregate particles and filler material is worn alike. Carbide formation in superficial pores, which often surrounds aggregate particles, leads to particle detachment and a coarse surface. Non-preferential wear and detachment of particles due to wear in the superficial porosity allows for coexistence of smooth and coarse surfaces at the cathode.

Bath have been found on the surface of a large amount of the cathode samples, supporting the assumption that there exists a bath layer between the carbon cathode and the metal pad.

Bath found in pores throughout the cathode samples seem to have precipitated into relatively distinct phases: Na_3AlF_6, NaF, CaF_2, and Al_2O_3. The precipitation of NaF indicates CR > 3 in the penetrating bath, and also the bath film at the carbon cathode surface.

Small metal droplets, mostly consisting of iron and aluminium, have frequently been observed enclosed in carbide in the cathode porosity of cells shut down due to increased levels of iron in the tapped metal. The amount of iron seemed to be higher at the sides, close to the current collector bars.

No significant differences have been observed between samples from high wear and low wear areas of the cathode. This can be interpreted as an indication of that wear occurs according to the same wear mechanisms in all areas of the cell, but at different rates.

Furthermore, no significant differences were observed between samples from different types of cathode blocks.

Chapter 6

Laboratory scale experiments

6.1 Introduction

A series of laboratory scale electrochemical experiments were conducted to study the behaviour of aluminium carbide in melts of similar composition as industrial bath, of which two are presented in this chapter. Open circuit voltage and steady state current-voltage measurements, cyclic voltammetry, and electrolysis were tested as possible techniques to obtain information about carbide formation and oxidation. More specifically, establishing whether aluminium carbide can be formed by an electrochemical reaction without the presence of aluminium, as well as any information about the kinetics of such a formation reaction, was the main objective of the experiments.

The two experiments treated in this chapter were performed in oxide depleted and alumina saturated melt, respectively. The oxide depleted melt introduced difficulties regarding choice of insulating materials for the reference electrode. Attempts were made to construct a stable Al/Al^{3+} reference electrode that would not introduce any foreign species to the melt. As this did not succeed, experimental techniques such as cyclic voltammetry and open circuit voltage (OCV) measurements were not performed in the oxide depleted melt. For the experiment with alumina saturated melt, alumina stands out as an obvious insulating material and the construction of a functional reference electrode is quite straightforward. For electrochemical measurements, the availability of a reference electrode greatly improves the premises for obtaining informative and credible data.

Due to the different premises for the two experiments, where only one was run with a functioning reference electrode, the results and discussion from the two experiments are treated separately. Furthermore, the different techniques are treated one by one in order to elucidate the informative value of the methods.

6.2 Theory of the electrochemical techniques

A typical electrode reaction, expressed by equation (6.1), involves a charge transfer between the electrode and a species in solution.

$$O + ne^- \leftrightarrow R \tag{6.1}$$

The reaction mechanism can be divided into a series of steps:

- Mass transport of reactant (O) to the interface.
- Electron transfer between electrode and reactant close to the electrode.
- Mass transport of product (R) away from the electrode to allow fresh reactant to the surface.

These steps proceed in sequence, and the slowest step is rate determining for the reaction. In many cases electron transfer is rapid, and the reaction rate is limited by mass transport. The effective mass transport is the sum of three transport mechanisms, convection, migration, and diffusion. Convection is mechanically induced movement and usually the fastest mass transport mechanism in a solution. Mass transport by convection is confined to the bulk solution, so the rate limiting transport step is likely to be diffusion or migration through a thin layer at the electrodes where convection does not contribute. Migration is movement of charged species due to a potential gradient. The forces leading to migration is purely electrostatic and the charge can be carried by any ionic species in the solution. If the solution contains a large excess of inert electrolyte, this carries the most of the charge, and transport of electroactive species by migration can be neglected [91]. Thus, diffusion through a thin layer at the electrode(s) can be considered as the rate determining mass transport mechanism in many electrochemical measurements. The thin layer, appropriately called the diffusion layer, typically has a thickness ranging from a few nanometers to several microns. Forced convection, i.e. stirring, is often used to reduce the thickness of the diffusion layer and consequently increasing the reaction rate.

Diffusion is movement of species due to a concentration gradient, and is explained by Fick's laws. Fick's first law describes the flux of specie, i, while Fick's second law describes the concentration change over time due to diffusion.

Fick's first law:
$$Flux = -D_i \frac{dc_i}{dx} \tag{6.2}$$

Fick's second law:
$$\frac{\partial c_i}{\partial t} = D_i \frac{\partial^2 c_i}{\partial x^2} \tag{6.3}$$

where D_i is the diffusion coefficient and x is the distance from the electrode.

Considering a reaction where diffusion of reactants, O, to the electrode surface is the limiting step, the current flow is proportional to the flux of reactants at the electrode interface.

$$i = -nFD_O \left(\frac{dc_O}{dx}\right)_{x=0} \tag{6.4}$$

6.2.1 Open circuit voltage measurements

The open circuit voltage (OCV) can be defined as the potential between two electrodes when there is no net current flow, $i = 0$. Consequently, there should not be any concentration gradients in the system. Considering reaction (6.1), the potential can be predicted by the Nernst equation:

$$E = E^0 - \frac{RT}{nF} ln \frac{a_O}{a_R} \tag{6.5}$$

where the activities a_O and a_R are products of the species' concentration and an activity coefficient, γ_i. In an ideal solution, when the activity coefficient is close to unity, the activity can be substituted with the dimensionless value of concentration.

It may be worth noting that the activity can be defined by several terms of concentration, whether it be as mass percent ($C_{i,wt\%}$), mol percent ($C_{i,mol\%}$), or mole fraction (χ_i). The activity coefficient is adapted accordingly, and must not be interchanged between different definitions of the concentration.

$$a_i = \gamma_{i,C} C_{i,wt\%} = \gamma_{i,c} c_{i,mol\%} = \gamma_{i,\chi} \chi_i \tag{6.6}$$

$$\gamma_{i,C} \neq \gamma_{i,c} \neq \gamma_{i,\chi}$$

6.2.2 Steady state current-voltage measurements

In the case of a diffusion controlled reaction, the current flow can be found from equation (6.4). Equilibrium will be established at the electrode interface, following the Nernst equation (6.5). As the cell voltage is increased, the equilibrium shifts to a decreased concentration of reactants, illustrated in Figure 6.1. When the concentration is close to zero at the electrode interface, further increase of the voltage does no longer affect the steady state concentration gradient, and the reactions diffusion limited current is reached.

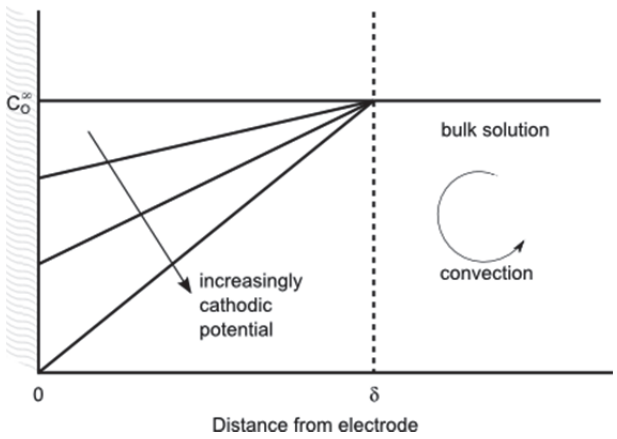

Figure 6.1: Steady state concentration profile for the reactant O in reaction (6.1) at increasingly cathodic electrode potentials. The sudden transition from pure diffusion to pure convection at δ is a simplification; in reality there must be a gradual change from a linear profile to a constant value.

If the electron transfer reaction is insufficiently fast to maintain Nernstian equilibrium, and the process can be regarded as irreversible, reaction kinetics can be obtained from steady-state current-voltage measurements. The current flow is dependent of a reaction rate constant and the activity of the electroactive species at the electrode surface.

$$\vec{\imath} = -nF\vec{k}a_O \text{ and } \overleftarrow{\imath} = nF\overleftarrow{k}a_R \tag{6.7}$$

where the rate constants, k, vary with the applied electrode potential. Eventually, this leads to the Butler-Volmer equation.

$$i = i_0\left[\exp\left(\frac{\alpha_A nF}{RT}\eta\right) - \exp\left(\frac{\alpha_C nF}{RT}\eta\right)\right] \tag{6.8}$$

where η is the overpotential, i.e. the difference between the electrode potential and the reversible potential of the reaction, and i_0 is the exchange current density, $i_0 = -\vec{\imath} = \overleftarrow{\imath}$ at $\eta = 0$.

Electrochemical electrode reactions, so-called faraday processes, are not ohmic. There is not a linear relation between voltage and current. If, however, there is an electronic contact between the electrodes, i.e. if the charge is carried by electrons in addition to ions, there will at least be some ohmic contribution to the current. In molten salts for example, dissolved metal can give rise to electronic conduction that may lead a significant amount of current between the electrodes. This current can be called ohmic current, as it follows Ohm's law:

$$U = IR \tag{6.9}$$

Consequently, ohmic current behaves linearly in a current-voltage plot.

When applying a voltage, the measured current is the sum of all contributions, faradaic and ohmic. The current-voltage plot in Figure 6.2 shows an example of how the measured current is affected by the ohmic and the faradaic contributions in a simple system with a diffusion controlled electrochemical reaction and relatively high electronic conductivity. When the reaction reaches its diffusion limiting current, further voltage increase will give a linear behaviour of the total current, parallel to the ohmic contribution.

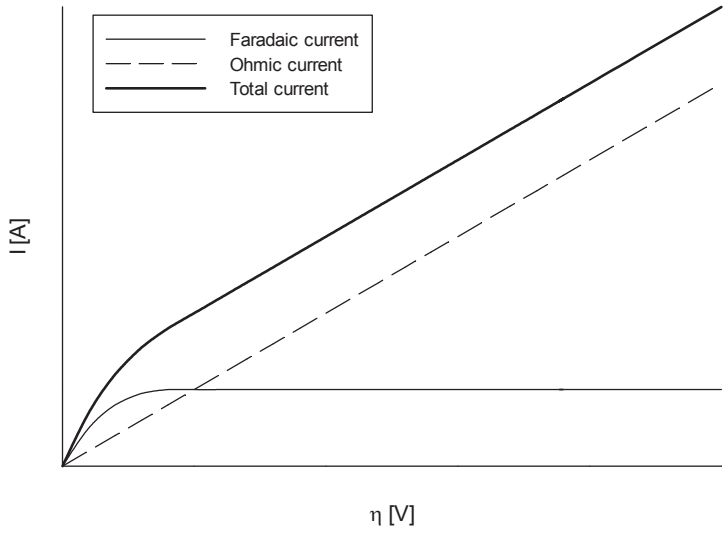

Figure 6.2: Illustration of how the faradaic and ohmic currents contribute to the total current in an electrochemical system.

6.2.3 Cyclic voltammetry

Cyclic voltammetry is a potential sweep technique widely used for qualitative and quantitative characterization of electrochemical systems. The technique is described in various text books, e.g [91]. The method requires a reference electrode and a counter electrode in addition to the working electrode. The potential is controlled between the working electrode and the reference electrode, while the current is measured between the working electrode and the counter electrode.

Figure 6.3(a) illustrates a typical potential-time profile where the voltage is swept between two values, E_2 and E_3, at a fixed rate, ν, starting at E_1. The starting potential, E_1, is normally set at a potential where there is no net current flow, e.g. the system resting. Figure 6.3(b) shows the resulting voltammogram for an electrochemical reduction of O to R, as shown in reaction (6.1). Given that the rate of electron transfer is fast compared to

the potential sweep rate, equilibrium will be established at the electrode interface, following the Nernst equation (6.5).

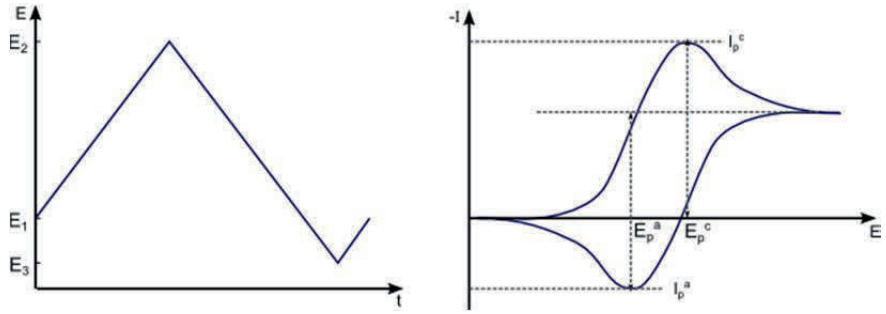

(a) (b)

Figure 6.3: (a) Typical potential – time curve for a single cyclic voltammetry sweep. The slope of the curve is given by the sweep rate, v. (b) Cyclic voltammogram for a reversible process.

As the potential is swept in cathodic direction, O is reduced to R and the concentration gradient between the electrode surface and the bulk bath increase. This gives rise to increasing current, according to equation (6.4). The maximum current, or peak current, I_p^c, is reached when the concentration gradient of O is at a maximum. This typically occurs when the concentration approaches zero and the relaxation of the gradient outweighs the concentration decrease at the electrode interface. The concentration gradient at the electrode surface decrease until a stable diffusion layer is established, as shown in Figure 6.4. Accordingly, the current decreases towards a limiting current and steady state. When the scan is reversed, the equilibrium shifts to the left and R is converted back to O. The anodic peak current, I_p^a, is obtained at the potential, E_p^a, at which the concentration of R at the electrode surface approaches zero.

The characteristics of the recorded voltammogram is dependent of a number of factors, such as the chemical reactivity of the electroactive species, the rate of electron transfer, and the potential scan rate, v, to name a few. The following tables list characteristics for three different cases, a reversible, a totally irreversible, and a quasi-reversible system. The latter can be regarded as a system that behaves as a reversible system at low sweep rates and as an irreversible system at high sweep rates. The transition from reversible to irreversible is called the quasi-reversible region, and it occurs when the rate of the electron transfer reaction is insufficient to maintain a Nernstian equilibrium at the electrode surface.

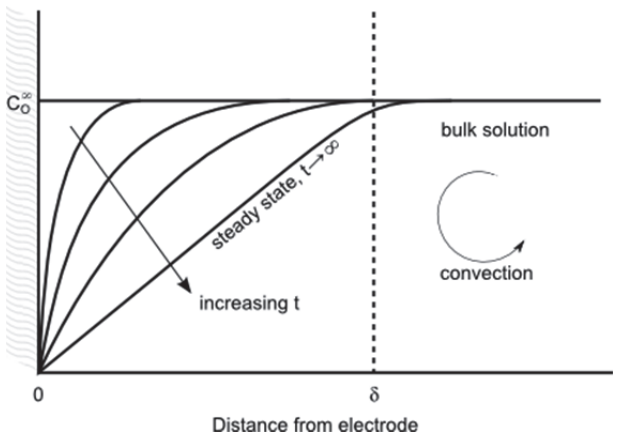

Figure 6.4: Concentration profile for the reactant O in reaction (6.1) illustrating relaxation of the concentration gradient after a sudden onset of external voltage. As a result of the relaxation, the diffusion limited current decreases until steady state is reached.

Table 6.1: Diagnostic tests for cyclic voltammograms of reversible processes, rewritten from [91].

1.	$\Delta E_p = E_p^A - E_p^C = \frac{RT\ln(10)}{nF}$	(6.10)
2.	$\left\|E_p - E_{p/2}\right\| = \frac{RT\ln(10)}{nF}$	(6.11)
3.	$\left\|I_p^A / I_p^C\right\| = 1$	(6.12)
4.	$I_p \propto \sqrt{v}$	(6.13)
5.	E_p is independent of v	
6.	$I^{-2} \propto t$ at potentials beyond E_p	

Table 6.2: Diagnostic tests for totally irreversible systems, rewritten from [91].

1.	No reverse peak	
2.	$I_p^C \propto \sqrt{v}$	(6.14)
3.	$E_p^C = K - \frac{RT\ln(10)}{2\alpha_C n_\alpha F}\log(v)$	(6.15)
4.	$\left\|E_p / E_{p/2}\right\| = \frac{1.857RT}{\alpha_C n_\alpha F}$	(6.16)

Table 6.3: Diagnostic tests for quasi-reversible systems, rewritten from [91].

1.	$\left\|I_p\right\|$ increases with, but is not proportional to $\sqrt{\boldsymbol{v}}$	(6.17)
2.	$\left\|I_p^A/I_p^C\right\| = 1$ provided $\alpha_C = \alpha_A = 0.5$	(6.18)
3.	$\Delta E_p > \frac{RT\ln(10)}{nF}$ and increases with increasing v	(6.19)
4.	E_p^C shifts negatively with increasing v	(6.20)

6.3 Experimental

6.3.1 Experimental set-up

A water cooled vertical tube furnace [92, 93] with inner diameter of 170 mm was used for the electrochemical experiments (Figure 6.5). The furnace was evacuated and flushed with argon prior to each experiment, and an argon flow of 0.3–0.5 L/min was maintained during operation. The furnace temperature was measured with a Pt-Pt10Rh thermocouple (outside the Pythagoras tube) and controlled by a PID temperature controller connected to a thyristor. Another thermocouple was used to log the temperature within the Pythagoras tube. The temperature gradients were measured with and without bath (see Appendix E).

A manually controlled DC power supply was used in experiments with oxide depleted melts, and a potentiostat was used in the experiment with alumina saturation. The equipment is listed in Table 6.4.

Table 6.4: Equipment used in electrochemical experiments.

Equipment	Description/Producer	Range
Thermocouple	Pt-Pt10Rh	0–1500°C
PID temperature controller	Eurotherm 2404	
Thyristor	Eurotherm 7100A	
Data acquisition unit	HP Agilent 3497A	
DC power supply	Hewlett-Packard 6269 B	0–40 V, 0–50 A
Potentiostat	Autolab PGSTAT 30	

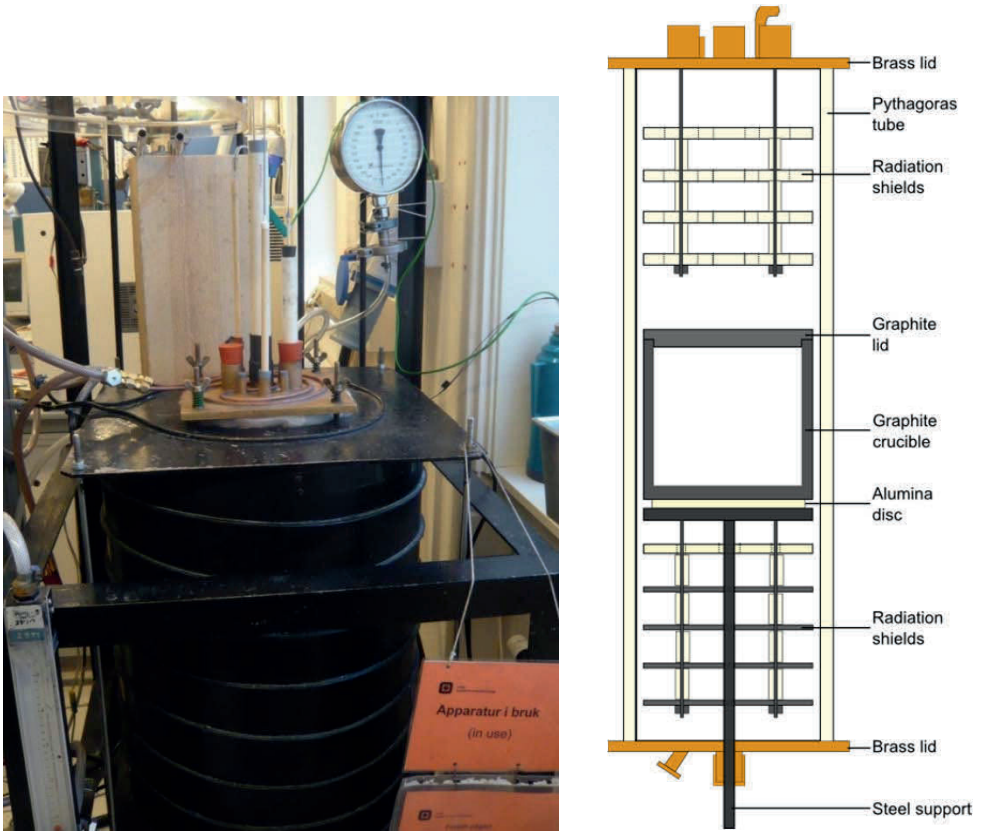

Figure 6.5: A picture of the vertical tube furnace used in the electrochemical experiments and a schematic drawing of the furnace interior, excluding electrodes, thermocouples, etc.

The graphite crucible (Svensk Specialgrafit, Ø 160 / 145 mm; h 150 / 140 mm) was placed on an alumina disc and held in place in the furnace by a steel support. A graphite lid was used to minimize loss of bath from the crucible. The holes for electrodes etc. were insulated with alumina rings to avoid stray current.

6.3.2 Electrolyte

A NaF-AlF_3-CaF_2 melt with composition similar to typical industrial bath was used as electrolyte in all electrochemical experiments. The chemicals used for the base electrolyte and additions are listed in Table 6.5, and the composition of the base electrolyte is given in Table 6.6. In molten state the depth of electrolyte in the carbon crucible was about 5.5 cm, about 6 cm with electrodes lowered to operational depth.

Table 6.5: Chemicals used in experiments.

Chemical	Supplier/Quality	Pre-treatment
Na_3AlF_6	Sigma-Aldrich, ≥97.0 %	Kept at 100°C for >24 h
AlF_3	Norzink, 93 %	Kept at 100°C for >24 h
CaF_2	Alfa Aesar, 99.5 %	Kept at 100°C for >24 h
Al_4C_3	Sigma-Aldrich, 99 %	Stored in argon atmosphere
Al_4C_3	Alfa Aesar, 99+%	Stored in argon atmosphere
Al_2O_3	Merck, 99 %	Heated to 1200°C for 5 h
Al	Vigeland Refinery, 99.99 %	

Table 6.6: Composition of base electrolyte.

Base electrolyte	Na_3AlF_6	AlF_3	CaF_2
≈ 1.9 kg	85 wt%	10 wt%	5 wt%

For the experiment with alumina saturated melt, about 13 wt% Al_2O_3 was added to the base electrolyte. Al_4C_3 was added to the melt during the experiments.

The oxygen content in the melts was established by combustion analysis of samples from the solidified melts after the experiments. The analyses were kindly performed by A. Støre at SINTEF, Trondheim, with a LECO® TC-436. The alumina depleted melt was found to contain about 0.8 wt% Al_2O_3, the low purity AlF_3 being the source of alumina. About 10 wt% Al_2O_3 was found in the alumina saturated melt.

XRF (X-ray fluorescence) analysis was performed on a selection of bath samples taken during the experiments to determine the presence of impurities, qualitatively and quantitatively. These analyses were kindly supplied by L. P. Lossius at Hydro Aluminium Technology Centre, Årdal. The results are shown in the tables below. Minor elements, as well as oxygen and carbon (which are not detectable with this analysis method), are omitted in these tables.

Table 6.7: XRF results for bath samples from the alumina depleted melt.

	Experiment duration	F [wt%]	Na [wt%]	Al [wt%]	Ca [wt%]	Si [ppm]	Mg [ppm]	Fe [ppm]
1	14.5 hours	53.8	26	14.3	2.55	847	58	93
2	67.5 hours	49.6	23.3	20.1	2.36	223	267	88

Table 6.8: XRF results for bath samples from the alumina saturated melt.

	Experiment duration	F [wt%]	Na [wt%]	Al [wt%]	Ca [wt%]	Si [ppm]	Mg [ppm]	Fe [ppm]
1	5.5 hours	48.5	24.6	16.8	2.37	855	190	52
2	31.5 hours	48.3	24.2	16.6	2.37	357	202	23
3	187 hours	47.9	22.4	17.9	2.45	335	285	55

6.3.3 Electrodes

A three electrode system, composed of working electrode, counter electrode, and reference electrode, was used in the electrochemical experiments. Details about the various electrodes are presented in the following.

Working electrodes

Graphite rods (Svensk Specialgrafit, CMG) of three different dimensions (Ø 1, 6, and 8 mm) and tungsten wire (Alfa Aesar, 99.95%, Ø 0.5 mm) were used as working electrodes in the experiments. The graphite rods were threaded on stainless steel rods insulated with alumina tubes. The 1 mm graphite electrodes were made by cutting the tip of 3 mm rods on the lathe. The tungsten electrodes were simply made by treading tungsten wire through alumina tubes.

Counter Electrode

The largest of the graphite rods (Ø 8 mm and Ø 6 mm) were also used as counter electrodes.

Reference electrode in alumina saturated melt

An Al/Al^{3+} reference electrode was used in the experiment with alumina saturated electrolyte. It consisted of an alumina tube (Ø 12 / 8 mm) with liquid aluminium in the bottom and a tungsten wire as current lead. A slit was made in the tube to attain electrical contact between the aluminium inside the tube and the electrolyte on the outside.

Reference electrode in oxide depleted melt

The reference electrode used in the alumina saturated melt could not be used in oxide depleted melt, as the alumina tube would corrode and ad oxide to the melt. Thus, a different design was composed (see Figure 6.6). A graphite vessel (Svensk Specialgrafit, FE250) with threaded transition to a stainless steel tube made up the outer shell of the electrode, so that only graphite would come in direct contact with the bulk electrolyte. A

small alumina crucible was filled with aluminium and placed in the bottom of the graphite vessel. A tungsten wire (Alfa Aesar, 99.95%, Ø 1.4 mm) insulated with an alumina tube was placed in the alumina crucible as current lead. To obtain electrolyte inside the graphite vessel, a hole was drilled in the wall about 5 cm above the bottom. When lowering the reference electrode entirely to the bottom of the graphite crucible (with about 6 cm deep bath), electrolyte would flow into the graphite vessel. The electrode was then raised so that the hole was above the bath level, hindering flow of electrolyte between bulk bath and the inside of the reference, which after a while would become oxide saturated due to dissolution of the alumina components. The theory being that the graphite vessel would provide electrical contact via electrolyte impregnation but hinder oxide flow from the reference into the bulk bath.

An analogous design with a graphite current lead was tried in preliminary experiments. Problems with poor contact between the graphite and the liquid aluminium led to the use of tungsten wire.

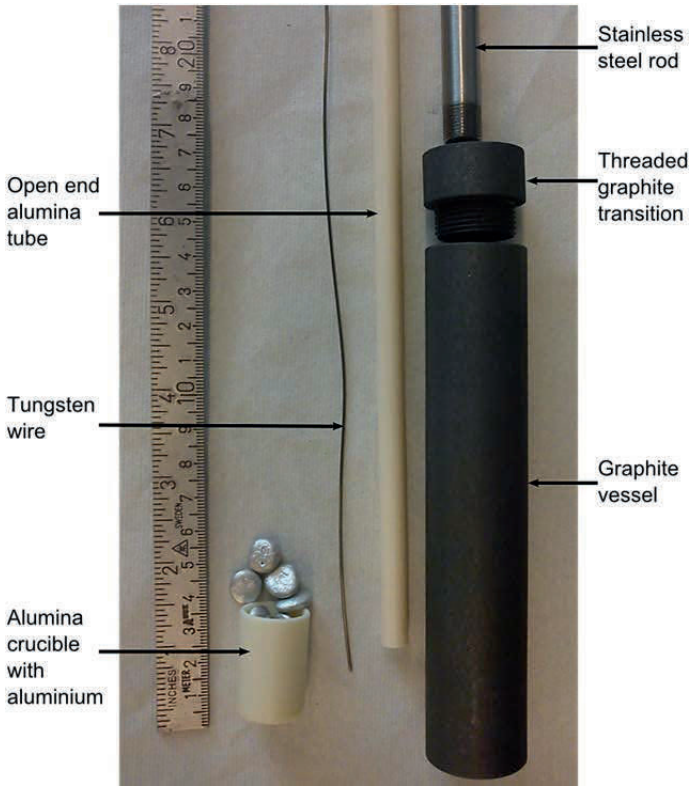

Figure 6.6: Illustrative picture of the components for the reference electrode used in the experiments with oxide depleted electrolyte.

6.3.4 Experimental procedure

The electrolyte was mixed in the graphite crucible and placed in the most temperature stable region of the furnace. Prior to heating, the furnace was evacuated with a rotary vacuum pump and flushed with argon. A stable argon flow of about 0.3 L/min was kept during the experiments. When the furnace reached the programmed temperature, the thermocouple was lowered into the melt (or right above in the experiments with oxide depleted melt). As the temperature stabilized at 1000°C, the electrodes were lowered into the melt and allowed to soak for some minutes before starting the measurements.

Steady state current-voltage plots were recorded manually by increasing the potential step-wise, letting the current stabilise for 2–5 minutes between each step. In the experiment with alumina saturated melt, slow potential sweeps (1 mV/s) were performed in addition. Graphite electrodes of the same size, Ø 6 or 8 mm, were used as working and counter electrodes for these measurements, as well as the electrolysis tests. The electrodes were taken out for inspection after each run. Wear was measured with a slide caliper/micrometer at 15 positions on the electrode (at 5 evenly distributed heights and 3 positions along the circumference), yielding an average change in diameter, ΔØ, and an estimate for the volumetric change of the electrode, ΔV. In cases where no wear was observed, the electrodes were cleaned mechanically and reused. The electrode immersion depth was 30–40 mm during the current-voltage measurements and electrolysis.

Cyclic voltammetry was performed on tungsten (Ø 0.5 mm) and graphite (Ø 1 mm) electrodes with an immersion depth of 3 mm and surface areas of approximately 0.05 and 0.1 cm^2, respectively. A Ø 8 mm graphite electrode, with immersion depth of about 40 mm, was used as counter electrode. The bath level was determined by slowly lowering a polarised electrode towards the melt. As the electrode came in contact with the melt, it created a closed circuit and a current response was observed. This approach gave less than 1 mm variance between the immersion depth reading and the observed bath line on the electrodes after removal.

Al_4C_3 was added to the melt batchwise through a feeding tube (alumina, Ø 24 / 19 mm) mounted in the centre hole of the lid. The carbide additions were weighed in a glove box with argon atmosphere and transported to the experimental furnace in a glass vessel, where it was attached to the feeding tube with a short rubber hose. This allowed the feeding tube to be sealed between and during carbide feedings, though the system was exposed to ambient atmosphere for a few seconds when the glass vessel with carbide was being attached to the feeding tube.

Bath samples were collected between every carbide addition by dipping a cold graphite rod into the bath, and rapidly removing it from the furnace with a layer of frozen bath

attached. The frozen bath was secured into a small glass container and placed in a glovebox with inert atmosphere, pending analysis.

After the experiments were shut down and the furnace had cooled down, the crucible and the frozen electrolyte were inspected.

6.4 Results and discussion

6.4.1 Experiment with oxide depleted melt

The results from the experiment with oxide depleted melt comprise steady state current-voltage plots for different Al_4C_3 concentration values, electrolysis results, and subsequent analysis of bath samples, electrodes and crucible. A brief assessment of the reference electrode is also given. In Table 6.9, a chronological overview of the measurements and carbide additions is given.

6.4.1.1 Assessment of the reference electrode

When not in use, the potential of the reference electrode was monitored against a graphite vessel with liquid aluminium inside. Figure 6.7 shows the fluctuation of this potential, illustrating the non-stable behaviour of the reference. All fluctuations cannot be directly attributed the reference electrode, though, as the graphite vessel with aluminium also constitute a dubious reference. Clear evidences of that the reference electrode had not worked as intended was shown during the subsequent autopsy. Not only had the aluminium disappeared, but the alumina crucible had also been completely dissolved (Figure 6.8). In addition, the tungsten current lead had been corroded, breaking the electronic contact at some point during the experiment.

6.4.1.2 Steady state current-voltage measurements

Steady state current-voltage plots were made manually for each carbide addition, shown in Figure 6.9. With a few exceptions it is clear that the current increases as carbide is added to the melt. The currents measured in series 3 are significantly higher than in series 4, though the measurements have been performed with the same amount of carbide. From Table 6.9 it can be seen that electrolysis has been performed in between the two current-voltage measurements. It is probable that some of the carbide has been oxidized during this electrolysis, lowering the actual Al_4C_3 concentration before the measurements for series 4. For series 7 and 8, however, this is not the case. These measurements were also performed with the same amount of carbide, but the currents are higher for series 8, after electrolysis. At this point the added carbide amounted to 1.7 wt% and saturation have probably been reached. It can thus be assumed that the concentration of Al_4C_3 is similar for the two series. There is another way the electrolysis can have led to increased

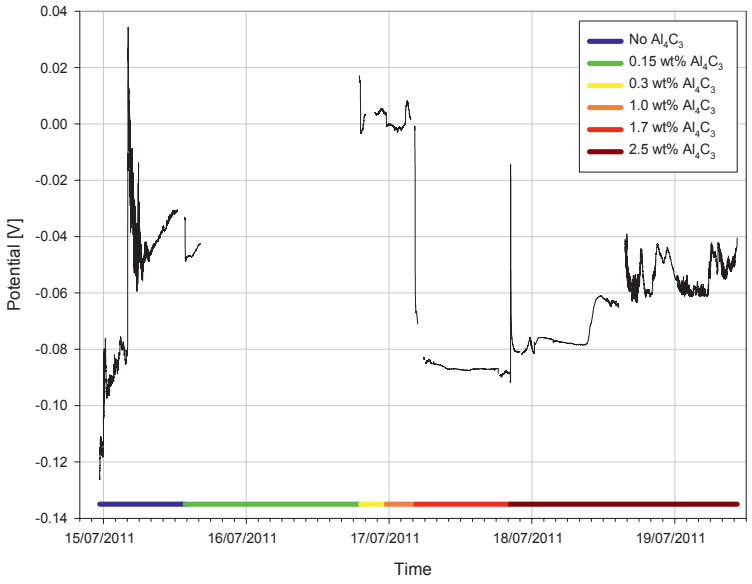

Figure 6.7: Graph showing the potential between the reference electrode and a graphite vessel containing liquid aluminium in oxide depleted melt. The coloured bar beneath shows the different Al_4C_3 concentration regimes over time. It was evident that the reference electrode did not work as intended, and the instability rendered it virtually useless for electrochemical measurements.

Figure 6.8: The bottom of the reference electrode during autopsy. A cross-sectional cut revealed that some parts were corroded away during the experiment. The alumina crucible which should have been at the bottom was gone, as was the aluminium inside it. Furthermore it was found that the tungsten current lead was corroded several cm up into the insulating alumina tube, which means that the electrical contact probably has been broken at some point during the experiment.

current densities in series 8. As electrolysis is performed, Al_4C_3 is oxidized, and carbon dust is introduced to the melt. If significant amounts of carbon dust attaches to the electrodes, the active electrode surface would increase, leading to higher currents and higher apparent current densities.

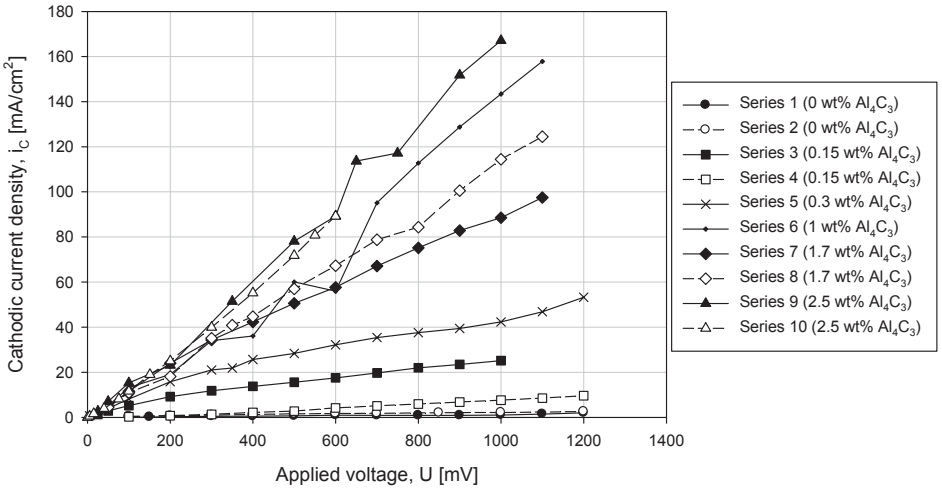

Figure 6.9: Steady state current-voltage plots for oxide depleted melt at various Al_4C_3 concentrations.

As can be seen from Figure 6.9, the current seems to increase proportionally to the applied voltage over the range investigated. The faradaic current from an electron transfer reaction would be expected to be low at low voltages and increase exponentially as the reversible potential of the reaction was reached, according to the Butler-Volmer equation (6.8). In the case of a diffusion controlled reaction, one would expect to observe a limiting current at some point, where further increase of the applied voltage gives no considerable effect on the current flow. The observed linear behaviour seems to be a result of ohmic current rather than an electrochemical reaction. Thus, an attempt to estimate the specific conductivity of the melt was made. The specific conductivity, κ, is simply expressed by the following equation.

$$\kappa = \frac{G}{R} \tag{6.21}$$

where G is the geometric factor of the electrochemical cell and R is the ohmic resistance of the electrolyte. The deduction of the geometric factor for the present cell can be found in Appendix F. The ohmic resistance was found from the slope of the current-voltage plots, $R = \Delta U/\Delta I$. The resistance through the electrodes and cables are assumed to negligible.

Table 6.9: Chronological overview of the electrochemical experiment with oxide depleted electrolyte. The values provided with the electrolysis operations are cell voltage, electrolysis time, and total charge passed. The values given with the Al_4C_3 additions are the accumulated total amount of carbide added, i.e. including previous additions.

Elapsed time [hh:mm]	Operation	Comment	Elapsed time [hh:mm]	Operation	Comment
0:00	Start	Stable temp. 1000°C	50:30	Current-voltage plot	Series 6
0:50	Current-voltage plot	Series 1	54:00	Al_4C_3 addition	34 g 1.7 wt%
3:10	Electrolysis	150 mV 9 h 83 C	55:40	Current-voltage plot	Series 7
12:10	Current-voltage plot	Series 2	57:00	Electrolysis	500 mV 11 h 27.2 kC
15:15	Al_4C_3 addition	3 g 0.15 wt%	68:10	Current-voltage plot	Series 8
17:05	Current-voltage plot	Series 3	69:50	Al_4C_3 addition	50 g 2.5 wt%
18:00	Electrolysis	1.0 V 22 h 12.2 kC	71:45	Current-voltage plot	Series 9
42:15	Current-voltage plot	Series 4	73:55	Electrolysis	700 mV 14 h 69.7 kC
44:40	Al_4C_3 addition	6 g 0.3 wt%	90:15	Current-voltage plot	Series 10
47:05	Current-voltage plot	Series 5	92:00	Electrolysis	550 mV 16 h 40.7 kC
49:00	Al_4C_3 addition	20 g 1 wt%	108:00	End	

Measured anodic and cathodic potentials were not reliable due to difficulties with the reference electrode, hence they are not included. Measured potentials for the experiment in oxide depleted electrolyte refer to the cell voltage.

The resulting conductivities were plotted against the accumulated amount of Al_4C_3 added to the melt, shown in Figure 6.10. The ohmic behaviour indicates that the conductivity can be regarded as electronic conductivity, as ionic conductance will be negligible and effects such as double layer charging can be disregarded in steady state DC measurements.

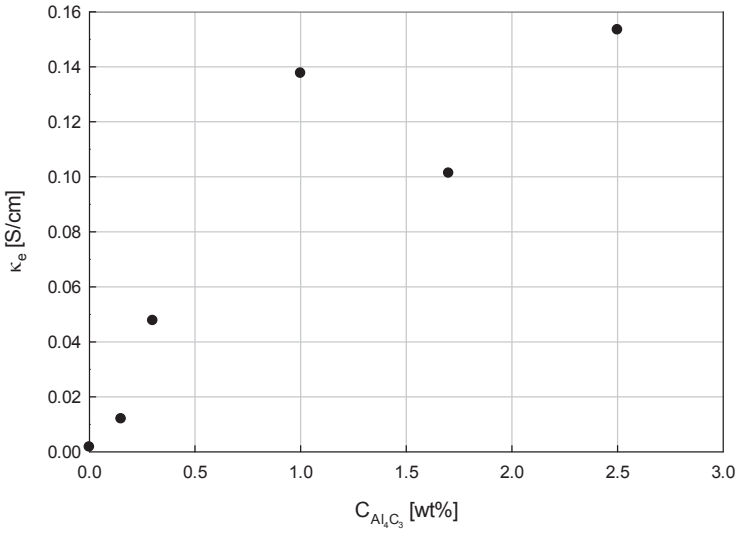

Figure 6.10: Conductivity of the oxide depleted melt at varying Al_4C_3 concentrations.

There is an increasing trend with increasing carbide concentration, and the estimated conductivities vary from about 0.002 S/cm^2 to about 0.15 S/cm^2. These values are comparable to the electronic conductivity in alumina saturated cryolite with sodium activity of 0.02 or less [94] (see Figure 6.25). The increase of the conductivity as the Al_4C_3 concentration increases in the lower scale is clear. At higher concentrations, above 1 wt%, the correlation between conductivity and Al_4C_3 concentration is less clear. Saturation is probably reached, and there might be something else contributing to the fluctuations of the current densities. Impurities introduced with the carbide additions, carbon dust formed by oxidation of carbide, and sodium intercalation/deintercalation are possible causes. Electrolysis tests, treated below, also give reason to believe that the estimated conductivities are too high, as the measured currents probably were partly associated with faradaic processes.

6.4.1.3 Electrolysis

Electrolysis was performed five times during the experiment, and the electrodes were investigated for wear and carbon deposits after each run. An overview of the electrolysis parameters is given in Table 6.10, as well as information about cathode wear and anode deposits.

It is obvious from Table 6.10 that higher concentrations of Al_4C_3 led to higher current. Even at half the cell voltage and half the electrolysis duration, the charge transferred in test 3 is more than double of test 2. The correlation between increasing current and increasing carbide concentrations, together with the deposited carbon on the anode (Figure 6.12a), indicates that electrochemical oxidation of aluminium carbide occurs at the anode.

Table 6.10: Overview of electrolysis tests in oxide depleted melt.

Electrolysis test No.	1	2	3	4	5
Duration	9 h	22 h	11 h	14 h	14 h
$\mathbf{C_{Al_4C_3}}$	0	0.15 wt%	1.7 wt%	2.5 wt%	2.5 wt%
Cell voltage	150 mV	1000 mV	500 mV	700 mV	550 mV
Charge passed	83 C	12.2 kC	27.2 kC	69.7 kC	40.7 kC
Cathode wear	-	ΔØ -0.5 mm ΔV -0.18 cm^3 CE = 99.5% 8.2 mm^3/h	-	ΔØ -1.1 mm ΔV -0.4 cm^3 CE = 38.7% 28.6 mm^3/h	ΔØ -0.2 mm ΔV -0.08 cm^3 CE = 13.3% 5.7 mm^3/h
Anode deposit (carbon dust)	-	Much	Some	Much	Dense layer *
Comments				Al found on cathode	Al found on cathode

* The thickness of the carbide layer (described later in Section 6.4.1.5) corresponded to an anodic CE of about 69%.

Assumed that cathode wear is caused by a carbide formation reaction involving 4 electrons per carbon atom, the current efficiency (CE) for this reaction was calculated on the basis of the volume change and density of the cathodes. As shown in Figure 6.11, there is a clear trend of increasing CE with increasing cell voltage from 500 mV and up. Thus there seems to be a correlation between cell voltage and the current efficiency of the wear reaction, i.e. that higher polarization of the cathode enhances the carbide formation reaction.

For electrolysis test 2, with 1 V cell voltage, the CE was found to be 99.5%. This is an unexpectedly high value, and is probably caused by inaccurate estimation of the electrode volume decrease. Likewise, the CE values for electrolysis test 4 and 5 should only be regarded as estimates.

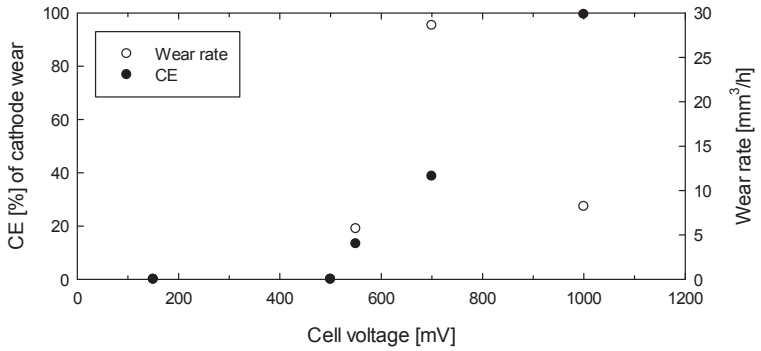

Figure 6.11: Estimated CE for cathodic dissolution of tetravalent carbon, C(-IV), as a function of the applied cell voltage.

After test 5 a dense carbon layer was found deposited on the anode, which made it possible to estimate the CE for the anodic carbon deposition, reaction (6.22). The thickness of the layer was found to correspond to a CE of about 69%. This is much higher than the CE for the cathodic carbide formation reaction, which was found to be about 13%. This reveals that at least 69% of the charge passed during this test was related to faradaic processes, of which the main cathodic reactions must have been aluminium reduction, sodium reduction and/or other reactions not contributing to cathode wear. Most of the deposited carbon thus originated from the Al_4C_3 previously added to the melt and not dissolved carbon from the cathode.

The results from the electrolysis tests, indicating that most of the current is associated with faradaic processes, are not in accordance with the ohmic behaviour observed from the steady state current-voltage plots (Figure 6.9). Even though the current-voltage plots display a linear behaviour, it seems that a significant amount of the measured current must have been related to faradaic processes.

For the electrolysis tests with cell voltage above 500 mV, cathode wear was observed. It is likely that this is due to formation and dissolution of aluminium carbide. Aluminium droplets were found on the surface of the cathode after test 4 and 5 (Figure 6.12b), proving that the cathode have been sufficiently cathodic for aluminium deposition (3.11). Some of the aluminium formed may then have reacted with the graphite cathode and produced carbide (2.1), which dissolves and gives rise to wear. Wear was not observed after electrolysis at 500 mV and less. At these low voltages, the main part of the observed currents was probably ohmic.

Anode: $$C^{4-} \rightarrow C(s) + 4e^{-}$$ (6.22)

Cathode: $$Al^{3+} + 3e^{-} \rightarrow Al(l)$$ (3.11)

Cathode: $$4Al(l) + 3C(s) \rightarrow Al_4C_3$$ (2.1)

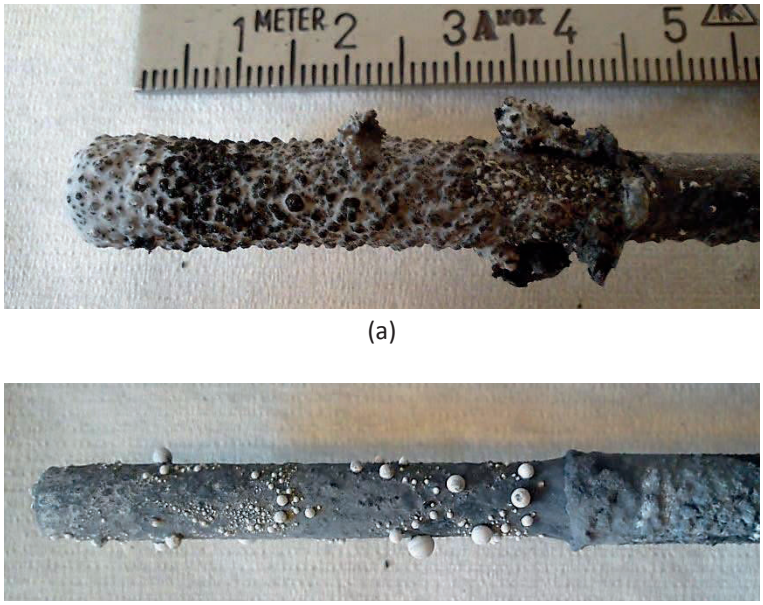

(a)

(b)

Figure 6.12: Electrodes after electrolysis at 700 mV for 14 hours, electrolysis test 4. (a) Anode with carbon deposits. (b) Visibly worn cathode with aluminium droplets attached to the surface.

Test 4 and 5 were performed with the same bath composition, and besides increased CE, increasing the cell voltage from 550 to 700 mV have led to a significantly increased wear rate. Test 2 was run with low carbide concentration at 1000 mV cell voltage, 300 mV more than test 4, but with less than a third of the wear rate, though the CE was very high. The amount of Al_4C_3 added to the melt obviously affects the wear mechanism, somehow increasing the rate of the wear. This seems peculiar, as one would normally not expect the rate of a reaction to increase by adding more of the reaction product to the electrolyte.

An explanation to why adding aluminium carbide to the melt increases the wear rate, i.e. the formation and dissolution of carbide, could be decreased anodic polarization, and hence increased cathodic polarization. For an electrochemical process to proceed there must be a reduction reaction at the cathode and an oxidation reaction at the anode. Considering a pure oxide free NaF–AlF_3–CaF_2 melt, possible anode reactions would be oxidation of dissolved Na and Al, and at sufficiently high anodic polarization, formation of perfluorocarbon gases (CF_4 and C_2F_8). The latter is known as anode effect in the aluminium

industry, and occurs when the melt is depleted of alumina. In this experiment, with fixed cell voltages, there is little risk of such an anode effect. The low solubility of metal in the bath effectively limits the current obtainable by oxidation of Na and Al. I.e. in a pure oxide free melt, very little faradaic current will flow at the cell voltages relevant in this work, 0–1.2 V. But, by introducing Al_4C_3 to the melt, deposition of carbon can occur at the anode at relatively low anodic polarization. Such a lowering of the anode potential could have been readily identified with a functioning reference electrode.

As Al_4C_3 is a reactant in the anodic reaction, increased faradaic currents with increasing carbide concentrations can be expected. This, of course, implies that the anode reaction is the rate determining step. With low concentrations of anodically electroactive species it is likely that the limiting step is found at the anode. In industrial cells, however, decomposition of alumina allows large current flow at the anodes and the wear will therefore not be inhibited by a slow anode reaction.

6.4.1.4 Inspection of crucible and solidified bath

After the experiment, when the furnace had cooled down, the crucible and the solidified bath were investigated. A simple pH indicator test [95] gave alkaline readings on the entire crucible, indicating presence of sodium. Underneath a thin layer of soot, the bulk bath had a yellow, cream coloured appearance. On the bottom a thick sludge layer of what appeared to be aluminium carbide was found together with droplets of aluminium (Figure 6.13). XRD analysis of the sludge, shown in Figure 6.14, confirmed the presence of Al_4C_3.

Figure 6.13: A picture of aluminium carbide and metal droplets at the bottom of the crucible.

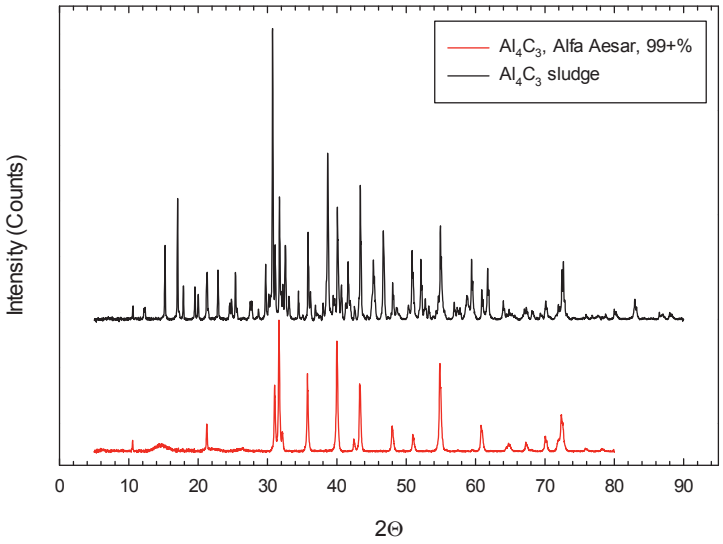

Figure 6.14: XRD profiles for pure Al_4C_3 and the aluminium carbide sludge found on the bottom of the crucible. Peaks related to Al_4C_3 are evident in both diffractograms. Bath components in the sludge give some extra peaks.

6.4.1.5 Anodically deposited carbon layer

A curious observation was made after electrolysis test 5, at 550 mV cell voltage. Carbon had deposited as a dense layer at the anode (Figure 6.15), rather than the typical particulates found after the other electrolysis tests (Figure 6.12a). The deposited layer was harder and more brittle than the electrode material (graphite).

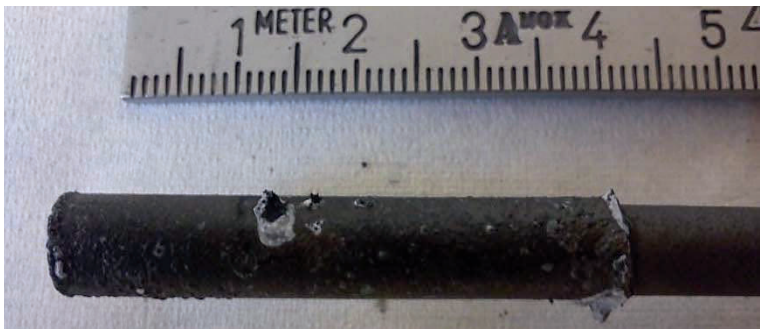

Figure 6.15: Anode after electrolysis test 5, 550 mV cell voltage for about 14 hours. Carbon has deposited as a smooth and dense layer rather than the usual particles as seen in Figure 6.12a.

The average thickness of the layer was measured to be 0.5 mm, corresponding to a volume of about 0.4 cm^3. Assuming the carbon deposition occurs according to reaction (6.22) and that the deposited layer had the same density as the graphite electrode,

2.1 g/cm^3, the CE of the anode reaction was 69%. As mentioned earlier, this is much higher than the CE of the carbon dissolution reaction estimated from the volumetric cathode wear (13%), which means most of the deposited carbon must have originated from the Al_4C_3 added to the melt prior to the electrolysis.

Cross-sectional cuts were made for microscopy investigation of the anode, and some pieces of the layer were broken off with pliers in order to run XRD analysis. The XRD diffractogram, shown in Figure 6.16, indicated amorphous carbon.

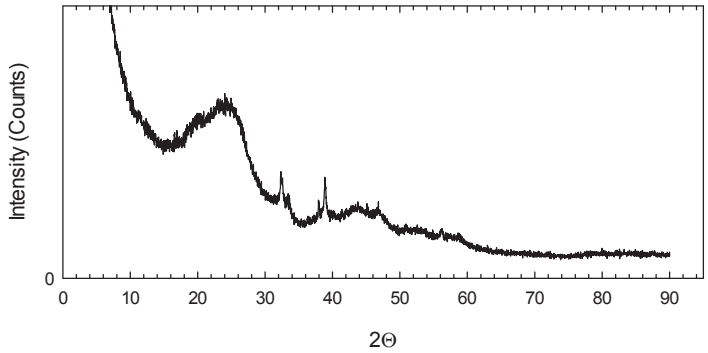

Figure 6.16: XRD profile for the anodically deposited carbon layer. With exception of two small defined peaks at 32 and 39 degrees (probably from bath inclusions in the layer), the pattern is typical for amorphous carbon [96, 97].

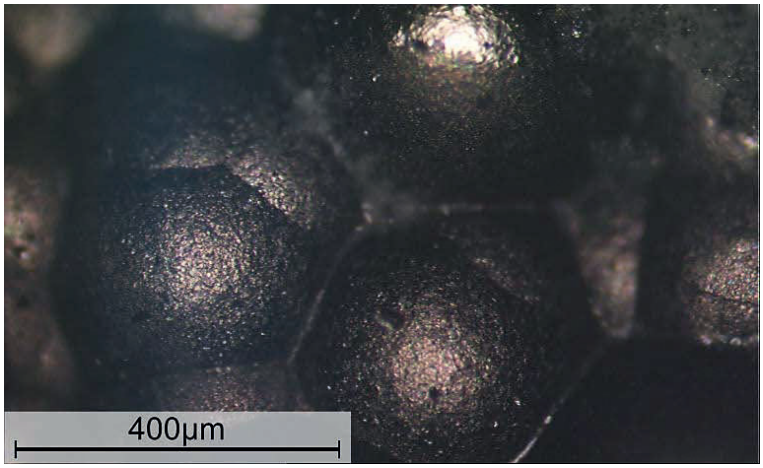

Figure 6.17: Optical micrograph of the anode surface after electrolysis test 5, at 550 mV cell voltage for about 14 hours.

The optical micrograph of the anode surface in Figure 6.17 shows that the surface is made up of a multitude of spherical shapes. Micrographs of a cross-section of the anode (Figures 6.18 and 6.19) show a clear transition between the initial electrode surface and the

deposited layer. Furthermore it seems that the layer can be divided into two zones, albeit the difference between these zones has not been investigated further. From the purple appearance in the polarized micrographs, it seems the layer is made up by amorphous carbon.

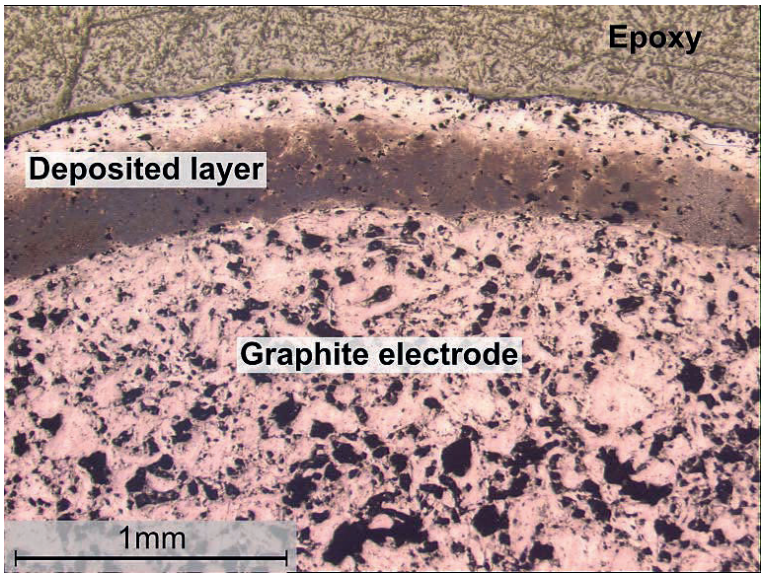

(a)

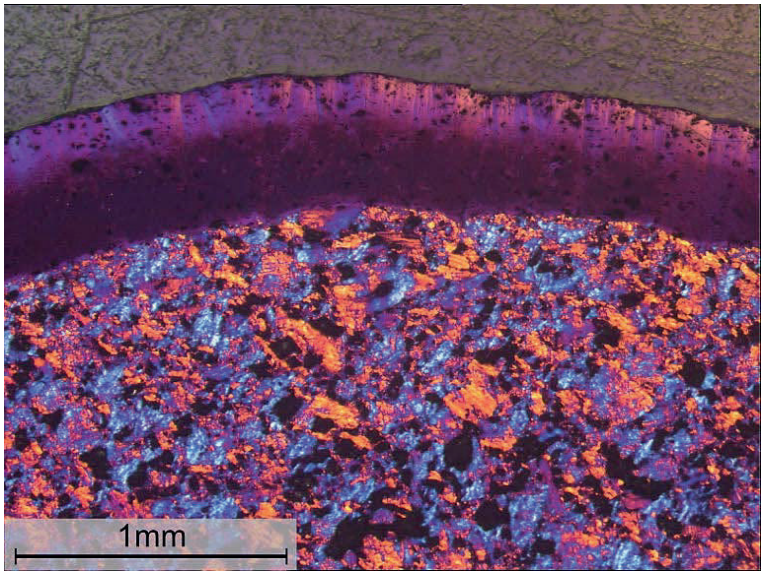

(b)

Figure 6.18: Optical micrographs of a cross-sectional area of the anode after electrolysis test 5. (a) Bright field. (b) Polarized.

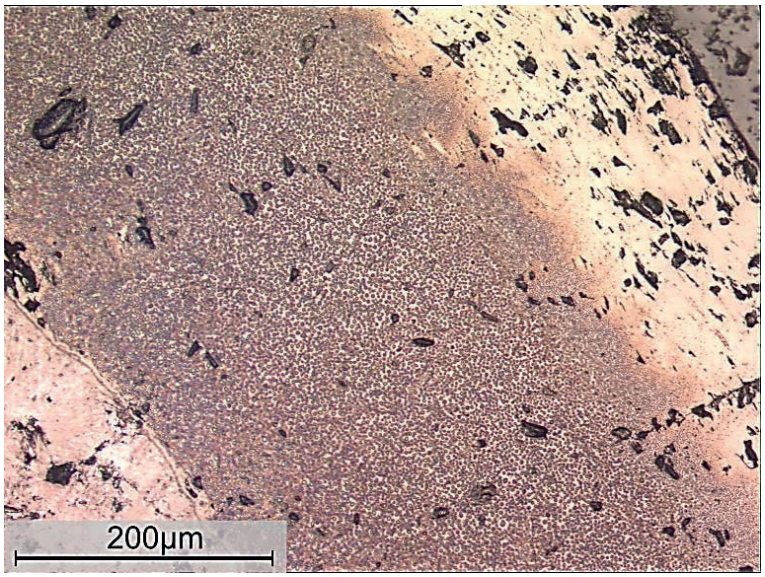

(a)

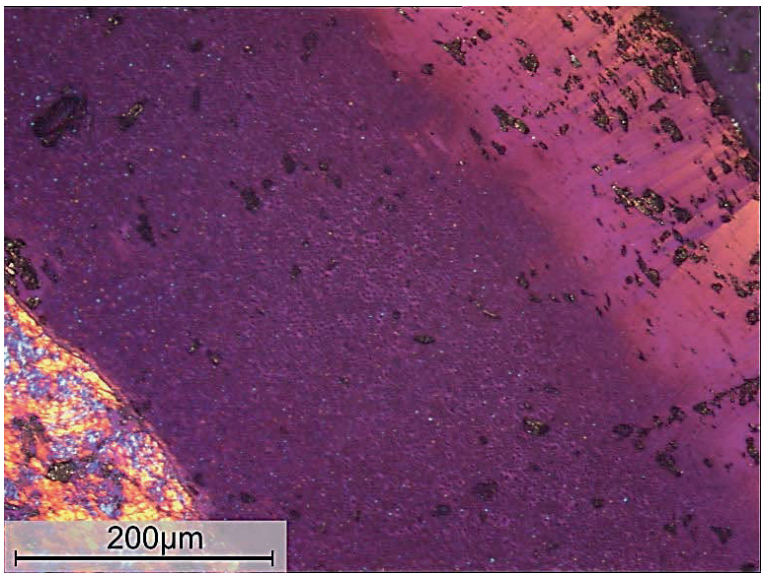

(b)

Figure 6.19: Optical micrographs of the deposited anode layer after electrolysis test 5. (a) Bright field. (b) Polarized.

6.4.2 Experiment with alumina saturated melt

The results from the experiment with oxide saturated melt comprise open circuit potential measurements, steady state current-voltage measurements, electrolysis and cyclic voltammograms for different Al_4C_3 concentration values, and also subsequent inspection of crucible and solidified bath. A chronological overview of carbide additions, current-voltage measurements and electrolysis tests are given in Table 6.11.

6.4.2.1 Open circuit voltage measurements

The open circuit voltage (OCV) between graphite and the Al reference electrode was registered at different Al_4C_3 concentrations. The measured values were expected to correspond to the reversible potential of cathodic dissolution of carbon, according to half-cell reaction (3.14). With addition of the other half-cell reaction (3.11) occurring at the reference electrode, the reversible potential of the total reaction (6.23) can be estimated from the Nernst equation (6.24).

$$3AlF_3(diss) + C(s) + 4e^- \leftrightarrow Al_3CF_8^{3-} + F^- \tag{3.14}$$

$$4Al^{3+} + 3e^- \leftrightarrow Al(l) \tag{3.11}$$

$$5AlF_3(diss) + 9NaF(l) + 3C(s) + 4Al(l) \rightarrow 3Na_3Al_3CF_8(diss) \tag{6.23}$$

$$E_{(6.23)} = E^0_{(6.23)} - \frac{RT}{12F}\ln\left(\frac{a^3_{Na_3Al_3CF_8}}{a^5_{AlF_3}a^9_{NaF}}\right) \tag{6.24}$$

Aluminium and carbon exist in standard state with unit activity, and can thus be omitted. The activities of NaF and AlF_3 were calculated based on work of Sterten et al. [98] Appendix G, and are treated as constants in the present system.

The activity of $Na_3Al_3CF_8$ is not known, but Ødegård [25] calculated the thermodynamic data for the dissolved carbide species based on the following definition of the activity:

$$a_{Na_3Al_3CF_8} = C_{Al_4C_3}[wt\%]/1wt\% \tag{6.25}$$

This gives 1 wt% dissolved Al_4C_3 as standard state for $Na_3Al_3CF_8$. He stressed that the obtained thermodynamic data should only be regarded as estimates, but argued that the values probably are of the right order and that the deviation from eq. (6.25) is small over the entire aluminium carbide concentration range.

Table 6.11: Chronological overview of the electrochemical experiment with oxide saturated electrolyte, with exception of cyclic voltammetry. The values provided with the electrolysis operations are cell voltage, electrolysis time, and total charge passed. The values given with the Al_4C_3 additions are total amount of carbide added, i.e. including previous additions.

Elapsed time [hh:mm]	Operation	Comment	Elapsed time [hh:mm]	Operation	Comment
0:00	Start	Stable temp. 1000°C	77:20	Al_4C_3	24.7 g 1.2 wt%
3:15	Current-voltage plot	Series 1	80:45	Current-voltage plot	Series 7
5:35	Al_4C_3	2.4 g 0.1 wt%	93:10	Al_4C_3	32.1 g 1.6 wt%
10:00	Current-voltage plot	Series 2	96:35	Al_4C_3	41.8 g 2.1 wt%
11:15	Al_4C_3	4.7 g 0.21 wt%	102:10	Current-voltage plot	Series 8
23:40	Current-voltage plot	Series 3	104:45	Electrolysis	25 mV * 12 h 5.2 kC
24:55	Al_4C_3	9.1 g 0.46 wt%	119:15	Electrolysis	0 V * 5 h 3.2 kC
30:20	Current-voltage plot	Series 4	126:00	Electrolysis	5 mV * 14 h 10.7 kC
32:35	Electrolysis	450 mV 10 h 1.6 kC	143:35	Electrolysis	500 mV * 20 h 27.6 kC
46:20	Al_4C_3	13.1 g 0.67 wt%	143:35	Current-voltage plot	Series 9
53:45	Current-voltage plot	Series 5	169:15	Electrolysis	50 mV * 17 h 9.1 kC
69:30	Al_4C_3	16.7 g 0.86 wt%	170:35	Electrolysis	500 mV * 24 h 18.6 kC
73:45	Current-voltage plot	Series 6	188:30	End	

* Potential between working electrode and Al/Al^{3+} reference electrode.

The potential can then be written as a function of the carbide concentration:

$$E_{(6.23)} = E_{1wt\%\ Al_4C_3} - \frac{RT \ln 10}{4F} \log C_{Al_4C_3} \tag{6.26}$$

where

$$E_{1wt\%\ Al_4C_3} = E^0_{(6.23)} + \frac{RT}{12F} \ln\left(a^5_{AlF_3}\ a^9_{NaF}\right) \tag{6.27}$$

The standard potential, $E^0_{(6.23)}$, is obviously the same as for the half-cell reaction (3.14).

$$E^0_{(6.23)} = E^0_{(3.14)} = 560 \text{ mV} \tag{6.28}$$

Figure 6.20 shows the measured potentials as a function of the logarithm of the carbide concentration. The dash line represents the potentials estimated from eq. (6.26). Evidently, there is a significant deviation between measured and estimated values.

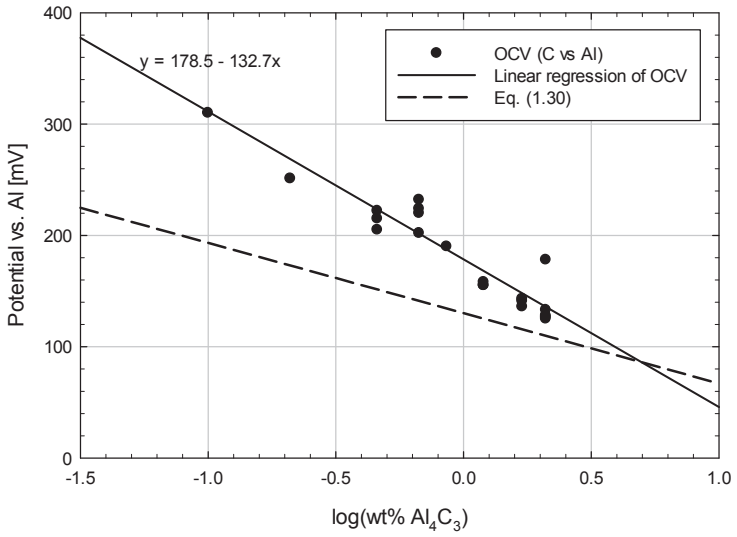

Figure 6.20: Open circuit voltage between graphite and the Al reference electrode as a function of Al_4C_3 concentration. The dash line represents the reversible potential of cathodic dissolution of carbon according to equation (6.26).

Linear regression of the measured OCV values yields the following relation between potential and carbide concentration:

$$E = 0.1785 - 0.1327 \log C_{Al_4C_3} \text{ [V]} \tag{6.29}$$

Assuming that the potential is correlated to a reaction where the activity of the electrochemically active species, a_i, is proportional to $C_{Al_4C_3}$, there will be a linear relation between the potential, E, and $\log C_{Al_4C_3}$, with a slope defined by:

$$slope = -\frac{RT\ln(10)}{nF} \tag{6.30}$$

Inserting the value of the slope from the linear regression of the OCV measurements, i.e. -0.1327, into eq. (6.30), yields n = 1.9 ≈ 2. This could imply that the measured potentials are related to a two-electron transfer reaction. Perhaps carbon is dissolved as a divalent species, C(-II), instead of the tetravalent C(-IV) in $Na_3Al_3CF_8$.

Another explanation for the discrepancy between the measured values and equation (6.26) may be that the activity coefficient for aluminium carbide is concentration dependent, i.e. that the definition in eq. (6.25) is erroneous. In that case the activity of the dissolved carbide must be redefined:

$$a_{Na_3Al_3CF_8} = \gamma_{Al_4C_3,wt\%}\, C_{Al_4C_3}[wt\%]/1wt\% \tag{6.31}$$

From equation (6.24), the activity coefficient can then be written as a function of the potential and the carbide concentration.

$$\log \gamma_{Al_4C_3,wt\%} = \frac{\left(E_{a_{C(-IV)}=1} - E_{(6.23)}\right)4F}{RT\ln 10} - \log C_{Al_4C_3} \tag{6.32}$$

where $E_{a_{C(-IV)}=1}$ = $E_{1wt\%\,Al_4C_3}$ from eq. (6.27).

Inserting E from eq. (6.29) as $E_{(6.23)}$ gives:

$$\log \gamma_{Al_4C_3,wt\%} = \frac{\left(E_{a_{C(-IV)}=1} - 0.1785\right)4F}{RT\ln 10} + \left(\frac{0.5308F}{RT\ln 10} - 1\right)\log C_{Al_4C_3} \tag{6.33}$$

or

$$\log \gamma_{Al_4C_3,wt\%} = -0.7671 + 1.1015 \log C_{Al_4C_3} \tag{6.34}$$

$$\gamma_{Al_4C_3,wt\%} = 0.1710\; C_{Al_4C_3}^{1.1015} \tag{6.35}$$

With this definition of $\gamma_{Al_4C_3,wt\%}$, the model fits the regression line in Figure 6.20 perfectly. Such a strong concentration dependence at the relatively low carbide concentrations used is not usual, however.

A third, and more likely explanation of the deviation between measured and estimated values, is inaccuracy of the measured potential and carbide concentration. The carbide concentration is estimated from the amount of Al_4C_3 added to the bath. As the experiment progressed, carbide will have been formed and oxidised, and there may have been

significant variance between the estimated and the actual carbide concentrations, especially at low concentrations. The measured potential may have been affected by Na intercalation in the graphite. If the graphite electrode has not been soaked in the melt for a sufficient amount of time, equilibrium will not have been established between Na in the melt and intercalated Na.

6.4.2.2 Steady state current-voltage measurements

Similar to the experiment with oxide depleted electrolyte, steady state current-voltage plots were made for each carbide addition. A potentiostat was used to sweep the cell voltage at a low sweep rate, v = 1 mV/s, over a set range while logging the current output. Manual measurements were also performed to ensure that the sweep rate was low enough to obtain steady state currents.

The resulting plot, Figure 6.21, show that the current increases with increasing amounts of carbide added. The increase seems slow at the lower carbide values, but becomes more pronounced at higher concentrations. Compared to the oxide depleted melt (Figure 6.9), the currents seem to be somewhat lower in the alumina saturated melt. It is well known that additions of alumina reduces the ionic conductivity in cryolitic melts [99-102], but to the author's knowledge, the effect on the electronic conductivity has not been established. Based on the reduced currents in the alumina saturated melt, it seems reasonable to assume that alumina also reduces the electronic conductivity.

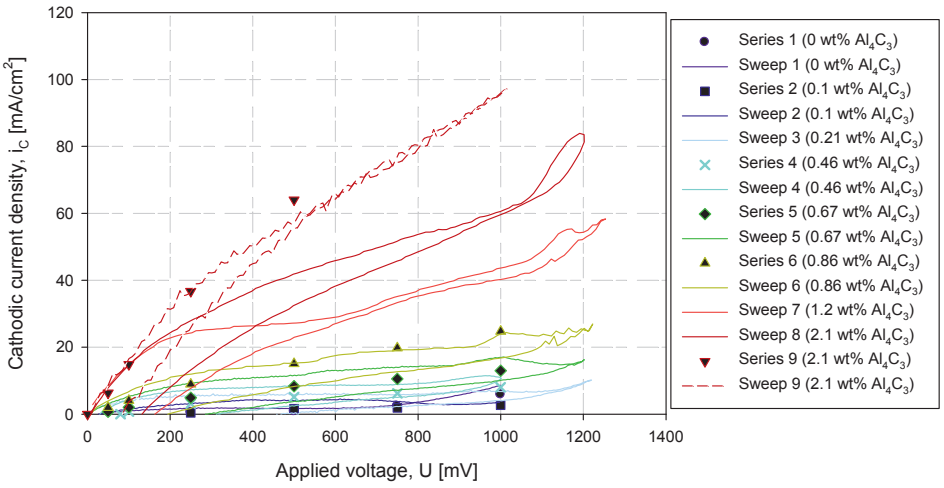

Figure 6.21: Steady state current voltage plots for alumina saturated melt at various Al_4C_3 concentrations. Manual measurements marked with symbols and slow potential sweeps (v = 1 mV/s) marked with coloured lines.

The plots in Figure 6.21, at least those at low Al_4C_3 concentrations, seem to be fairly linear at cell potentials less than 1 V. Similarly to the experiment with oxide depleted melt, a significant amount of the measured current seems to be ohmic. The sweeps performed at higher Al_4C_3 concentrations (sweep 7, 8 and 9) do show signs of a faradaic contribution from a diffusion controlled reaction. An initial steep current increase seems to be succeeded by a relatively linear behaviour between 400 and 1000 mV. In the steep region, the main portion of the current is probably faradaic, i.e. related to an electrochemical reaction. In the linear region, this reaction may have reached its diffusion limiting current, and the current increase is thus defined by the ohmic current. Above 1000 mV, another steep current increase indicates the occurrence of another electrochemical reaction (formation of CO/CO_2 at the anode).

Faradaic contribution

Sweep 8 is replotted in Figure 6.22. By subtracting the ohmic contribution, defined by the linear region, a limiting current of about 20 mA/cm^2 becomes apparent. Assuming that the rate determining reaction is formation or oxidation of aluminium carbide, the diffusion coefficient, $D_{Al_4C_3}$, can be estimated from the following equation.

$$i_{lim} = -4FD_{Al_4C_3}\frac{c_{bulk}}{\delta} \tag{6.36}$$

where c_{bulk} is the bulk concentration of Al_4C_3 in mol/cm^3, and δ is the thickness of the diffusion layer. Sweep 8 was performed with 2.1 wt% Al_4C_3, which correlates to about 3×10^{-4} mol/cm^3 (assuming ρ_{bath} = 2.05 g/cm^3). The diffusion layer thickness is assumed to be about 0.08 cm [89]. This yields $D_{Al_4C_3}$ = 1.4×10^{-5} cm^2/s.

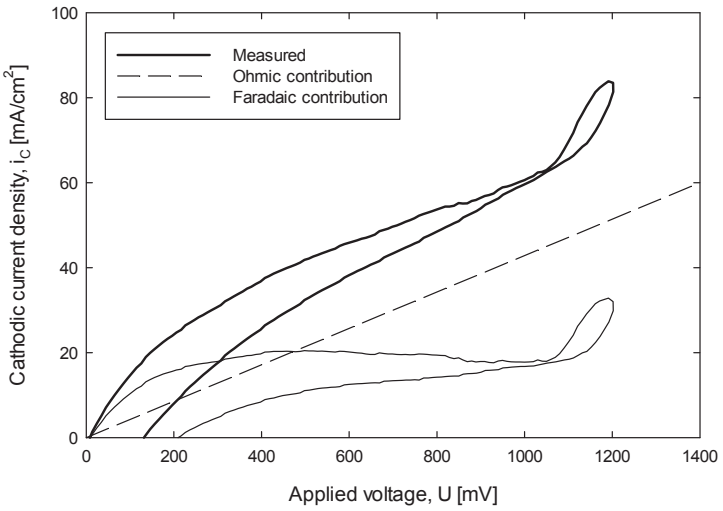

Figure 6.22: Sweep 8 from the steady state current-voltage measurements with alumina saturated melt, replotted from Figure 6.21.

Similar treatment of the other sweeps yielded varying diffusion coefficients, ranging from 6.9×10^{-6} cm^2/s to 3.5×10^{-5} cm^2/s.

Electronic conductivity

As for the oxide depleted melt, the ohmic resistance of the electrolyte was found from the slope of a linear section in the current-voltage plots. The specific conductivity was estimated and plotted against the carbide concentration, shown in Figure 6.23.

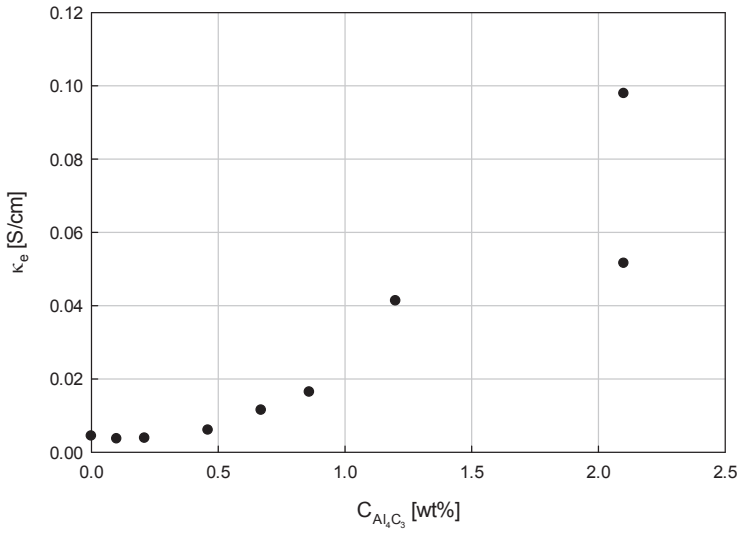

Figure 6.23: Conductivity of the alumina saturated melt at varying Al_4C_3 concentrations.

It is clear that that the electronic conductivity has increased with aluminium carbide additions. Electronic conductivity in cryolite melts is usually correlated to dissolved metal, more specifically sodium. The sodium activity at the electrode is dependent on the electrode potential according to the following equilibrium.

$$3NaF(l) + Al(l) \leftrightarrow 3Na(diss/C) + AlF_3(diss) \tag{6.37}$$

Previously the measured OCV was related to aluminium carbide. Assuming equilibrium between sodium and carbide in the melt, the OCV can also be used to estimate the sodium activity. As the reference is Al, i.e. a_{Al} = 1, the Nernst equation for reaction (6.37) yields:

$$a_{Na} = \frac{a_{NaF}}{\sqrt[3]{a_{AlF_3}}} \exp\left(\frac{(E^0_{(6.37)} - E_{\mathrm{OCV}})F}{RT}\right) \tag{6.38}$$

Estimates for the NaF and AlF_3 activities can be found in Appendix G, the standard potential $E_{(6.37)}$ is -439 mV (Table 3.3), and the correlation between the OCV and the Al_4C_3 concentration was given by reaction (6.29). Accordingly, the corresponding sodium activity can be calculated (Table 6.12).

Table 6.12: Corresponding values of Al_4C_3 concentration, OCV and sodium activity for the oxide saturated melt.

$C_{Al_4C_3}$ [wt%]	0	0.1	0.21	0.46	0.67	0.86	1.2	2.1
E_{OCV} [mV]	597	311	268	223	201	187	168	136
a_{Na}	0.0001	0.0015	0.0023	0.0034	0.0042	0.0048	0.0057	0.0076

In Figure 6.24 the conductivity is plotted against sodium activity. In the same graph is plotted the electronic conductivity as a function of sodium activity in $Na_3AlF_6 - Al_2O_3$ melt at 1000°C, as reported by Haarberg et al. [94]. It can be seen that the conductivity values from this work is somewhat lower than that of Haarberg et al. [94] at the low sodium activities, but at the highest activities there seems to be good agreement. It should be stressed that the range of the sodium activity investigated in this work is very small and does not provide a substantial basis for a thorough discussion about the relation between electronic conduction and the activity of sodium and aluminium carbide. The results, however, clearly indicate that the observed increase of current, seen in Figure 6.21, can be correlated to an increased activity of sodium as a consequence of aluminium carbide additions.

The short sodium activity range becomes more obvious when it is compared with the entire data set of Haarberg et al. [94], as seen in Figure 6.25.

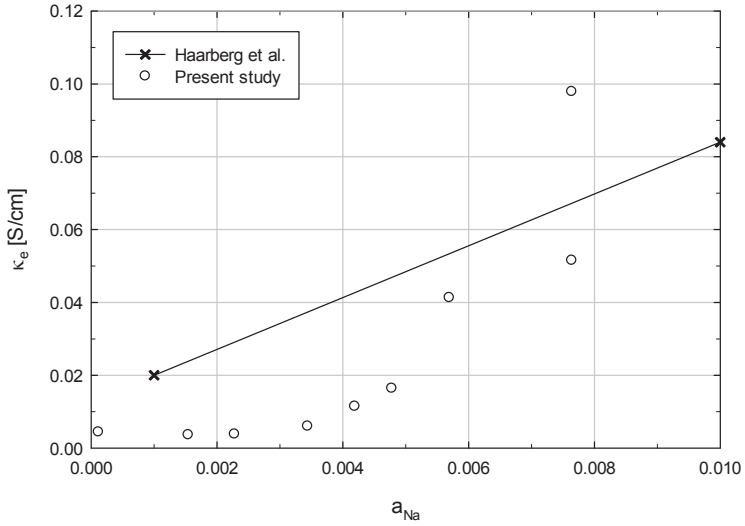

Figure 6.24: Electronic conductivity in the alumina saturated melt as a function of sodium activity, as a consequence of Al_4C_3 additions. The solid line represents electronic conductivity as a function of Na activity in Na_3AlF_6 – Al_2O_3(sat) at 1000°C as reported by Haarberg et al. [94].

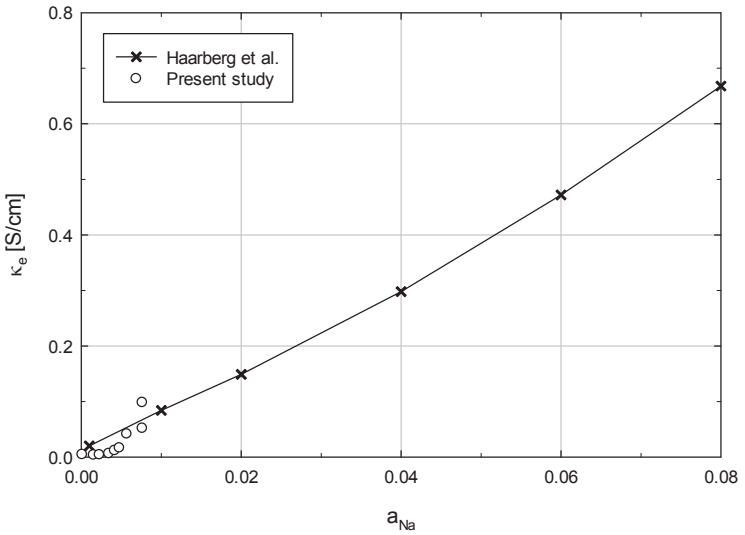

Figure 6.25: The same plot as in Figure 6.24, but the scales have been augmented to fit the entire data set from Haarberg et al. [94].

6.4.2.3 Electrolysis

Seven electrolysis tests were performed during the experiment. Two were run at constant cell voltage, the rest with a constant potential between the working electrode and the Al/Al^{3+} reference electrode. Table 6.13 gives an overview of the electrolysis parameters and observations of cathode wear and carbon deposition.

The first test, run at 450 mV cell voltage, did not result in any visible wear of the cathode and only small amounts of carbon deposits on the anode. During the electrolysis the cathode potential was more than 95 mV anodic of the Al reference electrode. Test 6 was run at constant cathodic potential of 50 mV, and similarly did not show any signs of cathode wear, though there was a considerable amount of carbon deposited on the anode. Cathode wear did occur in tests 2, 3, and 4, which were run between 0 and 25 mV anodic of the reference. In test 5 the working electrode was kept constant at 500 mV of the reference, which means the counter electrode worked as the cathode. The cathode potential was initially anodic to the reference electrode but drifted to -150 mV at the end of the electrolysis, with an average potential of 45 mV cathodic of aluminium. The reference electrode broke at the end of the experiment, and the last electrolysis test was performed with 500 mV cell voltage. The cathode potential during this test is thus unknown, but it has probably been well cathodic of the Al deposition potential. The cell potential during the preceding electrolysis test, where the cathode potential was kept at 50 mV, was about 200 mV.

Wear starts to occur at a potential between 25 and 50 mV anodic of the Al reference, which means the overpotential needed for carbide formation is about 100 mV. As aluminium is not likely to be deposited at these potentials, the wear mechanism is probably electrochemical formation of carbide, e.g. cathodic dissolution of carbon as proposed by Gudbrandsen, Sterten and Ødegård [33]:

$$C(s) + 3AlF_3(diss) + 4Na^+ + 4e^- \rightarrow Na_3Al_3CF_8(l) + NaF(l) \qquad (2.4)$$

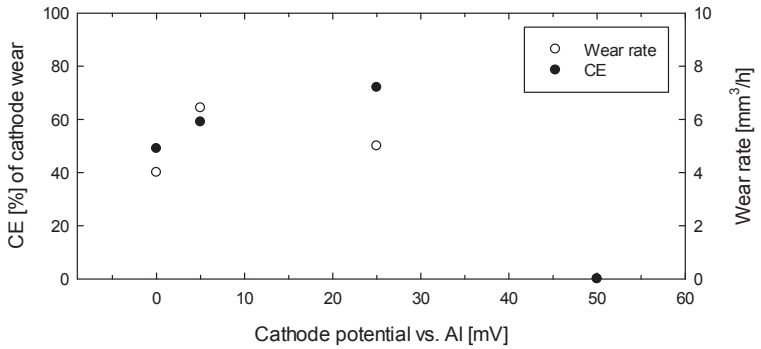

Figure 6.26: Current efficiency and wear rate plotted against cathodic potential for electrolysis tests in alumina saturated cryolitic melt at 1000°C.

Table 6.13: Overview of electrolysis tests in oxide saturated melt.

Electrolysis test No.	1	2	3	4	5	6	7
Duration	10 h	12 h	5 h	14 h	20 h	17 h	24 h
$C_{Al_4C_3}$	0.47 wt%	2.1 wt%	2.1 wt%	2.1 wt%	2.1 wt%	2.1 wt%	2.1 wt%
Cell voltage	450 mV						500 mV
Potential vs ref.		25 mV	0 V	5 mV	500 mV	50 mV	
Charge passed	1.6 kC	5.2 kC	3.2 kC	10.7 kC	27.6 kC	9.1 kC	18.6 kC
Cathode wear	-	ΔØ -0.3 mm ΔV -0.06 cm^3 CE = 72% wr = 5 mm^3/h	ΔØ -0.1 mm ΔV -0.02 cm^3 CE = 49% wr = 4 mm^3/h	ΔØ -0.3 mm ΔV -0.09 cm^3 CE = 59% wr = 6.4 mm^3/h	ΔØ -1.0 mm ΔV -0.26 cm^3 CE = 63% wr = 13 mm^3/h	-	ΔØ -1.4 mm ΔV -0.2 cm^3 CE = 74% wr = 8.3 mm^3/h
Anode deposits	Little	Some	Some	Some	Some	Much	Some
Comments					Anodic working electrode		No reference electrode

From Figure 6.26, it seems the CE is highest at potentials close to this initial potential of wear occurrence, and decrease at increasingly cathodic potentials. This is not unexpected, as higher cell voltages will give an increase of current related to other reactions and electronic conductivity. It was, however, unexpected that the wear rate in the test performed at a cathodic potential of 0 V (test 3) was lower than for the tests with 5 and 25 mV cathode potential. Test 3 was run for only 5 hours and the change in the electrode radius was small, which means there may have been significant measurement errors in this case. It may therefore be reasonable to omit the quantitative results of test 3. The results from test 2 and 4 indicate that the CE decrease and the wear rate increase with increasingly cathodic potentials beyond 50 mV anodic of Al deposition.

As mentioned earlier, the cathode potential in test 5 drifted in cathodic direction, and was cathodic of the Al deposition potential for most of the electrolysis duration. The wear rate in this test was more than double of the rates estimated for cathode potentials anodic of Al. The CE of the wear during this electrolysis run was found to be about 63%. According to the trend seen from the three preceding tests it should have been lower. It is highly likely that aluminium has formed on the cathode, which would then have reacted with the graphite. The wear mechanism may thus have changed from solely direct dissolution of carbon to also include aluminium deposition with subsequent carbide formation.

6.4.2.4 Cyclic voltammetry

Figure 6.27 shows a voltammogram for a graphite electrode in alumina saturated melt, obtained by starting the sweep from 0.5 V in cathodic direction at a sweep rate of 0.2 V/s. As aluminium was used as reference, aluminium deposition was expected at about 0 V, which corresponds well with the cathodic region A. The reverse peak, A*, is attributed to stripping of the cathodically deposited aluminium. In region X, there is a steadily increasing cathodic current. This is most likely due to intercalation of sodium. Correspondingly, sodium deintercalation gives rise to anodic current in region X*. Peak B is similar to the peak shown in Figure 2.17 (also labelled B) from one of the voltammograms of Raj and Skyllas-Kazacos [37]. They explained the broadness of the peak by stripping of partly soluble Al and/or as Al-Na alloy of varying activity, and possibly simultaneous oxidation of aluminium carbide and aluminium.

By reversing the potential sweep at a less cathodic potential, 0 V, and lowering the sweep rate, the voltammogram shown in Figure 6.28 was obtained. As little or no liquid aluminium is formed on the electrode, the aluminium stripping peak, A*, is not present on this voltammogram. A new peak, D, can be observed at about 450 mV. In the previous voltammogram (Figure 6.27), this peak is difficult to see, as it is “hidden” under the dominating peak B and current related to sodium deintercalation. Peak B may be correlated to oxidation of dissolved aluminium and sodium or aluminium carbide, while peak D may be correlated to reoxidation of the species reduced at peak C. Peak C was not

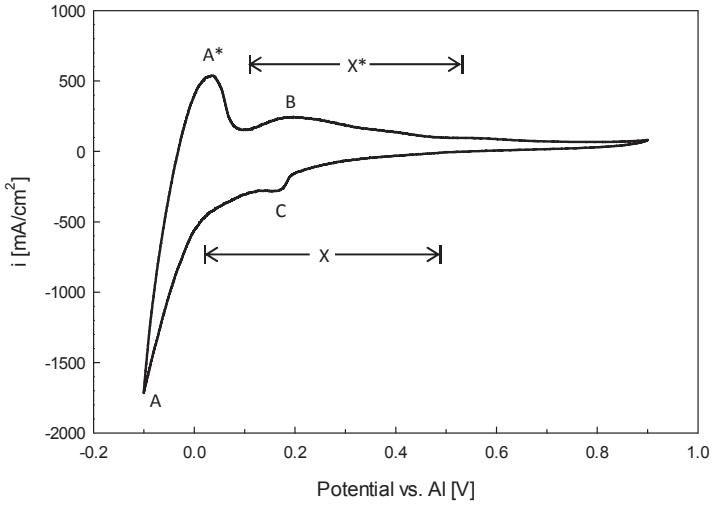

Figure 6.27: Cyclic voltammogram for graphite electrode (Ø 1 mm) in Al_2O_3 saturated cryolite melt with 10 wt% excess AlF_3 and 5 wt% CaF_2 at 1000°C. Sweep rate = 0.2 V/s, starting potential = 0.5 V, cathodic sweep direction.

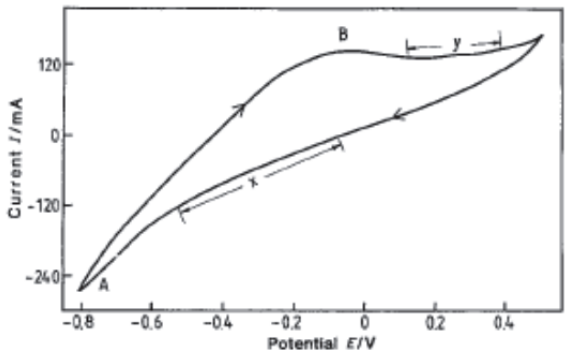

Figure 2.17: Cyclic voltammogram for graphite electrode against a tungsten reference electrode in Al_2O_3-saturated cryolite melt with 5 wt% excess AlF_3, sweep rate 0.1 V/s at 990°C [37].

observed by Raj and Skyllas-Kazacos [37] when using a graphite working electrode. Two peaks related to reduction of dissolved titanium and boron species were observed anodic to aluminium deposition, however, when using a TiB_2/C composite electrode (Figure 2.18). Peak C in this work is probably also related to impurities in the melt.

The voltammogram in Figure 6.29 is recorded on tungsten with a sweep rate of 50 mV/s. Peak A is somewhat distorted due to limiting current settings on the potentiostat, but it can clearly be related to aluminium deposition. Accordingly, peak A* is stripping of aluminium from the electrode surface. Peak B may be related to oxidation of a tungsten alloy. In a similar voltammogram (Figure 6.30), Sum and Skyllas-Kazacos [103] attributed a

peak similar to peak C to formation of W-Al alloy. The broad anodic peak (or series of peaks) denoted D (A' in Figure 6.30) was assumed to result from stripping of a number of W-Al alloys.

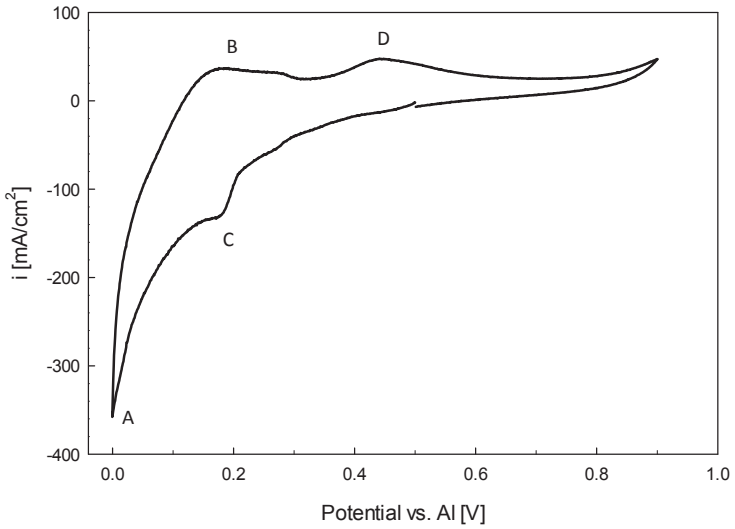

Figure 6.28: Cyclic voltammogram for graphite electrode (Ø 1 mm) in Al_2O_3 saturated cryolite melt with 10 wt% excess AlF_3 and 5 wt% CaF_2 at 1000°C. Sweep rate = 50 mV/s, starting potential = 0.5 V, cathodic sweep direction.

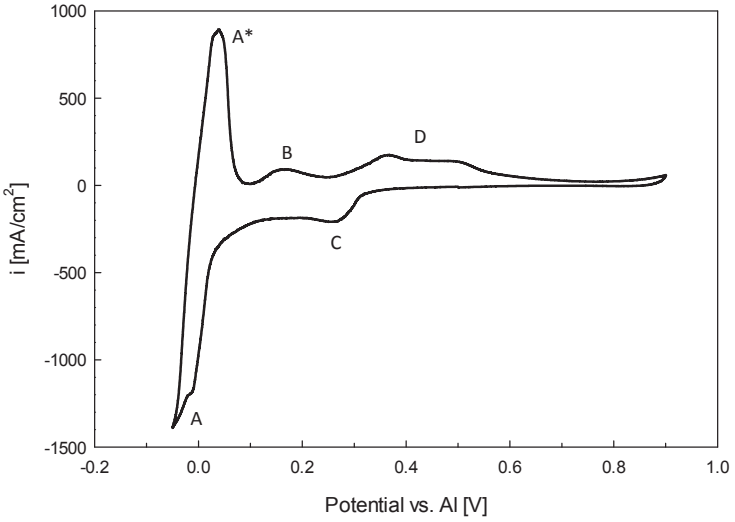

Figure 6.29: Cyclic voltammogram for tungsten electrode in Al_2O_3 saturated cryolite melt with 10 wt% excess AlF_3 and 5 wt% CaF_2 at 1000°C. Sweep rate = 50 mV/s, starting potential = 0.5 V, cathodic sweep direction.

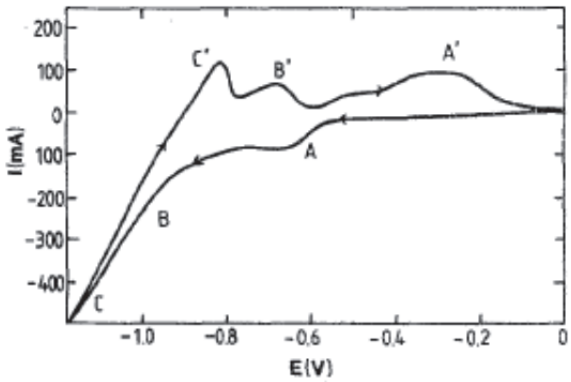

Figure 6.30: Cyclic voltammogram for tungsten electrode against a similar tungsten quasi-reference electrode in cryolitic melt with CR = 4.3 and 4 wt% Al_2O_3 at 1029°C and a sweep rate of 50 mV/s [103].

Cyclic voltammograms of aluminium deposition on tungsten in cryolite based melts produced by e.g. Duruz and Landolt [104] (Figure 6.31) and Brynjulfsen [38] Figure 2.19 did not show any signs of cathodic peak currents prior to aluminium deposition. Based on their findings it is likely that the peak currents, C and D, are related to impurities in the melt rather than W-Al alloys.

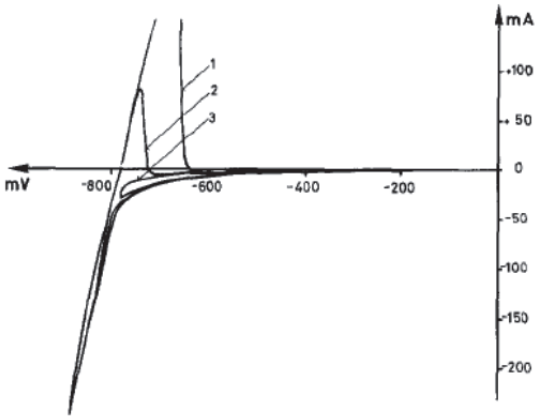

Figure 6.31: Voltammograms with tungsten electrode against a Ni/Ni^{2+} reference electrode in cryolite (CR = 3) at a sweep rate of 10 mV/s [104].

XRF analysis was performed on three bath samples taken during the experiment. The results, given in Table 6.8, show that Si stands out as the most abundant impurity. The concentration of Si early in the experiment was above 850 ppm, about 30 hours into the experiment the concentration had dropped to about 360 ppm. Figure 6.32 shows

voltammograms recorded about 2, 10, and 22 hours after start-up, at Al_4C_3 concentrations of 0, 0.1, and 0.2 wt%, respectively. It is evident that peak C and D have decreased during the experiment, which correlates well with the decrease of Si in the bath.

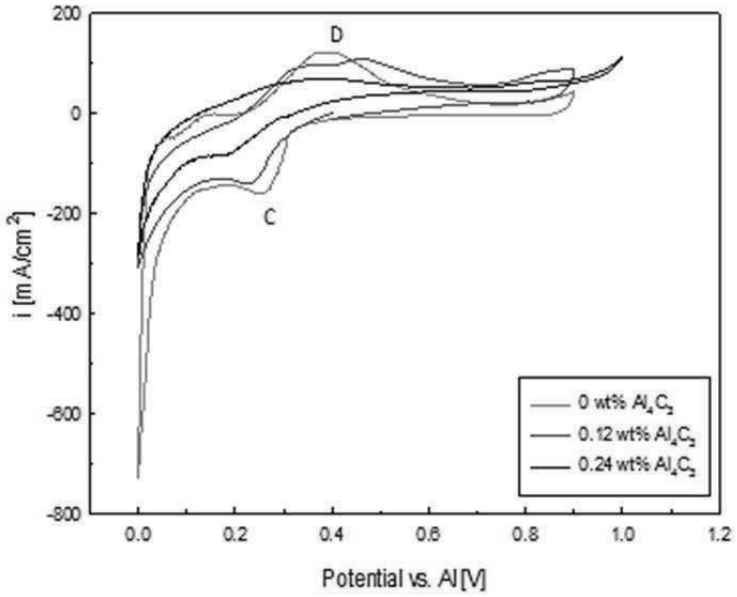

Figure 6.32: Cyclic voltammograms for tungsten electrode in Al_2O_3 saturated cryolite melt with 10 wt% excess AlF_3 and 5 wt% CaF_2 and varying Al_4C_3 concentrations at 1000°C. Sweep rate = 0.2 V/s.

Peak C and D observed in voltammograms on both graphite and tungsten is thus attributed to impurities in the melt, probably reduction and oxidation of Si species. A more comprehensive discussion on this matter can be found in Appendix H.

Upon additions of aluminium carbide the voltammograms became difficult to interpret. The shape of the voltammograms was not consistent and the effect of carbide additions could not be established. Except for the disappearance of peak C and D, the only consistent change in the voltammograms with increasing Al_4C_3 concentrations, was a general increase in the anodic current, illustrated by a few selected voltammograms shown in Figures 6.33 and 6.34.

The possibility of ohmic current being the cause of the increased anodic currents in the voltammograms was investigated. Previously, the electronic conductivity in the melt was estimated on the background of steady state current–voltage measurements. As the conductivity, κ_e, is inversely proportional to the electrolyte resistance, it should be directly

proportional to the slope of the voltammograms, assuming that the slope is caused by ohmic current. A modification of equation (6.21) gives:

$$\frac{\Delta i}{\Delta U} = \frac{\kappa}{G^*} \tag{6.39}$$

where G^* is the geometric cell factor, G, divided by the surface area of the working electrode.

The slope of the voltammograms, illustrated by grey dash lines in Figure 6.34, were plotted against the conductivity, κ_e. As can be seen from Figure 6.35, there seems to be a linear correlation, indicating that the increasing anodic currents in the voltammograms can be related to increased electronic conductivity of the melt.

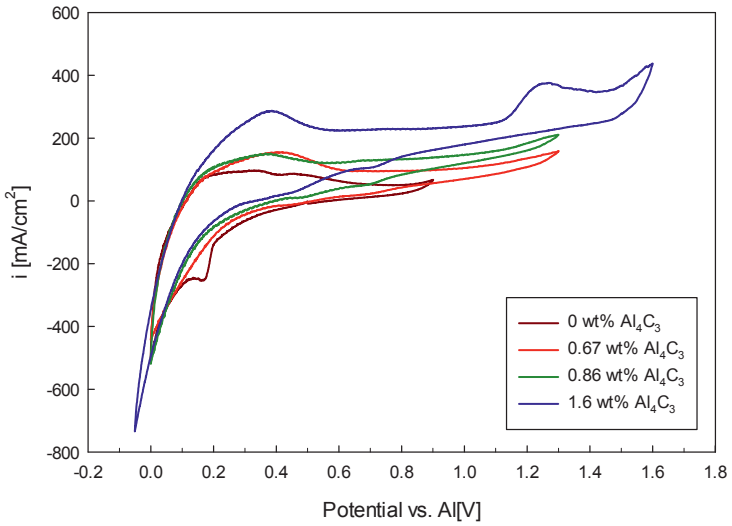

Figure 6.33: Cyclic voltammograms for graphite electrode in Al_2O_3 saturated cryolite melt with 10 wt% excess AlF_3 and 5 wt% CaF_2 and varying Al_4C_3 concentrations at 1000°C. Sweep rate = 0.2 V/s.

The results did not give any substantial basis for further investigation of the behaviour of aluminium carbide in cryolitic melts. The difficulties finding a clear "electrochemical fingerprint" of aluminium carbide could be attributed to a slow and/or a complicated reaction mechanism. The formation reaction may be a chemical reaction between aluminium and carbon, and would consequently not be identifiable by voltammetry. If electrochemical formation of carbide occurs, it does so close to the aluminium deposition potential. Thus, if the reaction is slow, distinguishing it from the aluminium deposition peak and the sodium intercalation will be difficult.

Likewise, for the anodic carbide oxidation, if the reaction is slow, the resulting current peaks may have been too low and broad to be distinguished in the conducted experiment.

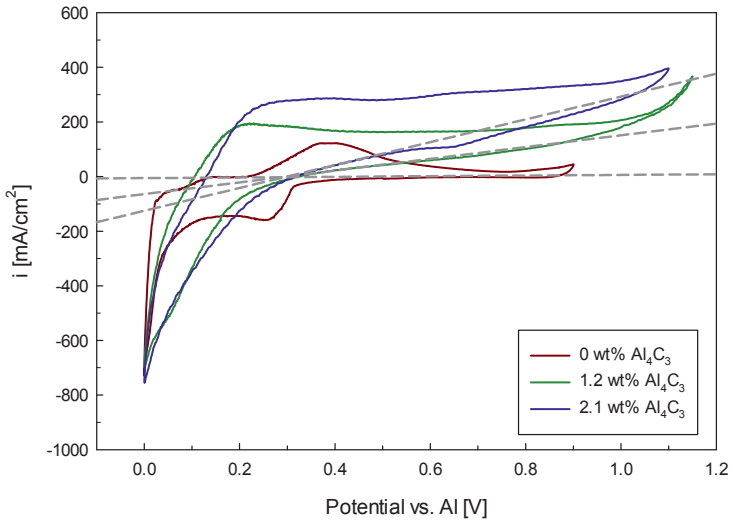

Figure 6.34: Cyclic voltammograms for tungsten electrode in Al_2O_3 saturated cryolite melt with 10 wt% excess AlF_3 and 5 wt% CaF_2 and varying Al_4C_3 concentrations at 1000°C. Sweep rate = 0.2 V/s. Grey dash lines illustrate the slope of the voltammograms close to the starting potential where i = 0.

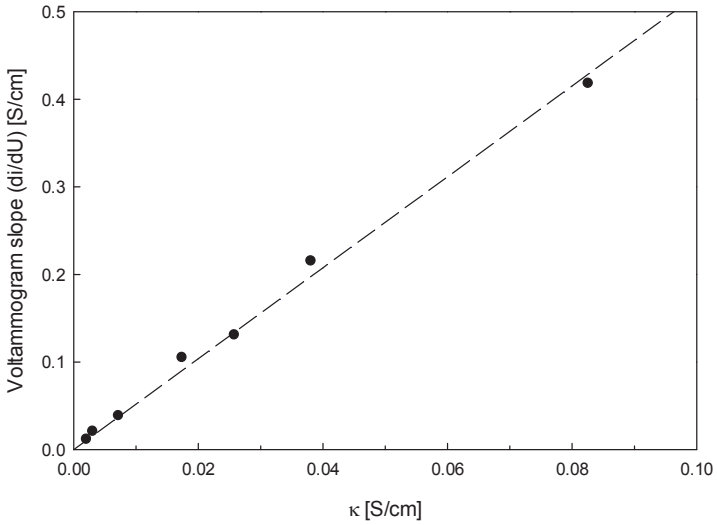

Figure 6.35: The slope of voltammograms recorded on tungsten at sweep rate 0.2 V/s plotted against previously estimated conductivity, κ_e.

6.4.2.5 Inspection of crucible and solidified bath

After the experiment, when the furnace had cooled down, the crucible and the solidified bath were investigated. As with the experiment with oxide depleted melt, a simple pH indicator test indicated presence of sodium in the crucible walls. Also after this experiment, a layer of soot lay on top of the solidified bath. The bulk bath had a grey, granulated appearance. On the bottom, a dense white layer was observed, which had probably been alumina sludge. On top of this layer, some undissolved aluminium carbide was observed.

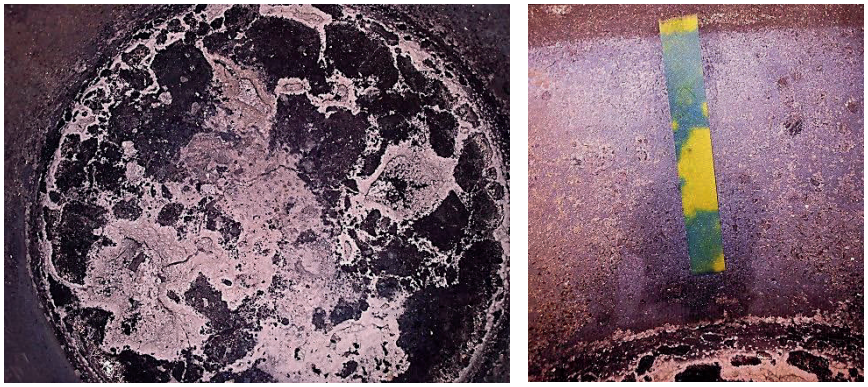

(a) (b)

Figure 6.36: Photographs showing (a) soot on the top of the solidified bath and (b) a strip of universal indicator paper turning blue, indicating alkalinity and thus presence of sodium in the crucible wall.

6.5 Summary

Electrolysis experiments showed that cathode wear requires cathode potentials less than 50 mV anodic of the reversible aluminium deposition potential. Wear was observed after electrolysis with a cathode potential of 25 mV, and the current efficiency of the wear mechanism decreased as the cathodic potential was reduced towards, and increased when it surpassed the aluminium deposition potential, indicating a shift in the mechanism. At potentials anodic of Al, cathodic dissolution of carbon can be regarded as the wear mechanism. The wear rate did increase with decreasing cathode potential, but it is likely that the rate of formation of dissolved Al and Na increased more, yielding lower current efficiency for the wear reaction. As Al(l) started to deposit at the cathode, formation of Al_4C_3 by chemical reaction between Al(l) and C(s) probably became a significant wear mechanism, giving a rise in both wear rate and current efficiency.

At the anode, electrochemical oxidation of dissolved carbide leading to carbon deposits has been proven.

Open circuit voltage (OCV) measurements did not fit the estimated model for carbide formation or cathodic dissolution of carbon. Three possible reasons for the discrepancy have been listed:

- Carbon may dissolve as a divalent C(-II) specie in the cryolitic melt, rather than the tetravalent C(-IV) found in Al_4C_3.
- The activity of dissolved aluminium carbide is not directly proportional to the concentration, but defined by a concentration dependent activity coefficient:

$$\gamma_{Al_4C_3,wt\%} = 0.1710\ C_{Al_4C_3}^{1.1015}$$

- The estimated carbide concentrations in this work are incorrect, especially at low values. Furthermore, intercalated sodium and sodium in the bath may not have been at equilibrium at all times, giving inaccurate potential measurements.

From steady state current-voltage sweeps, the diffusion coefficient of aluminium carbide, $D_{Al_4C_3}$, in alumina saturated cryolitic melt of CR=2 and 5 wt% CaF_2 at 1000°C, was estimated to be in the order of 10^{-5} cm^2/s. Extraction of precise data related to the faradaic processes was complicated by a significant ohmic contribution to the measured currents.

The electronic conductivity in the melt, both oxide depleted and alumina saturated, was found to increase with increasing aluminium carbide concentrations, which is believed to be correlated with increased concentrations of dissolved sodium metal. The correlation between aluminium carbide and sodium is given by the following equilibrium.

$$4AlF_3 + 12Na + 3C \leftrightarrow Al_4C_3 + 12NaF \tag{3.5}$$

Identifying carbide related reactions by cyclic voltammetry was proven to be difficult. No evidence of aluminium carbide formation, or oxidation, could be established. It is believed the reaction rates are slow, and that potential current peaks are effectively “hidden” by currents related to aluminium formation, sodium intercalation and deintercalation, impurities in the melt, and electronic conduction.

The currents measured in the alumina saturated melt seemed to be somewhat lower than corresponding measurements in oxide depleted melt. An explanation to this may be that alumina reduces the electronic conductivity in cryolite melts.

Chapter 7

Summarising discussion

In the present chapter the main observations made in this work, and also the literature review, are recapitulated. An overview of the effect of various parameters with regard to cathode wear is given and possible wear mechanisms are discussed. The author's point of view on the mechanisms behind the non-uniform wear resulting in a WW wear profile in modern aluminium reduction cells is also presented, as well as industrial implications based on these wear mechanisms.

7.1 Observations from the present work

The following observations have been made in the present work:

- Cathode wear has resulted in a "WW wear profile" of the cathode surface in the aluminium reduction cells investigated in this work. The outermost periphery of the cathode blocks is probably protected by a frozen bath ledge, and the area with highest wear is found just inside this ledge. The lowest wear is found in the middle of the cell, especially areas close to the point feeders, and also at the suction end of the cells. At the tapping end a local high wear area is observed where the tapping pipe is positioned, commonly referred to as a tap-hole.
- Estimates based on laser scans of two cathodes from Hydro Sunndal reveal that the cathode wear may account for an aluminium production loss corresponding to a CE loss of about 0.5%.
- An aluminium carbide layer up to more than 200 µm thick is found on the cathode surface, and it is likely that it is formed and exists during operation. Whether the layer is continuous or only occurs spot-wise is not established, but due to low conductivity it cannot be thick, dense and continuous. Aluminium carbide is also found in open porosity close to the cathode surface.

- The cathode wear seems to be non-preferential, i.e. aggregate particles and binder is worn at the same rate. Detachment of aggregate particles probably occurs due to formation of aluminium carbide in pores surrounding the particles.
- Findings of bath on the surface of cathode samples indicate presence of bath between the cathode and the metal pad.
- NaF was found as a separate phase in addition to Na_3AlF_6 in the cathode porosity, indicating CR>3 in penetrating bath and in the bath film between the carbon cathode and the metal pad.
- No significant differences are observed by microscopy between high wear and low wear areas of the cathode surface, nor is there observed any significant differences between samples from different cathodes. There does not seem to be any correlation between the thickness or appearance of the carbide layer and location in the cell.
- Indications of electrochemical formation/dissolution of carbide have been found. This occurs at potentials 25–50 mV anodic of aluminium deposition.
- Electrochemical oxidation of aluminium carbide and carbon deposition occurs at the anode, regardless whether aluminium carbide is formed chemically or electrochemically at the cathode.
- The diffusion coefficient of aluminium carbide in the alumina saturated melt was found to be in the order of 10^{-5} cm^2/s.
- The electronic conductivity in cryolitic melts was found to increase with Al_4C_3 additions, probably caused by the equilibrium between carbide and dissolved sodium metal (3.5).

7.2 Parameter effects on cathode wear

In the following, various parameters relevant for the aluminium electrolysis are discussed in regard to cathode wear.

7.2.1 Material properties

The properties of the carbon material are obviously an important factor when dealing with cathode wear. Anthracitic carbon have been found to be highly resistant against abrasion and mechanical wear [17, 19], but the low structural order gives rise to a higher reactivity to sodium and other alkalis in the smelt, leading to expansion, crack formation and severe deterioration of its mechanical strength [41, 43, 44, 46]. Graphite and graphitized carbons have the lowest abrasion resistance [17, 19], but are superior in respect to low sodium

expansion [41, 43, 44, 46], as well as higher electrical and thermal conductivity. Furthermore, for graphitized carbon, it has been found that a small grain size has a positive effect on the abrasion resistance [19]. The Semi-graphitic carbon seems to be an "all-rounder", ending up in the middle between the two extremities (graphite/graphitized carbon and anthracitic carbon) in almost all respects.

There does not seem to be any significant dependency between neither type of carbon material nor bulk density and the gravimetric rate of chemical wear [18, 27]. In terms of volumetric wear, however, a high density and low porosity is preferable.

Electrolysis tests for investigation of electrochemical wear have shown a slower and more uniform wear of graphite cathodes than of anthracitic ones, and that the amount of carbide formed increases with the disorder of the carbon [31]. This advocates preferential wear of the cathode, contrary to the indications of non-preferential wear seen in the present study. Rafiei et al. [31] observed irregular wear and degradation of the anthracitic carbon cathodes, and it is the current author's belief that this is more likely due to sodium intercalation and formation/propagation of cracks than preferential electrochemical wear. With more cracks in the anthracitic carbon than in the graphitic carbon, there will also be a larger area accessible for carbide formation, and thus higher wear rates can be expected. Large amounts of cracks and porosity will also lead to particle detachment and irregular wear, as illustrated in Figure 5.27 in Section 5.4.6.

The current density distribution on the carbon cathode is often broached as the main reason for the uneven cathode wear. In this regard the electrical conductivity of the cathode material, or more specifically, the difference between the conductivity of the cathode block and the current collector bar, is of an essence. Amorphous carbon blocks with low conductivity will yield a lower gradient in the current distribution along the cathode block, while a highly conductive graphitized block will experience high current densities at the periphery which rapidly decrease towards the mid-section. A schematic illustration is provided in Figure 7.1.

7.2.2 Bath composition

The cryolite ratio has a great impact on the aluminium carbide solubility in the bath [25]; CR = 1.8 gives the highest solubility and laboratory wear tests have confirmed that the cathode wear is at a maximum at this cryolite ratio [32]. Sodium penetration is also affected by the cryolite ratio, as a high cryolite ratio will lead to higher sodium concentration at the cathode interface and a larger driving force for the sodium to penetrate into the cathode [41, 42].

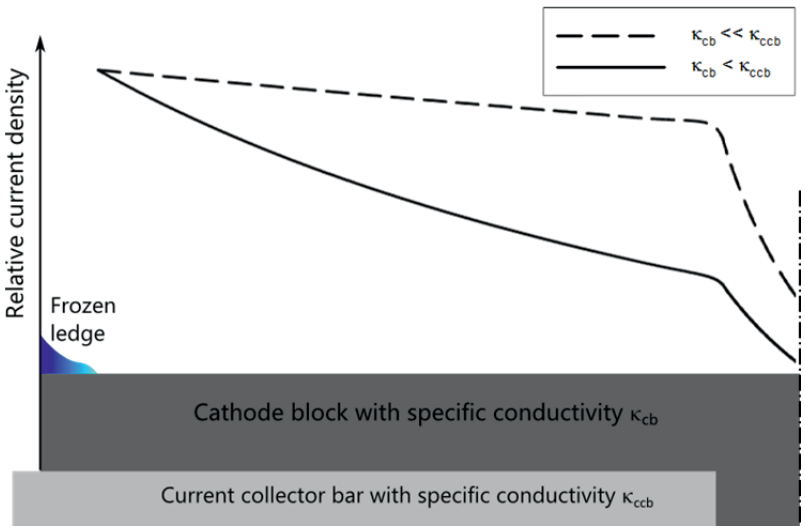

Figure 7.1: Schematic illustration of how the current density distribution may look like at the surface of an amorphous carbon block with low electrical conductivity ($\kappa_{cb} \ll \kappa_{ccb}$) and a graphitized cathode block with high electrical conductivity ($\kappa_{cb} < \kappa_{ccb}$).

Increasing concentrations of alumina results in reduced solubility of aluminium carbide in cryolitic melts [25], and it has been found that the amount of carbide formed decreases with increasing Al_2O_3 concentrations up to 4 wt% [21]. Above 4 wt% Al_2O_3 the carbide formation does not seem to be affected by further increase of the alumina content [21].

Presence of dissolved Al_4C_3 in the melt leads to higher wear rates at low current densities in electrochemical wear tests, but has the opposite effect at current densities above 0.4 A/cm^2. Liao and Øye [29] proposed three possible causes for the increased wear rate at low current densities: destabilization of alumina colloids that may constitute a protective layer on the carbon cathode, improved wetting between the melt and the cathode, and that aluminium deposition from aluminium carbide requires a lower cell voltage than deposition from alumina.

CaF_2 additions give a decrease in the aluminium carbide solubility [25], but any noticeable effect on the wear rate has not been established. LiF increases the electrical conductivity in the melt, and can give less sodium expansion due to reduced sodium activity. Reduced sodium activity can also be obtained by substituting with KF, but intercalation of the larger potassium atoms causes a much more detrimental expansion than sodium.

7.2.3 Bath, alumina and sludge at the cathode

The bath film at the cathode surface (which was reported in the microscopy investigations, Section 5.4.5) plays an important role in the cathode wear by dissolving

aluminium carbide. A high bath exchange between the bulk bath and the bath film will yield rapid carbide transport and high wear.

Bath is introduced to the cathode surface by Marangoni flow between the frozen side ledge and the metal pad, and also during alumina feeding, anode change and other operations involving breakage of the bath crust. Another, less obvious, mechanism for bath transport to the cathode surface is the crystallization of bath components at the metal-bath interface and subsequent gravitational transport through the metal pad. Indications of a solid material at the metal-bath interface has been observed in industrial cells [105], and there have been several reports of a solid cryolite deposit at this interface in laboratory cells [89, 106]. The theory behind this phenomenon is based on the concentration gradients induced by the electrochemical deposition of aluminium, as previously illustrated in Figure 5.15. The composition of the bath is changed at the interface and the liquidus temperature changes accordingly. With sufficiently high current density, the solidus temperature of the bath at the metal-bath interface may become higher than the operational temperature, triggering crystallisation of cryolite. A theoretical investigation by Solheim [107] showed that this crystallisation is likely to occur in industrial cells at normal operation. Thin cryolite films or flakes are probably broken up by waves in the metal surface and sink to the bottom of the cell.

Large amounts of undissolved alumina, i.e. abrasive particles, will naturally enhance abrasive wear on a cathode in motion relative to the alumina particles [17]. It has, however, been found, in laboratory experiments, that the wear rate drops with increasing amounts of excess alumina [18, 28]. An alumina-rich fluoride protective coating has been proposed as an explanation to this [28]. It is believed that stagnant layers of viscous alumina-fluoride sludge protects the cathode surface in the mid-section of industrial cells.

7.2.4 Temperature

Increased temperature leads to increased solubility of metals and carbide in the cryolitic melt [25], and have been shown to give higher chemical carbon wear in systems with cryolitic melt and aluminium present [27]. Low temperatures, however, may result in problems with increased sodium swelling in the carbon material [44, 45]. In industrial cells, the most dramatic effect of temperature is related to the freeze lining of the pot, which is crucial for protection of the cell lining materials and the cell lifetime.

7.2.5 Polarisation

The electrochemical experiments revealed that increased cathodic polarisation gives higher cathode wear rates. Wetting and bath penetration in carbon increases with increasingly negative polarisation [40, 42]. Obviously, higher cathodic polarisation leads to increased sodium activity and sodium intercalation in the carbon. If cathode wear by

formation of aluminium carbide occur according to reaction (3.5), increased sodium activity will give increased wear. Similarly, an electrochemical wear mechanism according to reaction (3.12) will also give increasing wear rates at increasingly cathodic potentials (until the reaction's limiting current is reached). If the wear mechanism is dependent on the presence of aluminium metal, i.e. a chemical reaction between aluminium and carbon (2.1), wear will not be affected by polarisation per se, but rather by the coverage and wetting of aluminium.

$$4AlF_3(diss) + 12Na(C) + C(s) \rightarrow Al_4C_3(s) + 12NaF(l) \quad (3.5)$$

$$4Al^{3+} + 3C(s) + 12e^- \rightarrow Al_4C_3(s) \quad (3.12)$$

$$4Al(l) + 3C(s) \rightarrow Al_4C_3(s) \quad (2.1)$$

7.2.6 Current density

Most laboratory scale studies show that the wear rate increases with increasing current density [29, 30, 32, 33]. The wear per charge transfer seems to be reduced by increasing current density, at least at current densities lower than 1 A/cm^2 [32]. A common similarity for the experiments that is run with a vertical cathode and no initial molten aluminium is that no wear is observed at zero current.

The laboratory studies correlate well with industrial observations. Higher current densities are expected at the periphery of the cell, and indeed, this is where the highest wear is observed. Even if not directly influencing the wear, increased current density gives rise to other possible wear enhancing factors, e.g. increased convection due to electromagnetic forces. In this regard the current distribution is an extremely important factor for the cathode wear rate. As illustrated in the flow chart in Figure 7.2, a poor current distribution will enhance all wear mechanisms, with exception of externally induced mechanical wear of course.

7.2.7 Convection and metal flow

All cathode wear tests investigated in this work are all pointing to the positive correlation between convection and wear. The wear rate increases with increasing stirring or rotation rate [17-19, 27, 28, 32]. Increased convection and flow leads to increased abrasive forces, increased mass transport in the melt and reduction of the boundary layer thickness at the electrodes. Thus, increased convection and metal flow will yield higher wear rates regardless of which wear mechanism is dominant.

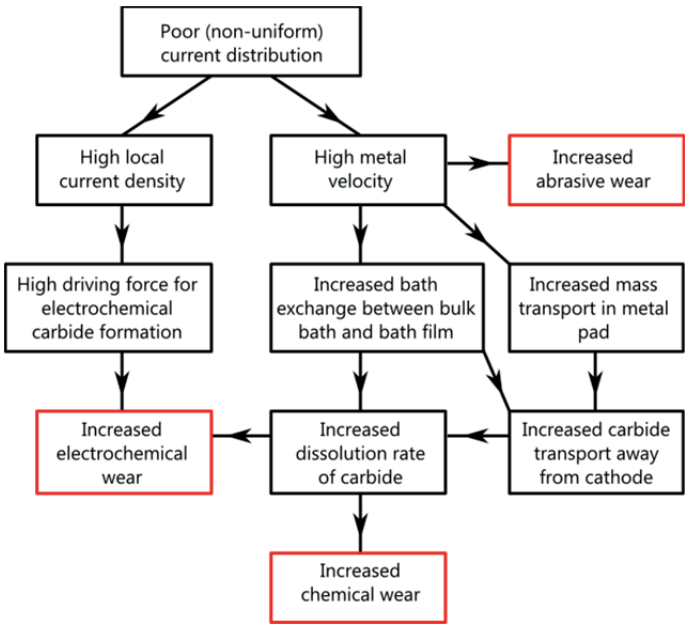

Figure 7.2: Flow chart illustrating how abrasive wear, chemical wear and electrochemical wear all can be linked to poor current distribution.

7.3 Wear mechanisms

7.3.1 Abrasion

As long as there are solid particles at the bottom of the cell moving due to metal flow, abrasive forces will act on the cathode surface. The question is how large these forces are in an industrial cell and how much cathode wear they can account for.

Laboratory abrasion test are typically performed with extreme conditions at short durations in order to rank different cathode materials. The results of the wear test of Liao and Øye [18], performed with a cryolitic melt-alumina slurry, gives an idea of how large effects abrasion can have. For slurry (cryolitic melt and alumina particles) velocities in the range of what can be expected of metal flow in aluminium cells (up to 0.5 m/s), their test showed wear rates of 0.65 cm/y and less. As can be seen from Table 2.1, however, Liao and Øye [18] expected the wear rate in industrial cells to be about 17 times higher. This because of the higher pressure acting on the industrial cathode, with about 45 cm of electrolyte and metal, compared to the lab-scale test [18]. The present author, however, is sceptical to this approach. If the alumina slurry was weighed down by solid particles or viscous “semi-solid” slurry, the assumption made by Liao and Øye [18] would be valid. The aluminium and bath surrounding the abrasive particles in industrial cells, however, are liquid, and in that case the pressure applies forces in all directions, not only downwards

against the cathode. From Archimedes' principle we know that an upward buoyant force is exerted on a submerged particle, dependent on the mass of the fluid displaced by the particle. Assuming that both the abrasive particle and the liquid is non-compressible, it doesn't matter whether there is 1 cm or 1 km of liquid above the particle; the vertical forces exerted on the particle, and thus the abrasive forces between the particle and the cathode surface, would still be the same. On the other hand, the metal height does affect the magneto-hydrodynamic metal flow in industrial cells and may thereby have an indirect influence on the abrasive wear through flow velocity.

The extrapolated results from the wear test mentioned above are believed to be far more reliable than the corresponding estimated wear rates for industrial cells. Any particular area on the cathode surface is probably not continuously subjected to abrasive sludge over the entire lifetime, though, and the wear rates reported by Liao and Øye [18] may be regarded as a worst case scenario. Based on this, the cathode wear rates caused by abrasion do probably not exceed 0.5 cm/y in industrial cells.

The extent of the aluminium carbide layers on the cathode surfaces investigated in the microscopy study indicates that abrasion is probably not the main wear mechanism. If it was, then one would not expect to find thick carbide layers as it would continuously be polished away.

Even when considering the estimated abrasion wear in industrial cells (which was considered to be 17 times higher), Liao and Øye [18] also concluded that chemical corrosion is a stronger wear process than physical abrasion.

7.3.2 Chemical formation of aluminium carbide

Chemical formation and dissolution of aluminium carbide does occur in a system with carbon, aluminium and cryolitic melt present at the temperatures relevant for aluminium electrolysis [18, 20, 25, 27-29]. Due to the poor wetting of aluminium on carbon, and the bath film present between the aluminium and the carbon cathode, formation of aluminium carbide is probably a reaction between the cathode carbon and aluminium dissolved in the bath (reaction (2.1)) [20]. An alternative reaction involving intercalated sodium rather than aluminium may also occur (reaction (3.5)) [2].

$$4Al(l, diss) + 3C(s) \rightarrow Al_4C_3(s) \quad (2.1)$$

$$4AlF_3(diss) + 12Na(C) + C(s) \rightarrow Al_4C_3(s) + 12NaF(l) \quad (3.5)$$

During electrolysis, when current runs through the system, concentration gradients exist at the metal pad interface and also at the carbon cathode. The concentration of AlF_3 is reduced and the concentration of Na and NaF is increased at these interfaces compared to

the bulk bath. The changes in reactant concentrations may obviously have an effect on the reaction rate; reduced concentration of AlF_3 reduces the rate of reaction (3.5), while increased concentration of intercalated Na increases the rate. As the reaction order in respect to the two species is not known, the total effect on the reaction rate cannot be predicted. In an ideal case, however, the Na concentration would be of a higher importance as reaction (3.5) contains 3 Na for every AlF_3.

The microscopy study showed that aluminium carbide is seldom found in cathode pores without aluminium metal, indicating that presence of aluminium may be a prerequisite for carbide formation. This could mean that reaction (2.1) is the more probable, or simply that the absence of Al is an indication of that the activity of Al^{3+} ions and Na are too low for reaction (3.5) to proceed. The electrochemical experiments in the current work showed that cathode wear occurred only at potentials very close to, or cathodic of Al deposition. The activities of Al and Na are closely linked by the equilibrium reaction (6.37), and if the activities of Na and AlF_3 are too low to produce Al in a pore, the driving force for producing Al_4C_3 is low.

$$3NaF(l) + Al(l) \leftrightarrow 3Na(diss/C) + AlF_3(diss) \tag{6.37}$$

7.3.3 Electrochemical formation of aluminium carbide

The cathode wear rate has been found to increase with increasing current density, suggesting electrochemical formation and dissolution of aluminium carbide [29, 30, 32, 33]. Electrochemical formation of Al_4C_3 may proceed according to reaction (2.5), which is based on reduction of aluminium fluoride in the bath film between the carbon cathode and the metal pad. As illustrated in Figure 7.3, the mechanism relies on a steady supply of Al^{3+} ions from the metal-bath film interface.

$$4AlF_3(diss) + 3C(s) + 12Na^+ + 12e^- \leftrightarrow Al_4C_3(s) + 12NaF(l) \tag{2.5}$$

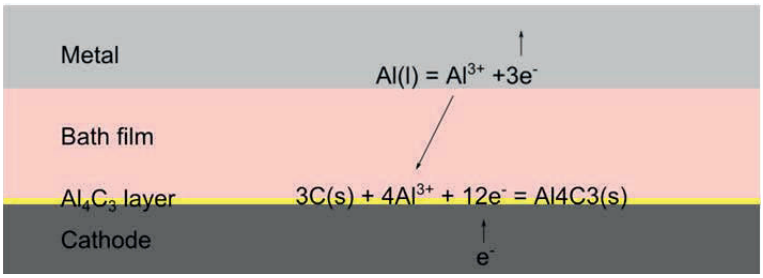

Figure 7.3: Electrochemical formation of Al_4C_3 at the cathode-bath film interface, with dissolution of aluminium at the metal-bath film interface as the anode reaction.

As the carbide formation creates a non-conductive layer on the cathode surface, Al_4C_3 must dissolve to allow fresh carbon at the interface and continued carbide formation.

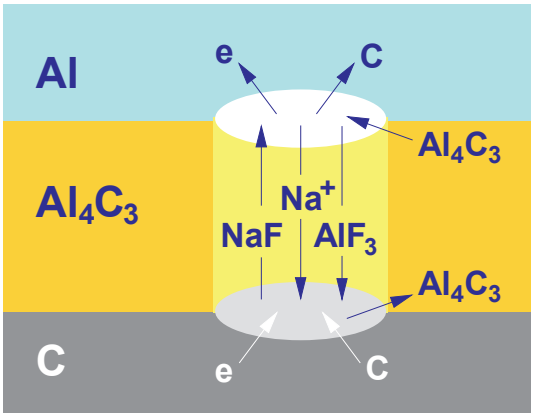

Figure 2.34: Schematic illustration of electrochemical formation and dissolution of aluminium carbide in a bath filled pore in the carbide layer [62].

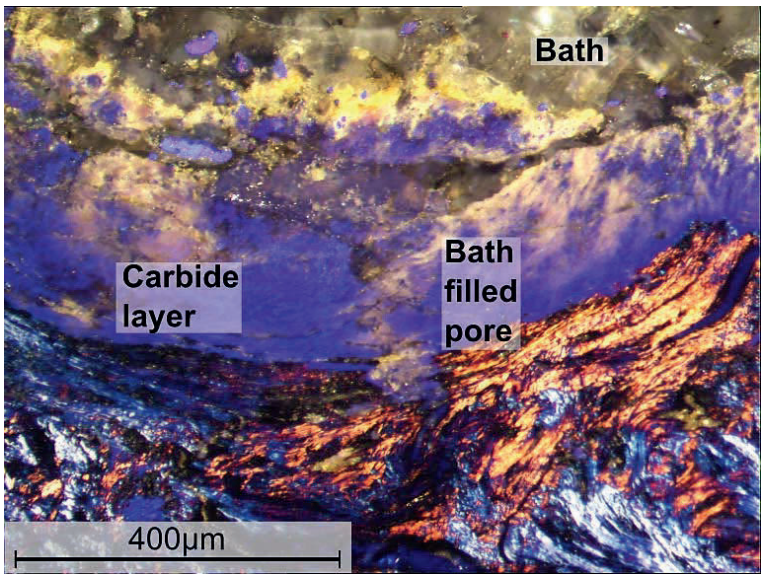

Figure 7.4: Optical micrograph (polarized) of a bath filled pore/crack in the aluminium carbide layer on a cathode sample from an industrial cell. The bath filled pore can be recognised by the yellow hue that is typically seen at the phase transition between carbide and the translucent bath.

Another mechanism, involving Al_4C_3 formation in bath filled pores in the carbide layer and anodic carbide dissolution into metal, has been proposed by Solheim [62]. In his model, illustrated in Figure 2.34, carbide is formed at the cathode surface according to reaction

(2.5) while carbide at the aluminium interface is oxidised according to the same reaction in opposite direction. The wear reaction can be regarded as a concentration cell as the species on the reactant and product side are the same, the only difference being location and concentration. The total turnover of this mechanism is basically transport of carbon from the cathode to the metal through an aluminium carbide layer with bath filled pores, described by Solheim [62] as a "carbon pump". In Figure 7.4, a micrograph of a cathode sample from an industrial cell, investigated in the present work, shows an example of the bath filled pore in Solheim's model.

The potential gradient through the carbide layer would be the driving force for this electrochemical wear mechanism. As the described reaction is a concentration reaction, the standard potential (E^0) is zero and the reversible potential is dependent on concentration gradients in the bath. The potential between the bottom and the top of the pore must be larger than the reversible potential in order for the reaction to occur, overpotentials must also be overcome. If assuming the relevant concentration gradients to be small within the bath filled pores, the reversible potential will also be small. In the present work it was found that the cathodic overpotential needed for electrochemical dissolution of carbon is close to 100 mV. The overpotential is linked to the polarization of the cathode, however, and the results from the present work can be expressed in another way: carbon dissolution require a cathodic potential of about 25 mV anodic of the aluminium deposition potential. Both the carbon cathode and the aluminium pad in industrial cells are polarized well cathodic of this, and the overpotential is thus already overcome.

In a more recent paper Solheim and Tschöpe [63] treats a model for the voltage drop through a carbide layer. Considering an aluminium carbide "island", surrounded by aluminium metal, of about 100 µm thickness and 30 mm^2 diameter on the cathode in an area with current density in the order 10^5 A/m^2 (corresponding to the high wear areas in industrial cells), the voltage drop was estimated to be in the order of 0.01 V. The maximum potential difference between the top and bottom of the carbide layer was found to behave linearly with the horizontal dimensions of the layer. As mentioned in Section 5.4.1, carbide layers much larger than 30 mm^2 were observed on the cathode surface of shut-down cells. Assuming that there are no cracks in the carbide layer which allows contact between aluminium and carbon, the voltage drop would be in the order of 100 mV at areas with extensive carbide layers (30 cm^2 and up).

Both the above electrochemical wear reactions assume that aluminium carbide is formed as a solid. A third proposition assumes formation of dissolved carbide, based on the anodic oxidation of carbide proposed by Ødegård [25]. The present work and Gubrandsen et al. [33] have demonstrated that the reaction proceed in the opposite direction, i.e. cathodic dissolution of carbon into cryolitic melts according to reaction (3.14).

$$3AlF_3(diss) + C(s) + 4e^- \rightarrow Al_3CF_8^{3-} + F^- \quad (3.14)$$

Gubrandsen et al. [33] did not use a reference electrode and could thus not monitor the cathode potential, but they assumed that aluminium deposition did not occur in their experiment as the theoretical potential of carbide formation is about 125 mV less cathodic than aluminium deposition.

In the current work it was found that the cathodic potential needed for cathode wear to occur is about 25–50 mV anodic of Al deposition. Though closer to the Al deposition potential than expected, it does strengthen the theory of electrochemical aluminium carbide formation. That the reaction requires an overvoltage of close to 100 mV on top of the theoretical reversible potential should perhaps not come as a big surprise. Many reactions involving detachment of carbon atoms from a carbon electrode require large overvoltages, e.g. the anodic overvoltage for CO_2 evolution in aluminium reduction cells is in the range of 300–500 mV [5].

7.3.4 Dissolution of aluminium carbide

Dissolution of aluminium carbide in cryolitic melt is believed to proceed according to reaction (2.3), as proposed by Ødegård [25].

$$Al_4C_3(s) + 5AlF_3(diss) + 9NaF(l) \rightarrow 3Na_3Al_3CF_8(diss) \quad (2.3)$$

The solubility of carbide is about 2.5 wt% in cryolitic melt with CR = 1.8 at 960°C [25]. At the metal interface, where AlF_3 is reduced, the cryolite ratio is higher [ref]. In the microscopy study bath in cathode pores was observed to have separated into cryolite and excess NaF, which indicates CR > 3. This is probably also valid for the bath film present between the metal pad and the cathode. In this bath film the carbide solubility can be assumed to be 1 wt% or less.

The solubility in molten aluminium is much lower than in bath, about 105 ppm [108]. Due to this, dissolution of aluminium carbide will probably be slower into metal than into the bath. The metal pad may thereby constitute a protective layer against cathode wear. The amount of carbide in the bulk bath and metal in industrial cells has been found to be well below saturation [108]. From this it can be concluded that the limiting step in the cathode wear mechanism is located at or below the metal pad interface towards the cathode.

7.3.5 Mass transport

Mass transport of dissolved carbide away from the cathode is an important step in the chemical wear mechanism. A good indication of its importance can be found in the results of Vasshaug's [32] electrochemical wear tests, where the wear rate of rotating vertical

cathodes in cryolitic melt (Figure 2.12(a)) were about 10 times larger than that of horizontal cathodes covered with molten aluminium(Figure 2.12(b)). The most important difference between the two test set-ups is the exposure to bath and the convection at the cathode surface. The high wear rates observed on the vertical cathodes is due to the steady supply of fresh bath and rapid transport of dissolved carbide away from the cathode. On the horizontal cathode the molten aluminium pad acts as a barrier, hindering free flow of bath to the cathode surface. As the solubility of carbon in aluminium metal is low, dissolution and transport of carbon into and through the metal pad will be much slower than in the bath.

As mentioned in the literature review, Solheim [62] estimated that stationary mass transport of carbon through the metal pad could account for an average wear rate of about 2 cm/year in a modern electrolysis cell. He argued that non-uniform mass transfer coefficients, due to variation in metal flow velocities, in principle could explain non-uniform wear of the cathode. It was stated that the flow variation is not likely to be large enough to explain the strongly non-uniform wear in industrial cells, however. Solheim [62] thus concluded that there have to be other mechanisms contributing to the cathode wear.

An illustration of aluminium carbide transport through the metal pad is shown in Figure 7.5, where the solid line represents the degree of saturation at various positions between the cathode and the anode. At the metal interface, towards the carbon cathode, saturation is assumed, while zero carbide is expected at the anode/anode gas interface where it is oxidised.

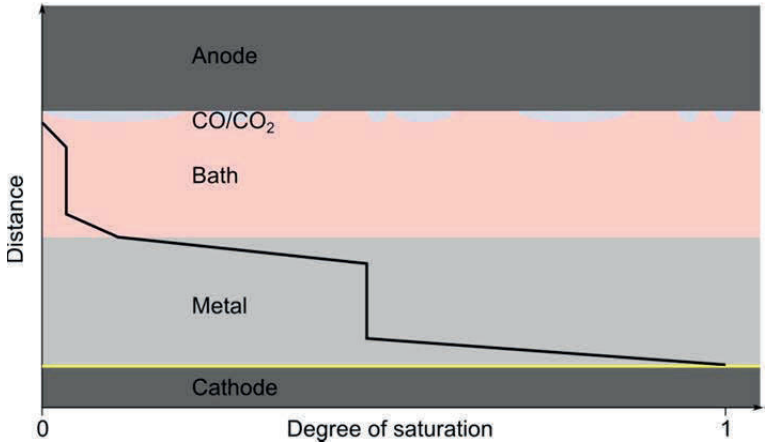

Figure 7.5: Transport of carbide through the metal pad and the bath, from the cathode to the anode where it is oxidised.

Transport of carbide via the bath film beneath the metal pad along the side ledge to the bulk bath could possibly explain the high wear at the cathode periphery. Thonstad et al.

[47] found that there is a fairly rapid exchange between sludge at the cell bottom and the bulk bath. By adding large lumps of cryolite, alumina and BaO (at quantities corresponding to 8 kg Ba) to the sludge layer at the bottom of a 140 kA prebake cell, they found that about half of the initially added amount of Ba found its way to the bulk bath in the matter of 2–4 days.

The bath flow in the thin film between the metal pad and the side ledge can be explained by the Marangoni effect, where mass transfer along an interface between two fluids is induced by surface tension gradients. Utigard and Toguri [109] calculated the flow rate between the sludge layer and the bulk bath due to Marangoni flow. The modified equation (7.1) based on their work gives an estimation of the volume flow rate between the bath and the sludge layer.

$$V_{Mf} = d^2 \, l_{ledge} \times 1.11 s^{-1} \tag{7.1}$$

where d is the thickness of the bath film and l_{ledge} is the length or circumference of the side ledge.

Assuming a bath film thickness of 0.3 mm [110], the Marangoni bath flow in the cells D105 and D107, treated in Chapter 4, would amount to about 140 m^3/y. Further assuming that the bath flowing from the sludge layer to the bulk contains 1 wt% Al_4C_3 (corresponding to a carbon concentration of 5.1 kg/m^3) the Marangoni flow could account for the loss of about 700 kg carbon per year. This is more or less half of the yearly cathode wear found in the mentioned cells, which was estimated to 8024 kg and 8940 kg over a period of 2088 and 2184 days, respectively.

In average the Marangoni flow may account for an average wear rate of about 1 cm/y, though it is likely that this wear is unevenly distributed. The highest wear is expected at the site of first contact between carbide and fresh bath from the bulk, i.e. at the cathode periphery, at the end of the frozen side/bottom ledge. Aside from that, the movement of bath and sludge on the cathode surface will be important for how the wear is distributed. This movement is probably in close relation with the flow of the above metal pad.

A close to vertical current is assumed to flow from the anode to the metal pad. As this is parallel to the direction of the magnetic field, bath flow due to Lorentz forces is believed to be small. At the carbon cathode surface the current density is much larger at the cell periphery, where the high wear areas are found [84]. This means that a large portion of the current flow horizontally in the aluminium pad, from close to the mid-section of the cell to the end of the frozen bottom ledge. This induces Lorentz forces and flow of metal, and the highest velocities are naturally expected where the current density is highest. The metal flow creates movements in the bath film and sludge layer on the bottom, and the

high velocities at the cell periphery probably adds to the exchange of bath between the bulk and the bath film.

7.4 The author's point of view concerning the non-uniform wear

It is the current author's opinion that wear due to physical abrasion is of minor importance, and that mass transport of aluminium carbide to the bulk bath is the rate determining step in the cathode wear mechanism. The typical WW wear pattern can be explained by metal and bath flow and bath exchange between the bulk and the film present beneath the aluminium metal pad.

In the mid-section of the cell (zone A in Figure 7.6), under the alumina point feeders, sludge will form at the cathode surface as undissolved alumina and pieces of the bath crust sinks to the bottom. With regularly additions of alumina, it is likely that a dense viscous alumina rich sludge will persist in this region. In this stationary and viscous sludge, transport of carbide can be assumed to be slow, as there is no convection and the diffusion coefficient of the bulky carbide complex is low. In the present work the diffusion coefficient in bath at 1000°C was found to be in the order of 10^{-5} cm^2/s, and it is probably lower in viscous sludge.

At the cathode periphery (zone E) the freeze lining will protect a small part of the cathode blocks. Right next to this protected zone, the most worn areas on the cathode is found (zone D). As mentioned earlier, the high wear in this zone is likely due to it being the first area of contact between cathode carbon/carbide and fresh bath transported through the thin bath film on the sides. The carbide concentration in the bath film will thus be lower here than closer to the middle and the carbide dissolution reaction may therefore proceed more readily. In addition, the highest current density is expected in this area [84], giving increased metal flow rate and mass transport, and also possibly increasing the rate of carbide formation.

The local summit (zone C) next to the high wear zone show a moderate wear, about 2 cm/y according to the investigation of cells D105 and D107 (Chapter 4). This is similar to the average wear rate Solheim [62] estimated based on stationary mass transport through the metal pad, which thus is believed to be the limiting step for the cathode wear in this zone.

Between the sludge protected mid-section (zone A) and the local summit (zone C), a local low point (zone B) is observed. In addition to stationary transport of carbon through the metal pad there is probably another transport mechanism causing the higher wear in this

region compared to zone C. As mentioned earlier, alumina and bath crust regularly sinks to the bottom close to the mid-section of the cell. While the most dense particles and sludge deposits in a protective layer at the middle, lighter and less viscous bath probably flows out to the sides, giving a reduced carbide concentration in the bath film in zone B. The amount of bath introduced to the bath film by the alumina feeding is far less than by the Marangoni flow and anode operations at the sides, but still enough to yield a noticeable difference in the wear rate compared to zone C.

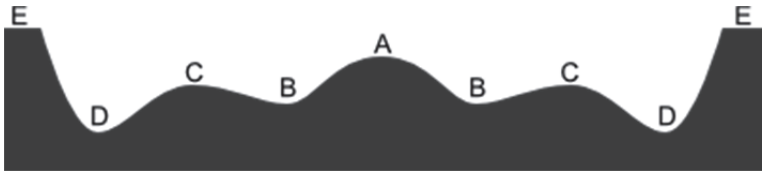

Figure 7.6: Sketch illustrating the WW wear pattern across a cathode block in an industrial cell, such as D105 and D107 from Chapter 4. With regard to the wear, the cross section can be divided into four distinct zones, here denoted A–E.

Another high wear area, the tap hole, is located at the mid-section of a cathode block. This is an area with low current density [84] and the high wear can thus not be explained by electrochemical mechanisms. At regular intervals, however, during metal taping, this region is subjected to high velocity flow in the metal. The tap hole is located at an end block, where bulk bath is introduced through Marangoni flow, and it is likely that the tapping results in increased bath exchange and thus increased dissolution rates and mass transport of carbide. There is also a possibility that direct mechanical wear due to contact between the tapping spout and the cathode block enhances the wear.

An observation that cannot be explained simply by bath or metal flow is the protruding ramming joints between the cathode blocks. Also, in the high wear zone, the cathode blocks seem to be more worn right above the steel current collector bars. In this work the wear was found to be non-preferential, so the only plausible explanation for the protruding ramming joints and the high wear above the current collector bars is that the wear is enhanced by high current density. The ramming joints have a higher electrical resistivity and thus lead less current. At the cathode blocks, the highest current density will obviously be located where the distance to the collector bars are shortest.

During anode change, pieces of bath crust breaks off and sinks to the bottom of the cell and a dredge is used to clean the cathode surface beneath the removed anode. During this operation, a large amount of bath is introduced to the cathode surface. In this period of time, it is likely that aluminium carbide dissolves rapidly, resulting in cathode wear where the carbide formation reaction is the rate limiting step. The carbide formation will thus occur more rapidly where the current density is highest. As the anodes have to be

changed every month, and it may be assumed that two or three cathode blocks are subjected to increased amounts of bath during each anode change, this could explain the correlation between high wear and high current density.

7.5 Industrial implications

In the introduction, Section 2.1, it was mentioned that aluminium smelters have been increasing the amperage of their cells in order to increase productivity. Simultaneously, anthracitic cathode blocks have gradually been replaced by graphitic and graphitized blocks, and the smelters have reported lower cathode lifetimes. Due to the correlation between the decreased cathode lifetime and the transition to graphitic and graphitized cathode blocks, perhaps together with reports of the superior abrasion resistance of anthracitic carbons [17-19], it has in the industry sometimes been assumed that the graphitic and graphitized cathode blocks have a lower wear resistance than anthracitic blocks. This is an inaccurate assumption. It would be more correct to address the aggravated current distribution as the cause of the increased cathode wear. As illustrated in Figure 7.1, the higher electrical conductivity of the graphitic or graphitized cathode blocks, relative to anthracitic grades, leads to a more uneven current distribution. The result is very high current densities at the cathode periphery, which increases the rate of carbide formation and leads to high metal velocities, and thus increased mass transport.

The rapid and non-uniform wear is believed to be related to the bath film beneath the metal pad and the bath exchange between the film and the bulk bath. Due to the poor wetting of aluminium, such a bath film can probably not be avoided on a carbon cathode. It is also quite possible that it is necessary. If the aluminium carbide was not continuously dissolved and removed, it might have formed a thick non-conductive layer on the entire cathode surface.

Reducing the rate of bath exchange between the cathode surface and the bulk bath may significantly reduce the highest wear rates. Marangoni flow along the frozen bath ledge is probably unavoidable, but additional bath exchange due to metal flow may be hindered. Anode changes, feeding and other operations should also be performed in such a way that the amount of crust, bath and alumina introduced to the cathode surface is as low as possible.

The transport rate of carbon through the metal pad may possibly be reduced somewhat with lower metal flow velocities, resulting in thicker diffusion layers at the interfaces. It is not believed that such a marginal reduction of the stationary mass transport through the metal will significantly affect the total wear rate, though.

Continued improvements on the magnetic compensation in order to reduce metal movements is believed to be an effective way of reducing cathode wear, and also rendering possible reduction of the cell voltage drop by lowering the interpolar distance.

A more even current distribution may yield significant improvements regarding the cathode wear. By lowering the current density at the high wear zones, the carbide formation reaction may proceed somewhat slower. In addition, the Lorentz forces due to horizontal currents would be reduced, consequently leading to lower metal velocities. With this in mind, the ongoing testing of variable resistivity graphite (VRG) cathodes, such as reported by Dreyfus et al. [58], is very interesting.

The principle behind VRG cathodes is to design cathode blocks with low electrical conductivity at the peripheries and higher conductivity towards the middle. This, of course, yields a higher voltage drop compared to cathode blocks with uniformly high electrical conductivity, which basically means higher energy loss. Another way to obtain more uniform current distribution, and in addition lower the cell voltage drop, is to improve the electrical conductivity of the current collector bars. This can be obtained by low resistivity steel alloys or simply implementing a copper core in the current collector bars. This is not a new idea, though. Already in 1970, a patent on copper and ferrous metal current collector bars was registered [111], and several others have followed [112-116].

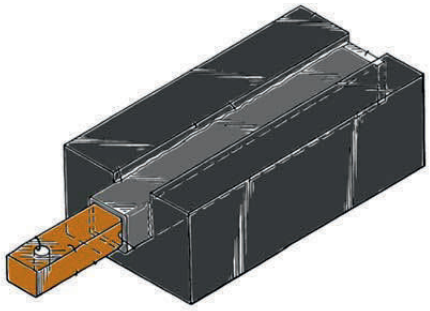

Figure 7.7: Sketch of current collector bar with copper core. Redrawn from [116].

A third possibility to reduce the uneven current distribution is to design cathode blocks with varying distance to the current collector bars. If the current must traverse longer distances in the carbon material at the cathode periphery than closer to the middle of the cell, the total resistance can be evened out along the cathode block, analogous to the VRG cathodes. An example of a design that could potentially contribute to a more even current distribution is given in Figure 7.8.

Figure 7.8: Sketch of a cathode block and a current collector bar with triangular profile.

It should be noted that a certain cathode wear may be needed to avoid a thick non-conductive carbide layer on the cathode surface. In the 1950's, with cells running low current and probably experiencing low metal velocities compared to modern cells, it was reported that cells had to be taken out of operation due to elevated voltage drop [16]. Thus, if the cathode wear is reduced too effectively, formation of an insulating carbide layer may become limiting for the operational lifetime of the aluminium reduction cells.

Chapter 8

Conclusions

The cathode wear in aluminium reduction cells has been investigated by means of visual inspection and laser scanning of worn industrial cathodes, microscopy study of cathode samples, and by laboratory experiments. Based on this work, the following conclusions have been drawn:

- Laser scanning technology can successfully be implemented in cathode wear investigations and give detailed 3D models of the cathode surface, which can be used to assess the cell performance with regard to cathode wear.
- Estimates based on laser scans of two cathodes from Hydro Sunndal reveal that the cathode wear may account for an aluminium production loss corresponding to a CE loss of about 0.5%.
- No significant differences have been observed by microscopy between high wear and low wear areas of the cathode surface that may be connected to variations in the wear mechanisms. Nor have there been found any significant differences between different cells. This can be regarded as an indication of that the wear mechanisms are the same over the entire cathode, but at varying rates.
- Aluminium carbide forms a layer on the cathode surface, up to more than 200 µm thick. Within thick layers, numerous bath containing horizontal cracks were observed. The thin layers (< 20 µm) appeared dense.
- No correlation between the occurrence of aluminium carbide layers and location on the cathode has been observed. Large portions of the carbide layer are removed together with solidified metal, complicating the establishment of whether the carbide layer is continuous or only occur spot-wise.
- Aluminium carbide was found in abundance in superficial pores and cracks in the cathode surface. Little carbide was found deeper than 5 mm into the cathode material.

- The presence of bath at the cathode surface supports the assumption that there exists a bath layer, continuous or spot wise, between the carbon cathode and the metal pad during operation.
- The cathode wear seems to be non-preferential. Aggregate particles and binder matrix in the cathode blocks are worn alike.
- Electrochemical oxidation of dissolved carbide at the anode, resulting in carbon deposition, has been established.
- Cathode wear in alumina saturated Na_3AlF_6–AlF_3 (10 wt%)–CaF_2 (5 wt%) melt at 1000°C (without presence of liquid aluminium) has been found to occur also at a potential 25 mV anodic of aluminium deposition. This indicates electrochemical formation of aluminium carbide.
- The diffusion coefficient for dissolved aluminium carbide in Na_3AlF_6–AlF_3 (10 wt%)–CaF_2 (5 wt%) melt at 1000°C has been found to be in the order of 10^{-5} cm^2/s.
- Additions of Al_4C_3 to the bath yields increased electronic conductivity, likely due to increased sodium levels.
- The reported increase in cathode wear accompanying the transition from anthracitic to graphitic and graphitized cathode blocks is probably not related to lower abrasion resistance of the graphitic and graphitized grades. The reason for the increased wear is most likely the aggravated current distribution and increased local current densities due to the higher electrical conductivity of the cathode blocks. This is based on the finding that the cathode wear process is non-preferential, on the assumption that abrasive wear is relatively slow, and on wear tests reporting little difference in chemical wear resistance between different carbon grades, or in fact marginally lower resistance of anthracitic carbon [31, 35].
- The cell types investigated have been found to be worn in a WW pattern along the longitudinal direction of the cathode blocks. A hypothesis for wear mechanisms leading to the non-uniform WW wear profiles was proposed in Section 7.4.
- Obtaining a more uniform current distribution on the cathode surface and reducing the metal velocity is believed to be important in order to prolong the lifetime of aluminium reduction cells. Decreased metal velocities can be achieved by further improvements of the magnetic compensation. Implementing cathode current collector bars with lower electrical resistivity and/or profiled collector bars with varying distance to the cathode surface will not only yield improvements in the current distribution and the metal velocity, but may also

result in energy savings due to reduced voltage drop. VRG cathodes are also likely to be effective in order to obtain a more uniform current distribution, but with this solution an increased voltage drop may be expected.

References

[1] *Code of Federal Regulations (U.S.A.), Environmental Protection Agency, Title 40: Protection of Environment — Hazardous wastes from specific sources,* §261.32, 2012.

[2] M. Sørlie and H. A. Øye, *Cathodes in aluminium electrolysis*, 3rd ed.: Aluminium-Verlag Marketing & Kommunikation Gmbh, 2010.

[3] *www.hydro.com*. (Aug. 26th 2012). *Qatalum restart imminent, full production expected by end-Q1*. Available: *http://www.hydro.com/en/Press-room/News/Archive/Stock-exchange-announcements/2010/Qatalum-restart-imminent-full-production-expected-by-end-Q1-2011/*

[4] H. A. Øye, "Long life for high amperage cells," *Scandinavian Journal of Metallurgy,* vol. 30, pp. 415–419, 2001.

[5] J. Thonstad*, et al.*, *Aluminium electrolysis. Fundamentals of the Hall-Héroult process*, 3rd ed.: Aluminium-Verlag, 2001.

[6] K. Grjotheim and H. Kvande, *Introduction to aluminium electrolysis*, 2nd ed.: Aluminium-Verlag GmbH, Düsseldorf, 1993.

[7] K. Tschöpe, "Degradation of cathode lining in Hall-Hèroult cells," Ph.D. thesis, Department of Materials Science and Engineering, Norwegian University of Science and Technology, Trondheim, 2010.

[8] P. L. T. Hèroult, "Apparatus for producing aluminium or other metals," United States Patent Office, Patent 473,118, 1892.

[9] S. Wilkening, "One hundred years of carbon for the production of aluminium," *Erdöl Kohle Erdgas Petrochem. Verein. Brennst.-Chem.,* vol. 39, pp. 551–560, 1986.

[10] K. H. Köchling*, et al.*, "International committee for characterization and terminology of carbon “first publication of 30 tentative definitions”," *Carbon,* vol. 20, pp. 445 - 449, 1982.

[11] M. B. Redmount and E. A. Heintz, "Manufacture of graphite electrodes," in *Introduction to carbon technologies*, H. Marsh*, et al.*, Eds., ed: University of Alicante, 1997, pp. 519–536.

[12] H. Marsh, "A tribute to Philip L. Walker," *Carbon,* vol. 29, pp. 703-704, 1991.

[13] M. Sørlie and H. A. Øye, *Cathodes in aluminium electrolysis*, 2nd ed.: Aluminium-Verlag, 1994.

[14] M. Sørlie*, et al.*, "Property changes of cathode lining materials during cell operation," *Light Metals 1995,* pp. 497-506, 1995.

[15] R. Fourcault and B. Samanos, in *2nd Australasian Aluminium Smelter Technology Course*, Sydney, 1987.

[16] J. B. Paulsen, "Ulike synspunkter ved konstruksjon og holdbarhet av katoder i elektrolyse-celler for aluminium," Metallurgisk Institutt, Norges Tekniske Høgskole, Trondheim, 1967.

[17] X. Liao and H. A. Øye, "Method for determination of abrasion resistance of carbon cathode materials at room temperature," *Carbon,* vol. 34, pp. 649-661, 1996.
[18] X. Liao and H. A. Øye, "Physical and chemical wear of carbon cathode materials," *Light Metals 1998,* pp. 667-674, 1998.
[19] S. Toda and T. Wakasa, "Improvement of abrasion resistance of graphitized cathode block for aluminium reduction cells," *Light Metals 2003,* pp. 647 - 653, 2003.
[20] R. C. Dorward, "Reaction between aluminium and graphite in the presence of cryolite," *Metallurgical and materials transactions B,* vol. 4, pp. 386–388, 1973.
[21] K. Grjotheim*, et al.*, "Formation of aluminium carbide in the presence of cryolite melts," *Light Metals 1977,* vol. 1, pp. 233–242, 1977.
[22] B. Novak*, et al.*, "Fundamentals of aluminium carbide formation," *Light Metals 2012,* pp. 1343–1348, 2012.
[23] W. R. King and R. C. Dorward, "Electrical resistivity of aluminium carbide at 990–1240 K," *J. Electrochem. Soc.,* vol. 132, pp. 388–389, 1985.
[24] R. Ødegård*, et al.*, "On the solubility of aluminium carbide in cryolitic melts - Influence on cell performance," *Light Metals 1987,* pp. 295 - 302, 1987.
[25] R. Ødegård, "On the solubility and electrochemical behaviour of aluminium carbide in cryolitic melts," Ph.D. thesis, University of Trondheim, 1986.
[26] M. Chrenková*, et al.*, "Dissolution of carbon and Al4C3 in cryolite," in *Slovak-Norwegian Symposium on Aluminium Electrowinning*, Trondheim - Bergen, Norway, 2001, pp. 271-279.
[27] E. A. Hollingshead and J. A. Brown, "Rate of solution of carbon in molten aluminium under a cryolite melt," *Light Metals 1982,* pp. 625-634, 1982.
[28] J. Xue and H. A. Øye, "Al_4C_3 formation at the interface of Al-graphite and Al-carbon/TiB_2 composite," *Light Metals 1994,* pp. 211-217, 1994.
[29] X. Liao and H. A. Øye, "Carbon cathode corrosion by aluminium carbide formation in cryolitic melts," *Light Metals 1999,* pp. 621 - 627, 1999.
[30] S. Wilkening and P. Reny, "Erosion rate testing of graphite cathode materials," *Light Metals 2004,* pp. 597-602, 2004.
[31] P. Rafiei*, et al.*, "Electrolytic degradation within cathode materials," *Light Metals 2001,* pp. 747-752, 2001.
[32] K. Vasshaug, "The influence of the formation and dissolution of aluminium carbide on the cathode wear in aluminium electrolysis cells," PhD Ph.D. thesis, Norwegian University of Science and Technology, 2008.
[33] H. Gudbrandsen*, et al.*, "Cathodic dissolution of carbon in cryolitic melts," *Light Metals 1992,* pp. 521 - 528, 1992.
[34] K. Tschöpe*, et al.*, "Investigation of the cathode wear mechanism in a laboratory test cell," *Light metals 2012,* pp. 1349–1354, 2012.
[35] K. Tschöpe*, et al.*, "Critical reflections on laboratory wear tests for ranking commercial cathode materials in aluminium cells," *Light Metals 2013,* (unpublished Sep. 2012).
[36] P. Patel*, et al.*, "Influence of internal cathode structure on behaviour during electrolysis. Part II: Porosity and wear mechanisms in graphitized cathode material," *Light Metals 2005,* pp. 757–762, 2005.

[37] S. C. Raj and M. Skyllas-Kazacos, "Aluminium deposition and redissolution at TiB_2/C composite cathodes in cryolite based melts," *Journal of Applied Electrochemistry,* vol. 23, pp. 257–264, 1993.

[38] S. Brynjulfsen, "Elektrokjemisk oppførsel av karbon i fluoridsmelter," M.Sc, Department of Materials Science and Engineering, NTNU, Trondheim, 2005.

[39] D. Liu*, et al.*, "Cathodic behaviour of graphite in KF-AlF_3-based melts with various cryolite ratios," *Journal of Solid State Electrochemistry,* vol. 15, pp. 615–621, 2011.

[40] H. Kvande*, et al.*, "Penetration of bath into the cathode lining of alumina reduction cells," *Light Metals 1989,* pp. 161-167, 1989.

[41] J. M. Peyneau*, et al.*, "Laboratory testing of the expansion under pressure due to sodium intercalation in carbon cathode materials for aluminium smelters," *Light Metals 1992,* pp. 801-808, 1992.

[42] P. Brilloit*, et al.*, "Melt penetration and chemical reactions in carbon cathodes during aluminium electrolysis. I. Laboratory experiments.," *Light Metals 1993,* pp. 321-330, 1993.

[43] H. Schreiner, "Sodium expansion of carbon cathodes for aluminium electrolysis," PhD thesis, University of Trondheim, 1994.

[44] Y. Mikhalev and H. A. Øye, "Absorption of metallic sodium in carbon cathode materials," *Carbon,* vol. 34, pp. 37-41, 1996.

[45] T. Naas, "Interactions of alkali metals and electrolyte with cathode carbons," PhD thesis, University of Trondheim, 1997.

[46] N. Akuzawa*, et al.*, "Reactivity of carbon materials against metallic sodium," *Light Metals 2003,* pp. 611 - 616, 2003.

[47] J. Thonstad*, et al.*, "Some properties of alumina sludge," *Light Metals 1980,* pp. 227-239, 1980.

[48] A. R. Johnson, "Metal pad velocity measurements in aluminum reduction cells," *Light Metals 1978,* vol. 1, pp. 45-58, 1978.

[49] A. T. Tabereaux and R. B. Hester, "Metal pad velocity measurements in prebake and Soderberg reduction cells," *Light Metals 1984,* pp. 519-539, 1984.

[50] B. F. Bradley*, et al.*, "Metal pad velocity by the iron rod method," *Light Metals 1984,* pp. 541-552, 1984.

[51] S. Matsui and A. Era, "Measurements of metal turbulence in aluminium reduction cell," *Light Metals 1982,* pp. 373-389, 1982.

[52] S. Cherchi and G. Degan, "Oscillation of liquid aluminium in industrial reduction cells," *Light Metals 1983,* pp. 457-467, 1983.

[53] J. Mittag*, et al.*, "Sodium, its influence on cathode life in theory and practice," *Light Metals 1992,* pp. 789-793, 1992.

[54] A. T. Taberaux*, et al.*, "Erosion of cathode blocks in 180kA prebake cells," *Light Metals 1999,* pp. 187-192, 1999.

[55] P. Reny and S. Wilkening, "Graphite cathode wear study at Alouette," *Light Metals 2000,* pp. 399-404, 2000.

[56] R. Bacchiega and I. Letizia, "Structural changes of carbon cathodes blocks during the alumina electrolysis," *Light Metals 1974,* vol. 1, pp. 97-102, 1974.

[57] S. M. El-Raghy*, et al.*, "Operational changes in carbon cathode of aluminium cell," *Light Metals 2003,* pp. 627-631, 2003.

[58] J.-M. Dreyfus*, et al.*, "Variable resistivity cathode against graphite erosion," *Light Metals 2004,* pp. 603-608, 2004.
[59] F. Naixiang*, et al.*, "New cathodes in aluminium reduction cells," *Light Metals 2010,* pp. 405–408, 2010.
[60] www.hydro.com. (Feb. 11th 2011). *Qatalum's first metal — "A great achievement"*. Available: http://www.hydro.com/en/Press-room/News/Archive/2009/12/Qatalums-first-metal--A-great-achievement/
[61] S. Jarek*, et al.*, ed. Personal communication, Jan. 14th 2011.
[62] A. Solheim, "Some hypotheses concerning cathode wear in aluminium electrolysis cells," in *MetSoc's Annual Conference of Metallurgists (COM 2011)*, Montreal, Canada, 2011.
[63] A. Solheim and K. Tschöpe, "Model for excessive cathode wear by a "carbon pump" at the cell bottom," *Light Metals 2013,* unpublished Sep. 2012.
[64] B. Sandberg, "Karbotermisk reduksjon av aluminiumoksyd," Dr.ing. thesis, Norges Tekniske Høgskole, Trondheim, 1981.
[65] K. Motzfeldt*, et al.*, *Carbothermal production of aluminium*: Aluminium-Verlag Gmbh, 1989.
[66] M. Eagleson, "Aluminium carbide," in *Concise encyclopedia chemistry*, H.-D. Jakubke and H. Jeschkeit, Eds., ed. Berlin: Walter de Gruyter & Co, 1994, p. p. 52.
[67] I. Barin, *Thermochemical data of pure substances*: VCH Verlagsgesellschaft mbH, 1989.
[68] J. M. Lihrmann*, et al.*, "Thermodynamics of the Al–C–O system and properties of SiC–AlN–Al_2OC composites," *Journal of the European Ceramic Society,* vol. 19, pp. 2781–2787, 1999.
[69] CRCT and GTT-Technologies, "FactSage," ed, 2001.
[70] P. Chartrand, "Virtal Lab for FactSage," CRCT, Ed., ed, 2005.
[71] C. J. Simensen, "Comments on the solubility of carbon in molten aluminum," *Metallurgical and materials transactions A,* vol. 20, p. 191, 1989.
[72] R. C. Dorward, "Aluminum carbide formation and removal during electrolytic reduction and hot metal processing operations," *Light Metals 1973,* vol. 1, pp. 105–118, 1973.
[73] E. Baur and R. Brunner, "Über die Schmeltzfläche im System Aluminium, Aluminiumoxyd, Aluminiumcarbid," *Z. Elektrochem.,* vol. 40, pp. 154–158, 1934.
[74] P. T. Stroup, "Carbothermic smelting of aluminium. The 1964 extractive metallurgy lecture," *Transactions of the Metallurgical Society of AIME,* vol. 230, pp. 356–372, 1964.
[75] H. Ginsberg and V. Sparwald, "Beiträge zur Aluminiumgewinning durch Carbotermische Reduktion Aluminiumoxids unter besondere Berücksichtigung des Systems Aluminium-Kohlenstoff," *Aluminium,* vol. 41, pp. 181–193, 1965.
[76] S. Gjerstad, "Chemical-metalurgical investigations concerning carbothermal reduction of alumina and silica," Dr.ing. thesis, Norges Tekniske Høgskole, Trondheim, 1968.
[77] L. L. Oden and R. A. McCune, "Phase equilibria in the Al-Si-C system," *Met. Trans.,* vol. 18A, pp. 2005–2014, 1987.

[78] J. M. Lihrmann*, et al.*, "High temperature behaviour of the aluminium oxycarbide Al_2OC in the system Al_2O_3–Al_4C_3 and with additions of aluminium nitride," *Journal of the American Ceramic Society,* vol. 72, pp. 1704–1709, 1989.

[79] C. Qui and R. Metselaar, "Thermodynamic evaluation of the Al_2O_3–Al_4C_3 system and stability of Al-oxycarbides," *Z. Metallk.,* vol. 86, pp. 198–205, 1995.

[80] A. Solheim and Å. Sterten, "Activity of alumina in the system NaF – AlF_3 - Al_2O_3 at NaF/AlF_3 molar ratios ranging from 1.4 to 3," *Light Metals 1999,* pp. 445–452, 1999.

[81] E. Skybakmoen*, et al.*, "Measurement of cathode surface wear profiles by laser scanning," *Light Metals 2011,* pp. 1061–1066, 2011.

[82] E. Skybakmoen*, et al.*, "Investigations of cathode wear profiles obtained by the laser scanner method," presented at the 10th Australasian Smelting Technology Conference, Tasmania, 2011.

[83] E. Skybakmoen*, et al.*, "Title," unpublished|.

[84] J.-M. Dreyfus and L. Joncourt, "Erosion mechanisms in smelters equipped with graphite blocks - a mathematical modeling approach," *Light Metals 1999,* pp. 199-206, 1999.

[85] C. J. Simensen, "Gas-chromatographic analysis of carbides in aluminium and magnesium," *Fresenius Zeitschrift für Analytische Chemie,* vol. 292, pp. 207–212, 1978.

[86] J. K. Solberg, *Lysmikroskopi*: Department of Materials Science and Technology, NTNU, 2000.

[87] A. R. Büchner, "Determination of the mean atomic number of alloys in quantitative microprobe analysis," *Arch Eisenhüttenwes,* vol. 44, pp. 143–147, 1973.

[88] I. Eick, "Personal communication," ed. Trondheim, 2011.

[89] J. Thonstad and S. Rolseth, "On the cathodic overvoltage on aluminium in NaF–AlF_3–Al_2O_3 melts — II," *Electrochimica Acta,* vol. 23, pp. 233–241, 1978.

[90] M. Lebeuf*, et al.*, "Towards a better understanding of the carburation phenomenon," *Light Metals 2011,* pp. 1097–1102, 2011.

[91] D. Pletcher*, et al.*, *Instrumental methods in electrochemistry*: Horwood Publishing, 2001.

[92] K. Motzfeldt, "Means of attending and controlling temperature," in *Physochemical measurements at high temperatures*, J. O. Bockris*, et al.*, Eds., ed London: Butterworths, 1959, p. 52.

[93] S. Rolseth, "Tilbakereaksjonen i aluminiumelektrolysen," PhD, University of Trondheim, 1980.

[94] G. M. Haarberg*, et al.*, "Measurement of electronic conduction in cryolite alumina melts and estimation of its effects on current efficiency," *Metallurgical Transactions B,* vol. 24B, pp. 729–735, 1993.

[95] C. Krohn*, et al.*, "Penetration of sodium and bath constituents into cathode carbon materials used in industrial cells," *Light Metals 1982,* pp. 311-324, 1982.

[96] Ishpal*, et al.*, "X-ray photoelectron spectroscopic study of nitrogen incorporated amorphous carbon films embedded with nanoparticles," *Applied surface science,* vol. 256, pp. 7371–7376, 2010.

[97] P. L. Walker*, et al.*, "Distinguishing between graphitic and amorphous carbon," *ASTM Bulletin,* vol. 208, pp. 52–54, 1955.

[98] Å. Sterten*, et al.*, "Activities and phase diagram data of $NaF–AlF_3–Al_2O_3$ mixtures derived from electromotive force and cryoscopic measurements. Standard thermodynamic data of β-Al_2O_3(s), Na_3AlF_6(s), $Na_5Al_3F_{14}$(s) and $NaAlF_4$(l)." *Acta Chemica Scandinavica,* vol. A 36, pp. 329–344, 1982.

[99] J. D. Edwards*, et al.*, "Electrical conductivity and density of molten cryolite with additives," *J. Electrochem. Soc.,* vol. 100, pp. 508–512, 1953.

[100] E. W. Yim and M. Feinleib, "Electrical conductivity of alkali fluorides, cryolites, and cryolite-base melts," *J. Electrochem. Soc.,* vol. 104, pp. 626–630, 1957.

[101] P. Fellner*, et al.*, "Electrical conductivity of molten cryolite-based mixtures obtained with a tube-type cell made of pyrolytic boron nitride," *Electrochimica Acta,* vol. 38, pp. 589–592, 1993.

[102] J. Híveš*, et al.*, "Electrical conductivity of molten cryolite-based mixtures obtained with a tube-type cell made of pyrolytic boron nitride," *Light Metals 1994,* pp. 187–194, 1994.

[103] E. Sum and M. Skyllas-Kazacos, "Aluminium dissolution in $NaF–AlF_3–Al_2O_3$ systems," *Journal of Applied Electrochemistry,* vol. 18, pp. 731–738, 1988.

[104] J. J. Duruz and C. Landolt, "Electrochemical deposition of aluminium on tungsten in cryolite based melts," *Journal of Applied Electrochemistry,* vol. 15, pp. 393–398, 1985.

[105] J. H. Kent, "Attainment of high current efficiency on aluminium reduction furnaces by cold running technique," *J. Metals,* vol. 22, pp. 30–36, 1970.

[106] W. C. Sleppy and C. N. Cochran, "Bench scale electrolysis of alumina in sodium fluoride-aluminium fluoride melts below 900 degree C," *Aluminium,* vol. 55, pp. 604–606, 1979.

[107] A. Solheim, "Crystallization of cryolite and alumina at the metal-bath interface in aluminium reduction cells," *Light Metals 2002,* pp. 225–230, 2002.

[108] J. Rødseth*, et al.*, "Solubility of carbon in aluminium and its effect upon the casting process," *Light Metals 2002,* pp. 883–887, 2002.

[109] T. Utigard and J. M. Toguri, "Marangoni flow in the Hall-Heroult cell," *Light Metals 1991,* pp. 273–281, 1991.

[110] W. E. Haupin, "Calculating thickness of containing walls frozen from melt," *Light Metals 1971,* pp. 188–194, 1971.

[111] C. J. McMinn and V. L. Bullough, "Copper and ferrous metal current collector and electrolytic cell therewith," United States Patent Office, Patent 3,499,831, 1970.

[112] G. E. Homley and D. P. Ziegler, "Cathode collector bar," United States Patent Office, Patent 6,231,745, 2001.

[113] D. Juric and R. Shaw, "Electrolytic reduction cell and collector bar," United States Patent Application Publication, Patent US2003/0173214 A1, 2003.

[114] B. Allano*, et al.*, "Electrolysis cell for the production of aluminium comprising means to reduce the voltage drop," United States Patent Application Publication, Patent 2008/0135417 A1, 2008.

[115] J. L. Mitchell and J. G. Tink, "Cathode connection for aluminium smelter pot and method," United States Patent Office, Patent 5,855,758, 1999.

[116] R. H. Pate, "Collector bar," United States Patent Office, Patent 5,976,333, 1999.

[117] K. Nisancioglu, "Corrosion basics and engineering (Compendium for lectures on corrosion)," NTH, Ed., ed. Trondheim, 1994.
[118] S. V. Devyatkin*, et al.*, "Electrochemical behaviour of titanium, silicon and boron oxides in cryolite-alumina melts," *ECS Transactions,* vol. 33, pp. 249–255, 2010.
[119] K. Grjotheim*, et al.*, "Electrochemical deposition of metals, alloys and oxygen from natural minerals—II. Cathode processes in the electrodeposition of Si and Al from K-feldspear dissolved in cryolite," *Canadian Metallurgical Quarterly,* vol. 30, pp. 107–111, 1991.

Nomenclature

Abbreviations

BSED	backscatter electron detector
CE	current efficiency
CR	cryolite ratio, $nNaF/nAlF_3$
CV	cyclic voltammetry
DTA	differential thermal analysis
ECA	electrocalcined amorphous carbon
EDS	energy-dispersive x-ray spectroscopy
FEM	finite element method
GCA	gas calcined amorphous carbon
GZ	see table 5.2
GZi	see table 5.2
ICP	inductively coupled plasma
OCV	open circuit voltage
SEM	scanning electron microscope
SGv	see table 5.2
SGZi	see table 5.2
SGZv	see table 5.2
TGA	thermal gravimetric analysis
VRG	variable resistivity graphite
XRD	x-ray diffraction
XRF	x-ray fluorescence

Symbols

Symbol	Meaning	Unit
Roman symbols		
a_i	activity of species i	1

c_i	concentration of species i		mol%
C_i	concentration of species i		wt%
d	thickness		m
D_i	diffusion coefficient of species i		m^2/s
E	electric potential		V
E^0	standard electrode potential		V
E^{rev}	reversible electrode potential		V
F	Faraday constant	96485.34	C
G	geometric cell factor		m^{-1}
ΔG	Gibbs free energy of reaction		J/mol
$\Delta_f G^0$	standard Gibbs free energy of formation		J/mol
$\Delta_f H^0$	standard enthalpy of formation		J/mol
I	current		A
i	current density		A/cm^2
i_0	exchange current density		A/cm^2
k	reaction rate constant		
l	length		m
n_i	amount of species i		mol
R	gas constant	8.314	J/K mol
R	resistance		Ω
T	Temperature		K
t	time		s
U	voltage		V
V	volume		m^3
V_{mf}	volumetric Marangoni flow		m^3/s
x_i	atomic fraction of element i		1
Z_i	atomic number of element i		1

Greek symbols

α	charge transfer coefficient		1
χ_i	mole fraction of species i		1
δ	diffusion layer thickness		m
γ_i	activity coefficient of species i		1

η	overpotential	V
φ	porosity	1
κ	specific conductivity	S/m
ν	sweep rate	V/s
ρ	density	g/cm^3

Other symbols

Ø	diameter	m

Appendices

Appendix A

Papers

The PhD candidate has participated in the two following papers:

- *"Measurement of Cathode surface wear profiles by laser scanning"*, E. Skybakmoen, S. Rørvik, A. Solheim, K.R. Holm, P. Tiefenbach and Ø. Østrem, Light Metals 2011.
- *"Investigations of cathode wear profiles obtained by the laser scanning method"*, E. Skybakmoen, S. Rørvik, A. Solheim and Ø. Østrem, presented at the 10th Australasian Smelting Technology Conference, 2011.

The papers are quoted in their entirety in the following pages, p. 198–203 and p. 204–214, respectively.

Light Metals 2011 *Edited by: Stephen J. Lindsay*
TMS (The Minerals, Metals & Materials Society), 2011

MEASUREMENT OF CATHODE SURFACE WEAR PROFILES BY LASER SCANNING

Egil Skybakmoen, Stein Rørvik, Asbjørn Solheim,
Knut Ragnar Holm*, Priska Tiefenbach* and Øyvind Østrem*

SINTEF Materials and Chemistry, NO-7465 Trondheim, Norway
*Norwegian University of Science and Technology, NO-7491 NTNU, Trondheim, Norway

Keywords: Cathode wear, laser scanning, wear profiles

Abstract

The service life time for high amperage aluminium reduction cells with graphitized cathodes is limited by cathode wear. The wear is normally very non-uniform, and it is commonly documented by photography and/or manual point measurements. In an attempt to record the wear pattern in a much more detailed way, a laser scanning procedure was developed. A laser scanner with a single point accuracy of 10 mm has been used to produce a 3D model based on three overlapping scans with an average resolution of about 1 cm. The same cathodes were also measured manually for comparison. The method developed gives detailed information regarding the wear at different positions within the cell, and it may become a valuable tool for investigating the influence of different parameters on the cathode wear.

Introduction

The very non-uniform wear observed in aluminium cells with graphitized cathodes is today limiting the cell life and it represents a great challenge for the aluminium industry.

The so-called w-wear profile is reported by several authors [1,2]. The mechanism for the wear observed is still not fully understood. It seems clear, however, that current densities and metal/bath movements play important roles together with the formation and dissolution of aluminium carbide. Higher wear is observed in areas with high current densities. The ramming paste between the cathode blocks normally shows less wear.

The documentation of the observed wear is usually made by photography and manual point measurements. This gives a crude overview of the wear pattern with little preservation of details. Therefore, there is a need for a new method which is more detailed and provides documentation that can easily be studied in retrospect. In this work the laser scanner method is reported and compared with a manual telescope leveling method. Both methods have been used during post mortem investigation of two cells at the Hydro Sunndal aluminium smelter.

Cells, Measurements, and Procedures

Cells

Two cathode linings (D105 and D107) from Hydro Sunndal Al plant (SU4) were investigated with respect to cathode wear profile. The cell design for both cells was similar and the surfaces consisted of 19 graphitic cathode blocks with ramming paste in between. Both cells were shut down due to high levels of iron in the metal. The cells were considered to be run under normal electrolysis conditions during the life time, which were 2088 and 2184 days, respectively. Pictures of the cathode surfaces of both cells are shown in Figure 1. The cathode surfaces were thoroughly cleaned before measuring started.

Cell D 105 (2088 days) Cell D107 (2184 days)

Figure 1. Cathode surfaces of cells D105 and D107.

Laser Scanning Method

The laser scanning method offers the possibility to capture a surface of an object — in this case a cathode — in great detail. It is a non-contact active measuring system which acts by sending and receiving laser light. The scanner shoots a laser beam and collects the reflected light. The result is a point cloud consisting of a resolution dependent number of points with 3D coordinates and often some additional attributes as well. One distinguishes between mainly two kinds of laser scanners which work with different techniques: triangulation and time-of-flight laser scanners.

A time-of-flight laser scanner, such as the one used (Riegl LMS-Z420i [3]), measures the time t a laser pulse needs to travel from the sender unit to the target surface and back to the receiver unit, and thus the distance d can be calculated.

$$d = ct / 2 \qquad c: \text{speed of light}$$

Together with the known horizontal and vertical angles – analogue a total station (tachymetry) - 3D coordinates can be computed. A laser scanner beam will be reflected from the first object it hits; hidden objects cannot be measured (shadow effect). Therefore, it is often necessary to work with more than one scan position.

The terrestrial time-of-flight laser scanner used in the present experiments has a measurement rate up to 11'000 pts/sec; measurement range 2–1'000 m; field of view 80 x 360 degrees,

and it consists of a fixed lower part (in this case mounted on a custom-made frame) and a rotating upper part analogous to a tachymetrical total station. The generated laser beam is diverted by a rotating respectively oscillating mirror. After measuring a vertical line with a given resolution/angle, the scanner turns horizontally at a given angle and continues scanning the next vertical line, as illustrated in Figure 2.

A calibrated digital photo camera Nikon D200 (f=20mm, 10.2 megapixels) was mounted on the scanner, making it possible to incorporate RGB values for the points obtained by the laser scanner.

Figure 2. Principle of the laser scanner.

Laser Scanning Configuration and Procedure

A custom-made steel frame constituted the platform for the laser scanner (Figure 3). With the help of a crane or a digger it was mounted on the steel shell of the cathode, and the laser scanner was fixed at the top. The construction could easily be moved along the pot shell while the laser scanner was attached.

Figure 3. Steel frame for placement of the laser scanner.

To obtain data for the entire cathode surface with approximately the same resolution and to avoid shadow effects, scans from three positions with overlapping areas were performed (as illustrated in Figures 4 and 5). 20-30 circular tape reflectors (target points) were distributed on and around the cathode to help aligning the three overlapping scans. This configuration also enhanced the point accuracy (the single point accuracy of Riegl LMS-Z420i is 10 mm). At each scan position a scan with a resolution of 0.05 degrees (approx. 5 mm at a distance of 6 m) was executed, and photos were automatically taken for the corresponding surface as well.

Figure 4. Laser scanner positioning above the cathode.

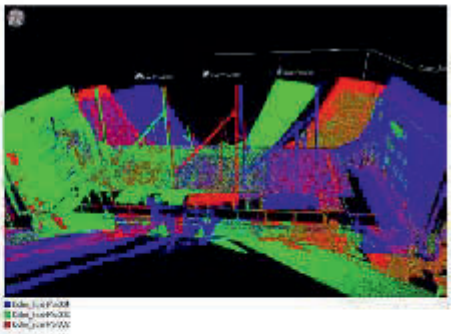

Figure 5. Three overlapping point clouds - the cathode, the steel frame and the surrounding area are visible.

Data Processing

To be able to get accurate results from the data processing of the geometrical laser scanning data together with the photos taken by the calibrated camera, calculation of the camera mounting calibration (camera position related to the scanner) was essential. Therefore, these calibration values are calculated for each of the three scan positions by using the scanned targets. Each point cloud (one per scan position) is then coloured by the photos taken at the same scan position. The working step 'registration' links together the different scan positions via the targets they have in common. This registered total point cloud had 3D coordinates (XYZ) in a casual local coordinate system which was then transformed to a cathode-adjusted one. For this step the three single point clouds had to be re-registered to one total point cloud.

The transformation results were as follows:

Standard deviation [mm] - Cell D105:

Point cloud system:	*3.2 (16 targets used)*	*1 to new coordinate*
*"	*2 "*	*2.6 (19 ")*
*"	*3 "*	*3.1 (19 ")*

Standard deviation [mm] - Cell D107:

Point cloud system:	*1.8 (27 targets used)*	*1 to new coordinate*

" 2" 2.0 (29")
" 3" 1.8 (25")

Useless or even disturbing points were deleted and the data were merged to one single 3D point cloud (5.3 million points). By using the scanner related software *RiScan Pro* and other programs, various types of visualisation could be obtained (using points and/or the triangulated surface).

Manual Method with Leveling Telescope

The current method for measuring the cathode wear profiles at Hydro Sunndal makes use of a leveling telescope and a measuring stick with a bubble level attached. The leveling telescope is placed on a stable surface outside the cathode shell from where one can read the measuring stick, which is placed at different locations on the cathode surface. On each corner of the steel shell there are reference points, from which the original depth of the newly installed cathode blocks is known. The difference in depth before and after operation can then be measured at several points on each cathode block. The typical number of measuring points is 7 points per cathode block, covering the deepest points on the sides, the highest point in the middle and the local high and low points in between.

The cathodes investigated in this work consisted of 19 cathode blocks, giving 133 measuring points. A team of three persons, one operating the leveling telescope, one holding the measuring stick, and one taking notes, needs about one hour to measure one cathode.

Results

Topographic Plots with Laser Scanner and Manual Method

Besides the forever reusable 3D point coordinates including additional values (i.e. intensity, RGB), saved in a common ASCII format, various meaningful products were created. For example 3D visualizations of the cathode where the point cloud is coloured by RGB were made (Figure 6), as well as a 3D model coloured according to the height or respectively the depth of the cathode surface (Figure 7). Also better known visualizations as i.e. height curves or horizontally and vertically surface cuts were calculated.

Figure 6. RGB-coloured scan data of cathode (Cell D105).

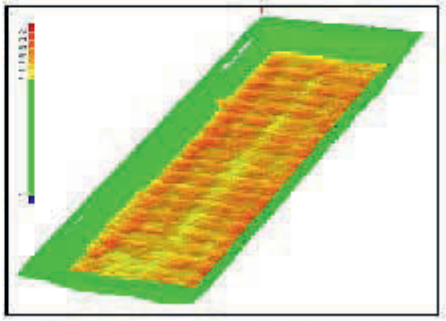

Figure 7. 3D model colored according to the depth of the cathode.

The 3D point coordinates from the laser scan were post-processed using Perl (a public domain data processing language) to resample the data to XYZ values at 1 cm resolution on each axis. The resampled data was converted to a grayscale image, where each pixel XY coordinate (column and row) corresponds to the respective XY position in cm, and the Z value (gray level) corresponds to the respective Z depth in cm. This picture was opened in the public domain image analysis program ImageJ for further visualization and plotting. These programs were chosen for convenience; the data could also have been plotted in other data plotting or image analysis software.

The manual method gives a set of XYZ values, where the X and Y values represent the measuring positions on the cathode surface and the Z values are the measured cathode depth. The amount of data is relatively small (133 points in this case), and interpolation is needed to create a good visualization of the wear profile. Just like the data from the laser scans, the data from the manual scans can be plotted like 3D models and contour plots. In this work linear interpolation was used to fill in the gaps between the measuring points. The data in the Z direction is quite reliable; the X and Y coordinates are usually not. For convenience the X values are determined by the cathode block number and the seven Y values on each block are assumed to be the same for every cathode block. In reality these points are not in the same spot on every cathode block. The measuring stick is typically placed at the deepest or the highest point (i.e. the most interesting point) in the relevant area to be measured. It is also worth noting that the less worn ramming paste between the cathode blocks was not measured with the manual method, according to the standard procedure.

The two methods are compared in Figure 8 and Figure 9. The pictures are sized and coloured using the same scale, from blue (highest) to red (deepest). It can be observed that while the average values are similar, the laser scans are much more detailed. The perimeter of each cathode block can be seen as areas of less wear in the laser scans. Obviously, this information is lacking in the recordings from the manual method.

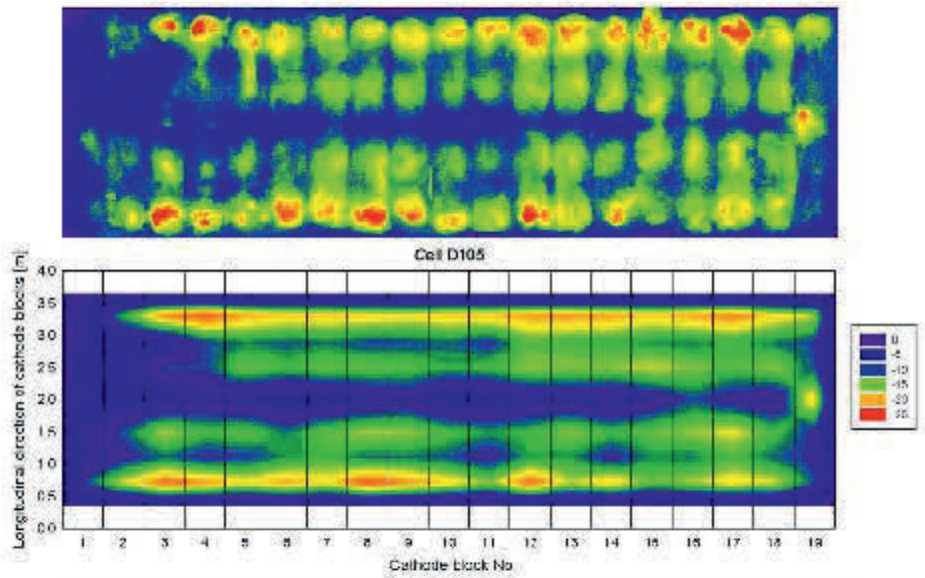

Figure 8. Comparison of the laser scanning method (top) and the manual measurement method (bottom) of cell D105.

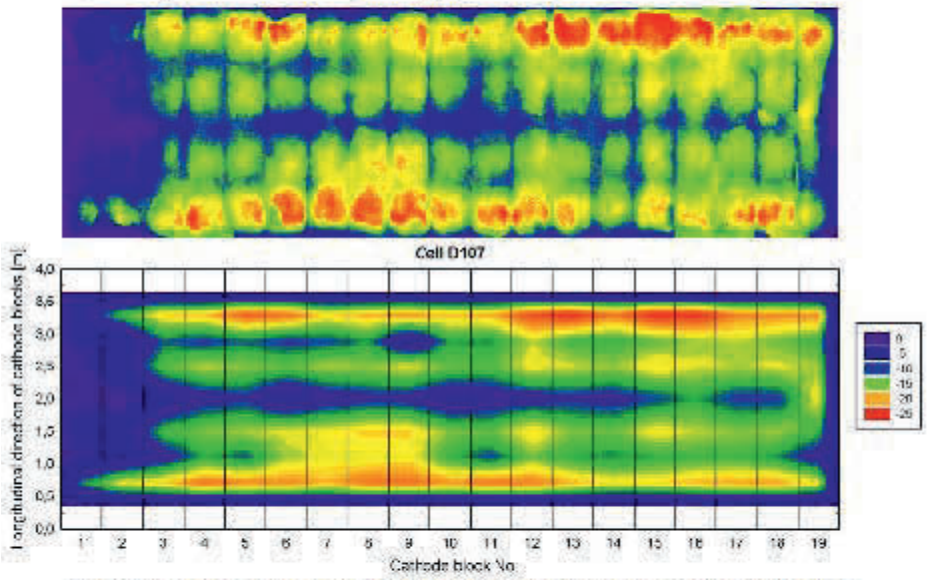

Figure 9. Comparison of the laser scanning method (top) and the manual measurement method (bottom) of cell D107.

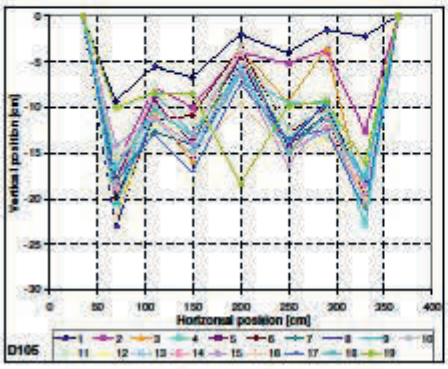

Figure 10. Wear profile of all 19 cathode blocks in cell D105, manual measurements method.

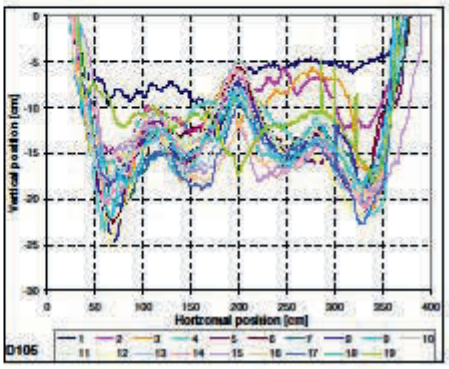

Figure 12. Wear profile of all 19 cathode blocks in cell D105, laser scan method.

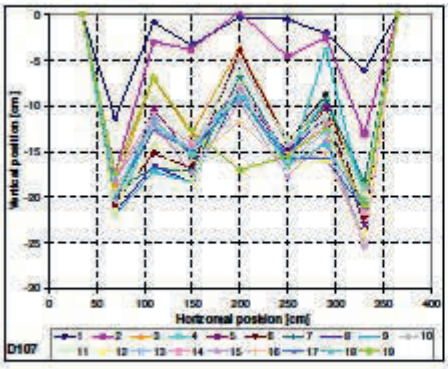

Figure 11. Wear profile of all 19 cathode blocks in cell D107, manual measurements method.

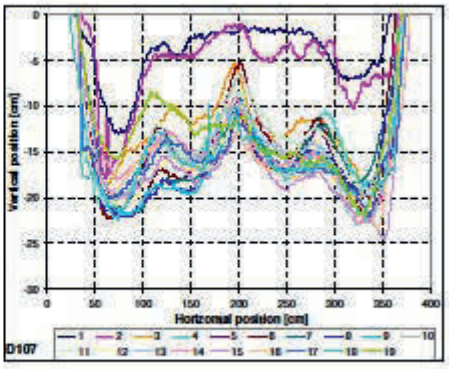

Figure 13. Wear profile of all 19 cathode blocks in cell D107, laser scan method.

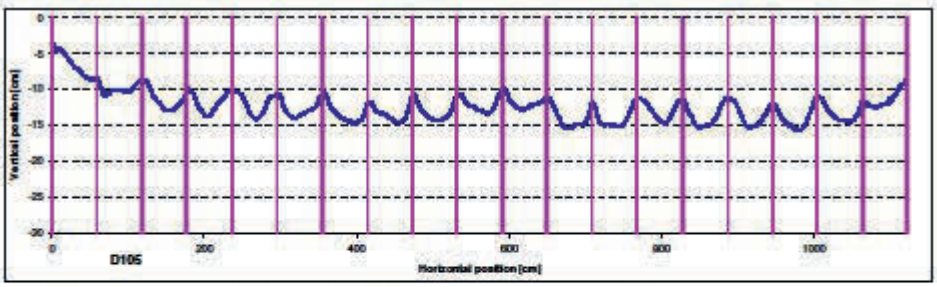

Figure 14. Wear profile lengthwise of all 19 cathode blocks in cell D105, laser scan method. Vertical lines indicate cathode bar separation.

Wear Profiles, Laser Scanner and Manual Method

A plot of wear profiles on each single cathode block numbered from 1–19 for the two cells by the manual method and laser scanning is shown in Figures 10–13. The initial cathode level before operation is used as reference and cathode heave has not been taken into account. Positive values mean that the cathode level after operation is higher than the initial level, which is a result of cathode heave. By assuming that the contribution of cathode heave is the same for all the measuring points, the cathode wear plots show good correlation with the real wear pattern of the cell.

Line plots of the data set from the manual method in the longitudinal direction of each cathode block reveal a general trend for both cells; a WW-profile, as shown in Figures 10 and 11. The same trend can be seen from the plots obtained from the laser scanning data shown in Figures 12 and 13. Cathode blocks no. 1, 2 and 19 stand out; 1 and 2 being less worn and 19 more worn in the mid section of the block. Cathode block no. 19 is located at the metal tapping end of the cell, while block no. 1 is at the suction end. Figures 15 and 16 compare line plots from the two methods for two single cathode blocks.

A plot of the wear profile in the longitudinal direction of the entire cathode is shown in Figure 14. It is evident that the ramming paste between the graphitic cathode blocks is less worn.

Summary

The laser scanning method gives several advantages:

- Much more detailed measurements than the manual method.
- The detailed wear pattern and shape of the cathode surface can easily be visualized in several ways.
- The high resolution makes it possible to zoom in and study local areas inside the cell (for instance tap pot holes or other local areas of interest).
- Wear profile plots can easily be made with high accuracy at different positions within the cathode surface inside the cell.
- Local areas of high wear (weak points of the cathode) are easily found.
- If the extent of cathode heave is known, the average cathode wear rate and the total carbon consumption can be easily and accurately estimated.

The more detailed measurements give more information and may provide more knowledge regarding cathode wear phenomena. Especially when considering modelling data of metal flow, cathodic current density, alumina distribution and also type of cathodes and linings the wear can be explained in a better manner than before. We regard that this method will be a valuable tool in deriving the mechanism for cathode wear in aluminium cells.

Acknowledgement

Thanks to Hydro and Research Council of Norway for financing the work through the research program Process Innovations for High Current Density (PI-HCD). Permission to publish the work is gratefully acknowledged.

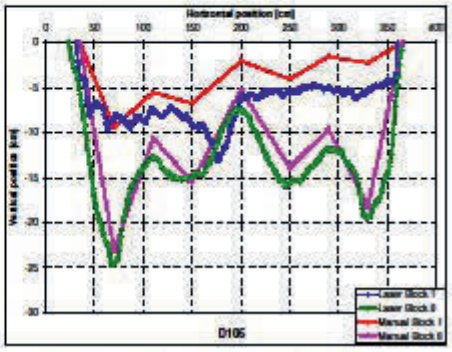

Figure 15. Wear profiles of two selected cathode blocks in cell D105, comparing laser scan and manual measurement methods.

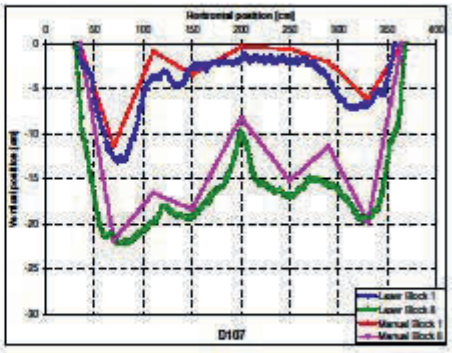

Figure 16. Wear profiles of two selected cathode blocks in cell D107, comparing laser scan and manual measurement methods.

Thanks to Alf Inge Ulvund and Tore Engen (Alf Engen AS) for design and construction of the steel frame for placement of the laser scanner instrument and all help and good advice during the scanning procedures. We appreciate also the assistance from the following personnel at the Hydro Sunndal plant: Jana Hajasova, Svein Kåre Sund, and Anders Børste.

References

[1] M.Sørlie, H.A.Øye, "Cathodes in Aluminium Electrolysis", 3rd edition, Aluminium Verlag 2010.
[2] P.Reny, S.Wilkening, "Graphite cathode wear study at Alouette", Light Metals 2000, pp 399-405.
[3] http://www.riegl.com (1.9.2010).

Proceedings of the 10th Australasian Aluminium Smelting Technology Conference.

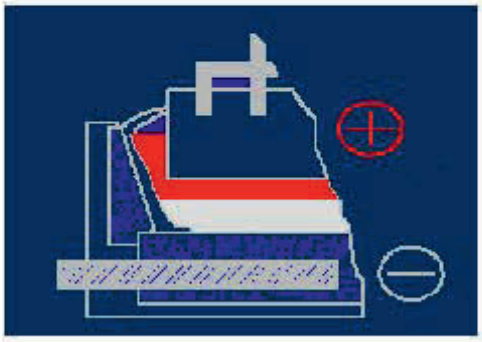

Launceston, Australia
9th to 14th October 2011.

Editors: Barry Welch, Gretta Stephens, Jim Metson and Maria Skyllas-Kazacos

ISBN: 978-0-7334-3054-1

Organised by:
The Australasian Aluminium Industry:
Alcoa of Australia
Hydro Kurri Kurri
Rio Tinto Alcan

In conjunction with:

The University of New South Wales
School of Chemical Engineering

INVESTIGATIONS OF CATHODE WEAR PROFILES OBTAINED BY THE LASER SCANNER METHOD

Egil Skybakmoen, SINTEF Materials and Chemistry, Trondheim (Norway).
egil.skybakmoen@sintef.no
Stein Rørvik, SINTEF Materials and Chemistry, Trondheim (Norway)
stein.rorvik@sintef.no
Asbjørn Solheim, SINTEF Materials and Chemistry, Trondheim (Norway)
asbjorn.solheim@sintef.no
Øyvind Østrem, NTNU, Trondheim (Norway)
oyvind.ostrem@ntnu.no

Abstract

In order to investigate and document the typical non-uniform wear of graphitized cathodes in greater detail than by traditional methods, the cathode surface of two 300 kA industrial cells was characterized by means of a laser scanner. The laser scanner was used to produce a 3D representation of the cathode based, on three overlapping scans with an average resolution of about 1 cm. The wear pattern registered can be visualized in several ways; *e.g.*, as wear profiles at different positions inside the cells. Local areas with high wear rate can be accurately described, and the average cathode carbon consumption can be estimated. The wear pattern observed is discussed with respect to some process parameters.

Keywords: Cathode wear, wear profiles, laser scanning

Introduction

The cathode wear for graphitized cathodes represents a great challenge for the aluminium industry today, since it determines the lifetime of the cells. Actually, the cell lifetime has decreased the latest years in high amperage cells, after introducing graphitized cathodes to increase the current and the efficiency of the cells. This fact is of course unwanted; besides the cost related to re-lining of cells it also leads to more spent potlining (SPL).

In modern cells, the cathode wear appears to be very non-uniform. The wear is more pronounced at some locations at the cathode, and the cell is normally taken out of production when the metal contacts the cathode collector bars, which is detected by a sudden increase in the iron content in the metal. Normally, the cathode is stronger worn along the periphery, and this is described as "w-profile wear". In some cases, even a "ww profile" can be observed, as will be described later in the present paper.

The actual mechanisms behind the observed wear patterns are not clearly understood. In an attempt to understand more, it was decided to try to document the wear pattern in more detail by introducing laser scanning technology. The project was carried out by SINTEF/NTNU with support from Hydro and the Research Council of Norway. The method is described in detail by Skybakmoen *et al.* [1].

Laser scanning method used on cathode surfaces

Two cathodes from the SU4 line at the Hydro Sunndal smelter were investigated with respect to cathode wear. The design was similar for the two cells. The cathode panel consisted of 19 graphitic carbon blocks with ramming paste in between. Both cells were shut down due to high levels of iron in the metal. The cells were considered to be run under normal electrolysis conditions during the entire lifetime, which was 2088 days and 2184 days, respectively. Pictures of the cathode surfaces of both cells are shown in Figure 1. The cathode surfaces were thoroughly cleaned before measuring started.

a) Cell D 105 (2088 days) b) Cell D107 (2184 days)

Figure 1. Cathode surfaces of cell D105 (a) and Cell D107 (b).

A time-of-flight laser scanner, as the one used (Riegl LMS-Z420i [2]), measures the time t a laser pulse needs to travel from the sender unit to the target surface and back to the receiver unit, and thus the distance d can be calculated,

$$d = ct / 2 \qquad c: \textit{speed of light}$$

Together with known horizontal and vertical angles – analogous to tachymetry – 3D coordinates can be computed. The laser scanner was placed on a steel frame around 6 m above the cathode surface. The scan was performed at three different positions. Useless or even disturbing points were deleted and the data were merged to one single 3D point cloud (5.3 million points). By using the scanner related software *RiScan Pro* and other programs, various types of visualisation could be obtained, using points and/or the triangulated surface.

The laser scanner had a single point accuracy of 10 mm with a resolution of about 5 mm. The high resolution makes it possible to zoom in and study local areas inside the cell (for instance tap pot holes or other local areas of interest). Wear profile plots can easily be made with high accuracy at different positions within the cathode surface inside the cell, and local areas of high wear (weak points of the cathode) are easily found. If the extent of cathode heave is known, the average cathode wear rate and the total carbon consumption can be easily and accurately estimated.

The more detailed measurements give more information and may provide more knowledge regarding cathode wear phenomena. Especially when related to various kinds of data such as metal flow patterns (modelling and measured), cathodic current density, alumina distribution, and also type of cathodes and linings, the wear can be explained in a better manner than before. Therefore, the authors regard that the method will be a valuable tool in deriving the mechanism for cathode wear in aluminium cells.

Results and discussion: Analysis of laser scanning data

Overview: Topography plots

As already mentioned, the cells had 19 cathode blocks with ramming paste in between. Topography plots of the wear for the two cells is shown in Figure 2, and each cathode block is numbered from 1 (suction end) to 19 (tap end). The oldest cell (2184 days) shows generally more wear than the other (2088 days), but it can also be observed that the wear patterns are quite similar for both cathodes. The downstream part of the cell is generally more worn than the upstream part, block 19 at the tap end is worn in the middle (referred to as taphole) and block 1 and 2 at the suction end show little wear. The ramming paste in between the cathode blocks is less worn and protrudes by several centimetres, which is typical for graphitized cathodes.

Average wear and estimated amount of worn carbon

Based on the laser scanning data we can easily estimate the average wear and, therefore, also calculate the total carbon dissolved during the lifetime of the cell. The calculation was based on the difference between the original position and the actual position of the cathode surface. The density for virgin cathode material was used in the calculations, and the area of the cathodes was measured by the laser scanner. However, the cathode heave was not measured in the two cells, and it was not taken into consideration in the carbon wear calculation. Cathode heave is a phenomenon taking place during the entire cell life, and it has been observed that the cathode typically rises up to 5-10 cm in the middle part of the cell. Therefore, the amount of carbon dissolved shown in Table 1 is probably considerably underestimated.

The average wear rate of around 2.1 - 2.3 cm/year agrees well with a stationary mass transfer model, but higher wear rates must probably be explained by other mechanisms [3]. By comparing the data in Table 1 with the original height of the cathode carbon, it can be estimated that about 30 percent of the carbon is worn away (more, if the cathode heave is taken into consideration). The maximum wear in the most critical part of the cell was 27 cm for both the cells, corresponding to wear rates of 4.5 cm/year (D105) and 4.7 cm/year (D107). It is possible that the difference in wear rate is related to different extents of cathode heave.

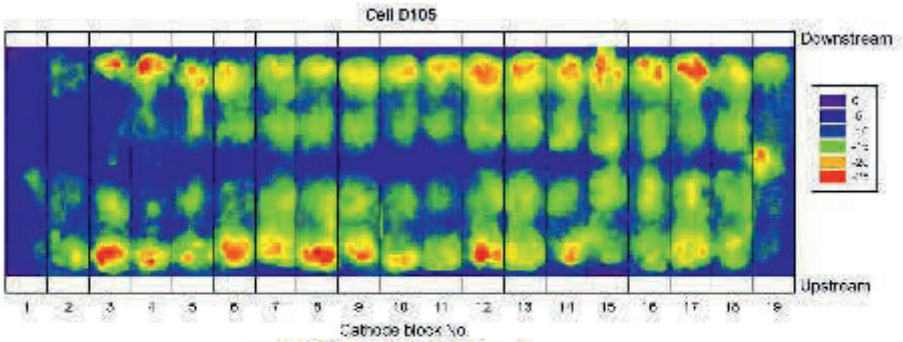

a) Cell D 105 (2088 days)

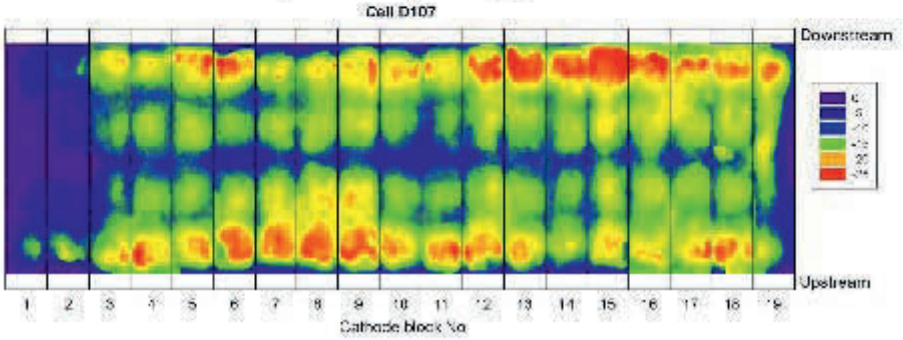

b) Cell D 107 (2184 days)

Figure 2. Topography plots of cell D105 (a, 2088 days), cell D107 (b, 2184 days). The wear depth is given in cm.

Table 1. Average wear and estimation of total carbon dissolved for cell D105 and D107.

Cell	Age (days)	Avg. wear (cm)	Wear pr year (cm)	Total C (kg)	C per day (kg)
D105	2088	12.35	2.1	8024	3.8
D107	2184	13.76	2.3	8940	4.1

Wear profiles for different cathode blocks

The wear profile for each cathode block can easily be visualized. Examples are shown in Figure 3 and Figure 4, where the wear profiles are shown for cathode block no. 2, 8 and 12 for the two cells. The data shown is the average wear along a 12 cm wide strip along the middle part of the cathode block.

As can be observed, the wear depth for block no. 2 is smaller than the wear depths for block no. 8 and block no. 12 for both the cells. The wear profiles for block no. 8 and 12 follow a typical ww-profile.

It is believed that an area at the suction end of the cell has relatively low metal flow. Sludge and particles will typically settle in such areas with low metal velocities, leading to higher electrical resistance by reduction of the accessible surface. In the case where the sludge lies stationary at the cathode surface for longer time intervals, it will inhibit dissolution of aluminium carbide [3]. This may explain the low wear at cathode blocks 1 and 2. This theory is supported by current distribution measurements conducted after two years of operation, where the current collector bars in blocks 1 and 2 was observed to draw lower current than the rest of the collector bars.

At cathode block 19 metal tapping is regularly performed, which induce metal flow and thus higher wear, explaining the observed taphole.

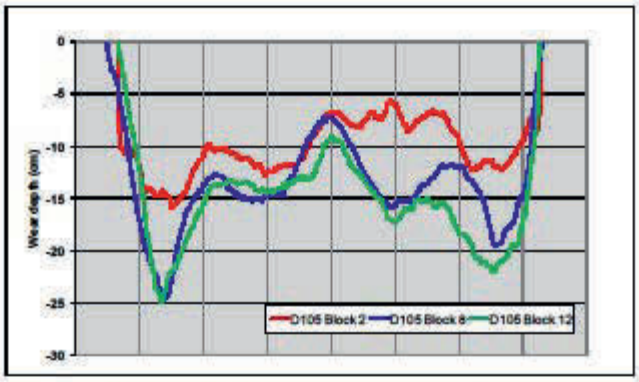

Figure 3. Wear profiles for cathode no. 2, 8 and 12 in cell D105.

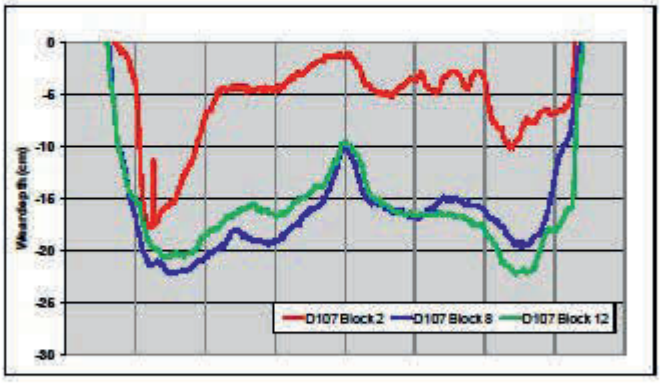

Figure 4. Wear profiles for cathode no. 2, 8 and 12 in cell D107.

A direct comparison between profiles at the same positions for the two cells is provided in Figures 5 and 6. As can be observed, cell D 107 is more worn, but the wear pattern is slightly more uniform.

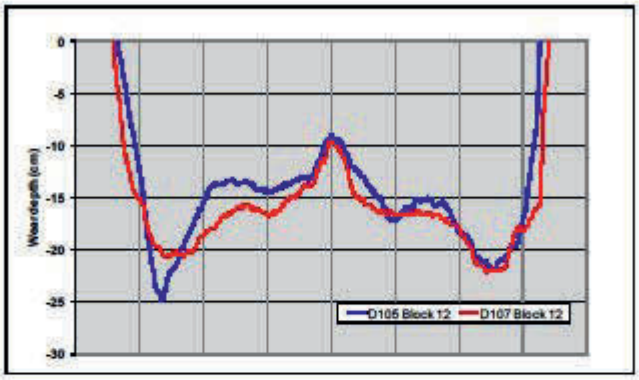

Figure 5. Wear profiles for block no. 12 for cell D105 and D107.

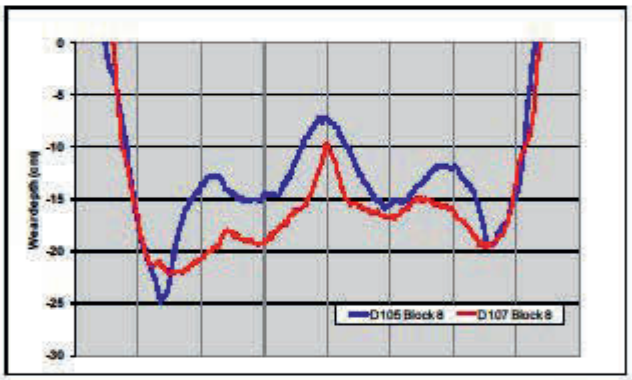

Figure 6. Wear profiles for block no. 8 for cell D105 and D107.

Average wear, downstream and upstream

The average wear was estimated for the downstream half and the upstream half of each cathode block. The result is shown in Figures 7 and 8. As can be observed, there is a tendency that the upstream end of the cathode block is more worn at the suction end of the cell, while the downstream end of the cathode block is more worn at the tap end of the cell. This is also illustrated in Table 2 and Figure 9, which shows the average wear in the four quadrants in the two cells.

This peculiar pattern can, possibly, be related to the metal flow in the cells. Since we do not have reliable measured and calculated metal flow patterns, we cannot elaborate further on this.

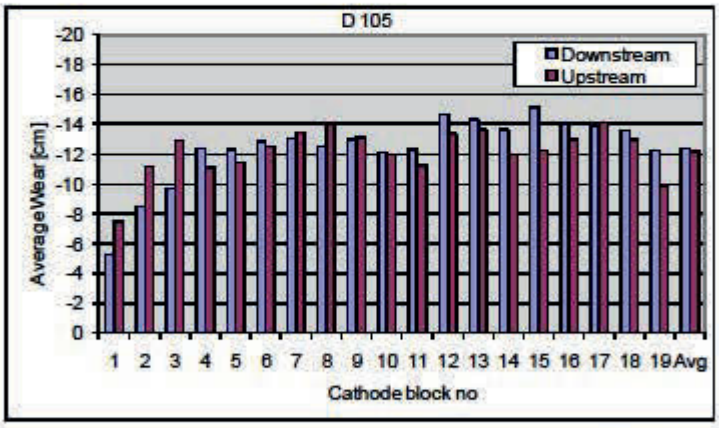

Figure 7. Average wear downstream and upstream in cell D105.

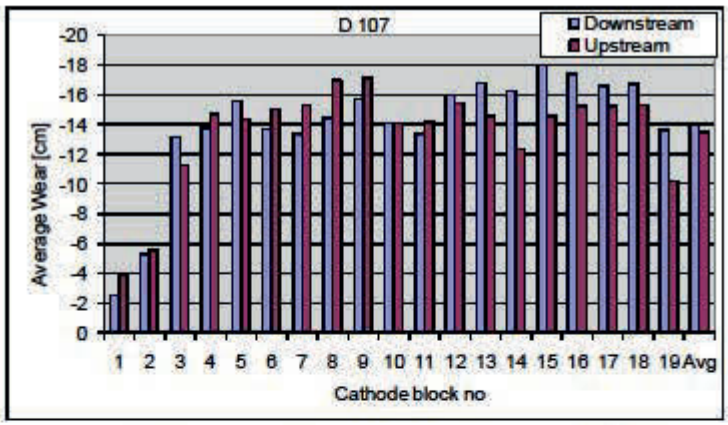

Figure 8. Average wear downstream and upstream in cell D107.

Table 2. Average wear for the four quadrants of the cathodes in the two cells.

	Average Wear, Downstream (cm)	Average Wear, Upstream (cm)
D105, suction end	-11.18	-11.92
D105, tap end	-13.74	-12.48
D107, suction end	-12.15	-12.82
D107, tap end	-16.05	-14.10

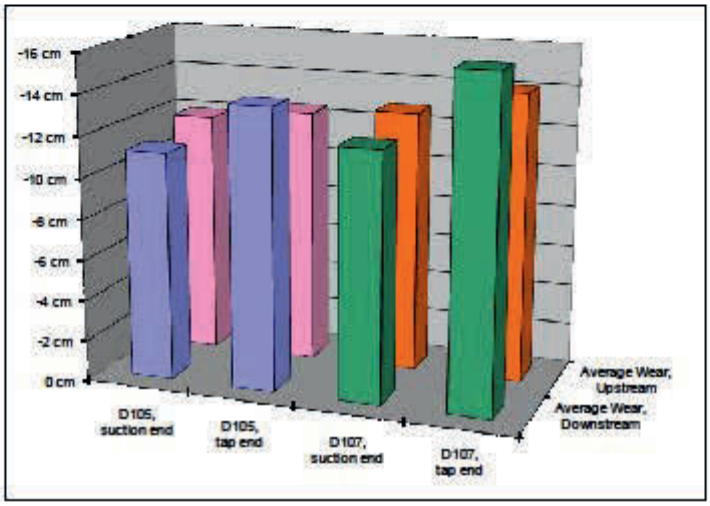

Figure 9. Average wear for the four quadrants of the cathodes in the two cells.

Protruding ramming joints

The anthracite based ramming paste in between the cathode blocks is less worn and protrude by several centimetres. This is typical for graphitized cathodes and the phenomena can be explained by different mechanical and electrical properties of the two materials. The anthracitic ramming joints are harder than the graphitized blocks and more resistant to abrasion, and higher electrical resistance gives lower current densities at the joints, which gives lower electrochemical wear.

Cathode wear and cathodic current density

The current passing through each cathode block was measured after 2 years of operation. Based on those measurements, we have investigated the relationship between maximum wear and current density on each cathode. The relationship is shown in Figure 10. The data show that the downstream side of the cell draws somewhat more current, and there seems to be a

weak correlation between the current and the maximum wear. However, if the cathode blocks with the lowest wear are skipped (blocks 1 and 2), the relationship is less clear.

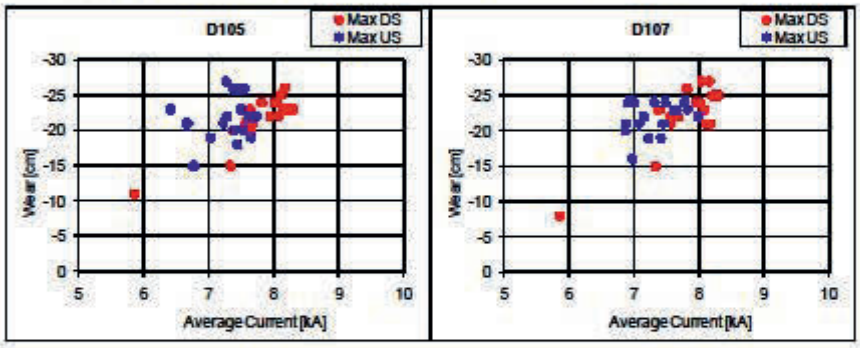

Figure 10. Maximum wear as a function of the current through each cathode block, downstream and upstream.

Cathode wear and alumina feeding

The cells contained five point feeders with locations as shown in Figure 11. As can be observed, there is a tendency that there is less wear nearby the feeders. The reason might be formation of a heap of sludge underneath the feeders, which protects the cathode by slowing down the dissolution of carbon [3].

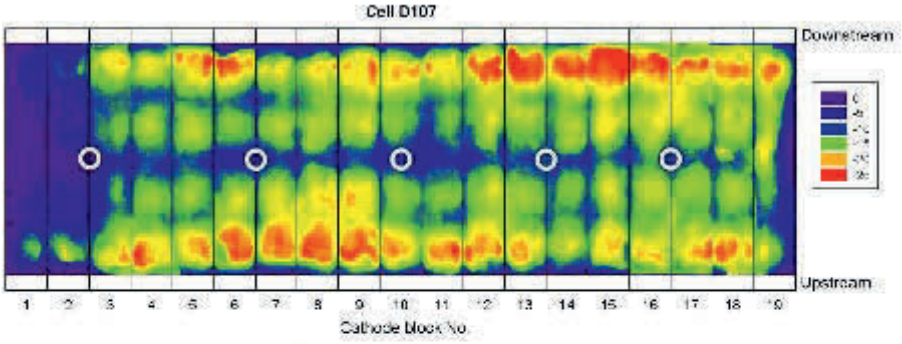

Figure 11. Location of point feeders, cell D107.

Concluding remarks

As already mentioned, it is the authors' opinion that the laser scanning method may become a valuable tool in deriving the mechanism for cathode wear in aluminium cells. However, the full potential of the method can only be reached by combination of different sources of information in a much more comprehensive way than hitherto. Besides the need for measurements in different cell technologies including different types of cathode carbon, the wear data should be correlated with all kinds of operational data, including the history of the cathodic current distribution, flow patterns in the metal and in the bath, and side- and bottom ledge thicknesses. An interesting parameter that should be mapped, if possible, is the amount and distribution of sludge at the cathode bottom.

Acknowledgement

The initial work with developing the laser scanning method was carried out in the research program Process Innovations for High Current Density (PI-HCD), financed by Hydro Primary Metal Technology and the Research Council of Norway. Further investigations to reveal the potentials of the method was carried out in the project Durable Materials in Primary Aluminium Production (DuraMat), financed by the Research Council of Norway, Hydro Primary Metal Technology, Sør-Norge Aluminium, and Elkem Carbon. Permission to publish the results is gratefully acknowledged.

Knut Ragnar Holm (NTNU) and Priska Tiefenbach (NTNU) were strongly involved in the development of the laser scanning method, and they also participated in the measurements at the Hydro Sunndal plant. The assistance by personnel at Hydro Sunndal is highly appreciated.

References

[1] E. Skybakmoen, S. Rørvik, A. Solheim, K. R. Holm, P. Tiefenbach and Ø. Østrem, "Measurement of Cathode Surface Wear Profiles by Laser Scanning", *Proceedings Light Metals 2011*, San Diego, pp 1061-1066.

[2] http://www.riegl.com (1.9.2010)

[3] A. Solheim, "Some Hypotheses Concerning Cathode Wear in Aluminium Electrolysis Cells", MetSoc's Annual Conference of Metallurgists (COM 2011), Montreal, Canada, 2-5 October, 2011.

Appendix B

Thermodynamic data

The Gibbs free energies of formation that are used for thermodynamic calculations in this work are presented in Table B.1. Thermodynamic data for Al_4C_3 from Barin [67] are listed in Table B.2.

Table B.1: Gibbs free energies of formation at 1000°C.

Specie	$\Delta_f G^0$ [J/mol]	Ref.	Comment
Al_4C_3	-135419	Lihrmann et al. [78]	
Al_4O_4C	-1750961	Lihrmann et al. [78]	
Al_2O_3	-1271041	Lihrmann et al. [78]	
NaF	-435411	Barin [67]	Extrapolated
Na_3AlF_6	-2589883	Barin [67]	Extrapolated
$NaAlO_2$	-842408	Barin [67]	Extrapolated
AlF_3	-1179261	Barin [67]	Extrapolated
$Na_3Al_3CF_8$	-3487767	Ødegård [25]	Extrapolated

Table B.2: Thermodynamic data for Al_4C_3 (s) [67].

T [K]	C_p [J/(K mol)]	S [J/(K mol)]	-(G-H298)/T [J/(K mol)]	H [kJ/mol]	H-H298 [kJ/mol]	G [kJ/mol]	ΔH_f [kJ/mol]	ΔG_f [kJ/mol]	Log K_f [–]
298.15	116.075	88.952	88.952	-208.798	0.000	-235.319	-208.798	-196.464	34.420
300.00	116.709	89.672	88.954	-208.583	0.215	-235.484	-208.810	-196.387	34.194
400.00	139.969	126.852	93.865	-195.603	13.195	-246.344	-208.969	-192.202	25.099
500.00	152.278	159.525	103.806	-180.938	27.860	-260.701	-208.861	-188.024	19.643
600.00	160.277	188.038	115.52	-165.287	43.511	-278.110	-208.970	-183.852	16.006
700.00	166.241	213.211	127.714	-148.950	59.848	-298.197	-209.435	-179.634	13.404
800.00	171.12	235.737	139.833	-132.075	76.723	-320.665	-210.340	-175.321	11.447
900.00	175.368	256.142	151.64	-114.746	94.052	-345.274	-211.863	-170.860	9.916
1000.00	179.224	274.821	163.038	-97.014	111.784	-371.836	-256.269	-163.156	8.522
1100.00	182.825	292.074	173.994	-78.910	129.888	-400.191	-257.431	-153.787	7.303
1200.00	186.251	308.129	184.51	-60.455	148.343	-430.210	-258.412	-144.320	6.282
1300.00	189.555	323.169	194.604	-41.664	167.134	-461.815	-259.195	-134.780	5.416
1400.00	192.769	337.334	204.298	-22.547	186.251	-494.815	-259.765	-125.187	4.671
1500.00	195.918	350.742	213.618	-3.112	205.686	-529.225	-260.107	-115.560	4.024
1600.00	199.016	363.485	222.59	16.635	225.433	-564.941	-260.211	-105.919	3.458
1700.00	202.076	375.642	231.238	36.690	245.488	-601.902	-260.068	-96.279	2.958
1800.00	205.106	387.279	239.586	57.049	265.847	-640.052	-259.669	-86.655	2.515

Appendix C

Typical EDS analysis results

Some examples of typical EDS results for different species found in cathode samples and appurtenant micrographs are presented in the following.

Table C.1: Examples of typical EDS results for species found in the cathode samples. Micrographs showing the analysed areas are shown in Figures C.1–C.5.

Compound	From fig.	EDS results [at%]							
		C	O	F	Na	Al	Si	Ca	Fe
Al_4C_3	C.1	52.5	2.0	1.4	0.7	43.4			
Al_2O_3	C.2	1	64.6			34.4			
Na_3AlF_6	C.3	12.6		61.8	19.6	6			
CaF_2	C.4	12.0		57.0		12.4		18.6	
Iron	C.5	6.1				27.7	9.8		56.4

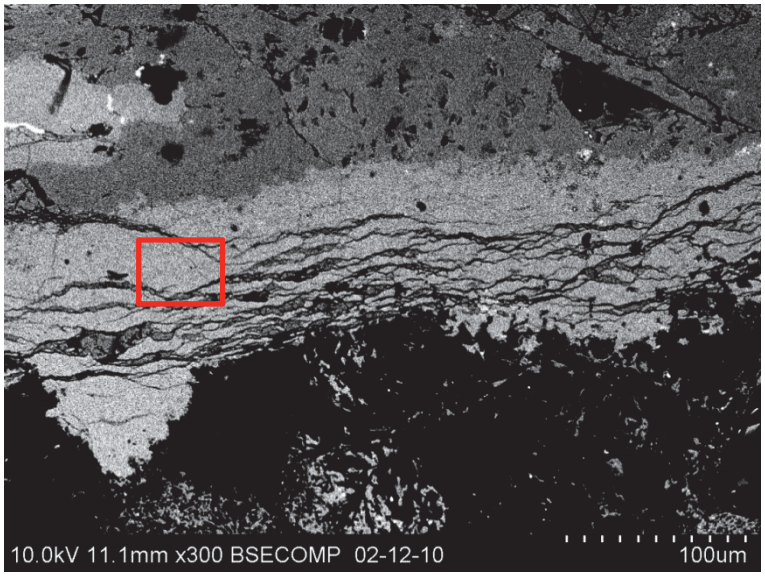

(a)

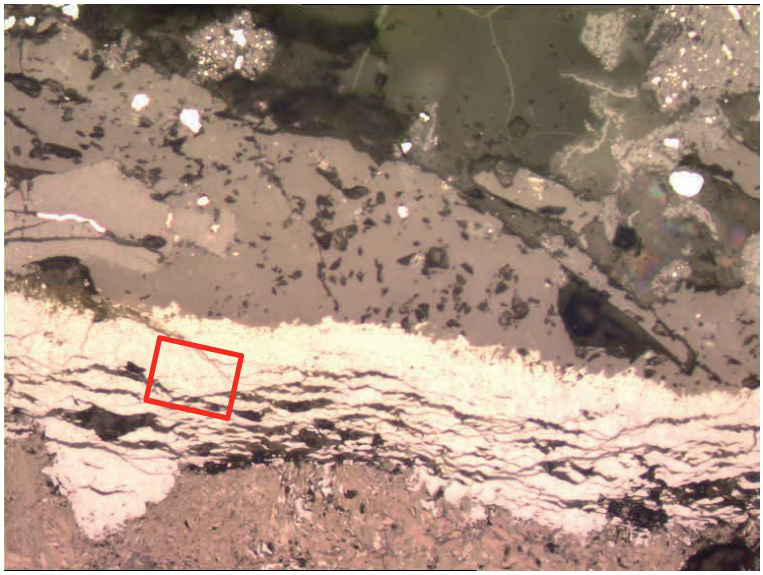

(b)

Figure C.1: (a) SEM and (b) optical micrograph of aluminium carbide layer. Red box marks the area analysed by EDS.

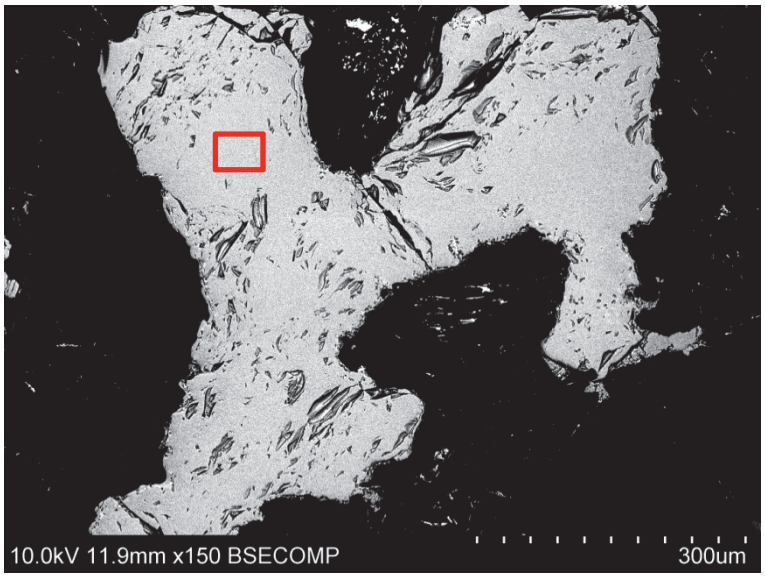

(a)

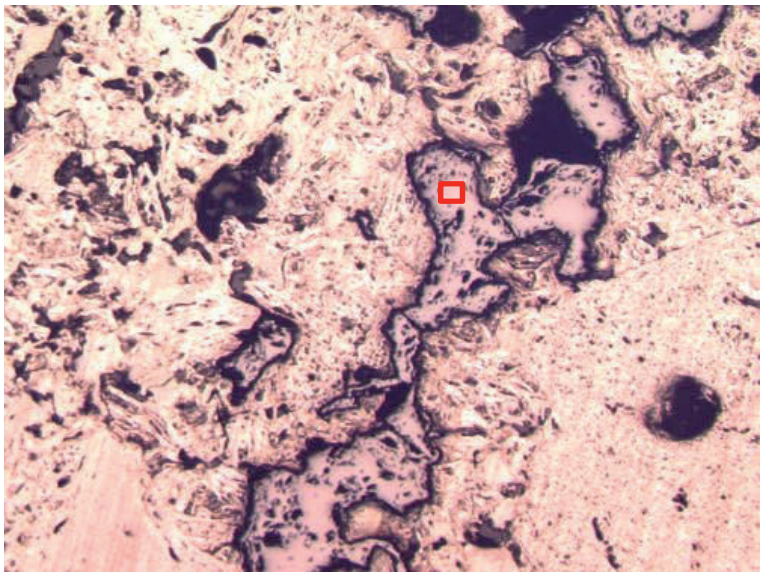

(b)

Figure C.2: (a) SEM and (b) optical micrograph of aluminium oxide in a pore in a cathode sample. Red box marks the area analysed by EDS.

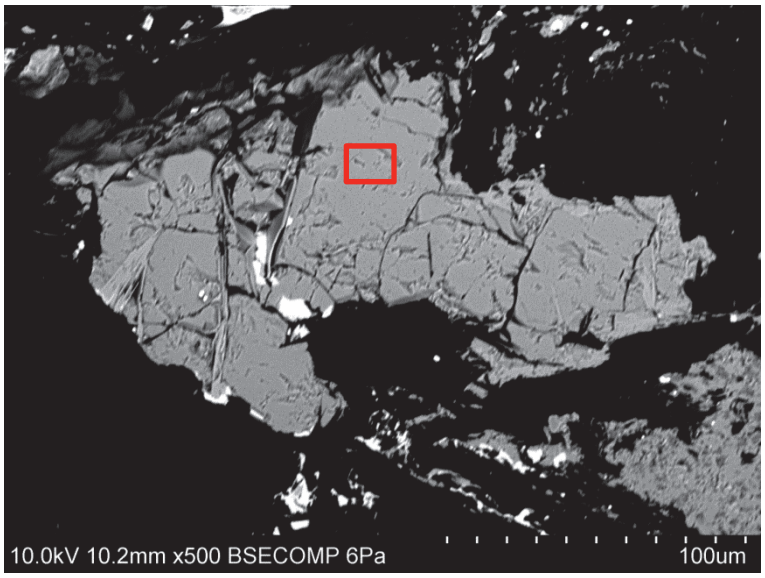

(a)

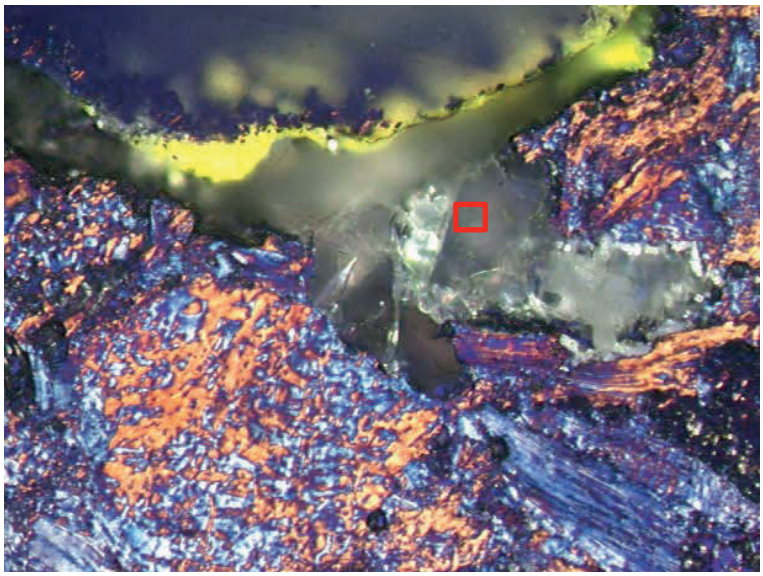

(b)

Figure C.3: (a) SEM and (b) optical micrograph of bath (cryolite) in a superficial pore in a cathode sample. Red box marks the area analysed by EDS.

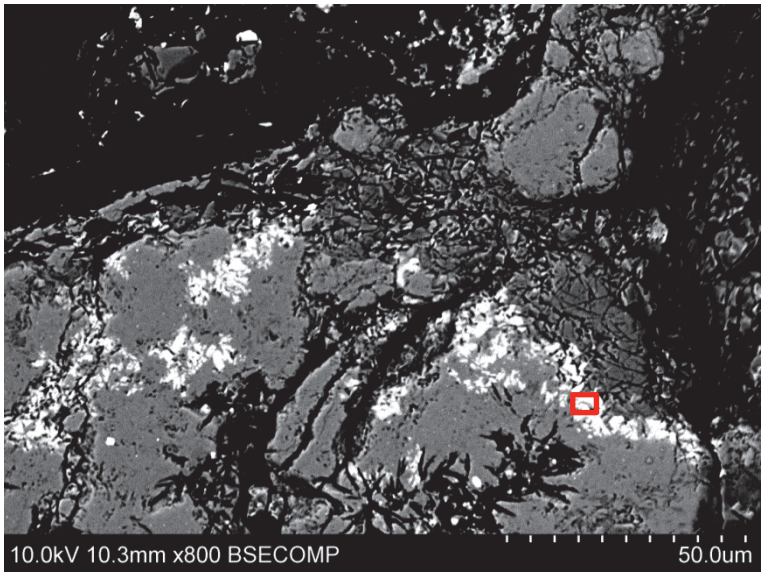

(a)

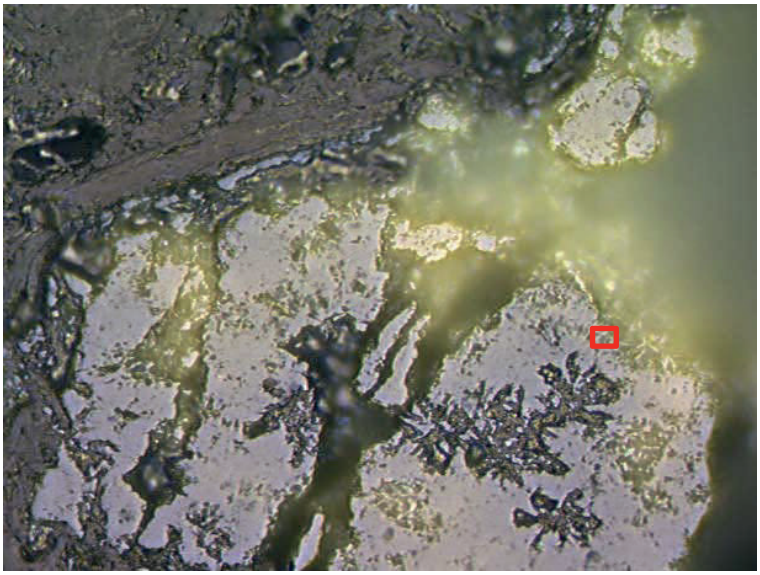

(b)

Figure C.4: (a) SEM and (b) optical micrograph of bath and calcium fluoride in a pore in a cathode sample. Red box marks the area analysed by EDS.

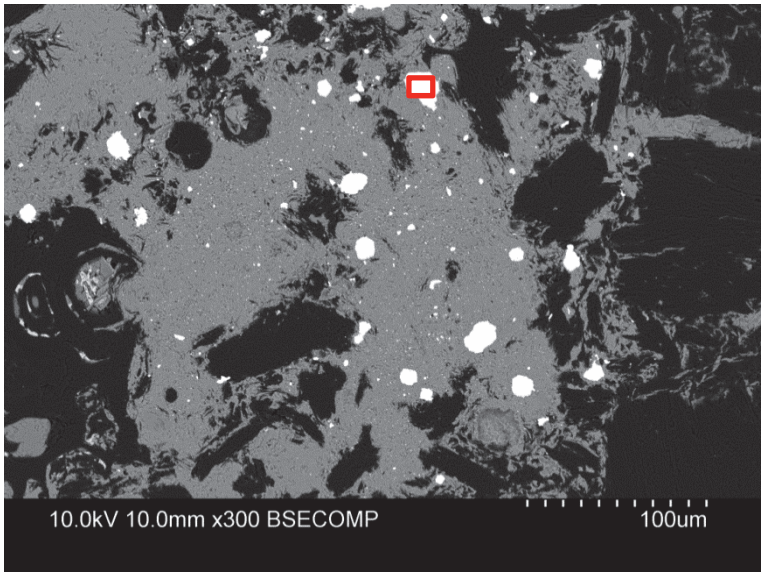

(a)

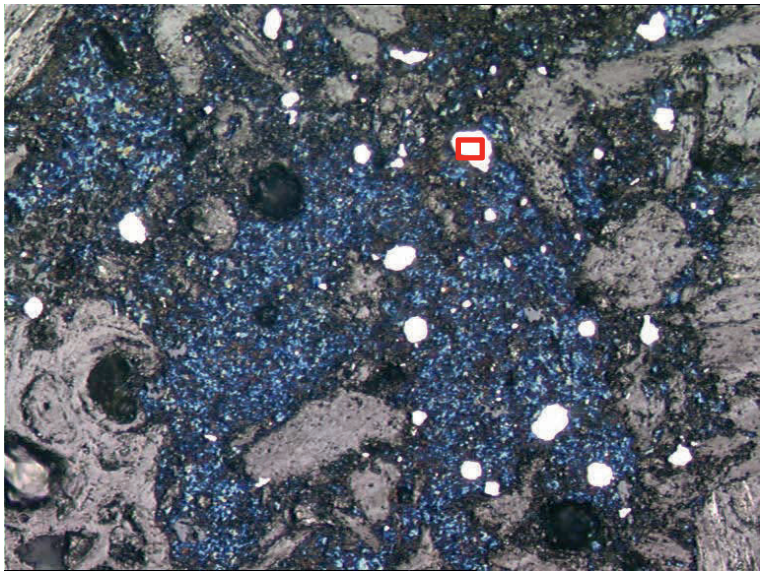

(b)

Figure C.5: (a) SEM and (b) optical micrograph of iron rich metal droplets enclosed in aluminium carbide in a pore in a cathode sample. Red box marks the area analysed by EDS.

Appendix D

Additional micrographs

Some additional micrographs of samples from industrial cathodes are presented in the following. Directions for interpretation of the micrographs are found in Section 5.3.

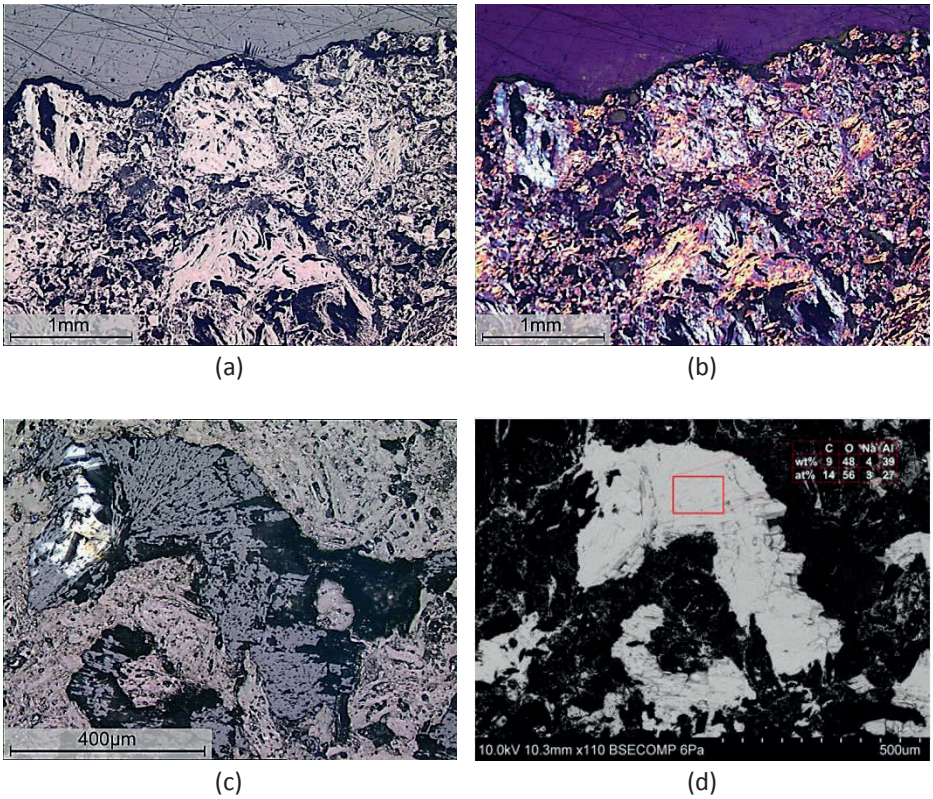

(a) (b)

(c) (d)

Figure D.1: Micrographs from low wear areas of a GZ cathode. (a and b) Surface without carbide layer. (c and d) Pore with alumina and possibly aluminium oxycarbide.

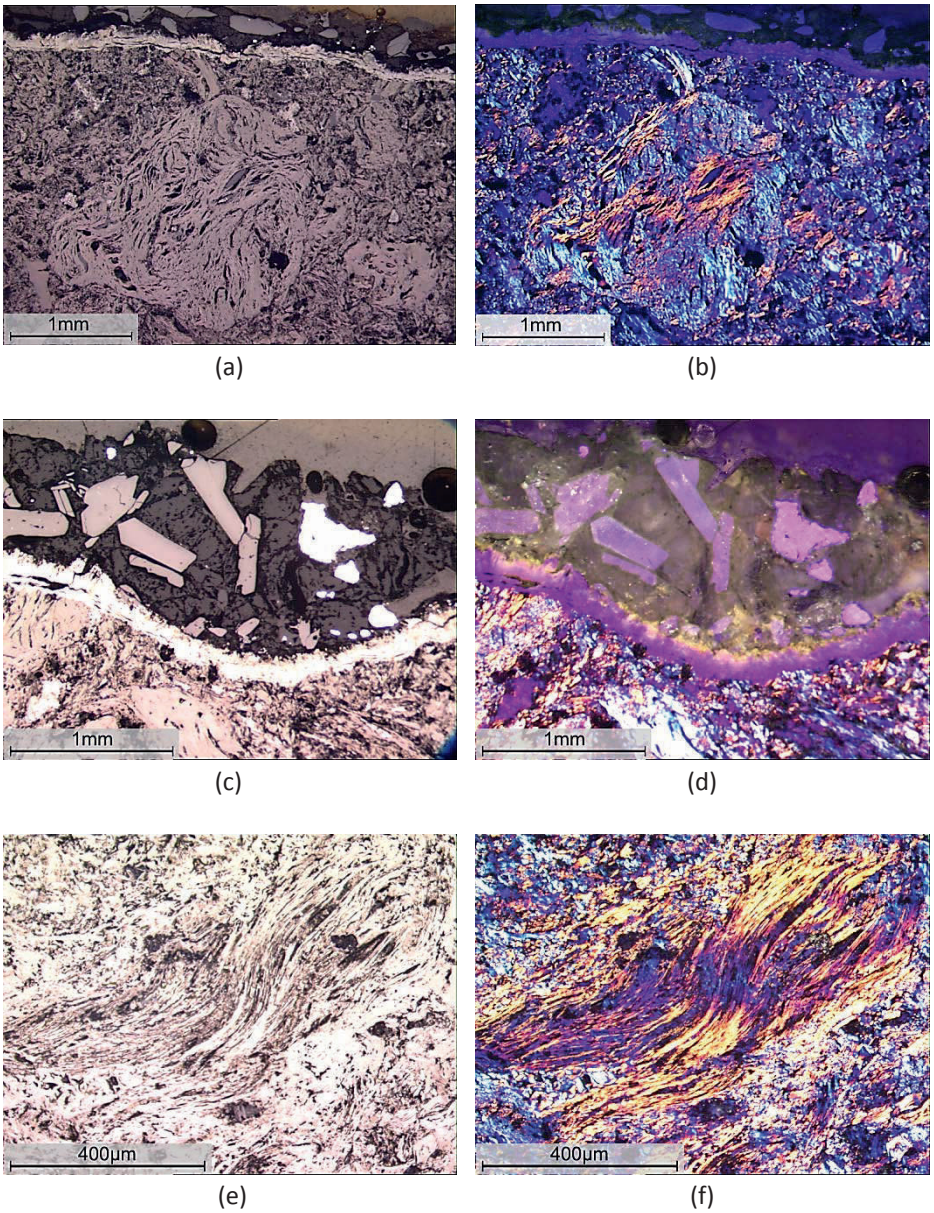

Figure D.2: Micrographs from low wear area of a GZ cathode. (a–d) Surface with carbide layer, protected by a layer of bath with alumina particles and aluminium metal. (e and f) Carbon microstructure within the sample.

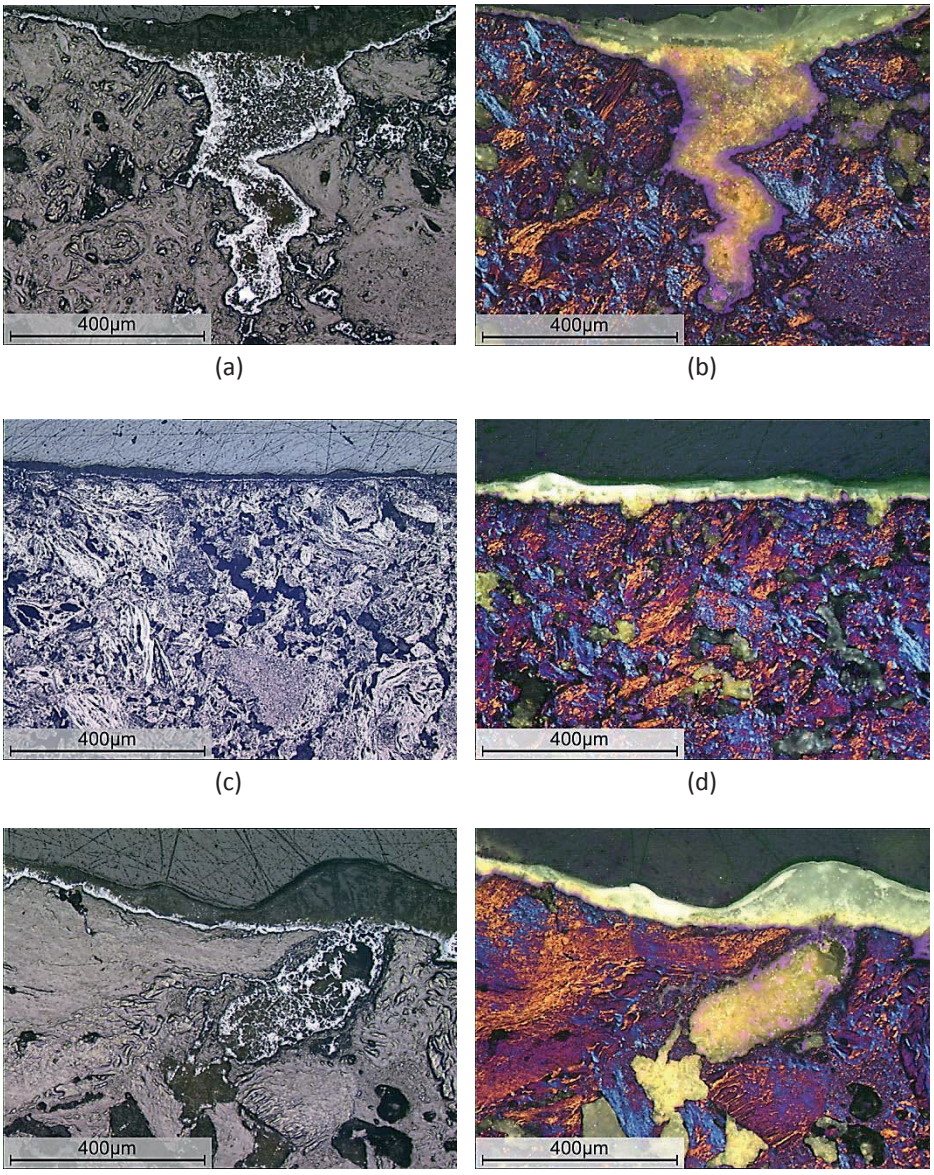

Figure D.3: Micrographs of cathode surface from high wear areas of a GZi cathode.

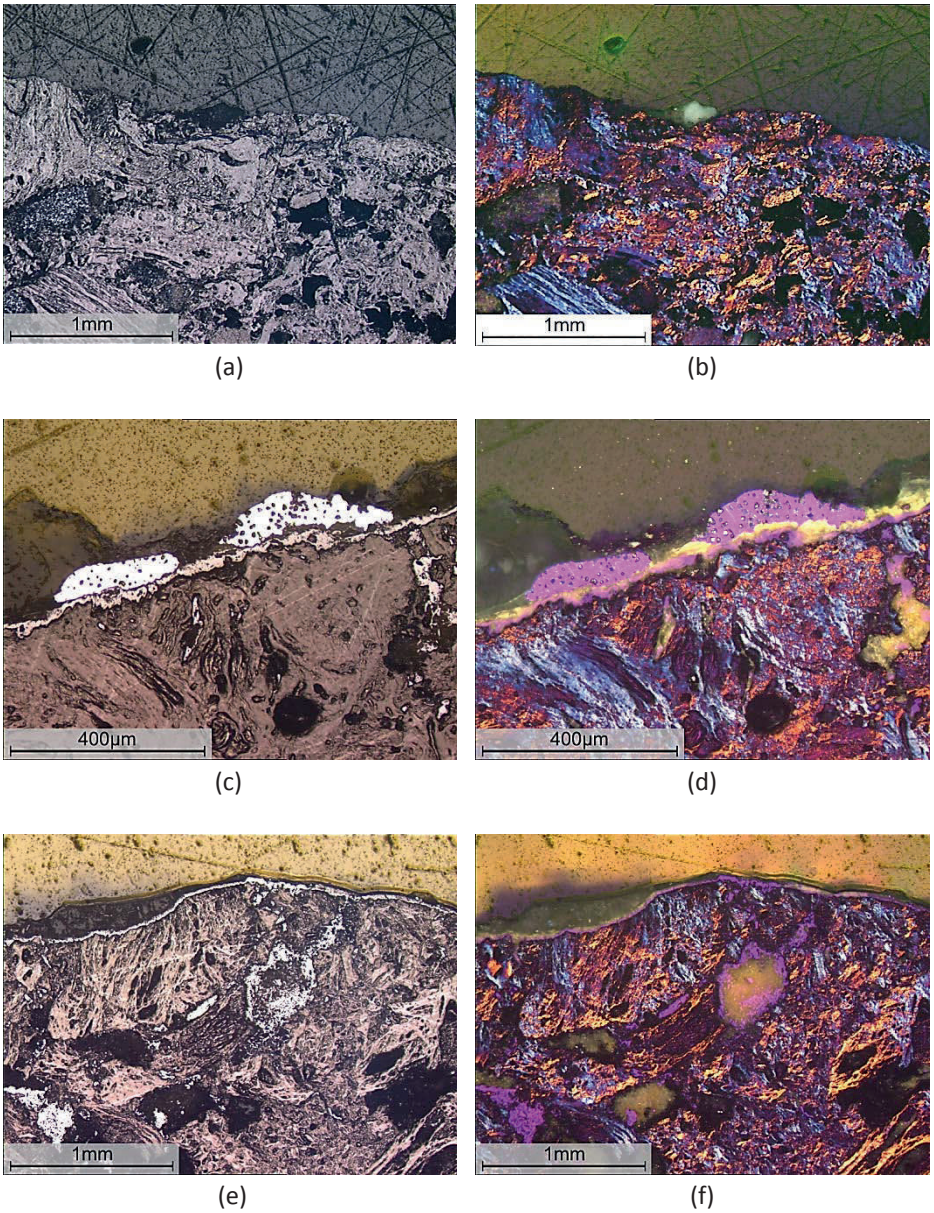

Figure D.4: Micrographs of cathode surface from low wear areas of a GZi cathode.

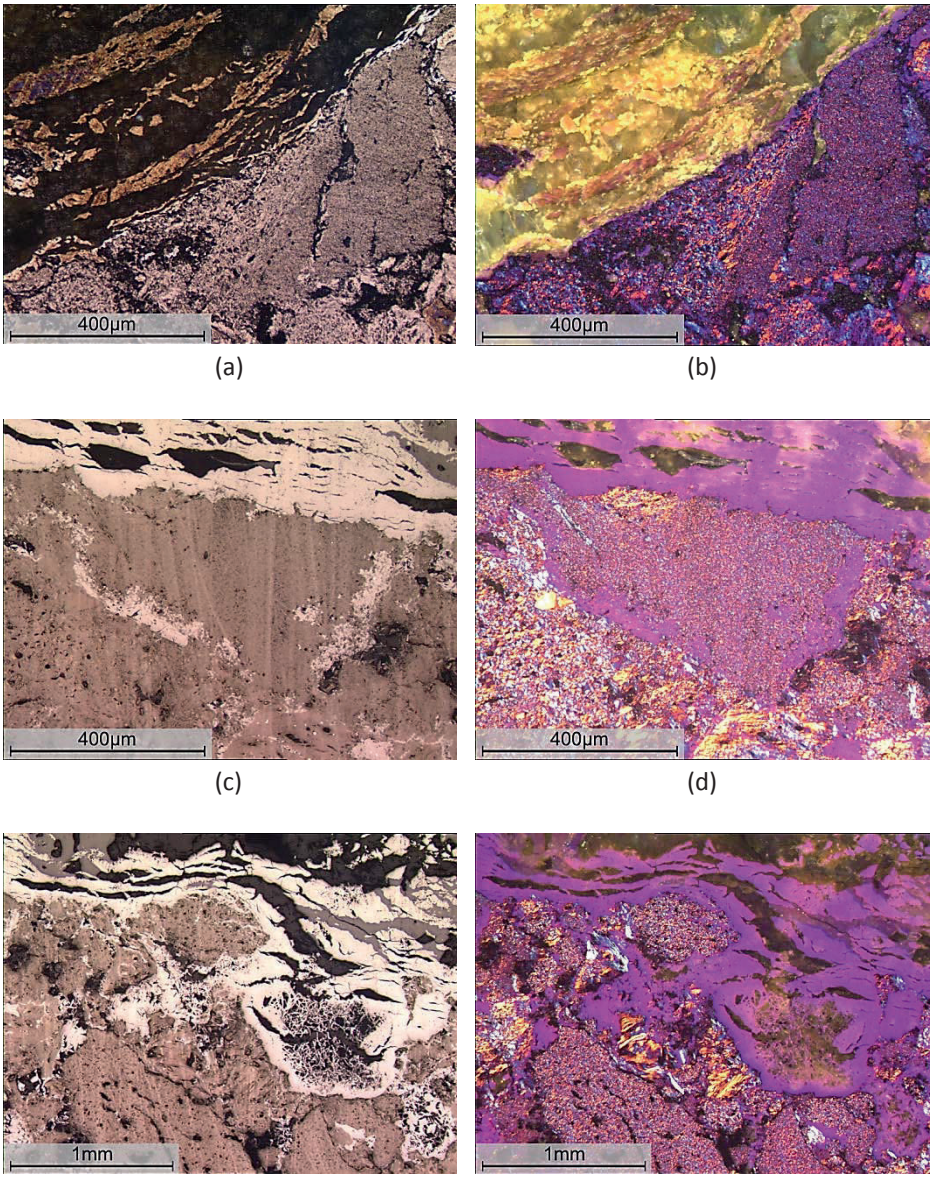

(a) (b)

(c) (d)

(e) (f)

Figure D.5: Micrographs of cathode surface from high wear areas of a SGZi cathode.

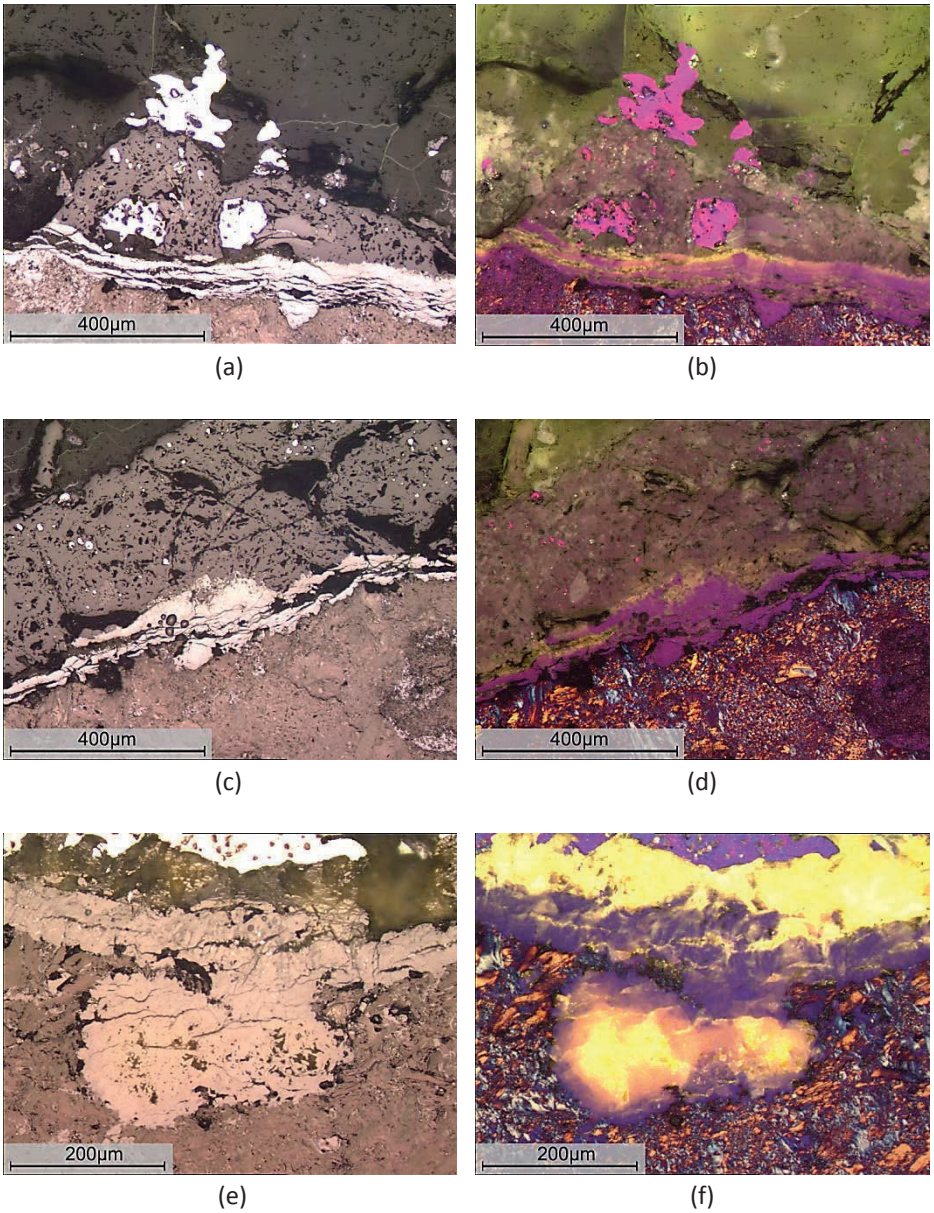

(a) (b)

(c) (d)

(e) (f)

Figure D.6: Micrographs of cathode surface from low wear areas of a SGZi cathode.

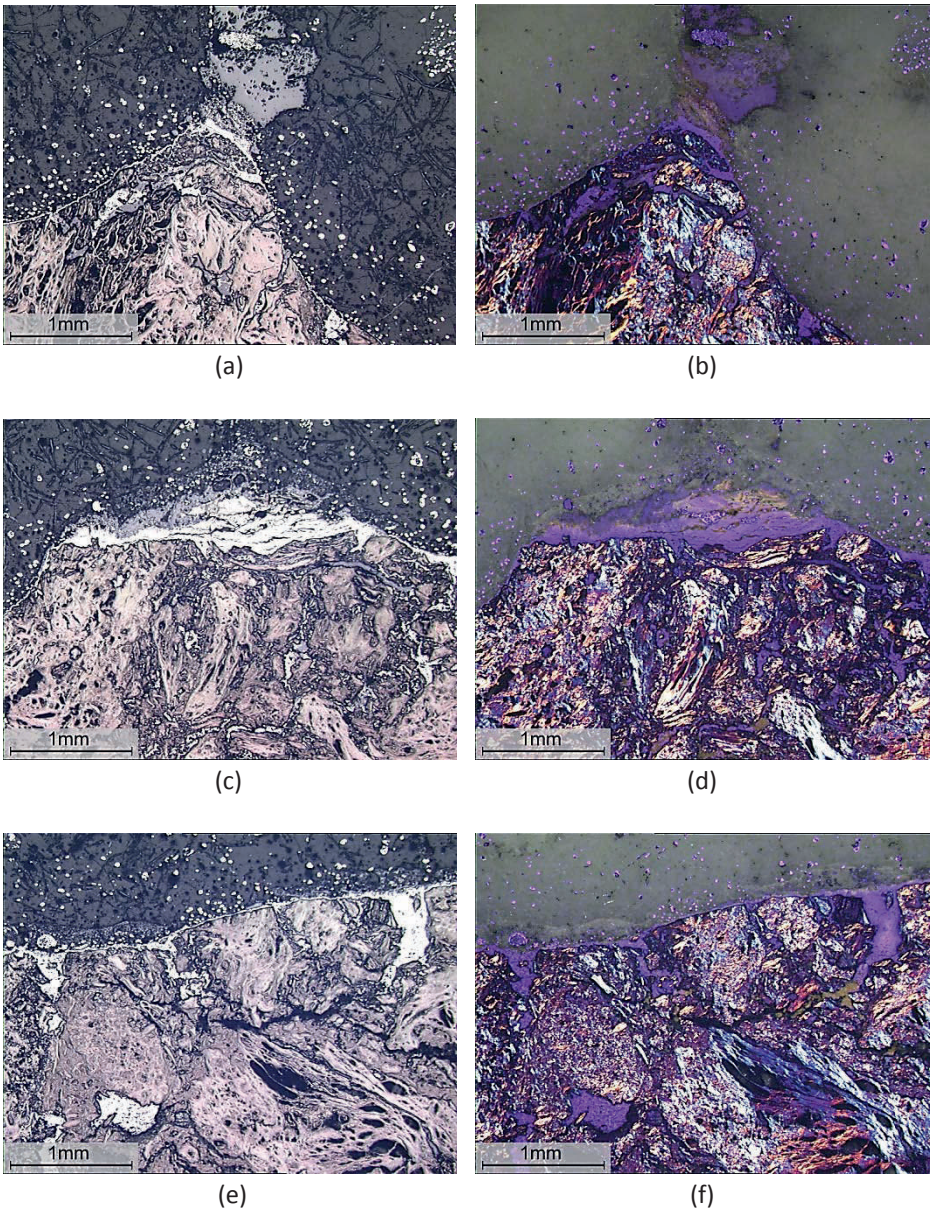

Figure D.7: Micrographs of cathode surface from high wear areas of a SGZv cathodes.

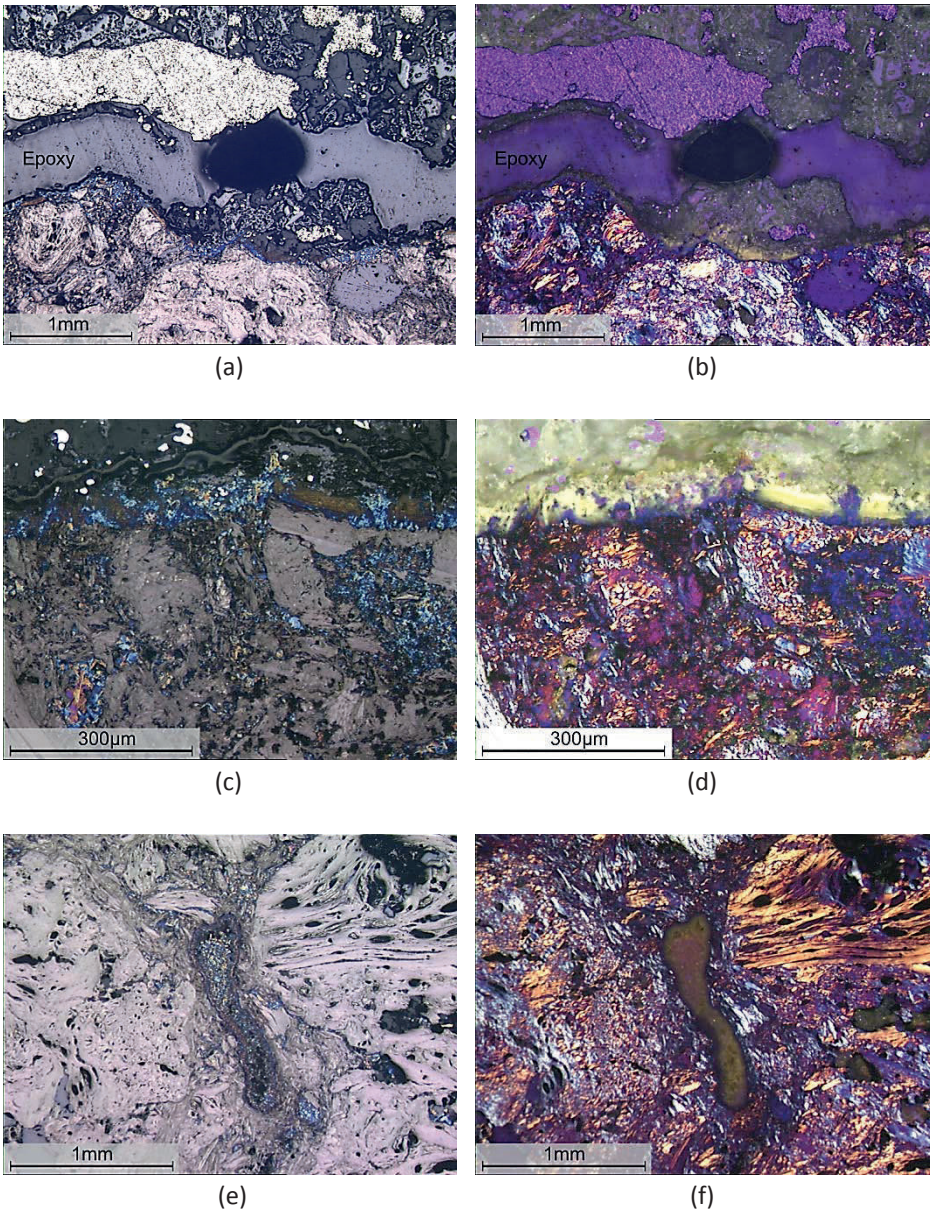

Figure D.8: Micrographs from low wear areas of a SGZv cathode. (a–d) Cathode surface. (e–f) Pore less than 0.5 cm from the surface.

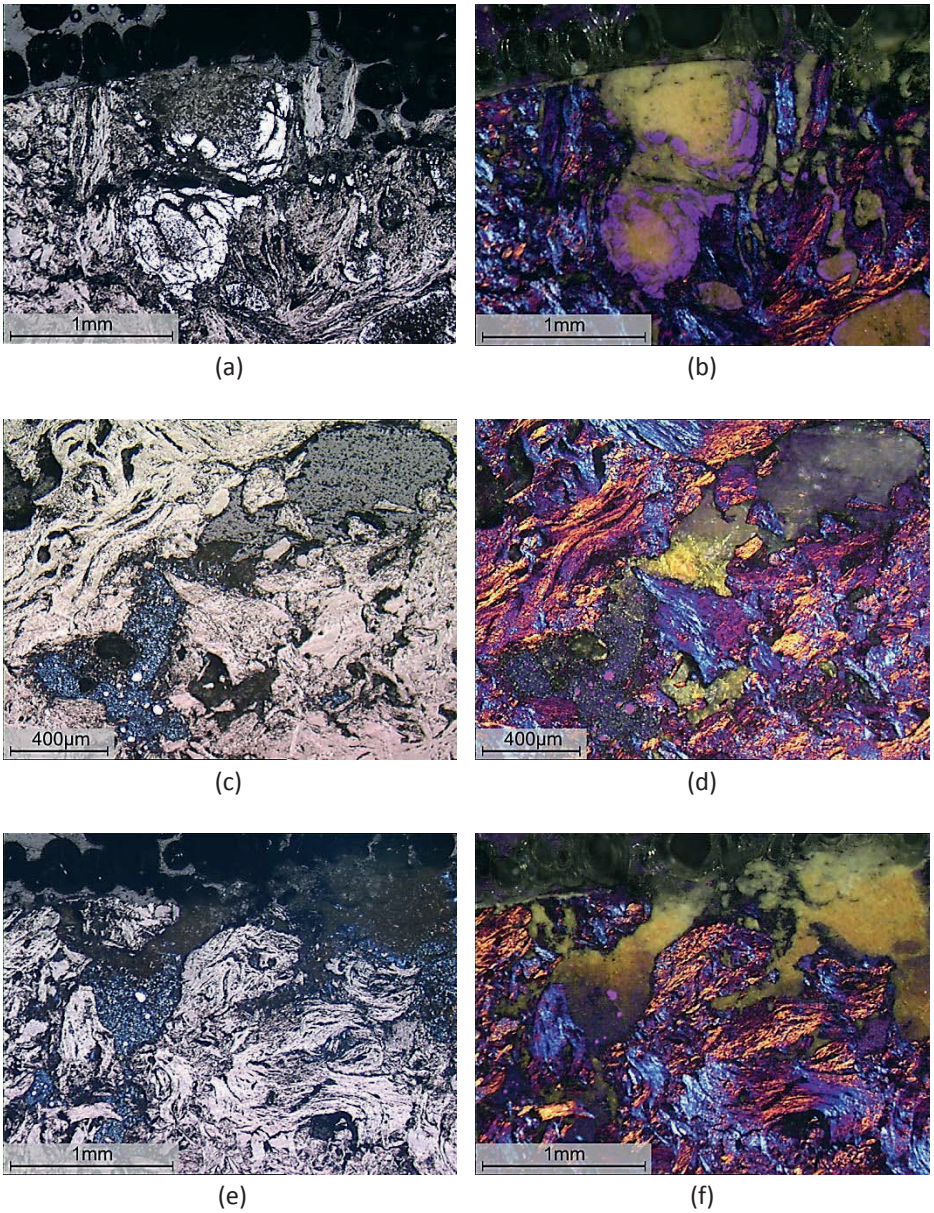

Figure D.9: Micrographs from high wear areas of a SGv cathode. (a–b and e–f) Cathode surface. (c–d) Pore less than 0.5 cm from the surface.

Appendix E

Thermal gradients in the lab. furnace

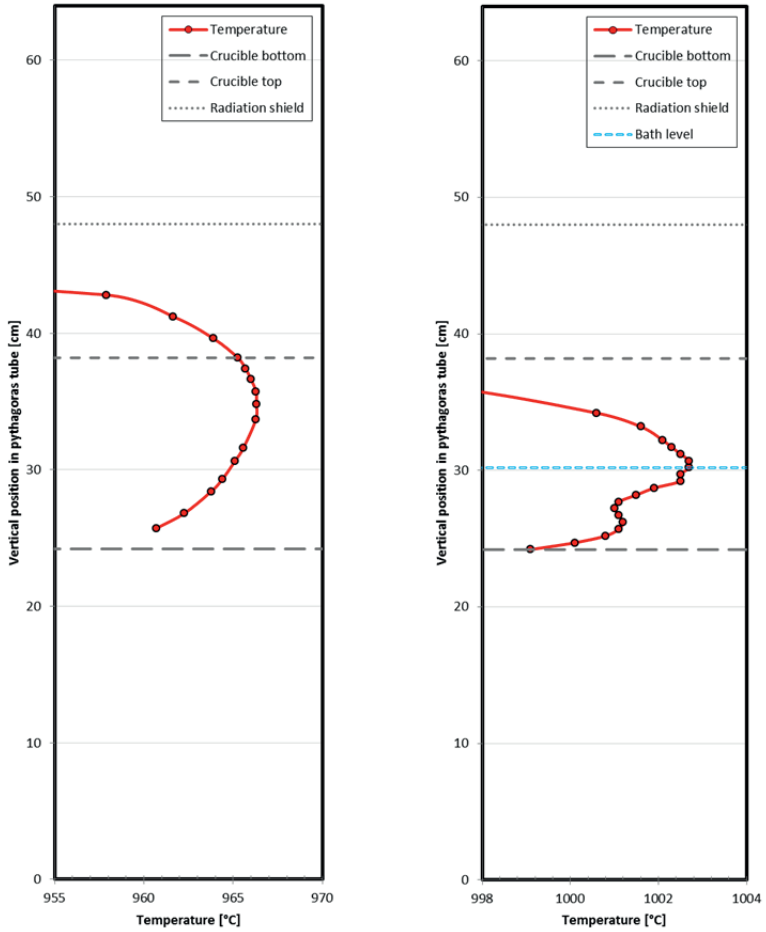

Figure E.1: Temperature measurements in the furnace (a) with an empty crucible and (b) crucible with bath.

Appendix F

Ohmic resistance of a solution

The voltage drop, or IR drop, between two electrodes in a solution due to ohmic resistance is dependent on the electrical conductivity of the solution and the geometry of the cell. Consider a simple geometry, as illustrated in Figure F.1, with two identical parallel plate electrodes with area A placed at a distance, L, away from each other. A uniform solution with specific conductivity, κ, occupies the volume between the electrodes. Except for the electrode-solution interfaces, all borders are insulated, negating any edge effects.

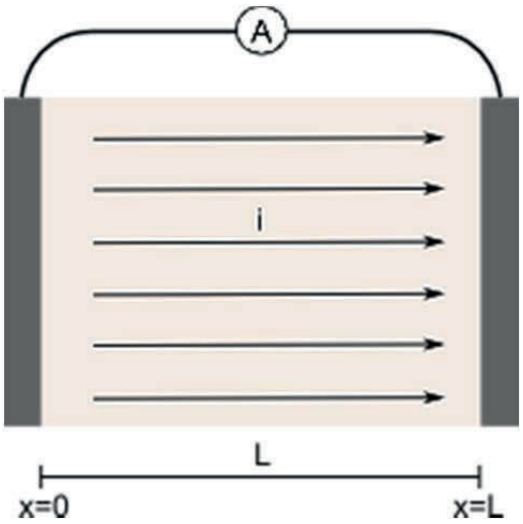

Figure F.1: Galvanic cell for calculating the ohmic resistance between two parallel plate electrodes.

The current density, i, through the solution is proportional to the electric field [117]:

$$i = \kappa \frac{dE}{dx} \tag{F.1}$$

Integration between the plates gives:

$$i\int_0^L dx = \kappa\int_{E_0}^{E_L} dE \tag{F.2}$$

$$iL = \kappa(E_L - E_0) = \kappa\Delta E_\Omega \tag{F.3}$$

where ΔE_Ω is the ohmic potential difference between the two electrodes.

$$\Delta E_\Omega = IR = \frac{iL}{\kappa} = \frac{IL}{\kappa A} \tag{F.4}$$

Thus, the ohmic resistance in the solution is given by

$$R = \frac{L}{\kappa A} \tag{F.5}$$

where $\frac{L}{A}$ can be considered as a geometrical cell factor, G.

$$R = \frac{G}{\kappa} \tag{F.6}$$

The geometry of an electrochemical cell is often more complicated than the one treated above, and the geometrical factor is often found by empirical means, using a solution with a known conductance.

In order to estimate the geometrical factor for the cell used in this work, some simplifications were required. Consider a horizontal cross section of a crucible with inner diameter 2b containing electrolyte and two vertically placed cylindrical electrodes with diameter 2a, illustrated by Figure F.2. The electrodes are placed on a line of symmetry with equal distance to the crucible wall, $l_{e\text{-}c}$, and with an interpolar distance of l_i. Calculating the geometry factor for such a cell is complicated. An approximation can be obtained from the simplified geometry illustrated in Figure F.3.

In Figure F.3 the electrodes are treated as parallel plate electrodes, similar as in Figure F.1. l_{max} is the longest path between the two electrodes. In Figure F.2 this corresponds to the sum of the distance from the backside of the anode to the crucible wall ($l_{e\text{-}c}$), one half of the crucible circumference (πb), and the distance from the crucible wall to the backside of the cathode ($l_{e\text{-}c}$), i.e.

$$l_{max} = 2l_{e\text{-}c} + \pi b \tag{F.7}$$

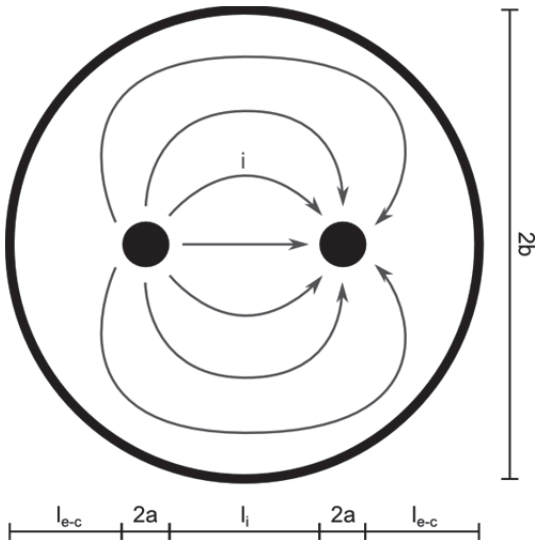

Figure F.2: Horizontal cross section of an electrochemical cell similar to that used in this work.

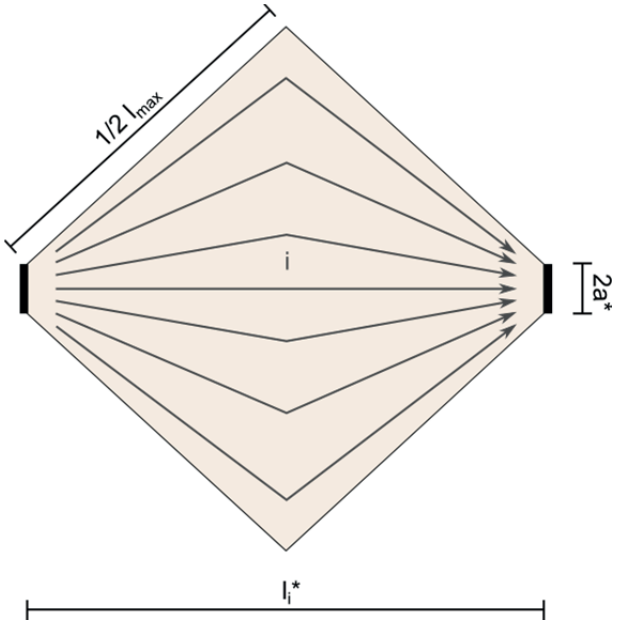

Figure F.3: Simplified geometry of cell in Figure F.2.

In the case of cylindrical electrodes, the interpolar distance is not the same at every point on the electrode surface, as illustrated in Figure F.4. On the front side, i.e. for $0 \leq \theta \leq \pi/2$

$$\Delta l_i(\theta) = a - a\cos\theta \qquad \text{(F.8)}$$

On the backside, i.e. for $\pi/2 < \theta \leq \pi$

$$\Delta l_i(\theta) = \Delta l_i(\pi/2) + a(\theta - \pi/2) = a + a(\theta - \pi/2) \tag{F.9}$$

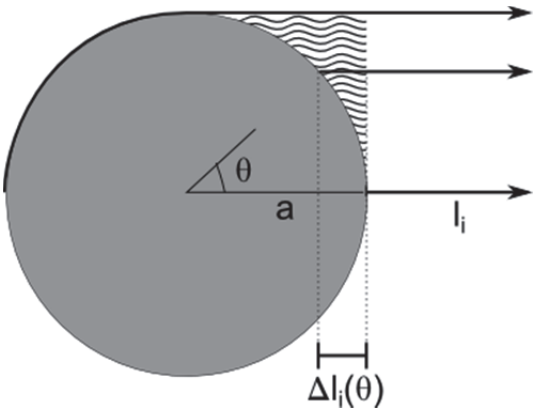

Figure F.4: Cross section of cylindrical electrode illustrating the variation of the interpolar distance as a function of the position on the electrode interface.

The marked area on the front side of the electrode in Figure F.4 depicts the integral of $\Delta l_i(\theta)$ for θ values from zero to $\pi/2$.

$$A = a^2 - \frac{\pi a^2}{4} \tag{F.10}$$

Over a vertical distance a, this gives a mean difference in the interpolar distance for the front side of the electrode

$$l_{i\_front} = a - \frac{\pi a}{4} \tag{F.11}$$

The increase of the interpolar distance at the back side of the electrode is proportional to θ, and over a distance of $\pi a/2$ the mean difference in interpolar distance is equal to $\Delta l_i(3\pi/4)$.

$$l_{i\_back} = a + \frac{\pi a}{4} \tag{F.12}$$

The mean difference in the interpolar distance for the planar electrode in Figure F.3 can then be found from the following equation.

$$2a^*\Delta l_i^* = 2a\, l_{i\_front} + \pi a\, l_{i\_back} \tag{F.13}$$

where $2a^* = 2a + \pi a$. Equations (F.11)–(F.13) then yields:

$$\Delta l_i^* = \frac{2 + \frac{\pi}{2} + \frac{\pi^2}{4}}{2 + \pi} a \tag{F.14}$$

The interpolar distance, l_i*, in Figure F.3 is thus

$$l_i^* = l_i + 2\Delta l_i^* = l_i + \frac{4+\pi+\frac{\pi^2}{2}}{2+\pi} a \tag{F.15}$$

The simplified geometry factor of Figure F.3 can now readily be found by integration according to Eq. (F.2), where the current density is a function of x.

$$\int_0^{l_i^*} i(x)\,dx = \kappa \int_{E_0}^{E_{l_i^*}} dE = \kappa \Delta E_\Omega \tag{F.16}$$

$$\int_0^{l_i^*} i(x)\,dx = 2\int_0^{\frac{l_i^*}{2}} i(x)\,dx = \frac{2}{L}\int_0^{\frac{l_i^*}{2}} \frac{I}{2\left(a^* + \frac{l_{max}}{l_i^*}x\right)}\,dx \tag{F.17}$$

$$\int_0^{l_i^*} i(x)\,dx = \frac{I}{L}\frac{l_i^*}{l_{max}}\left[\ln\left|a^* + \frac{l_{max}}{l_i^*}x\right|\right]_0^{\frac{l_i^*}{2}} \tag{F.18}$$

$$\int_0^{l_i^*} i(x)\,dx = \frac{I}{L}\frac{l_i^*}{l_{max}}\ln\left(1 + \frac{l_{max}}{2a^*}\right) \tag{F.19}$$

where L is the length, or the immersion depth of the cylindrical electrodes. It is assumed that there is no solution under the electrodes and, thus, no edge effects.

This means the geometric cell factor in this case is:

$$G = \frac{l_i^*}{L\,l_{max}}\ln\left(1 + \frac{l_{max}}{2a^*}\right) \tag{F.20}$$

In some of the electrochemical experiments discussed in Chapter 6 the parameters were as following: b = 14.5 cm, a = 0.4 cm, L = 4 cm, l_i = 7.7 cm. This yields G = 0.115 cm^{-1}. It is assumed that this value is a reasonable estimate, even though electrolyte was present beneath the electrodes and there will have been edge effects.

Appendix G

Activity of AlF_3 and NaF

For NaF–AlF_3 melts saturated with alumina, Sterten et al. [98] expressed the activities of NaF and AlF_3 as functions of the temperature and the molar ratio, $r = n_{NaF}/n_{AlF_3}$.

For $r* < r < 1.24$

$$\ln a_{AlF_3} = \frac{F}{RT}\left[1.361 \ln \frac{(3+r)(0.3+0.9r*)}{(3+r*)(0.3+0.9r)} + 0.9(r* - r) + 2.7 \ln \frac{3+r}{3+r*}\right] \quad \text{(G.1)}$$

For $1.24 < r < 15$

$$\ln a_{AlF_3} = \frac{F}{RT}\left[1.361 \ln \frac{(3+r)}{(0.3+0.9r)} - 1.493\right] + \ln a_{AlF_3}(r = 1.24) \quad \text{(G.2)}$$

and

$$\ln a_{NaF} = \frac{F}{RT}[3.63 \ln r + 0.454 \ln(3+r) - 4.084 \ln(0.3+0.9r) - 0.423] - 0.106 \quad \text{(G.3)}$$

$r*$ is the NaF/AlF_3 molar ratio of a melt saturated with both Al_2O_3 and AlF_3. The numerical value can be estimated from the following equation.

$$T(K) = 3282 \ln\left[\frac{0.3}{r*} + 0.9\right] - 271.2r* + 801 \quad \text{(G.4)}$$

For a melt with NaF/AlF_3 molar ratio of 2.2 at 1000°C, the above equations yield a_{AlF_3} = 1.855×10^{-3} and a_{NaF} = 1.770×10^{-1}. It is assumed that these values are a reasonable approximation for the alumina saturated melt used in electrochemical experiments described in Chapter 6, even though this melt also contain 5 wt% CaF_2 and varying amounts of Al_4C_3.

Appendix H

Addendum to the CV discussion

In Section 6.2.4.2 it was assumed that some of the peaks seen in the voltammograms were a result of Si impurities. This addendum covers further elaboration on this matter.

Figure H.1 shows voltammograms of varying sweep rates recorded on graphite in alumina saturated cryolitic melt without additions of Al_4C_3. The voltammograms have been normalised, i.e. the current density (i) has been divided by the square root of the sweep rate ($v^{1/2}$). In the case of a simple reversible reaction with soluble species, i is proportional to $v^{1/2}$, and normalised voltammograms for varying sweep rates should thus overlap. Peak B is obviously growing with increasing sweep rates, but is not proportional to $v^{1/2}$. This behaviour excludes the possibility of a reversible reaction or a totally irreversible reaction. Furthermore, peak B is being shifted in anodic direction while peak C is shifted in cathodic direction, closer to the aluminium deposition potential. This "stretching" of the voltammogram may be an indication of uncorrected IR drop between the electrodes. It is also one of the characteristics of a quasi-reversible system. Assuming the anodic and the cathodic transfer coefficients are not equal, i.e. $\alpha_A \neq \alpha_C$, all the diagnostic tests for quasi-reversible systems, according to Table 6.3, are fulfilled.

Peak D does not seem to be affected noticeably by the sweep rate, and is completely engulfed by peak B at sweep rates higher than 200 mV/s.

In the voltammograms shown in Figure H.2, the starting potential was set more cathodic than above. In this case peak C did not occur in the first sweep, nor did it appear in the second sweep when the anodic vertex potential was lower than 0.6 V. Peak C was first observed when the potential was reversed at 0.7 V or higher, as can be seen from Figure H.2. A possible explanation to this behaviour is that the reaction related to peak C is the formation of a thin carbide layer at the surface of the electrodes. Note that in this case the carbide is the carbide of an impurity in the melt, e.g. SiC. The electrode was kept at the starting potential, 0.3 V, for a few seconds before each run. Assuming the carbide formation proceeds to some extent at this potential, the electrode surface may have been covered by a thin carbide layer at the start of the potential sweep. This layer would then

have had to be oxidised and removed for further carbide formation to occur, which seems to be related to the anodic current rise at 0.7–0.9 V.

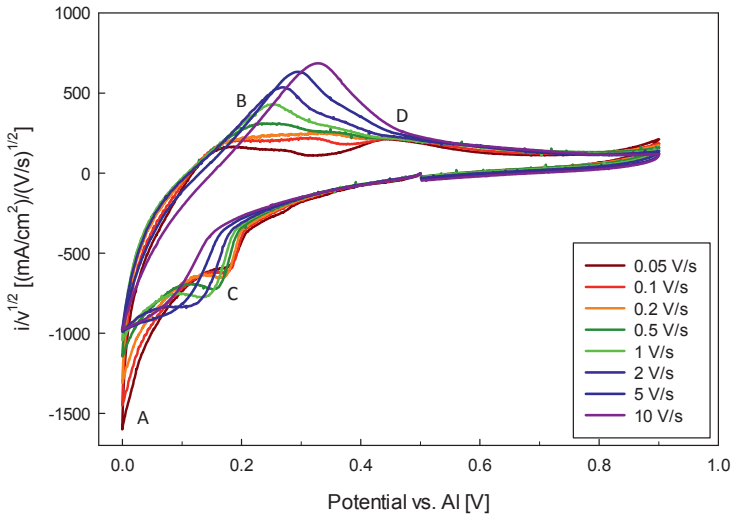

Figure H.1: Normalised cyclic voltammograms for graphite electrode (Ø 1 mm) in Al_2O_3 saturated cryolite melt with 10 wt% excess AlF_3 and 5 wt% CaF_2 at 1000°C. Varying sweep rates, starting potential = 0.5 V, cathodic sweep direction.

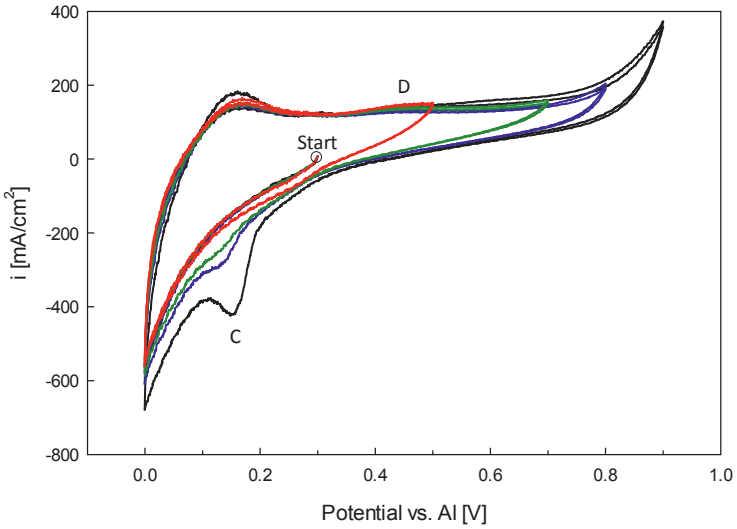

Figure H.2: Cyclic voltammograms for graphite electrode (Ø 1 mm) in Al_2O_3 saturated cryolite melt with 10 wt% excess AlF_3, 5 wt% CaF_2, and 0.2 wt% Al_4C_3 at 1000°C. Two or more cycles were recorded each run, with a starting potential of 0.3 V, a cathodic vertex potential of 0 V, a varying anodic vertex, and at a sweep rate of 0.2 V/s.

Normalised voltammograms of varying sweep rates recorded on tungsten, shown in Figure H.3, display a fairly good overlap of peaks C and D, indicating that the system is close to reversible. The overlap is not perfect, however, and there is a small shift of peak C in cathodic direction for increasing sweep rates. In this, the system resembles a quasi-reversible system.

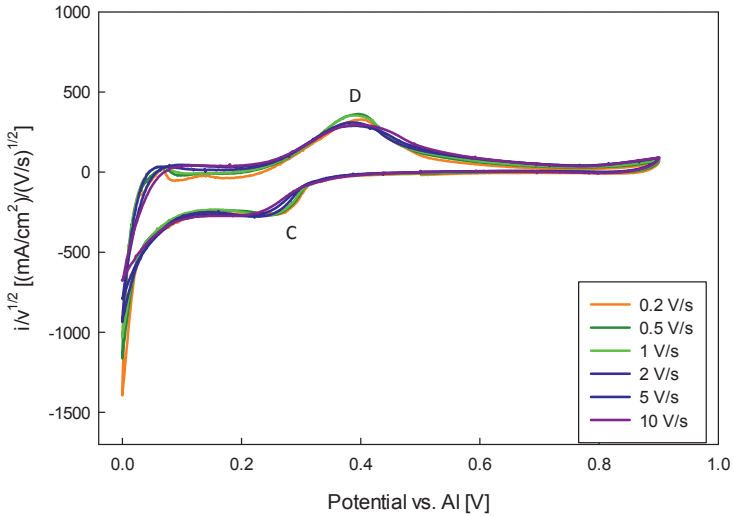

Figure H.3: Normalised cyclic voltammograms for tungsten electrode in Al_2O_3 saturated cryolite melt with 10 wt% excess AlF_3 and 5 wt% CaF_2 at 1000°C. Varying sweep rates, starting potential = 0.5 V, cathodic sweep direction.

According to Table 6.1, the potential difference between the cathodic and the anodic peak for a reversible system can be found by the following equation.

$$\Delta E_p = \frac{RT\ln(10)}{nF} \tag{6.10}$$

For a quasi-reversible system, ΔE_p is greater than that found from eq. (6.10), and increases with increasing sweep rate.

It can be assumed that a quasi-reversible system will behave in a reversible manner as the sweep rate approaches zero. ΔE_p was found to increase proportionally to the square root of the sweep rate and could thus be extrapolated to ν = 0, shown in Figure H.4. Inserting the extrapolated value, 129 mV, into equation (6.10) yields n = 2. This indicates that the peak currents C and D are related to reduction and reoxidation of a divalent species.

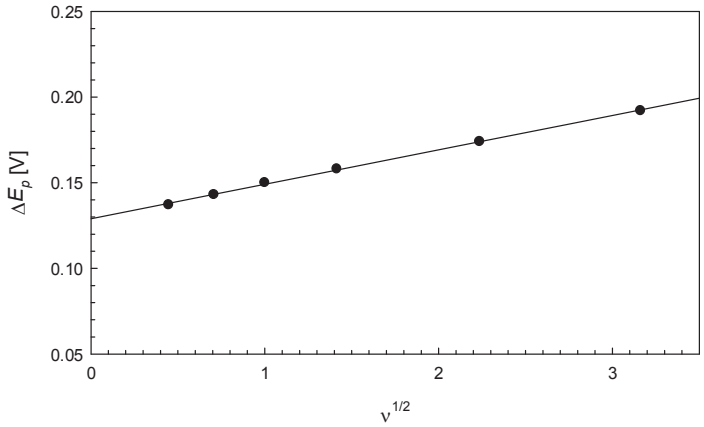

Figure H.4: The peak gap between peak C and D for the voltammograms in Figure H.3 plotted against the square root of the sweep rate. Linear extrapolation gives 129 mV at ν = 0.

Considering a totally irreversible system, the cathodic peak potential, E_p^C, varies with the sweep rate according to:

$$E_p^C = K - \frac{RT\ln(10)}{2\alpha_C n_\alpha F}\log(v) \tag{H.1}$$

where K is a system dependent constant, α_C is the transfer coefficient for the cathodic process and n_α is the number of electrons transferred up to, and including, the rate determining step.

As the cathodic peak potential E_p^C seems to be proportional to $\log(v)$, see Figure H.5, it can be assumed that equation (H.1) gives a reasonable estimate for the peak potential in this quasi-reversible system. The slope of the extrapolated line in Figure H.5 gives a decrease of 35 mV per decade increase of the sweep rate. Based on eq. (H.1), this yields $\alpha_C n_\alpha$ = 3.5, which means $n_\alpha \geq 4$.

Given that the above assumptions are reasonable, peak C can be ascribed to a two-step reduction of a species of valence four or more, of which the rate determining step is a two electron transfer reaction. And in that case, peaks C and D are probably not related to Al-W alloy formation. It rather seems probable that the peaks are related to an impurity in the melt. Si was the most abundant impurity, according to XRF analysis of bath samples (Table 6.8), and is therefore the most likely element to be ascribed to the current peaks.

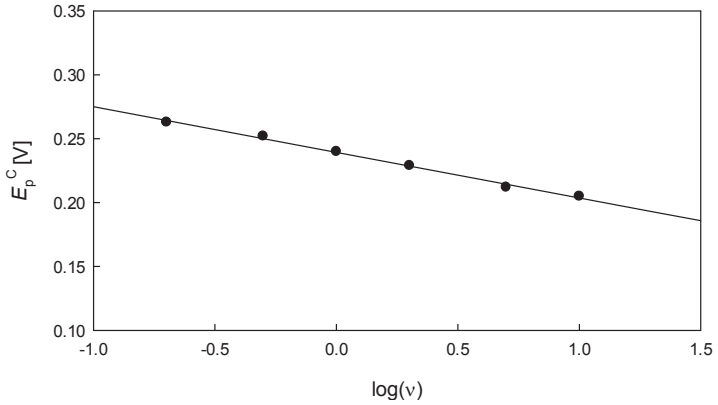

Figure H.5: The peak potential of peak C in the voltammograms in Figure H.3 plotted against the logarithm of the sweep rate.

Devyatkin et al. [118] observed reduction and oxidation peaks related to Si anodic of aluminium deposition on a platinum electrode, using cyclic voltammetry to study the behaviour of titanium, silicon, and boron oxides in cryolite-alumina melts. A SiO_2 concentration of 0.35 mmol/cm^3 was used in those experiments, which is approximately equivalent to 1 wt% SiO_2 or 4700 ppm Si. In a cryolite – K-feldspar (Na_3AlF_6 – $KAlSi_3O_8$) system, Grjotheim et al. [119] identified two peaks related to Si reduction anodic of aluminium deposition on a graphite electrode. They concluded that the reduction mechanism for Si involved a two-step reduction of Si containing species:

$$Si(IV) + 2e^- \rightarrow Si(II) \quad \text{(H.2)}$$

$$Si(II) + 2e^- \rightarrow Si(0) \quad \text{(H.3)}$$

This is in good agreement with the findings in this work.